

Fluid-structure interaction during hydraulic transients in pressurized pipes: experimental and numerical analyses

THÈSE N° 7099 (2016)

PRÉSENTÉE LE 14 OCTOBRE 2016

À L'ÉCOLE POLYTECHNIQUE FÉDÉRALE DE LAUSANNE
À LA FACULTÉ DE L'ENVIRONNEMENT NATUREL, ARCHITECTURAL ET CONSTRUIT
LABORATOIRE DE CONSTRUCTIONS HYDRAULIQUES

ET

À L'INSTITUTO SUPERIOR TÉCNICO (IST) DA UNIVERSIDADE DE LISBOA

PROGRAMME DOCTORAL EN GÉNIE CIVIL ET ENVIRONNEMENT
DOUTORAMENTO EM ENGENHARIA CIVIL

POUR L'OBTENTION DU GRADE DE DOCTEUR ÈS SCIENCES (PhD)

PAR

David FERRÀS SEGURA

acceptée sur proposition du jury:

Prof. A. Rinaldo, président du jury
Prof. A. Schleiss, Prof. D. I. Cameira Covas, directeurs de thèse
Dr C. Nicolet, rapporteur
Prof. B. Brunone, rapporteur
Prof. F. Avellan, rapporteur



Suisse
2016

Martin Heidegger

Questioning is the piety of thinking

Acknowledgements

This research is supported by the Portuguese Foundation for Science and Technology (Fundação para a Ciência e a Tecnologia) through the project ref. PTDC/ECM/112868/2009 “Friction and mechanical energy dissipation in pressurized transient flows: conceptual and experimental analysis” and the PhD grant ref. SFRH/BD/51932/2012 also issued by FCT under the IST-EPFL joint PhD initiative.

I would like to express my sincere gratitude to my supervisors Prof. Dídia I.C. Covas (Instituto Superior Técnico, Universidade de Lisboa) and Prof. Anton J. Schleiss (École Polytechnique Fédérale de Lausanne) for their continuous interest, support and guidance during this study. Equally, I would like to thank Dr. Pedro A. Manso (École Polytechnique Fédérale de Lausanne) for his orientation. He has been always readily available to provide his valuable perspective and expertise.

I am specially grateful to the research group formed by Prof Dídia I.C. Covas, Prof. Helena Ramos and their respective students. The strong commitment and high-up skillfulness of the team together with a contagious vocational spirit provided an extraordinary atmosphere to carry out this research work with joy. Some instances of this are the priceless support from Dr. Nuno Martins on the experimental work in the laboratory, as well as Moisés and Pierfabrizio’s help, or the discussions held with Nuno, João or Mariana, which prompted brainstorming and mind-broadening.

My stays in both cities Lisbon and Lausanne have been complemented with invaluable friendships, travelling companions that made this journey a sweet endeavour. Such as José Pedro and Natércia with their ungauged hospitality, he may not remember but José Pedro was the first introducing me to LCH team; lucky me! Artur, the perfect office mate and lunch mate, together with Pedro Morgado, they showed me crucial things in life such as the fransesinha taste. Italians, Lisbon would not have been the same without you two Teresa and Fede. Gondolera I want another red-carpet day. Not to mention ‘el surtido de ibéricos’: Carmelo, Mário and Sebastián, let’s go to Crazy Piano’s and then to Frankenstein’s street? And talking about Crazy Piano’s, Estíbaliz, this last year you became my undercover personal advisor, high-class luxury. Ben, also a good advisor you are. IPA expert thanks for leading the steep club. Not for the sake of comparison, but the Italians in Lisbon were the Greeks in Lausanne, you are an awesome company Fotini and Mariangela! And to all the colleagues from both labs LCH and Cehidro, thank you very much for your daily companionship.

Lausanne, September 27, 2016

D. F.

Abstract

The aim of the present research is to identify, describe and quantify the principal mechanic-hydraulic relationships during hydraulic transients in pressurized pipe flows in view of improving pipe design and reduce pipe and system failure. Phenomena affecting the transient wave, such as fluid-structure interaction, unsteady skin friction, dry friction or pipe-wall viscoelasticity are analysed from both the experimental and numerical standpoints. The main goal is the improvement of one-dimensional (1D) waterhammer modelling in the time-domain by means of the well-known method of characteristics approach.

Experimental work is presented for three different experimental facilities: a straight copper pipe, a coil copper pipe and a coil polyethylene pipe. The analysis of the experimental data highlights differences in the response of each system in terms of wave shape, damping, and dispersion. The straight copper pipe behaviour is highly dependent on the pipe supports and anchoring; the coil copper pipe to the deformation in the radial direction; while the polyethylene facility to the pipe-wall viscoelasticity.

In a second stage, the research focuses on the numerical modelling of hydraulic transients in pipe coils. The analysis is based on the experimental data collected in the coil copper pipe facility. First, a structural analysis is carried out for static conditions and then for dynamic. A four-equation model is implemented incorporating the main interacting mechanisms: Poisson, friction and junction coupling. The model is successfully validated for different flow rates showing a good performance of the dynamics of the coil behaviour during hydraulic transients.

Finally, the research focuses on the straight copper pipe facility, for which the simplicity of the set-up allows deepening on the basic modelling assumptions in fluid-structure interaction. First, friction coupling is assessed using the basic four-equation model and unsteady skin friction and dry friction are incorporated in the solver. The analysis shows the dissipative effect of dry friction phenomenon, which complements that of skin friction. In a second approach junction coupling is tackled and the resistance to movement due to inertia and dry friction of the pipe anchor blocks is analysed. Numerical results successfully reproduce laboratory measurements for realistic values of calibration parameters.

The work successfully identifies, describes and quantifies different physical phenomena related with FSI by means of experimental modelling and valid numerical reproduction of experimental results. Experimental modelling approaches are developed and data is made available for benchmark testing of numerical tools considering facilities with different set-up geometries and materials. A new standpoint based on pipe-degrees-of-freedom is suggested

Abstract

for facing FSI problems, the structural behaviour of pipe coils is successfully described and FSI in straight pipelines is analysed focusing on both junction and friction coupling. A new set of numerical solvers are developed, presented and thoroughly discussed, which can be readily used for the design of new industrial piping systems or the safety assessment of existing piping facilities.

Key words: hydraulic transients; waterhammer; fluid-structure interaction; experimental data; straight pipelines; stress-strain analysis; membrane theory of shells of revolution; junction coupling; Poisson coupling; friction coupling; viscoelasticity; hysteresis; dry friction; skin friction; stick-slip instability.

Résumé

Le but de la présente recherche est de identifier, décrire et quantifier les principales relations mécaniques-hydrauliques lors des transitoires hydrauliques dans les écoulements sous pression dans le but d'améliorer la conception des tubes et réduire la défaillance du système. Les phénomènes affectant l'onde transitoire tels que les interactions fluide-structure, la frottement superficiel instationnaire, le frottement sec ou la viscoélasticité de la paroi du tube sont analysés de manière expérimentale et numérique. L'objectif principal est l'amélioration de la modélisation 1D du coup de bélier dans le domaine temporel au moyen de la méthode des caractéristiques.

Une revue de la littérature sur l'interaction fluide-structure des coups de bélier est présentée. Les mécanismes d'amortissement qui affectent l'onde transitoire sont examinés, y compris le frottement superficiel, le frottement sec et de structure. Enfin, un aperçu des principales applications industrielles de l'interaction fluide-structure est fournie. L'analyse montre le manque général de FSI dans la modélisation des du coup de bélier 1D, l'absence de directives pratiques indiquant pour quelles installations de tuyauterie FSI doivent être considérés lors de la conception, ainsi que la non-disponibilité d'outils de modélisation FSI couvrant les phénomènes physiques les plus importants. La viscoélasticité de la paroi du tube, le frottement superficiel instationnaire et le frottement du Coulomb sont des phénomènes à inclure dans les solveurs IFS. En plus, le besoin d'outils plus précis pour la description et la conception des blocs d'ancrage est mis en évidence.

Des essais expérimentaux effectués au *Laboratoire de l'Hydraulique et de l'Environnement de l'Instituto Superior Técnico* (LHE/IST), Lisbonne, Portugal, sont présentés pour trois installations expérimentales différentes : un tuyau droit en cuivre, un tuyau en bobine en cuivre et un tuyau en bobine en polyéthylène. L'analyse des données expérimentales met en évidence les différences dans la réponse de chaque système en termes de forme d'onde, d'amortissement, et la dispersion. Le comportement de tuyau droite de cuivre est fortement dépendant des supports et les conditions d'ancrage en raison de l'interaction fluide-structure qui se produit lorsque la conduite est autorisée à se déplacer dans la direction longitudinale. L'interaction fluide-structure a également un rôle important dans le tuyau en bobine en cuivre, qui est autorisée à se déformer dans la direction radiale. Enfin, l'effet dominant dans l'installation en polyéthylène est le comportement viscoélasticité de la paroi du tube, où la réponse retardée de la déformation du matériau (hystérésis) augmente l'amortissement de l'onde transitoire. Dans une deuxième étape, la recherche se concentre sur la modélisation numérique des transitoires hydrauliques en bobines. L'analyse est basée sur les données expérimentales

Abstract

recueillies dans l'installation de tuyaux en bobine de cuivre. Tout d'abord, une analyse de déformation-contrainte est effectuée afin de comprendre les déplacements de la bobine dans des conditions statiques pour des chargements de pression interne. Ensuite, une analyse dynamique est effectuée dans le but de coupler l'écoulement de la conduite transitoire avec le mouvement axial du tuyau tout en négligeant l'inertie radiale, la flexion et la torsion du système de tuyauterie. Par conséquent, un modèle à quatre équations est mis en œuvre en incorporant les mécanismes de interaction principaux : Poisson, friction et jonction. Le modèle est validé avec succès pour différents débits montrant une bonne performance de la dynamique du comportement de la bobine lors des transitoires hydrauliques.

Enfin, la recherche se concentre sur l'installation de tuyau droit de cuivre, pour lequel la simplicité de la mise en place permet d'approfondir sur les hypothèses de modélisation de base en interaction fluide-structure. Tout d'abord, le couplage de friction est évalué en utilisant le modèle de base à quatre équation et friction superficiel variable et de frottement du Coulomb sont incorporés dans le code. L'analyse montre l'effet dissipatif du phénomène de frottement du Coulomb, qui complète celle de la friction superficiel. Dans un second approche couplage de jonction est abordée et la résistance au mouvement en raison de l'inertie et de frottement du Coulomb des blocs d'ancrage de tuyauterie est analysé. Les résultats numériques reproduisent avec succès des mesures de laboratoire pour des valeurs réalistes des paramètres d'étalonnage.

La thèse, avec succès, identifie, décrit et quantifie les différents phénomènes physiques liés à FSI au moyen de la modélisation expérimentale et de reproduction numérique valide de résultats expérimentaux. Approches de modélisation expérimentales novatrices sont développées et les données sont mises à disposition pour les tests d'évaluation des outils numériques en tenant compte des installations avec différentes géométries et matériaux. Une nouvelle série de solveurs numériques sont développés, présenté et discuté à fond, qui peut être facilement utilisé pour la conception de nouveaux systèmes de tuyauterie industrielle ou l'évaluation des installations de tuyauterie existantes de sécurité.

Mots clefs : transitoires hydrauliques; coup de bélier; interaction fluide-structure; données expérimentales; conduites droites; analyse de contrainte-déformation; théorie de coque; couplage de jonction; couplage Poisson; couplage de friction; viscoélasticité; hystérèse; frottement du Coulomb; friction superficiel; stick-slip instabilité.

Resumo

O objetivo do presente estudo é identificar, descrever e quantificar as relações mecânico-hidráulicas principais durante transientes hidráulicos em sistemas pressurizados com o objetivo de melhorar a concepção de tubulação e falha no sistema. Fenômenos que afetam a onda transiente como a interação fluido-estrutura (FSI), o atrito superficial variável, a fricção de Coulomb ou a viscoelasticidade da parede de tubo são analisados do ponto de vista experimental e numérico. O objectivo principal é a melhoria da modelação 1D do golpe de aríete no domínio do tempo, por meio do método das características.

Uma extensa revisão do estado de arte sobre interação fluido-estrutura em sistemas em pressão é apresentado. Mecanismos de amortecimento que afectam a onda transitória são bem revistas, incluindo o atrito superficial, a fricção de Coulomb e o amortecimento estrutural. Finalmente uma visão sobre as principais aplicações industriais de interação fluido-estrutura é apresentada. A análise observa a falta geral de FSI no modelo 1D de golpe de aríete, a falta de orientações práticas, indicando, para que as instalações de tubulação deve FSI ser considerados durante o projeto, bem como a indisponibilidade de ferramentas de modelagem FSI cobrindo os fenômenos físicos mais importante. A viscoelasticidade da parede de tubo, o atrito superficial variável e a fricção de Coulomb são fenômenos a serem incluídos no modelo FSI. Também a necessidade de ferramentas mais precisas para o desenvolvimento e definição de ancoragens e suportes da tubulação é evidenciado.

O trabalho experimental foi realizado no *Laboratório de Hidráulica e Recursos Hídricos e Ambientais do Instituto Superior Técnico* (LHE/IST), Lisboa, Portugal, contando com três instalações experimentais diferentes: tubagem rectilineade cobre, tubo bobinado de cobre e tubo bobinado de polietileno. A análise dos dados experimentais evidencia diferenças na resposta de cada sistema em termos de forma de onda, de amortecimento e de dispersão. O comportamento da tubagem rectilinea é altamente dependente dos suportes e das condições de ancoragem, devido à interacção fluido-estrutura que ocorre quando o tubo se desloca na direcção longitudinal. A interacção fluido-estrutura tem também um papel importante no tubo bobinado de cobre, quando este permite deformação na direcção radial. Finalmente, o efeito dominante na unidade de polietileno é o comportamento viscoelástico da parede do tubo, em que a resposta retardada da deformação do material (histerese) aumenta o amortecimento da onda transitória.

Numa segunda fase, a investigação centra-se na modelagem numérica de transientes hidráulicos em tubos bobinados. A análise baseia-se nos dados experimentais recolhidos na instalação de tubo bobinado de cobre. Em primeiro lugar uma análise de tensão-deformação é levada

Abstract

a cabo de modo a compreender os deslocamentos da bobina em condições estáticas para cargas de pressão interna. Desta forma, uma análise dinâmica é realizada para o acoplamento do fluido com o movimento axial da parede de tubo, negligenciando a inércia radial, flexão e torção do sistema de tubulação. Consequentemente, um modelo de quatro equações é implementado incorporando os principais mecanismos de acoplamento: Poisson, fricção e junção. O modelo é validado com êxito, para diferentes caudais iniciais, mostrando um bom desempenho da dinâmica do comportamento da bobina durante transientes hidráulicos.

Finalmente, a investigação centra-se na instalação rectilínea de cobre, para o qual a simplicidade da configuração permite aprofundar sobre as premissas de modelagem básicas da interacção-fluido-estrutura. Em primeiro lugar, o acoplamento de fricção é avaliado usando o modelo de base de quatro equações, incorporando o atrito superficial variável e a fricção de Coulomb. A análise mostra o efeito da dissipação do fenómeno de fricção de Coulomb que complementa o atrito superficial. Em segundo, o acoplamento da junção é abordado e a resistência ao movimento devido à inércia e à fricção de Coulomb dos blocos de ancoragem da tubulação são analisados. Os resultados numéricos reproduzem com sucesso as medições do laboratório para valores realistas de parâmetros de calibração.

A tese, com sucesso, identifica, descreve e quantifica diferentes fenómenos físicos relacionados com FSI por meio de modelagem experimental e reprodução numérico válido de resultados experimentais. Inovadoras abordagens de modelagem experimentais são desenvolvidos e os dados são disponibilizados para teste de desempenho de ferramentas numéricas considerando instalações com diferentes geometrias e materiais. Um novo conjunto de códigos numéricos são desenvolvidos, apresentado e amplamente discutido, o que pode ser facilmente utilizado para a concepção de novos sistemas de tubulação industrial ou a avaliação da segurança de instalações de tubagens existentes.

Palavras-chave: transientes hidráulicos; golpe de aríete; interacção fluido-estrutura; dados experimentais; análise tensão-deformação; teoria de membrana; acoplamento de junção; acoplamento de Poisson; acoplamento de fricção; viscoelasticidade; histerese; fricção de Coulomb; atrito superficial; instabilidade de deslizamento intermitente.

Resumen

El objetivo de la presente investigación es identificar, describir y cuantificar las principales relaciones mecánico-hidráulicas durante flujos transitorios a presión a fin de mejorar el diseño de sistemas de tuberías y reducir roturas y accidentes. Factores que afectan la onda transitoria, como interacción fluido-estructura, fricción fluido-sólido, fricción sólido-sólido o viscoelasticidad de la pared de la tubería son analizados desde ambos puntos de vista, experimental y numérico. El objetivo final es la mejora de modelos unidimensionales (1D) de golpe de ariete basados en el conocido método de las características.

El trabajo presenta una extensiva revisión de literatura en el campo de interacción fluido-estructura en modelos unidimensionales de golpe de ariete. Los efectos de amortiguación de onda son también revisados, incluyendo fricción fluido-sólido o histéresis de la tubería. Finalmente, las principales aplicaciones industriales de interacción fluido-estructura son descritas. En general, el análisis realza el desuso en un contexto FSI de las conocidas herramientas de modelaje comúnmente aplicadas en el modelo clásico de golpe de ariete, la falta de guías de diseño y dimensionamiento indicando cuando FSI debe de ser considerado, así como la falta de disponibilidad de modelos de simulación que cubran los fenómenos físicos más importantes. La viscoelasticidad de la pared de tubería, fricción fluido-sólido y fricción sólido-sólido son factores que deberían de estar incluidos en códigos FSI y los criterios para su consideración y evaluación deberían de estar clarificados. La necesidad de herramientas más fiables y precisas para el diseño de los soportes y fijaciones de las tuberías es también realizada.

El análisis experimental, llevado a cabo en el Laboratorio de Hidráulica y medio-ambiente del Instituto Superior Técnico (LHE/IST), Lisboa, Portugal, es presentado para tres distintas instalaciones experimentales: una tubería de cobre recta, una tubería de cobre en bobina y una tubería de polietileno también en bobina. El análisis subraya las diferencias en la respuesta de cada uno de los sistemas en términos de forma, amortiguación y dispersión de onda. El comportamiento de la tubería de cobre recta depende, en gran medida, de los soportes y las condiciones de fijación del sistema debido a la interacción fluido-estructura que ocurre por el movimiento axial de la tubería. Interacción fluido-estructura tiene también un impacto importante en la tubería de cobre en bobina, la cual se deforma en la dirección radial. Finalmente, el efecto dominante en la instalación de polietileno es la viscoelasticidad de la pared de tubería, puesto que la respuesta retardada de la deformación de la pared (histéresis) causa un incremento de la amortiguación de la onda transitoria.

En una segunda fase, la investigación se centra en el desarrollo del modelo numérico en

Abstract

tuberías en bobina. El análisis se basa en datos experimentales recogidos en la instalación de cobre. Primero el comportamiento estructural del sistema es analizado para cargas estáticas de presión interna. Luego, un análisis dinámico estudia la interacción entre el flujo de la tubería y los desplazamientos axiales de esta, despreciando la inercia radial, la flexión y la torsión del sistema. Un modelo de cuatro-ecuaciones es implementado incorporando los tres mecanismos básicos de interacción: Poisson, fricción e interacción de juntas. El modelo es validado con éxito para diferentes condiciones iniciales, ofreciendo, en todos los casos, una buena representación del comportamiento dinámico de la instalación durante transitorios hidráulicos.

Finalmente el trabajo se centra en la tubería de cobre recta, su simplicidad geométrica permite profundizar en las simplificaciones básicas de simulación numérica de interacción fluido-estructura. Primero la interacción por fricción es estudiada usando el código básico de cuatro-ecuaciones con fricción variable fluido-sólido y fricción sólido-sólido de Coulomb. El análisis destaca la importancia de tener presente los dos fenómenos disipadores. En una segunda fase, la interacción por junta es analizada y la resistencia al movimiento por inercia y fricción de los bloques de anclaje es considerada. Los resultados numéricos reproducen con precisión las mediciones experimentales para valores realísticos de los parámetros del modelo. El presente trabajo identifica, describe y cuantifica con éxito los diferentes fenómenos físicos relacionados con FSI por medio de experimentos de laboratorio y modelación numérica. Novedosos enfoques de experimentación y los datos resultantes quedan disponibles como referencia para la verificación y validación de herramientas de simulación numérica, teniendo en consideración instalaciones con distintos materiales de tuberías, geometrías y configuraciones. Nuevos códigos de modelación han sido desarrollados, presentados y analizados. Su uso queda disponible para el diseño de nuevos sistemas de tuberías o para la evaluación y diagnóstico de instalaciones existentes.

Palabras clave: transitorios hidráulicos; golpe de ariete; interacción fluido-estructura; datos experimentales; tuberías rectas; análisis de tensiones y deformaciones; teoría de membrana; interacción por junta; interacción por Poisson; interacción por fricción; viscoelasticidad; histéresis; fricción de Coulomb; fricción superficial; inestabilidad de deslizamiento intermitente.

Contents

Acknowledgements	i
Abstract (English/Français/Português/Español/Català)	iii
List of figures	xv
List of tables	xxvii
List of acronyms and notation	xxix
1 General introduction	1
1.1 Research scope	1
1.2 Historical background	1
1.3 Aims and objectives	3
1.4 Methodology	4
1.5 Organization of the report	4
2 State-of-the-Art Review	7
2.1 Introduction	7
2.2 Definitions and basic concepts	8
2.2.1 Transient pipe-flow	8
2.2.2 Fluid-structure interaction:	9
2.2.3 Degrees-of-freedom in fluid-filled pipes	11
2.2.4 Vibration modes in fluid-filled pipes	13
2.2.5 Coupling mechanisms and modelling approaches	13
2.2.6 Classification of vibration and damping	14
2.2.7 Classic waterhammer theory	15
2.3 Damping mechanisms	18
2.3.1 Skin friction	18
2.3.2 Hysteretic damping	22
2.3.3 Dry damping	24
2.4 The most relevant experimental work programmes	26
2.4.1 Introduction and summary table	26
2.4.2 Research in the U.K.	28
2.4.3 Research in Germany	31

Contents

2.4.4	Research in The Netherlands	31
2.4.5	Research in the U.S.A.	32
2.4.6	Research in Mexico	35
2.4.7	Research in other regions	36
2.5	Numerical research	36
2.5.1	One degree-of-freedom models	36
2.5.2	Models with up to three degrees-of-freedom	38
2.5.3	Models for more than three degree-of-freedom	41
2.5.4	Coupling between different software	46
2.6	Engineering applications	46
2.6.1	FSI consideration in codes and standards	46
2.6.2	Anchor and support forces	47
2.6.3	Vibration damping and noise reduction	49
2.6.4	Earthquake engineering	49
2.6.5	Aerospace engineering	50
2.6.6	Biomechanics	50
2.7	Accidents and post-accident analyses related with FSI	51
2.8	Motivation and gaps of knowledge	52
3	Experimental work	55
3.1	Introduction	55
3.2	Experimental data collection	57
3.2.1	Straight copper pipe	57
3.2.2	Coil copper pipe	60
3.2.3	Coil polyethylene pipe	63
3.3	Experimental analysis	64
3.3.1	Pressure data analysis	64
3.3.2	Strain data analysis	73
3.4	Discussion of results	77
3.4.1	Fluid structure interaction	77
3.4.2	Pipe-wall rheological behaviour	79
3.5	Overview and concluding summary	81
4	Fluid-structure interaction in coils	83
4.1	Introduction	83
4.2	Stress-strain analysis	84
4.2.1	Introduction and background theory	84
4.2.2	Data collection	85
4.2.3	Model development	86
4.2.4	Model application	92
4.2.5	Model validation	99
4.2.6	Validation of the simplified equations	105

4.2.7	Pipe displacements using the elliptic torus model and the simplified equations	105
4.2.8	Research outcome	107
4.3	Fluid-structure interaction	108
4.3.1	Introduction and background theory	108
4.3.2	Data collection	109
4.3.3	Model development	111
4.3.4	Modelling approaches	113
4.3.5	Results discussion	125
4.3.6	Research outcome	128
4.4	Overview and concluding summary	129
5	Fluid-structure interaction in straight pipelines	131
5.1	Introduction	131
5.2	Friction coupling mechanisms	132
5.2.1	Introduction and background theory	132
5.2.2	Experimental data collection	133
5.2.3	Numerical model development	136
5.2.4	Model testing	142
5.2.5	Model application	146
5.2.6	Research outcome	152
5.3	Pipelines anchored against longitudinal movement	153
5.3.1	Introduction and background theory	153
5.3.2	Experimental data collection	154
5.3.3	Numerical model development	156
5.3.4	Model testing	163
5.3.5	Model application	167
5.3.6	Research outcome	174
5.4	Overview and concluding summary	175
6	General conclusions and future research	177
6.1	Research overview	177
6.2	Main scientific outcome	177
6.3	Engineering applications and future research	178
A	Derivation of governing equations	181
A.1	Governing equations	181
A.2	Derivation of the governing equations for the classic waterhammer theory . . .	184
A.3	Derivation of the governing equations for the four-equation model	186
A.3.1	Continuity in 1-DOF	186
A.3.2	Continuity in 3-DOF	187

Contents

B	MOC transformation for four-equation models	189
B.1	Introduction	189
B.2	System of equations	189
B.3	Transformation matrix	190
B.4	Compatibility equations	194
B.5	Application to the standard four-equation model	195
B.5.1	Poisson-uncoupled four-equation model	195
B.5.2	Poisson-coupled four-equation model	197
B.6	Summary table	199
C	Verification of the four-equation model	201
D	Dry friction implementation in a four-equation model	205
D.1	Modification of the momentum conservation equation of the pipe-wall	205
D.2	MOC transformation	208
D.2.1	System coefficients	208
D.2.2	Eigenvalues	208
D.2.3	Compatibility equations	208
E	Extended Joukowski equation	211
E.1	Introduction	211
E.2	Governing equations	212
E.3	Pressure rise in a conduit only anchored at the upstream end	213
E.3.1	Pressure rise in a conduit only anchored at the upstream end	213
E.4	Application and validation of the equations	215
F	Experimental work in the Straight Copper Pipe facility	217
F.1	Introduction	217
F.2	Summary test tables	217
F.3	Experimental tests	219
F.3.1	Tests with anchored downstream end (SCP1)	219
F.3.2	Tests with no anchors throughout the pipe (SCP2)	224
F.3.3	Tests with pipe midstream section anchored (SCP3)	229
F.3.4	Tests with pipe midstream and downstream sections anchored (SCP4)	234
	Bibliography	259
	<i>Curriculum vitae</i>	261

List of Figures

1.1	Summary of the main research work.	5
2.1	Sources of excitation and interaction between liquid and piping (Wiggert & Tijsseling, 2001).	10
2.2	Classification of fluid-structure interaction phenomena.	11
2.3	Spatial reference system and signs convention in a straight pipe element	12
2.4	Numerical approaches used in waterhammer research for FSI problems.	14
2.5	Comparison between quasi-steady friction (classic elastic model), Vítkovský and Vardy-Brown models during a hydraulic transient caused by a pump trip (Soares <i>et al.</i> , 2012).	20
2.6	Comparison of classic waterhammer model with adding first unsteady friction and then both unsteady friction plus pipe-wall viscoelasticity <i>vs.</i> experimental observations at the downstream pipe-end during a waterhammer event (Covas <i>et al.</i> , 2005).	23
2.7	Measured axial pipe velocity (a), and measured pressures at two different pipe locations (b,c) for a water-filled pipe excited by a steel rod impact (Tijsseling & Vardy, 1996a).	26
2.8	Facility set-up used by Thorley (1969) (a); and measured precursor wave in different sections of the pipe (b).	28
2.9	Single pipe axial impact experiment set-up (a); and T-piece pipe impact experiment set-up (b) (Vardy <i>et al.</i> , 1996)	29
2.10	Pressures and strains time series in the single pipe axial impact experiment (a) and in the T-piece pipe impact experiment (b). Solid lines correspond to experimental measurements and dashed lines to numerical output (Vardy <i>et al.</i> , 1996).	30
2.11	Vertical pipe line located in a subterranean salt cavern for de-brining under direct circulation (Bürmann, 1975).	31
2.12	FSI experimental set-up at Delft Hydraulics (Kruisbrink & Heinsbroek, 1992) . .	32
2.13	Experimental set-up (a) and pressure measurements (b) next to the downstream valve and at the bend-C (Wiggert <i>et al.</i> , 1987).	33
2.14	Experimental straight pipe rig used in A-Moneim & Chang (1978) (a); and pipe equipped with an elbow used in A-Moneim & Chang (1979) (b).	34

List of Figures

2.15	Experimental set-up (a); and fluid pressure and pipe-wall acceleration measurements (b) in the x, y, z coordinates Simão <i>et al.</i> (2015c).	35
2.16	Model set-up (a); and comparison between two-equation and four-equation models (b) for the Delft Hydraulics Benchmark Problem A, considering an anchored (top) or non-anchored valve (bottom) (Tijsseling, 2003).	40
2.17	Numerical evidence of the Poisson coupling beat (Tijsseling, 1997).	40
2.18	Frequency and time-domain solutions of a six-equation model (Walker & Phillips, 1977).	41
2.19	Pipe rig set-up (a) and numerical output (b) for: a free moving valve (black dashed line), anchored (red solid line) and for classic waterhammer model (purple dotted line) (Gale & Tiselj, 2006).	42
2.20	Set-up of the Delft Hydraulics Benchmark Problem F (a); and numerical output (b) for: Poisson and junction coupling (solid line), only junction coupling (dashed line) and for classic waterhammer model (dash-dotted line) (Tijsseling & Lavooij, 1990).	44
2.21	Experimental set-up (a) and output in the frequency-domain (b) for Bourdon coupling analysis (Brown & Tentarelli, 2001b).	45
2.22	System response to waterhammer tests varying bend rigidities. Pressure output at the downstream valve from classic and extended models (Heinsbroek & Tijsseling, 1994).	48
3.1	Simplified schematic of the straight copper pipe set-up.	57
3.2	View of the straight copper pipe set-up (a); detail of downstream valve (b); and detail of pipe support (c).	58
3.3	Supporting configurations of the SCP facility with (a) valve anchored and (b) valve released.	58
3.4	Pressure data acquired at the straight copper pipe for an anchored downstream end: (a) at the downstream end (PT3); and (b) at the midstream section (PT2).	59
3.5	Pressure data acquired at the straight copper pipe for a non-anchored downstream end: (a) at the downstream end (PT3); and (b) at the midstream section (PT2).	60
3.6	Schematic and photograph of the coil copper pipe facility.	61
3.7	Detail of the assembled strain-gauges.	61
3.8	Measured pressure data for the tests carried out at the coil copper pipe: (a) at the downstream end (PT3); and (b) at the midstream section (PT2).	62
3.9	Schematic and view of the coil polyethylene pipe facility.	63
3.10	Measured pressure data of the tests carried out at the coil PE pipe (PT2): (a) at the downstream end; and (b) at the midstream section (PT1).	64
3.11	Dimensionless transient pressures in the four assessed set-ups at the downstream pipe section. a) SCP02 test (anchored valve), b) SCP05 test (non-anchored valve), c) CCP03 test and d) CPP03 test.	66

3.12 Dimensionless transient pressures in the four assessed set-ups at the midstream pipe section. a) SCP02 test (anchored valve), b) SCP05 test (non-anchored valve), c) CCP03 test and d) CPP03 test.	67
3.13 Dimensionless transient pressures, time-envelopes and regression curves (dashed lines) in the four assessed set-ups at the downstream pipe section. a) SCP02 test (anchored valve), b) SCP05 test (non-anchored valve), c) CCP03 test and d) CPP03 test.	69
3.14 First pressure peak corresponding to SCP05 test at the downstream section. . .	70
3.15 (a) Dimensionless pressure time series at the downstream pipe-end; and (b) detail of the valve manoeuvres of the selected tests.	71
3.16 Dimensionless pressure time series at the downstream pipe-end for tests SCP02 (anchored end) and SCP05 (released end).	72
3.17 Dimensionless pressure time series at the downstream pipe-end for tests SCP02 and CCP03.	72
3.18 Dimensionless pressure time series at the downstream pipe-end for tests SCP02 and CPP03.	73
3.19 Dimensionless transient circumferential strain (solid lines) and axial strain (dotted lines) at the <i>midstream</i> pipe sections for: a) SCP02 (anchored end), b) SCP05 (released end), c) CCP03 and d) CPP03.	74
3.20 Precursor stress waves during the tests SCP02 (a) and SCP05 (b). Solid lines: circumferential strain; and dashed lines: axial strain.	75
3.21 Axial strain sub-peaks observed in the straight copper pipe facility for a free valve. 75	75
3.22 Circumferential (solid lines) and axial (dashed lines) strains measured in the coil PE pipe facility for the different tests carried out.	76
3.23 Corrected Joukowsky overpressure for the test SCP05.	78
3.24 Measured pressures <i>vs.</i> measured axial (grey solid line) and circumferential (black solid line) strains during the transient tests carried out at a) SCP02 (fixed valve set-up), b) SCP05 (released valve set-up), c) CCP03 and d) CPP03.	79
3.25 Measured pressures <i>vs.</i> circumferential strains during the transient test CPP03. 80	80
4.1 Strain and pressure measurements: (a) circumferential strain test and (b) axial strain test. ◦ strain at top side (SG-1 and SG-4); ◊ strain at outer side (SG-2 and SG-5); * strain at bottom side (SG-6); • strain at inner side (SG-3 and SG-7). Pressure measurements in dashed lines (PT-2).	86
4.2 Element of the axisymmetrically loaded shell of revolution	87
4.3 Schematics of radial loads balance in (a) an elliptic cross-section and (b) detail of stresses over the upper generatrice	89
4.4 Schematic for bending moment $M(\theta)$ derivation	90
4.5 Balance of forces of a control volume, pipe-wall stress forces versus centrifugal force	91

List of Figures

4.6	Measured versus computed circumferential and axial strains using elliptic torus. ◦ measured strain at top side; ◊ measured strain at outer side; * measured strain at bottom side; • measured strain at inner side. Computed strain at top side in solid line (SG-1 and SG-4); computed strain at outer side in dashed line (SG-2 and SG-5); computed strain at bottom side in dash-dot line (SG-6); and computed strain at inner side in dotted line (SG-3 and SG-7).	93
4.7	Measured versus computed circumferential and axial strains for a circular torus. ◦ measured strain at top side; ◊ measured strain at outer side; * measured strain at bottom side; • measured strain at inner side. Computed strain at top side in solid line (SG-1 and SG-4); computed strain at outer side in dashed line (SG-2 and SG-5); computed strain at bottom side in dash-dot line (SG-6); and computed strain at inner side in dotted line (SG-3 and SG-7).	94
4.8	Circumferential strains over the cross-section when focal distance d_F is changed	96
4.9	Circumferential strains as a function of focal distance d_F	96
4.10	Empirical laws relating pressure p and focal distance d_F	97
4.11	Circumferential strains corrected and not corrected versus experimental data: a) in the outer side, b) in the inner side, and c) in the top side of the pipe. ◦ measured data; output from elliptic torus model in dotted lines; from circular torus model in dashed lines; and from elliptic torus model taking into account bending effect in solid lines.	98
4.12	Circumferential (top) and axial (down) strains (in $\mu m/m$) in the outer side of the cross-section during transient test at the middle section of the pipe and detail of the first peaks (right). Measured data in grey solid lines and computed data in black dashed lines.	100
4.13	Computed displacements of the pipe wall over the coil cross-section (left) and in the horizontal plane(right)	105
4.14	Measured hydraulic head at the downstream (a) and midstream (b) pipe positions for the transient tests carried out in the experimental facility.	110
4.15	Measured hydraulic head at the downstream boundary in comparison with the classic waterhammer theory solution for a fast hydraulic transient generated after an initial discharge $Q_0 = 400 \text{ l/h}$	110
4.16	Scheme of the characteristic lines for the wave celerities adjustment $\frac{a_h^*}{a_p^*} = \frac{4}{11}$	112
4.17	Results of Model-1: a) simulated piezometric head at the pipe downstream end for a free moving massless valve versus results of classic waterhammer solver; b) detail of the first peak. Notice that the pressure traces corresponding to the classic model with steady and unsteady friction are almost overlapped.	115
4.18	Feasible solution region of Model-1 output for a free moving valve with variable mass (a); and Mean Square Error (MSE) values computed for the first pressure peak taking as reference experimental observations (b).	116
4.19	Model-2: independent vibrating rings described by FSI sub-models which assume straight pipes with closed free moving ends.	117

4.20	Model-2 output considering a varying mass of the rings in comparison with measured pressure data at the downstream end (a); and Mean Square Error (MSE) values as a function of ring mass variation computed for the first pressure peak taking as reference experimental observations (b).	118
4.21	Model-2 output (a) of the first pressure peak for a set of simulations by allowing the free movement of the rings except one. The position of the fixed ring is changed in each simulation (1 = upstream ring; 36 = downstream ring). Mean Squared Error (b) computed taking as reference the massless rings solution. . .	119
4.22	Mass distribution of the rings throughout the coil after calibration.	120
4.23	Model-2 output after calibration, either with homogeneous rings mass or distributed, and in comparison with measured pressure data at the downstream end.	120
4.24	Schematic of Model-3: (a) general overview and (b) detail of balance of forces carried out at the end of the pipe-segments.	121
4.25	Model-3 output (a) for a set of simulations varying the Coulomb's dry friction coefficient. (b) Mean Squared Error computed taking as reference the measurements.	123
4.26	Distribution of Coulomb's friction coefficients, kinematic and static, along the pipe rig.	124
4.27	Model-3 output after calibration (according Fig 4.26) <i>v.s.</i> experimental data at the downstream end section.	124
4.28	Pressure outputs at the downstream section of the pipe from the best simulations of Model-1 and Model-2 in comparison with measurements. Computed MSE are shown for both models.	125
4.29	Pressure outputs at the middle section of the pipe from the best simulations of Model-1 and Model-2 in comparison with measurements. Computed MSE are shown for both models.	126
4.30	Pressure outputs for initial discharges $Q_0 = 100 \text{ l/h}$, $Q_0 = 200 \text{ l/h}$ and $Q_0 = 400 \text{ l/h}$ at the downstream section of the pipe from the selected solution of Model-2 in comparison with measurements.	127
4.31	Pressure outputs for initial discharges $Q_0 = 100 \text{ l/h}$, $Q_0 = 200 \text{ l/h}$ and $Q_0 = 400 \text{ l/h}$ at the middle section of the pipe from the selected solution of Model-2 in comparison with measurements.	127
5.1	Pressure data acquired at the downstream end (PT3) of the straight copper pipe for an <i>anchored</i> (a) and for a <i>non-anchored</i> (b) downstream end.	135
5.2	Circumferential (solid lines) and axial (dashed lines) strain data acquired at the downstream section of the straight copper pipe for an <i>anchored</i> (a) and for a <i>non-anchored</i> (b) downstream end.	136
5.3	Numerical scheme of the four-equation model. Characteristic lines at different sections of the pipe.	138

List of Figures

5.4	Frictionless four-equation FSI model output for (a) anchored and (b) non-anchored downstream pipe-end <i>vs.</i> classic theory. Simulation period of 0.3 s	143
5.5	Frictionless four-equation FSI model output for (a) anchored and (b) non-anchored downstream pipe-ends <i>vs.</i> Joukowsky overpressure. Simulation period of 3 s.	143
5.6	Quasi-steady friction (SF-1) <i>vs.</i> (a) Brunone's (SF-2) and (b) Trikha's (SF-3) unsteady friction. The horizontal dashed line represents Joukowsky overpressure.	144
5.7	Quasi-steady friction (SF-1) <i>vs.</i> Brunone's (SF-2) and Trikha's (SF-3) unsteady friction models. Simulation period of 3 s.	144
5.8	Axial stress of a vibrating fluid-emptied conduit excited by hammering and damped by dry friction. The horizontal dashed line represent Rankine axial stress rise.	145
5.9	Four-equation FSI model output for (a) anchored and (b) non-anchored downstream pipe-ends; for a frictionless systems (FSI-1,2) and taking into account only dry friction (DF-1,2).	146
5.10	Numerical output considering Brunone's and Trikha's unsteady friction <i>vs.</i> measurements for: (a) test SCP03 with anchored pipe-end; and (b) test SCP06 with non-anchored pipe-end. Output form the downstream end section. Dry friction is not considered.	147
5.11	Experimental measurements <i>vs.</i> numerical output considering Brunone's unsteady and including and excluding dry friction for: (a) test SCP03 with anchored pipe-end; and (b) test SCP06 with non-anchored pipe-end. Output form the downstream end section.	148
5.12	Numerical output (solid lines) considering FSI, Brunone's unsteady friction and dry friction <i>vs.</i> experimental measurements (dashed lines) for the tests SCP01 and SCP04 (black), SCP02 and SCP05 (dark grey), SCP03 and SCP06 (light grey). (a) for anchored pipe-end, (b) for non-anchored pipe-end. Pressure history at the downstream pipe-end.	148
5.13	Numerical output (solid lines) considering FSI, Brunone's unsteady and Coulomb's dry friction losses <i>vs.</i> experimental measurements (dashed lines) for: (a) test SCP03, with anchored downstream end; and (b) test SCP06, with non-anchored downstream end.	150
5.14	Numerical output for Brunone's and Trikha's friction losses <i>vs.</i> experimental measurements for the test with anchored downstream end (SCP03). Time window between $t = 1$ s and $t = 1.5$ s.	151
5.15	Experimental measurements (black lines) <i>vs.</i> numerical output considering Brunone's friction losses and with (blue lines) or without (red lines) dry friction for the tests: SCP03, with anchored downstream end (a); and SCP06, with non-anchored downstream end (b). Time window between $t = 1$ s and $t = 1.5$ s.	152

5.16 Different tested configurations: (a) setup-1 where the conduit is anchored at both pipe ends; (b) setup-2 where the conduit is only anchored at the upstream end; and (c) setup-3 where the conduit is anchored at the midstream and upstream sections of the pipe.	155
5.17 Waterhammer tests carried out for a conduit anchored at the upstream and downstream pipe-ends (setup-1); anchored only at the upstream end (setup-2); and anchored at the upstream and midstream pipe sections (setup-3), for $Q = 300 \text{ l/h}$	155
5.18 Set of waterhammer tests consisting of releasing one support at a time, from the downstream to the upstream pipe-end, starting from a fully anchored pipe against longitudinal movement, for $Q = 426 \text{ l/h}$ and 23 tests in total.	156
5.19 Numerical scheme of the four-equation model. Characteristic lines at different sections of the pipe: (a) at the interior nodes; (b) at the upstream boundary; and (c) at the downstream boundary.	157
5.20 Numerical scheme of the four-equation model. Characteristic lines at (a) anchor block nodes and (b) in their vicinity. The dashed and continuous lines represent characteristic lines in the pipe-wall and in the fluid, respectively.	160
5.21 Balance of forces at anchor blocks.	161
5.22 Pipe-block system for one degree-of-freedom. (a) schematic of the modelled system; (b) velocity of the anchor block U	163
5.23 Pipe-block system for three degrees of freedom and second vibration mode: (a) schematic of the modelled system; (b) velocity of the anchor block U	164
5.24 Pipe-block-pipe fluid-filled system for one degree of freedom: (a) velocity of the anchor block U .; and (b) velocity of the fluid V at the anchor block section.	165
5.25 Fluid-filled system for three degrees-of-freedom and second vibration mode: (a) velocity of the anchor block U .; and (b) velocity of the fluid V at the anchor block section.	166
5.26 Spectral density plot corresponding to flow velocity output data V from the three degrees-of-freedom set-up.	166
5.27 Transient pressures at the downstream pipe-end for a variable valve mass.	167
5.28 Transient pressures at the downstream pipe-end for the varying mass of an anchor block located at the midstream section of the pipe: (a) the conduit is anchored at both pipe-ends; and (b) the conduit is only anchored at the upstream pipe-end.	168
5.29 Transient pressures at the downstream pipe-end for the series of simulations varying the dry friction coefficient for a 6 kg mass valve.	169
5.30 Transient pressures at the downstream pipe-end for the series of simulations varying the dry friction coefficient at the midstream section of the pipe: (a) the conduit is anchored at both pipe-ends; (b) the conduit is anchored only at the upstream end.	170

List of Figures

5.31	Numerical pressure output <i>vs.</i> pressure measurements for a waterhammer test carried out in a conduit anchored against longitudinal movement at both pipe-ends.	172
5.32	Numerical pressure output <i>vs.</i> pressure measurements for a waterhammer test carried out in a conduit anchored against longitudinal movement only at the upstream pipe-end.	172
5.33	Numerical pressure output <i>vs.</i> pressure measurements for a waterhammer test carried out in a conduit anchored against longitudinal movement at the midstream section.	173
5.34	Transient pressures at the downstream pipe-end. Measurements (a) <i>vs.</i> numerical pressure output (b) for a set of waterhammer tests consisting on releasing, one support at a time and from downstream to upstream, a fully anchored pipe against longitudinal movement.	174
C.1	Delft Hydraulics benchmark Problem A with (a) fixed boundaries and (b) with a free moving valve.	202
C.2	Delft Hydraulics benchmark Problem A: (a) pressure output for $\nu = 0.3$ and fixed valve (Poisson coupling beat); (b) pressure output for Poisson-uncoupled and a free moving valve.	203
D.1	Schematic of forces acting in the pipe-wall in the axial direction.	206
E.1	Characteristic grid for a four-equation model at the downstream boundary. . .	213
E.2	Comparison of pressure rise output from Eq. E.2 (grey dotted line), Eq. E.11 (black dotted line) and Eq. E.17 (black dashed line). a) corresponds to the test SCP04, b) to SCP05 and c) to SCP06 (<i>cf.</i> Chapter 3).	215
F.1	(a) Pressure signal at the downstream pipe end; (b) measured strains at the downstream pipe section in the circumferential (solid line) and in the axial (dashed line) directions; (c) pressure signal at the midstream pipe section; (d) measured strains at the midstream pipe section in the circumferential (solid line) and in the axial (dashed line) directions.	219
F.2	Pressure signal at the downstream pipe end.	219
F.3	(a) Pressure signal at the downstream pipe end; (b) measured strains at the downstream pipe section in the circumferential (solid line) and in the axial (dashed line) directions; (c) pressure signal at the midstream pipe section; (d) measured strains at the midstream pipe section in the circumferential (solid line) and in the axial (dashed line) directions.	220
F.4	Pressure signal at the downstream pipe end.	220

E5	(a) Pressure signal at the downstream pipe end; (b) measured strains at the downstream pipe section in the circumferential (solid line) and in the axial (dashed line) directions; (c) pressure signal at the midstream pipe section; (d) measured strains at the midstream pipe section in the circumferential (solid line) and in the axial (dashed line) directions.	221
E6	Pressure signal at the downstream pipe end.	221
E7	(a) Pressure signal at the downstream pipe end; (b) measured strains at the downstream pipe section in the circumferential (solid line) and in the axial (dashed line) directions; (c) pressure signal at the midstream pipe section; (d) measured strains at the midstream pipe section in the circumferential (solid line) and in the axial (dashed line) directions.	222
E8	Pressure signal at the downstream pipe end.	222
E9	(a) Pressure signal at the downstream pipe end; (b) measured strains at the downstream pipe section in the circumferential (solid line) and in the axial (dashed line) directions; (c) pressure signal at the midstream pipe section; (d) measured strains at the midstream pipe section in the circumferential (solid line) and in the axial (dashed line) directions.	223
E10	Pressure signal at the downstream pipe end.	223
E11	(a) Pressure signal at the downstream pipe end; (b) measured strains at the downstream pipe section in the circumferential (solid line) and in the axial (dashed line) directions; (c) pressure signal at the midstream pipe section; (d) measured strains at the midstream pipe section in the circumferential (solid line) and in the axial (dashed line) directions.	224
E12	Pressure signal at the downstream pipe end.	224
E13	(a) Pressure signal at the downstream pipe end; (b) measured strains at the downstream pipe section in the circumferential (solid line) and in the axial (dashed line) directions; (c) pressure signal at the midstream pipe section; (d) measured strains at the midstream pipe section in the circumferential (solid line) and in the axial (dashed line) directions.	225
E14	Pressure signal at the downstream pipe end.	225
E15	(a) Pressure signal at the downstream pipe end; (b) measured strains at the downstream pipe section in the circumferential (solid line) and in the axial (dashed line) directions; (c) pressure signal at the midstream pipe section; (d) measured strains at the midstream pipe section in the circumferential (solid line) and in the axial (dashed line) directions.	226
E16	Pressure signal at the downstream pipe end.	226
E17	(a) Pressure signal at the downstream pipe end; (b) measured strains at the downstream pipe section in the circumferential (solid line) and in the axial (dashed line) directions; (c) pressure signal at the midstream pipe section; (d) measured strains at the midstream pipe section in the circumferential (solid line) and in the axial (dashed line) directions.	227
E18	Pressure signal at the downstream pipe end.	227

List of Figures

F.19	(a) Pressure signal at the downstream pipe end; (b) measured strains at the downstream pipe section in the circumferential (solid line) and in the axial (dashed line) directions; (c) pressure signal at the midstream pipe section; (d) measured strains at the midstream pipe section in the circumferential (solid line) and in the axial (dashed line) directions.	228
F.20	Pressure signal at the downstream pipe end.	228
F.21	(a) Pressure signal at the downstream pipe end; (b) measured strains at the downstream pipe section in the circumferential (solid line) and in the axial (dashed line) directions.	229
F.22	Pressure signal at the downstream pipe end.	229
F.23	(a) Pressure signal at the downstream pipe end; (b) measured strains at the downstream pipe section in the circumferential (solid line) and in the axial (dashed line) directions; (c) pressure signal at the midstream pipe section; (d) measured strains at the midstream pipe section in the circumferential (solid line) and in the axial (dashed line) directions.	230
F.24	Pressure signal at the downstream pipe end.	230
F.25	(a) Pressure signal at the downstream pipe end; (b) measured strains at the downstream pipe section in the circumferential (solid line) and in the axial (dashed line) directions; (c) pressure signal at the midstream pipe section; (d) measured strains at the midstream pipe section in the circumferential (solid line) and in the axial (dashed line) directions.	231
F.26	Pressure signal at the downstream pipe end.	231
F.27	(a) Pressure signal at the downstream pipe end; (b) measured strains at the downstream pipe section in the circumferential (solid line) and in the axial (dashed line) directions; (c) pressure signal at the midstream pipe section; (d) measured strains at the midstream pipe section in the circumferential (solid line) and in the axial (dashed line) directions.	232
F.28	Pressure signal at the downstream pipe end.	232
F.29	(a) Pressure signal at the downstream pipe end; (b) measured strains at the downstream pipe section in the circumferential (solid line) and in the axial (dashed line) directions; (c) pressure signal at the midstream pipe section; (d) measured strains at the midstream pipe section in the circumferential (solid line) and in the axial (dashed line) directions.	233
F.30	Pressure signal at the downstream pipe end.	233
F.31	(a) Pressure signal at the downstream pipe end; (b) measured strains at the downstream pipe section in the circumferential (solid line) and in the axial (dashed line) directions; (c) pressure signal at the midstream pipe section; (d) measured strains at the midstream pipe section in the circumferential (solid line) and in the axial (dashed line) directions.	234
F.32	Pressure signal at the downstream pipe end.	234

E33	(a) Pressure signal at the downstream pipe end; (b) measured strains at the downstream pipe section in the circumferential (solid line) and in the axial (dashed line) directions; (c) pressure signal at the midstream pipe section; (d) measured strains at the midstream pipe section in the circumferential (solid line) and in the axial (dashed line) directions.	235
E34	Pressure signal at the downstream pipe end.	235
E35	(a) Pressure signal at the downstream pipe end; (b) measured strains at the downstream pipe section in the circumferential (solid line) and in the axial (dashed line) directions; (c) pressure signal at the midstream pipe section; (d) measured strains at the midstream pipe section in the circumferential (solid line) and in the axial (dashed line) directions.	236
E36	Pressure signal at the downstream pipe end.	236
E37	(a) Pressure signal at the downstream pipe end; (b) measured strains at the downstream pipe section in the circumferential (solid line) and in the axial (dashed line) directions; (c) pressure signal at the midstream pipe section; (d) measured strains at the midstream pipe section in the circumferential (solid line) and in the axial (dashed line) directions.	237
E38	Pressure signal at the downstream pipe end.	237
E39	(a) Pressure signal at the downstream pipe end; (b) measured strains at the downstream pipe section in the circumferential (solid line) and in the axial (dashed line) directions; (c) pressure signal at the midstream pipe section; (d) measured strains at the midstream pipe section in the circumferential (solid line) and in the axial (dashed line) directions.	238
E40	Pressure signal at the downstream pipe end.	238

List of Tables

2.1	Summary table of the most relevant experimental work in the research of fluid-structure interaction in hydraulic transients.	27
2.2	Table of Codes and Standards in industries where waterhammer analyses are frequent.	46
2.3	Summary table of historical accidents in pressurized pipe systems.	52
3.1	Characteristics of the straight copper pipe (SCP) selected tests.	58
3.2	Characteristics of the coil copper pipe (CCP) selected tests.	62
3.3	Characteristics of the coil polyethylene pipe (CPP) selected tests.	63
3.4	Main properties of the selected tests.	66
3.5	Characteristics of the damping laws in the four assessed set-ups	69
3.6	Summary of the qualitative importance of damping mechanisms in the analysed experimental set-ups.	82
4.1	Volume change for a steady pressure of $6 \times 10^5 Pa$ (i.e. 60m)	106
4.2	Dimensionless parameters for the experimental facility	109
4.3	Main modelling assumptions for the simulation of the coil system.	114
5.1	Characteristics of the experimental tests.	134
5.2	Summary of simulations carried out for model verification. (✓) activated mechanism, (-) deactivated mechanism.	142
5.3	Input parameters for the simulation of combined effects.	146
5.4	Tests carried out for the sensitivity analysis.	167
5.5	Input parameters	171
B.1	Coefficients for factor matrices A and B and right-hand-side vector r	195
B.2	Coefficients for factor matrices A and B and right-hand-side vector r	197
B.3	Compatibility equations coefficients for FSI four-equation model Poisson-uncoupled and Poisson-coupled.	200
D.1	Coefficients for factor matrices A and B and right-hand-side vector r	208
D.2	Compatibility equations coefficients for FSI, skin friction and dry friction terms.	210
E.1	Coefficients for extended Joukowsky equation	216

List of Tables

F1	Summary table for SCP1 tests.	217
F2	Summary table for SCP2 tests.	218
F3	Summary table for SCP3 tests.	218
F4	Summary table for SCP4 tests.	218



List of acronyms and notation

Notation

Symbols:

A	cross-sectional area (m^2)
a	wave speed (m s^{-1})
D	pipe diameter (m)
E	pipe-wall Young's modulus (Pa)
e	pipe-wall thickness (m)
F	force (N)
f	Darcy skin friction coefficient (-)
G	pipe-wall shear modulus (Pa)
H	hydraulic head (m)
h	dimensionless hydraulic head (-)
h_f	skin friction losses (m)
I	second moment of area (m^4)
J	polar second moment of area (m^4)
K	bulk modulus of compressibility (Pa)
L	pipe length (m)
M	moment (N m)
m	mass (kg)
p	fluid pressure (Pa)
Q	discharge ($\text{m}^3 \text{s}^{-1}$)
R	rotational velocity (rad s^{-1})
r	pipe radius (m)
Re	Reynolds number (-)
T	wave period (s)
t	time (s)
U	pipe-wall velocity (m s^{-1})
V	flow velocity (m s^{-1})
W	pipe-wall radial movement (m s^{-1})
ϵ	strain (-)
ν	Poisson's ratio (-)
ρ	density (kg m^{-3})
σ	pipe-wall stress (Pa)
τ	shear stress fluid-pipe (Pa)

Subscripts:

b	thrust or anchor block
c	coil
f	fluid
f_s	steady friction
f_u	unsteady friction
HK	Helmholtz-Korteweg
h	hammer
JK	Joukowsky
MK	Moens-Korteweg
N	normal
p	pipe-wall
r	relative
v	valve
W	weight
x	Cartesian coordinate system axis
y	Cartesian coordinate system axis
z	Cartesian coordinate system axis
1, ... 8	pipe degrees-of-freedom
θ	azimuth
σ	stress

Acronyms

<i>ABS</i>	acrylonitrile butadiene styrene
<i>CCP</i>	coil copper pipe
<i>CPP</i>	coil polyethylene pipe
<i>CFD</i>	computational fluid dynamics
<i>DF</i>	dry friction
<i>DOF</i>	degree-of-freedom
<i>EPFL</i>	École Polytechnique Fédérale de Lausanne
<i>FDM</i>	finite difference method
<i>FEM</i>	finite element method
<i>FSI</i>	fluid-structure interaction
<i>FVM</i>	finite volume method
<i>HDPE</i>	high density polyethylene
<i>IST</i>	Instituto Superior Técnico
<i>LCH</i>	Laboratoire de Constructions Hydrauliques
<i>LHE</i>	Laboratory of Hydraulics and Environment
<i>MOC</i>	method of characteristics
<i>PE</i>	polyethylene
<i>PT</i>	pressure transducer
<i>PVC</i>	polyvinyl chloride
<i>SCP</i>	straight copper pipe
<i>SF</i>	skin friction
<i>SG</i>	strain gauge
<i>UF</i>	unsteady friction
<i>VE</i>	viscoelasticity
<i>MSE</i>	mean square error
<i>1D</i>	one-dimension

1 General introduction

1.1 Research scope

As a product of several sciences, waterhammer theory is multidisciplinary. The description of pressurized transient flow in closed conduits is its main focus, hence the dominant discipline is hydraulics. Nonetheless, its essence is not complete without the standpoint of other disciplines such as structural mechanics, material science or acoustics. This research deals mainly with two sciences: fluid dynamics and structural mechanics. Fluid-structure interaction (FSI) in one-dimensional (1D) pressurized transient flow in the time-domain is the ground-base in which the present work is developed. Issues like unsteady skin friction, dry friction and pipe-wall viscoelastic behaviour are deeply analysed.

1.2 Historical background

Scientific theories in normal science are the result of a step-wise aggregation of research contributions, like pieces of a puzzle that are added to solve preconceived problems (Kuhn, 2012). The hindered pieces of the waterhammer theory puzzle may be unfolded by explaining those preconceived solutions that at each stage were envisaged. The ultimate solution is a numerical model which is a theory itself or, in other words, 'a collection of signs that serve as a sign' (Abbott, 1993). The 1D FSI model, as a self-standing theory, is capable of outputting those historically targeted solutions.

Consider the most elementary hypothetical case of a reservoir-pipe-valve system composed of a frictionless straight pipe of infinite length with frequent expansion joints, rigid, thin-walled and containing incompressible fluid for which a steady flow is interrupted by an instantaneous valve closure. In such set-up the pressure wave speed would be infinite and any flow change at any section of the pipe would represent an instantaneous infinite change of momentum all throughout the infinite length of the pipe. Hence, no transients would be physically feasible, as there were no valves nor pipe elements capable of resisting such an infinite momentum. Add, to this initial set-up, some more realistic assumptions that will unfold, one by one, the

Chapter 1. General introduction

puzzling of the historical background on 1D waterhammer and fluid-structure interaction research:

1. **Compressible fluid:** the waterhammer wave celerity is finite, equal to the fluid acoustic wave speed in unconfined media, and Newton-Laplace equation (Newton, 1686; Lagrange, 1788; Laplace *et al.*, 1829) can be applied for its computation. The wave length is infinite (as the pipeline is infinite) and the wave amplitude is proportional to the wave celerity and can be computed by Joukowsky equation (Von Kries, 1883; Frizell, 1898; Allievi, 1902; Joukowsky, 1904).
2. **Elastic pipe-wall:** the distensibility of the pipe-wall slows down the wave propagation speed, which can be computed by Helmholtz-Korteweg equation (Korteweg, 1878; Halliwell, 1963). The wave length is infinite and its amplitude can be computed by Joukowsky equation.
3. **Pipe of finite length:** the waterhammer wave propagates back and forth throughout the pipe according to the boundary conditions. To describe such oscillating flow a two-equation model to solve mass and momentum conservation in the fluid is at least required (Braun, 1909, 1910; Allievi, 1902, 1913).
4. **Wave dissipation:** assumptions such as skin friction, dry friction or hysteretic damping must be added and the waterhammer wave dampens towards a final steady state. The most common approach is the insertion of quasi-steady skin friction which can be computed by Darcy-Weisbach friction formula (Streeter & Wylie, 1978; Chaudhry, 2014).
5. **No expansion joints:** the fluid interacts with the axial movement of the pipe. A four-equation model to solve mass and momentum conservation in the fluid and in the structure is at least required. Skalak (1955); Bürmann (1979); Wiggert *et al.* (1985a); Tijsseling (2003), amongst others, contributed to the development of such models.
6. **The pipe has an elbow:** in-plane shear and bending occurs during the waterhammer wave and an eight-equation model is at least required for its description (Valentin *et al.*, 1979; Hu & Phillips, 1981).
7. **The pipe has two out-of-plane elbows:** there is shear and bending in two planes and additionally torsion in the cross-sectional plane, hence a fourteen-equation model is at least required (Wilkinson, 1977; Wiggert *et al.*, 1985a; Wiggert, 1986; Wiggert *et al.*, 1987).
8. **Thick-walled pipe:** radial inertia of the pipe-wall must be taken into account and a sixteen-equation model is required. Walker & Phillips (1977) proposed a model to account for radial inertia.

This sequence of assumptions, which emulates the main historical milestones of waterhammer research, can be applied, one by one, to a state-of-the-art sixteen-equation model, revealing

the background lying beneath the model. A more detailed state-of-the-art review is presented in Chapter 2.

Nowadays, 1D waterhammer researchers are mainly focused on the improvement of the description of physical phenomena affecting the transient wave taking as basis the classical waterhammer solver. However, 1D FSI represents an extension of the classical theory, and some of the developments carried out for the classical theory have not been transferred yet to the state-of-the-art 1D FSI framework.

The present work aims at contributing to 1D FSI knowledge, first, by providing and interpreting experimental evidence, then carrying out numerical modelling developments and confirmation, and finally by developing add-ons for the basic four-equation FSI solver.

1.3 Aims and objectives

The aim of the present research is to identify, describe and quantify the principal mechanic-hydraulic relationships during hydraulic transients in pressurized pipe flows in view of improving pipe design and reduce pipe and system failure. Phenomena affecting the transient wave, such as fluid-structure interaction, unsteady skin friction, dry friction or pipe-wall viscoelasticity are analysed from both the experimental and numerical standpoints. The main goal is the improvement of one-dimensional (1D) waterhammer modelling in the time-domain by means of the well-known method of characteristics approach.

The targeted objectives can be summarized in the following points:

- To identify and evaluate from the experimental standpoint FSI, pipe-wall viscoelasticity, and unsteady skin friction using pressure and strain measurements from different pipe rigs.
- To assess, describe and understand, by means of a static stress-strain analysis, the behaviour of pipe coils under inner pressure loads.
- To incorporate the achieved stress-strain relations in a dynamic analysis based on a FSI solver.
- To assess different approaches for implementing numerically friction coupling in four-equation models applied in straight pipes.
- To incorporate in the four-equation solver internal conditions (*i.e.* junction coupling) aiming at simulating the behaviour of pipe anchoring supports.

1.4 Methodology

The research focuses on the description of the propagation of transient waves, therefore, all the assessments presented hereby, either empirical or numerical, are approached in the time-domain. Numerical models based on the method of characteristics (MOC) are developed, the implementations are verified by means of benchmark problems and model validation by experimental data acquired in different experimental set-ups. Three experimental facilities, assembled at the Laboratory of Hydraulics and Environment of Instituto Superior Técnico (LHE/IST), Lisbon, Portugal, have been used for the experimental data collection: (i) a straight copper pipe, which is tested for different supporting set-ups; (ii) a coil copper pipe, whose response in transient conditions is strongly affected by the coil geometry; and (iii) a coil polyethylene pipe, that allows the study of the pipe-wall viscoelasticity.

For the numerical work first a stress-strain analysis is carried out with the goal to understand the structural behaviour of pipe coils in static conditions. Then FSI is approached and dynamic interactions between the fluid and the structure are considered by means of a four-equation model. Once FSI implementations are verified, add-ons considering the main dissipation phenomena are included and finally validated by empirical observations. The same four-equation solver is used for the description of the straight copper pipe, for which friction and junction coupling are assessed aiming at describing the effect of pipe supports and anchoring blocks.

1.5 Organization of the report

First an extensive review of the main developments in 1D fluid-structure interaction analyses in the time-domain is provided in Chapter 2. In the review the background theory is presented and the gaps of the current state-of-knowledge all identified. Additionally, the main engineering applications of waterhammer developments related with FSI are reported. In Chapter 3 the experimental data collected from the three different pipe rigs are presented. Pressure and strain measurements are analysed and fluid-structure interaction, unsteady skin friction and pipe-wall rheological behaviour effects are discussed for the three pipe systems. Chapter 4 deals with the fluid-structure interaction occurring in coils. It is subdivided in two main sections: firstly, a stress-strain analysis targets the study of the static structural behaviour coil pipes; and, secondly, a FSI analysis shows the dynamic behaviour of coils during hydraulic transients. Chapter 5 deepens on the fluid-structure interaction in straight pipelines. This chapter is also subdivided in two sections, the first deals with friction coupling considering unsteady skin friction and dry friction; the second focuses on the junction coupling and the resistance to movement of thrust and anchor blocks. Finally, conclusions highlighting the main contributions of each chapter are reported and the outlook for future research is introduced.

A collection of appendices complete the subjects presented in each chapter. In Appendix A

the fundamental transient equations in pipe systems are introduced and the governing equations, used in the present dissertation, are derived. Appendix B develops the compatibility equations for the implementation of the four-equation model. Implementations are verified in Appendix C by means of benchmark problems. Appendix D describes an upgrade of the four-equation model based on a friction coupling that considers skin and dry dissipation effects. Appendix E presents an extended version of the well known Joukowsky formula. The new formula takes into account the additional pressure rise caused when a straight pipe is allowed to move in the longitudinal direction. Finally, in Appendix F additional experimental data from the straight copper pipe facility, complementing the one shown in Chapters 3, 4 and 5, is presented for broader flow rates and pipe anchoring conditions.

Therefore, as depicted in Fig. 1.1 the presented research work can be divided in two main parts: experimental and numerical analysis. The first part is oriented to the experimental identification and evaluation of the targeted wave damping phenomena by means of three different experimental facilities. The goal of the second part is the numerical simulation of those phenomena by means of different modelling approaches.

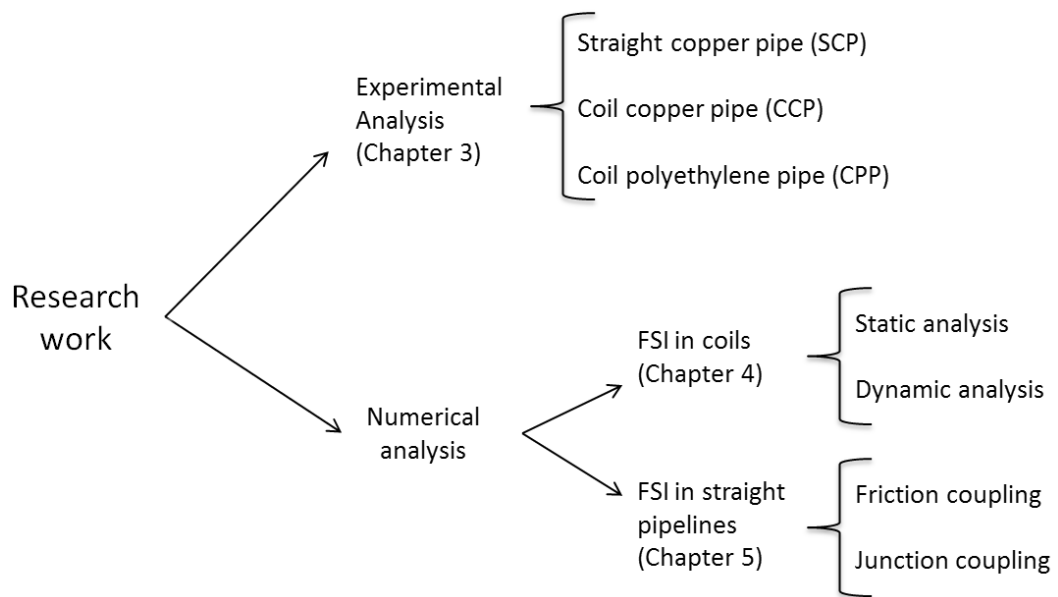


Figure 1.1 – Summary of the main research work.

Chapter 3 and sections 4.2, 4.3, 5.2 and 5.3 have been prepared as scientific publications. Nevertheless they have been arranged in a way to avoid repetitions.

2 State-of-the-Art Review

2.1 Introduction

The first scientific contributions in the field of fluid-structure interaction in transient pipe flow took place in the 19th century when authors like Korteweg (1878) or Helmholtz (1882) realized about the need of considering both interacting mechanisms fluid compressibility and pipe-wall distensibility. Classical waterhammer theory is also based on this principle. Since then, many researchers have added their contributions in a step-wise manner, building up and shaping the theory of hydraulic transients in pipe flow. From this main body of knowledge, subtheories improving the basic assumptions are added, such as unsteady friction, pipe-wall viscoelasticity or cavitation.

Fluid-structure interaction (FSI) should not be understood as an add-on complement of the basic classical waterhammer model. FSI is a self-sustaining theory. Each FSI model is an approach to tackle the original principle of considering waterhammer waves as result of the effect between fluid and pipe behaviours. Skalak (1955) presented a milestone paper entitled '*An extension of the theory of waterhammer*'. The basis of FSI was established, pipe vibration modes were described and basic formulation for straight pipes was presented. Skalak's paper triggered the FSI research in the two-way coupling between fluid dynamics and structural mechanics. Contributions such as Wilkinson (1977), Walker & Phillips (1977), Valentin *et al.* (1979), Wiggert *et al.* (1985a), Wiggert (1986), Joung & Shin (1987), Bürmann & Thielen (1988a), Wiggert & Tijsseling (2001) and Tijsseling (2003) developed and completed the theory for all the basic degrees-of-freedom of pipe-systems.

Some historical reviews on hydraulic transients in pipe flow are given by Wood (1970), Thorley (1976), Anderson (1976), Tijsseling & Anderson (2004) and Tijsseling & Anderson (2004). The developments in waterhammer research before the 20th century are well summarized in Boulanger (1913). Also Lambossy (1950) and Stecki & Davis (1986) presented in-depth reviews that served, at that time, as vision papers. More recently, Ghidaoui *et al.* (2005) presented a complete state-of-the-art review focusing on both historic and most recent research and practice and tackling most of the waterhammer research topics. Surveys more specific in the

field of fluid-structure interaction are given by Wiggert (1986), Tijsseling (1996) and Wiggert & Tijsseling (2001). For the present research, the author has found a very valuable groundwork in the latter two publications. Since Wiggert & Tijsseling (2001), no other review papers have been published on fluid-structure interaction. The aim of the current chapter is to report most significant contributions carried out in waterhammer research related to fluid-structure interaction in 1D hydraulic transients modelling, giving emphasis on the time-domain analyses and focusing on most recent research.

The chapter starts with the basic definitions and background theory that frame the research of FSI in waterhammer modelling. Also the basic wave damping phenomena are briefly reviewed and the most noteworthy contributions are reported. A review on the experimental research is provided, presenting the main empirical achievements that contributed on the extension of FSI theory. Numerical research is also overviewed following a physically-based classification of pipe degrees-of-freedom. Finally, some insights of engineering applications of fluid-structure interaction developments in pipe flow are pointed out.

2.2 Definitions and basic concepts

2.2.1 Transient pipe-flow

Transient flow is the intermediate-stage flow, when the flow conditions are changed from one steady-state condition to another steady-state (Chaudhry, 2014). This definition includes no-flow and steady flow, in which the initial and the final steady states are equal.

The unsteadiness of the flow depends on: (1) the time scale of the transient event, which is the time lag between the initial and the final steady states; (2) the time scale of the system response, related to the period of the system vibration; (3) the time scale of the transient excitation, which refers to the duration of the disturbance that causes the transient event.

Seven types of pipe-flow are distinguished in Tijsseling & Vardy (2004) depending on the three previous time scales:

- **No-flow:** static laws are considered for the no-flow conditions (*i.e.* $V(t) = 0$). The representative time scale is $t = \infty$.
- **Steady flow:** similar conditions stand for steady flow in which velocity is a constant value during all the considered period (*i.e.*, $V(t) = k$). The representative time scale is as well $t = \infty$.
- **Quasi-steady flow:** velocity varies slowly enough to assume the conditions are identical to those of a steady flow with the same instantaneous mean velocity. Representative time scale: $2D/(fV) \ll t < \infty$.
- **Rigid column:** in this type of flow inertia significantly impedes changes in velocity,

but compressibility of the fluid can be ignored. The velocity along the pipe can be assumed uniform (as long as the pipe cross-section is constant). Representative time scale: $t \sim 2D/(fV)$.

- **Waterhammer and 1D-FSI:** for highly accelerated flow, fluid compressibility may not be negligible and non-uniformity of the flow velocity along the pipe must be considered. These conditions occur for representative time scales of $t \lesssim L/a_h$, where a_h is the wave speed of the hammer wave and L the representative length scale which frequently corresponds to the distance between extreme boundaries or the pipe length.
- **2D-FSI:** the flow is assumed axisymmetric and radial inertia of the fluid and the pipe-wall are taken into account. The characteristic time scale is $t = D/a_h$. This time scale is very low, that is why radial inertia is frequently neglected.
- **3D-FSI:** this is the most general case, 3D Navier-Stokes equations for the fluid and shell equations for the structure are required. The characteristic time scale is the lowest: $t = e/a_h$.

2.2.2 Fluid-structure interaction:

Fluid-structure interaction (FSI) in pipe systems consists of the transfer of momentum and forces in both ways, between the pipe-wall and the contained fluid during unsteady flow (Wiggert, 1986). Hence, both the fluid and the structure transmit an effect upon one another (*v.i.* Fig. 2.1).

From the modelling standpoint, fluid-structure interaction is a multiphysics coupling between the laws that describe fluid dynamics and structural mechanics. Pipe systems experience severe dynamic forces during a waterhammer event, when these forces make the system move, significant FSI may occur, so that liquid and pipe systems cannot be separately treated in a theoretical analysis: interaction mechanisms have to be taken into account (Tijsseling, 1996). Moreover, this is a fundamentally interactive process, thus explaining why an uncoupled analysis (where fluid force histories are used as input data in a structural dynamics code for the pipes, without coupling back) may give erroneous results (Tijsseling & Vardy, 2004).

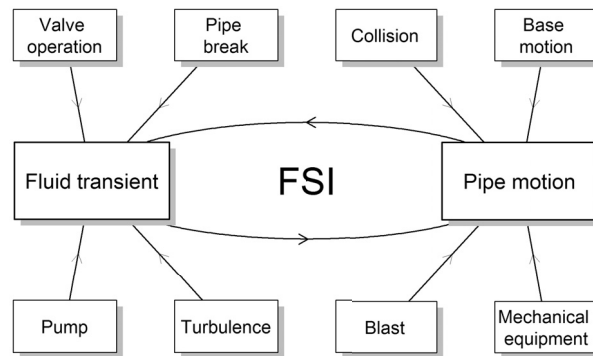


Figure 2.1 – Sources of excitation and interaction between liquid and piping (Wiggert & Tijsseling, 2001).

In a broader sense, fluid-structure interaction embraces any form of transfer of energy, one upon another, between the fluid and the structure. In common engineering problems, this transferred energy is typically either kinetic or heat. The former is termed mechanical fluid-structure interaction and the latter thermal fluid-structure interaction. Heat exchange effect in transient pipe flow is barely significant, processes are assumed isothermic, and FSI analyses are mainly focused on the momentum exchange between the fluid and the pipe structure.

Two different approaches may be followed to account for the momentum transfer into the structure (Giannopapa, 2004): considering either the structure moves as a rigid solid or by the propagation of a local excitation/deformation of the solid. In the first no transient event is considered propagating throughout the solid, the structure element moves as a rigid body and its effect over the fluid is analysed. In the second, the modes of vibration of the structure element are excited and their respective transients are taken into account and coupled with the fluid transient. The present review is focused on the second.

Finally, FSI analyses may be further classified according to the dimensions and the degrees-of-freedom with which the pipe system is allowed to move. Normally, in 1D waterhammer research the classification criteria is based on the modes of vibration of the pipe, which is quite convenient for frequency-domain approaches. However, for time-domain analyses a classification based on the pipe degrees-of-freedom seems more physically intuitive. The latter is the classification criterion used hereby (*v.i.* Fig. 2.2).

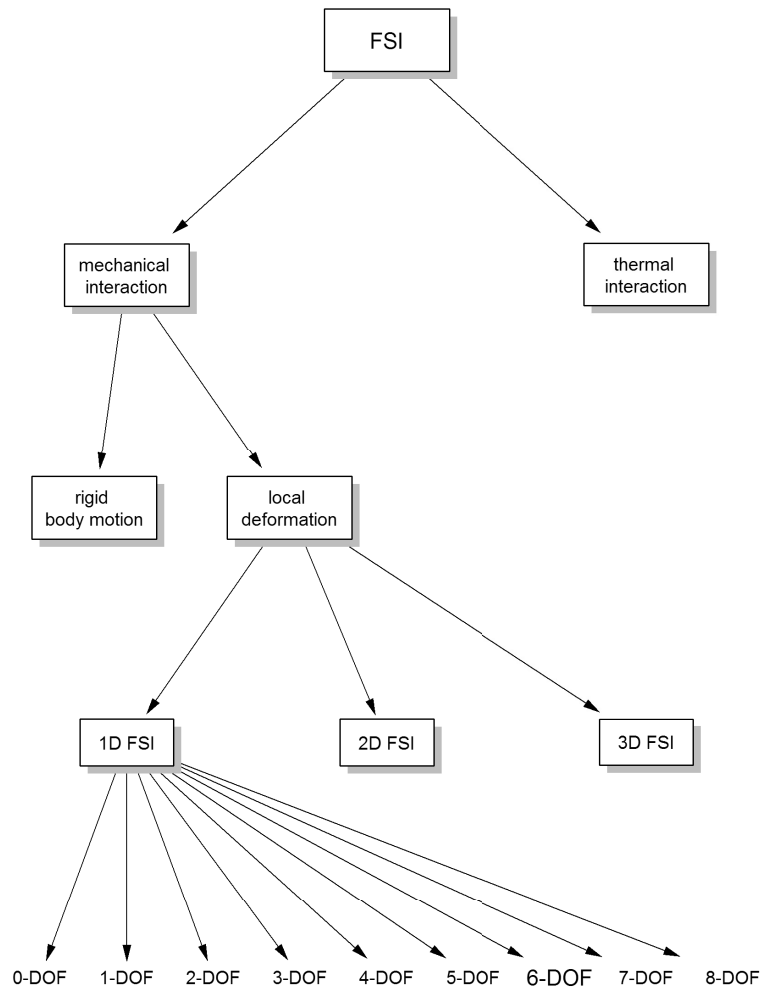


Figure 2.2 – Classification of fluid-structure interaction phenomena.

2.2.3 Degrees-of-freedom in fluid-filled pipes

Degrees-of-freedom (**DOF**) are the number of independent coordinates or parameters that describe the position or configuration of a mechanical system at any time (Sinha, 2010). Systems with finite number of degrees-of-freedom are called discrete systems, and those with infinite degrees-of-freedom are called continuous systems. Pipe systems are continuous systems which can be treated as discrete systems for numerical modelling purposes.

Pipes are svelte elements, therefore, a 1D approach assuming the fluid pressure propagates axially during hydraulic transients seems to be reasonable. However, transient pressures transmit forces over the pipe wall that make the piping system move in a 3D space. The basic degrees-of-freedom for a rigid body in a 3D space are three for translation (*i.e.* heaving, swaying and surging) and three for rotation (*i.e.* pitching, yawing, rolling). An infinitesimal control volume of pipe-segment (like in Fig. 2.3) will have the six basic degrees-of-freedom.

Chapter 2. State-of-the-Art Review

The pipe control-volume is a hollowed cylinder, therefore axisymmetric vibration due to hoop strain must be as well considered, adding another degree-of-freedom. Additionally, the infinitesimal control volume of the 1D inner fluid accounts for another degree-of-freedom. Henceforth, in the present 1D FSI analysis eight degrees-of-freedom compose the infinitesimal control volume of a pipe system.

In each degree-of-freedom momentum and mass conservation laws are applied giving as result a set of 16 partial differential equations (*cf.* Appendix A), with time and space coordinates as independent variables, aiming to solve two basic dependent variables related with the loading and the movement in each degree-of-freedom (*i.e.*, load and deformation relation). Depending on the pipe geometry, axial, shear, bending and torsional forces and displacements alternate throughout the pipe. A schematic of such displacements is shown in Fig. 2.3.

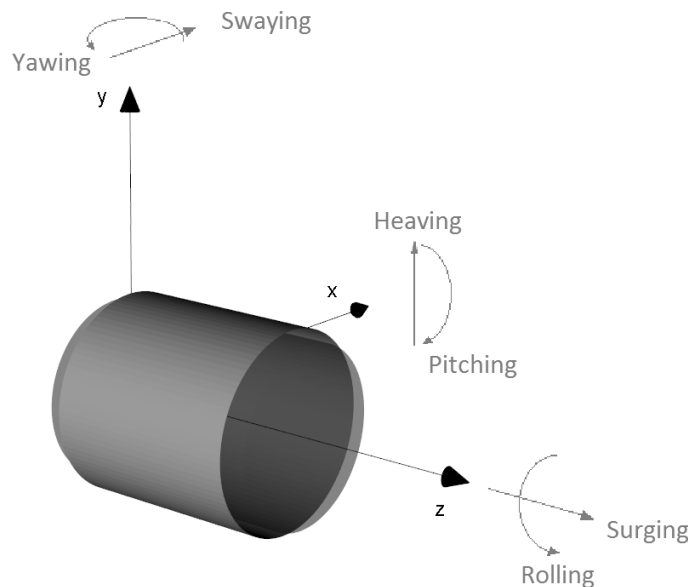


Figure 2.3 – Spatial reference system and signs convention in a straight pipe element

FSI models in 1D waterhammer analyses can be classified following the pipe degrees-of-freedom they are aimed to describe (*u.s.*, Fig. 2.3):

- **1-DOF (fluid)**: only the axial fluid transient event is described.
- **2-DOF (breathing)**: radial inertia of the fluid and the pipe is taken into account.
- **3-DOF (surging)**: refers to the axial movement of the pipe.
- **4-DOF (swaying)**: includes the effect of lateral displacement of the pipe.
- **5-DOF (heaving)**: includes the effect of vertical displacement of the pipe.
- **6-DOF (yawing)**: includes the rotation of the pipe on the \widehat{xz} plane.

- **7-DOF (pitching)**: includes the rotation of the pipe on the $\widehat{y\hat{z}}$ plane.
- **8-DOF (rolling)**: includes the rotation of the pipe on the $\widehat{x\hat{y}}$ plane.

The fundamental mass and momentum conservation equations for the eight degrees-of-freedom of the pipe systems and the respective wave propagation speeds were presented in Walker & Phillips (1977) and Wiggert *et al.* (1987), and in the present document can be found in Appendix A.

2.2.4 Vibration modes in fluid-filled pipes

The modes of vibration of a physical system are determined by the degrees-of-freedom of that system. Depending on its configuration, a pipe system allowed to move in one degree-of-freedom might present more than one vibration modes. In a mode of vibration the overall system experiences simple-harmonic-motion, and the characteristic frequency of this simple-harmonic-motion is called natural frequency. When a physical system is excited, only those modes of vibration whose natural frequencies are lower than the half of the duration of the source of excitation are properly excited. Any vibration of the system can be decomposed into its basic modes of vibration, which are also called natural modes or mode shapes, each mode of vibration has a specific shape. This is the reason why a classification of numerical models based on vibration modes is convenient in frequency-domain analyses.

2.2.5 Coupling mechanisms and modelling approaches

There are three basic kinds of coupling mechanisms (Tijsseling, 1996): (i) *Poisson coupling* describes the interaction between the axial motion of the pipe-wall and the pressure in the fluid occurring by means of the Poisson effect; (ii) *friction coupling* arises from the shear stress between the pipe-wall and the fluid; (iii) and *junction coupling* results from unbalanced local forces and by changes in the fluid momentum that occur in pipe bends, T-junctions or cross-section changes.

Two main approaches can be followed for solving FSI problems: analysis in the time-domain and in the frequency-domain. In the first, the dependent variables are directly assessed with respect the independent variable time; whereas in the second, with respect to frequency. In time-domain analyses the Method of Characteristics (MOC), the Finite Element Method (FEM), the Finite Difference Method (FDM) or the Finite Volume Method (FVM) are discretization methods used to solve the governing differential equations. In the frequency-domain, Harmonic, Fourier, or Laplace analyses are used to replace the time variable in the governing equations by a frequency parameter, and then the partial differential equations are transformed into a set of ordinary differential equations which can be analytically integrated and solved.

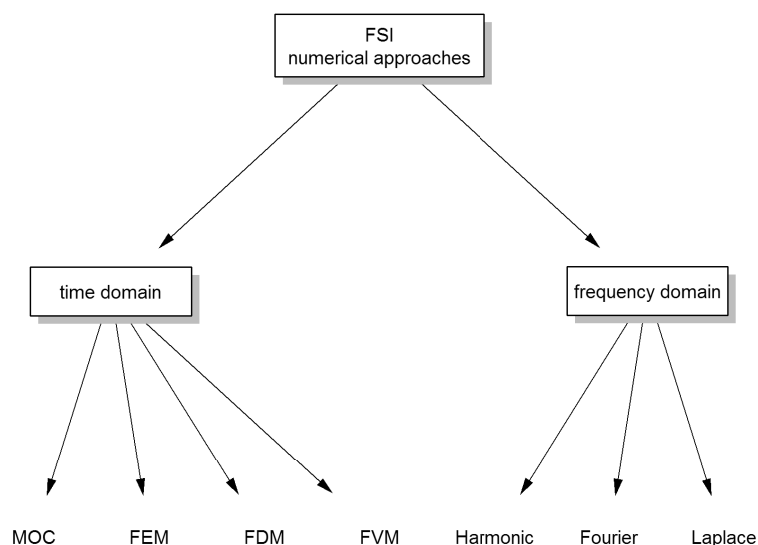


Figure 2.4 – Numerical approaches used in waterhammer research for FSI problems.

In the time-domain approach, either a single or multiple numerical methods can be used for the description of the different degrees-of-freedom of the pipe. The method of characteristics (MOC) and the finite-element method (FEM), or a combination of both, are the most common numerical methods used for solving the one-dimensional basic equations (Tijsseling, 1996). One single integrating approach, such as MOC-MOC or FEM-FEM, is convenient as all the information flows into the same numerical scheme (Wiggert & Tijsseling, 2001). Other combinations are not that common in one-dimensional analyses; FVM is rather used for 3D simulations.

2.2.6 Classification of vibration and damping

The vibration of physical systems can be classified according to different criteria (Dwivedy, n.d.):

- For a system vibrating on its own the resulting vibration is called *free vibration*. If it is subjected to an external force then it is called *forced vibration*.
- If damping is present, the ensuing vibration is called *damped vibration*, otherwise, it is called *undamped vibration*. It can be also called under-damped, critically-damped or over-damped depending on the damping ratio of the system. In the cases of critical and over-damping there is no oscillation of the system.
- If the basic components of a vibratory system (*i.e.* the spring, the mass and the damper) behave linearly, the resulting vibration is known as *linear vibration*. Principle of superposition is valid in this case. *Nonlinear vibration* occurs when one, or more basic components of the vibratory system are not linear.

- If the value of excitation can be predicted at any given time, then it is called deterministic vibration. If not, then the resulting vibration is called *random vibration*.

Several physical phenomena affect the waterhammer waveform, timing and damping, such as unsteady friction, cavitation (including column separation and trapped air pockets), a number of fluid–structure interaction (FSI) effects, viscoelastic behaviour of the pipe-wall material, leakages and blockages (Bergant *et al.*, 2008a). Amongst these, damping may be attributed to three main sources:

- *skin friction damping*, which is related to skin friction between the fluid and the pipe-wall, either steady or unsteady;
- *dry friction damping* caused by the dry friction between the moving pipe structure and its surroundings;
- and *structural or hysteretic damping*, which is associated with the pipe-wall rheological behaviour and movement.

Pipe systems subjected to waterhammer transients are free-damped-deterministic vibrating systems with multiple modes of vibration, coupled or uncoupled, according to the degrees-of-freedom of the conduit and exposed to skin friction, dry friction and structural/hysteretic damping. All these damping mechanisms convert hydraulic transients into aperiodic and non-linear phenomena difficult to describe. In Section 2.3 the fundamentals of wave damping mechanisms are further developed and a review assessment provided.

2.2.7 Classic waterhammer theory

The classic waterhammer theory is the product of accumulation of scientific achievements in a well defined framework, starting by Newton (1686) and Lagrange (1788), with studies on the acoustic wave speed in air; passing by Helmholtz (1882) and Korteweg (1878), who established waterhammer wave celerity formulae based on the criterion that hydraulic transients in pipe flow are dominated by fluid compressibility and pipe-wall distensibility; Menabrea (1858) (Anderson, 1976) whose work is attributed to be the first contribution in waterhammer; and Von Kries (1883) and Joukowsky (1904) who developed the equation for the waterhammer wave amplitude; and finishing by Braun (1909, 1910) and Allievi (1902, 1913), who presented the fundamental equations in which the waterhammer theory is based. Authors such as Michaud (1878), Jouguet *et al.* (1914) or Mendiluce (1987) contributed to the development of rigid column theory, which is ignoring the compressibility of the fluid and elasticity of the pipe-wall.

Waterhammer wave celerity: The Newton-Laplace equation corresponds to the speed of sound for a compressible fluid in an infinite medium (unconfined fluid):

$$a_1 = \sqrt{\frac{K}{\rho_f}} \quad (2.1)$$

However, a waterhammer wave is the result of a combination of several degrees-of-freedom of the pipe system, each one with its own propagation speed. Helmholtz (1882) was the first who suggested that the speed of propagation of waterhammer waves not only depends on the acoustic speed in the fluid but also on the pipe-wall deformability.

In parallel, Young (1808), Webber (1866), Resal (1876) and Moens (1998) contributed to the development of Eq. 2.2, which is also called the Moens-Korteweg equation and represents the speed of propagation of a waterhammer wave for an incompressible fluid. This equation is valid for rubber hoses and blood vessels, where the pipe-wall distensibility dominates over the fluid compressibility during the propagation of a disturbance.

$$a_{MK} = \sqrt{\frac{Ee}{\rho_f D}} \quad (2.2)$$

Korteweg (1878), in order to calculate the waterhammer wave celerity considering both fluid compressibility and pipe-wall distensibility, combined Eqs. 2.1 and 2.2 obtaining the Helmholtz-Korteweg equation:

$$a_{HK} = \sqrt{\frac{K}{\rho_f \left(1 + \frac{DK}{eE}\right)}} \quad (2.3)$$

which is equivalent to

$$\frac{1}{a_{HK}^2} = \frac{1}{a_1^2} + \frac{1}{a_{MK}^2} \quad (2.4)$$

The three travelling time scales derived from Eqs. 2.1, 2.2, and 2.3 follow, therefore, a Pythagorean relation: for a rigid pipe of finite length containing incompressible fluid, the time scale of the system response is 0 (Tijsseling & Vardy, 2004); for an elastic pipe with compressible fluid, the square of the resultant waterhammer travelling time scale is the summation of the squares of the time scales due to pipe distensibility and fluid compressibility.

A more general expression of the previous Eq. 2.4 can be found in Anderson & Johnson (1990):

$$\frac{1}{a_{HK}^2} = \frac{\partial \rho_f}{\partial p} + \frac{\rho_f}{A} \frac{\partial A}{\partial p} \quad (2.5)$$

Hence, any pressure-excited pipe degree-of-freedom affecting the cross-sectional area affects, as well, the waterhammer wave celerity. If the pipe-wall is fully rigid (only 1-DOF considered),

the waterhammer wave speed is the same as that of Eq. 2.1, which is the sound in unconfined water (Frizell, 1898). If the radial deformation of the pipe is considered (2-DOF), then the wave speed is reduced according to Eq. 2.3. If the cross-sectional area is additionally affected by the Poisson effect, the 3-DOF has to be considered. And so on for any pipe degree-of-freedom affecting the pipe cross-section. For instance, Anderson & Johnson (1990) derived a wave celerity equation considering the vibrating mode caused by an elliptic conduit.

Finally, Halliwell (1963) presented the pressure wave celerity formulae most commonly used in the classic waterhammer theory:

$$a_h = \sqrt{\frac{K}{\rho_f \left[1 + \frac{K}{E} \psi\right]}} \quad (2.6)$$

where ψ is a coefficient that depends on the pipe-wall setting (*i.e.* thin or thick-walled) and on the anchoring conditions: (a) pipe anchored against longitudinal movement throughout its length; (b) anchored against longitudinal movement at the upper end; (c) conduit with frequent expansion joints. Quasi-static conditions of the structure deformation are assumed in the derivation of ψ coefficients. Values of ψ can be found in Streeter & Wylie (1978) and Chaudhry (2014).

Fluid-structure interaction, therefore, considerably affects the waterhammer wave celerity in fluid-filled conduits. An example of this can be found in Hachem & Schleiss (2011), where a review of the wave celerity in frictionless and axisymmetrical steel-lined pressure tunnels is made. In this review the authors point out the significant difference in wave speed values due to the fluid-structure interaction and its dependence to the stiffness of the steel liner and penstock.

Waterhammer wave amplitude: To understand the historical evolution of the well known Joukowsky equation, which relates pressure variation with confined liquid column velocity changes, its analogous formulation have to be first traced in solid mechanics. Young (1808) and Clebsch (1883) developed Eq. 2.7, which is essentially the same expression for longitudinal waves in solid bars.

$$\Delta\sigma_z = -\rho_p a_3 \Delta V \quad (2.7)$$

In shock waves theory, Rankine (1870) generalized the previous expression to any substance, whether gaseous, liquid or solid (Anderson, 2000; Tijsseling & Anderson, 2004). Finally, Von Kries (1883), Joukowsky (1904), Frizell (1898) and Allievi (1902) adapted the formula for pressurized conduits.

$$\Delta p = \rho_f a_h \Delta V \quad (2.8)$$

Eq. 2.8 has been extensively used in pipe system design due to the easy applicability and good accuracy for estimating maximum pressures for fast hydraulic transients. However, in the context of fluid-structure interaction, the pressure rise computed by Eq. 2.8 may underestimate maximum transient pressures influenced by several FSI phenomena. For instance, Wood (1969) experimentally observed significantly higher pressures than the Joukowsky's, claiming FSI as the cause. Tijsseling & Heinsbroek (1999) measured pressure rises up to 100% higher than Joukowsky's pressure rise caused by FSI. Jones & Wood (1972) derived Joukowsky-like expressions in order to account for 3-DOF FSI effects in the computation of maximum pressure rise.

2.3 Damping mechanisms

2.3.1 Skin friction

Skin friction equally, but oppositely, affects the 1-DOF and the 3-DOF of a pipe system by means of the shear stress occurring between fluid and the pipe-wall. Friction coupling is the mechanism that describes this action-reaction relation in FSI models. The pipe structure is not very sensitive to friction coupling in comparison to other coupling mechanisms, such as junction or Poisson coupling. Though, in the fluid skin friction plays an important role for the pressure wave damping, which, in classic waterhammer theory, is regarded as the only wave dissipating mechanism. In waterhammer literature, skin friction losses are frequently decomposed in steady and unsteady friction losses.

$$h_f = h_{f_s} + h_{f_u} \quad (2.9)$$

Steady skin friction

Quasi-steady conditions are frequently assumed for skin friction computation (Wylie *et al.*, 1993; Chaudhry, 2014). The flow is assumed to be steady at any instant, enabling the application of steady formulae, such as Darcy-Weisbach equation, for the wall shear stress computation.

$$\tau(t) = \frac{1}{8} \rho_f f V(t) |V(t)| \quad (2.10)$$

The use of steady-state wall shear relations in unsteady problems is satisfactory for very slow transients, so slow that they do not properly belong to the waterhammer regime (Ghidaoui *et al.*, 2005). Discrepancies between experimental data and numerical output frequently arise when computations assume quasi-steady skin friction in fast transient events (Vardy & Hwang, 1991; Axworthy *et al.*, 2000; Silva-Araya & Chaudhry, 1997; Brunone *et al.*, 1995; Ramos *et al.*, 2004; Bergant *et al.*, 2008a).

Unsteady skin friction

Friction has frequently a non-linear behaviour in physical systems. The relation between the parameters defining the unsteadiness of friction has motivated research on waterhammer during the last decades. Fast transients have a strong 2D nature of the flow field (Brunone *et al.*, 1995, 2000). Consequently, a dimension-reduction problem must be added to the already mentioned intrinsic non-linear problem of the friction. The unsteady term in Eq. 2.9 is aimed to represent the unsteady friction losses caused by flow reversal and strong velocity gradients close to the pipe-wall caused by the transient flow conditions (Ghidaoui *et al.*, 2005). Szymanski (1930) is one of the first researchers addressing unsteady friction, clearly explaining the underlying physics with rigorous mathematics (Urbanowicz & Tijsseling, 2015).

Unsteady friction in 1D pipe flow models is one of the factors that generates dissipation, dispersion and shape-change of the pressure wave. Its importance depends on the system considered and the operating conditions. In most of the laboratory waterhammer test rigs made of metal pipes, unsteady friction dominates over steady friction (Bergant *et al.*, 2008a), in particular for fast transients.

Unsteady friction models can be classified, according to their basic modelling assumptions, into four categories: (i) based on instantaneous mean flow velocity (Hino *et al.*, 1977; Brekke, 1984; Cocchi, 1988); (ii) based on instantaneous mean flow velocity and instantaneous local acceleration (Daily *et al.*, 1955; Carstens & Roller, 1959; Safwat & Van der Polder, 1973; Kurokawa *et al.*, 1986; Shuy & Apelt, 1987; Golia, 1990; Kompare *et al.*, 1995); (iii) based on instantaneous mean flow velocity, instantaneous local acceleration and instantaneous convective acceleration (Brunone *et al.*, 1991; Vitkovsky *et al.*, 2000; Ramos *et al.*, 2004); and finally, (iv) unsteady friction models based on instantaneous mean flow velocity and weights of past velocity changes (convolution based models) (Zielke, 1968; Trikha, 1975; Kagawa *et al.*, 1983; Schohl, 1993; Vardy & Brown, 1996, 1995, 2003, 2004; Zarzycki, 1997, 2000).

An extensive review of unsteady friction models is presented in Bergant *et al.* (2001) and a comparison is carried out between Brunone's model, which is based on instantaneous local and convective acceleration, and Zielke's model, which is based on weights of past velocity changes. Soares *et al.* (2012) also compares an instantaneous acceleration model (Vítkovský) and a convolution based model (Vardy-Brown) for cavitating transient flow (*v.i.* Fig. 2.5).

Martins *et al.* (2015b, 2016) proved that the transient wall shear stress during waterhammer events in pipe flow has a strong dependence on the flow time history and the local velocity variation, suggesting that this should be the basis for unsteady friction models. Hence, the research pointed out that models based on past velocity changes are more faithful to reality. Ghidaoui *et al.* (2002), based on two different turbulence models, also supported the assumptions taken in weighting function unsteady friction models. Wall shear stresses computed from numerical output using different 1D unsteady friction models are compared with CFD output, proving the better performance of convolution based models.

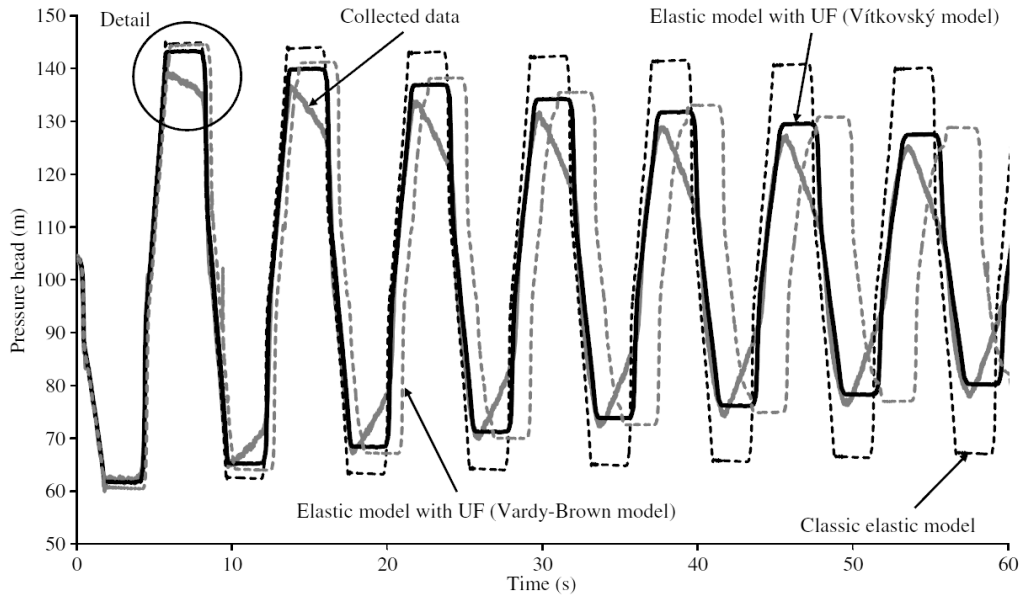


Figure 2.5 – Comparison between quasi-steady friction (classic elastic model), Vítkovský and Vardy-Brown models during a hydraulic transient caused by a pump trip (Soares *et al.*, 2012).

Szymkiewicz & Mitosek (2005, 2007) proposed a modified finite element method for the solution of the two-equation model. Numerical output was compared with measurements concluding that the dissipation observed in the real waterhammer wave cannot be described only focusing on the skin friction source term of the momentum equation. These authors claimed that the waterhammer equations should include another additional mechanism of physical dissipation.

With the aim to analyse the effect of unsteady friction on FSI models, in the present research friction coupling is implemented considering Brunone (Brunone *et al.*, 1995) and Trikha (Trikha, 1975) unsteady friction formulations, which, as mentioned, belong to two different families of approaches.

Brunone's unsteady friction model

With the idea that during fast transients both, local and convective accelerations are correlated to friction forces, Brunone *et al.* (1991) proposed a single expression to calculate the unsteady component that requires an empirical coefficient k :

$$h_{f_u} = \frac{k}{2g} \left(\frac{\partial V}{\partial t} - a_h \frac{\partial V}{\partial x} \right) \quad (2.11)$$

In the present study the k coefficient is computed as suggested by Bergant *et al.* (2001):

$$k = \frac{\sqrt{C^*}}{2} \quad (2.12)$$

where the Vardy's shear decay coefficient C^* is given by (Vardy & Brown, 1995):

$$C^* = 0.00476 \quad (2.13)$$

for laminar flow, and

$$C^* = \frac{7.41}{Re^{\log \frac{14.3}{Re^{0.05}}}} \quad (2.14)$$

for turbulent flow.

By means of this method the k coefficient is computed as function of the Reynolds number and there is no need for calibration.

Trikah's unsteady friction model

The weighting-function models take into account the 2D nature of the velocity profile that causes the frequency-dependent attenuation and dispersion of the hydraulic transient. The first model of this kind was proposed by Zielke (1968), who developed an analytical solution for unsteady friction for laminar flows, where the unsteady head loss term is the convolution of the past fluid accelerations with a weighting function (full convolution method) described by:

$$h_{fu}(t)_{exact} = \frac{16\nu}{gD^2} \left(\frac{\partial V}{\partial t} * W \right) (t) \quad (2.15)$$

where $*$ indicates convolution and W the weighting function. The convolution in Zielke's model is approximated using the rectangular rule and the acceleration term is approximated using a central difference. However, this scheme is very expensive from the computational point of view. Trikha (1975) simplified this computation reducing the weighting function to the summation of three exponential terms and eliminating the need for convolution with an approximate recursive relationship:

$$h_{fu}(t)_{app.} = \frac{16\nu}{gD^2} \sum_{k=1}^n Y_k(t) \quad (2.16)$$

where, Y_k is a function that represents the exponential terms:

$$Y_k(t + \Delta t) = m_k [V(t + \Delta t) - V(t)] + e^{-n_k \Delta \tau} Y_k(t); \quad (2.17)$$

n = the number of exponential terms ($n = 3$ in the case of Trikha formulation); τ_t = is the dimensionless time step, $\tau_t = \frac{4v\Delta t}{D^2}$; n_k and m_k = coefficients of the exponential summation, $n_k = (26.4, 200, 8000)$ and $m_k = (1, 8.1, 40)$.

2.3.2 Hysteretic damping

The ratio between stress and strain, the Young's modulus of elasticity, is an intrinsic property of the pipe material that is affected by its molecular structure, temperature, material ageing and stress-strain history (Jones & Ashby, 2005; Ward & Sweeney, 2012). The dependence on stress-strain history is an important damping phenomenon during hydraulic transients in plastic pipes, which present a strong non-elastic pipe-wall rheological behaviour (Covas, 2003). Experimental evidence has certainly shown that the elastic assumption for plastic pipes can lead to the underestimation of the pressure wave damping effect (Fox & Merckx, 1973; Meibner & Franke, 1977; Williams, 1977; Sharp & Theng, 1987; Mitosek & Roszkowski, 1998; Pezzinga & Scandura, 1995; Covas *et al.*, 2004c,d; Soares *et al.*, 2008).

Several authors proposed mathematical models to describe the viscoelasticity of pipe-wall during hydraulic transients (Gally *et al.*, 1979; Rieutord & Blanchard, 1979; Rieutord, 1982; Franke, 1983; Suo & Wylie, 1990; Covas *et al.*, 2002; Covas, 2003; Covas *et al.*, 2004a, 2005; Keramat & Tijsseling, 2012; Duan *et al.*, 2009). Either frequency or time-domain approaches can be followed to describe the effect of the viscoelastic pipe-wall behaviour in hydraulic transients.

Due to its time-dependency, pipe-wall viscoelasticity can be described in the frequency-domain in terms of angular frequency. Freitas Rachid *et al.* (1994) and Freitas Rachid & Costa Mattos (1995) pointed out the importance of considering a variable wave speed for hydraulic transient analysis in plastic pipes. The modulus of elasticity of the pipe material used in the wave speed computation is replaced by the inverse of the creep function, J (Covas *et al.*, 2004c). Meibner & Franke (1977) and Franke (1983) studied the damping of steady-oscillatory flows in PVC and steel pipes, deriving wave speed and damping formulae. Rieutord (1982) proposed a 'one Kelvin-Voigt element model' to describe creep and included it in the wave speed formula. For flexible hydraulic hoses, Yu & Kojima (1998) used two Kelvin-Voigt elements connected in series. Suo & Wylie (1990) modelled pipe-wall viscoelasticity in both oscillatory and non-periodic flows. Covas *et al.* (2004c, 2005) compared the results of this approach with experimental data (*v.i.* Fig. 2.6). Additionally, unsteady friction was incorporated in the solver, pointing out the importance of considering simultaneously both phenomena and the difficulty to distinguish them.

Viscoelastic models in time-domain approach incorporate an additional term to the mass balance equation of the fluid. The rheological viscoelastic behaviour of the pipe wall in the classic waterhammer equations is divided in two parts, an instantaneous elastic response (included in the elastic wave speed) and a retarded-viscoelastic response due to the creep of the viscoelastic material added to the mass balance equation. This formulation has been

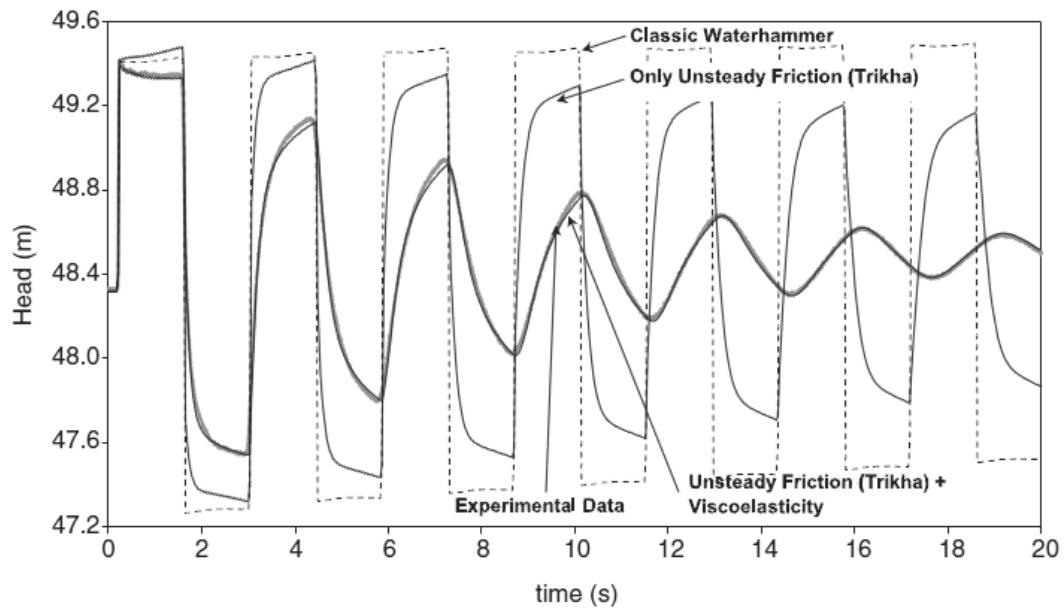


Figure 2.6 – Comparison of classic waterhammer model with adding first unsteady friction and then both unsteady friction plus pipe-wall viscoelasticity *vs.* experimental observations at the downstream pipe-end during a waterhammer event (Covas *et al.*, 2005).

proposed by Gally *et al.* (1979) and Rieutord (1982). Rachid *et al.* (1992, 1991) and Rachid & Mattos (1994) extended the development of the general constitutive theory and implemented several types of non-elastic rheological behaviour. Metal at elevated temperatures or when subjected to fast loading-rates presents a hysteretic behaviour. Anelasticity is the term used to describe the hysteretic elastic behaviour of metals. The analysis of structural and atomistic features responsible for anelasticity has shown that metallic atoms are capable of moving relative to one another in much the same way that long polymer chains (Courtney, 1990). This phenomenon, which has not been studied yet in the field of hydraulic transients, can cause damping of the waterhammer wave in metallic pipes in a similar manner as viscoelasticity in plastic pipes, though with lower intensity.

Duan *et al.* (2009) assessed a quasi-2D waterhammer model taking into account unsteady friction and viscoelasticity and compared the model output with experimental data from Covas *et al.* (2004c). He concluded that the viscoelastic effect is more severe for low frequencies whereas unsteady friction is more intense for high frequencies of the wave oscillation. FSI and pipe-wall viscoelasticity were combined in Weijde (1985), Stuckenbruck & Wiggert (1986) and Keramat & Tijsseling (2012). The latter is provably the most complete analysis. A four-equation model was implemented including Poisson coupling, column separation and pipe-wall viscoelastic behaviour based on Soares *et al.* (2008), which included the latter two.

Rachid & Stuckenbruck (1989) modelled viscoelastic pipe behaviour coupled and uncoupled with fluid-structure interaction in a four-equation model. Rachid & Costa Mattos (1998) included Poisson coupling in the computations and Rachid & Mattos (1999) presented a

parametric study. Structural damping was theoretically and experimentally studied by Budny *et al.* (1991), Budny *et al.* (1990) and Jeleu (1989). Williams (1977) combined FSI effects with pipe-wall viscoelasticity by carrying out tests in steel, ABS and PVC for different FSI configurations. Tijsseling & Vardy (1996b) and Hachem & Schleiss (2012) analysed the hysteretic damping caused by a short plastic pipe segment embedded in a metallic pipe rig. With different experimental configurations both reached similar conclusions, stating that the vibration could be adapted and modified in function of the segment material and geometry. In the field of biomechanics, pipe-wall viscoelastic behaviour is also considered an important effect for the description of the physiological flow in veins and arteries (Rutten, 1998).

The viscoelastic behaviour of pipe walls has a dissipative and dispersive effect in the pressure wave, similar to unsteady friction losses. Although the viscoelastic behaviour of polymers is well-known, this behaviour tends to be forgotten in hydraulic transient analyses of plastic pipes (Covas *et al.*, 2005). Furthermore, in these set-ups the damping of the waterhammer wave is higher due to viscoelasticity than to unsteady friction (Ramos *et al.*, 2004; Soares *et al.*, 2008). In Soares *et al.* (2009) unsteady friction losses, pipe-wall viscoelasticity and wave speed variation due to the formation of localised gas cavities were assumed to be described by the creep function. The effects of unsteady friction and pipe-wall viscoelasticity are hard to distinguish (Covas *et al.*, 2004b) and, to the knowledge of the authors, unsteady friction effect has never been separately assessed in a two-mode FSI model. Due to FSI, the pipe-wall vibrates axially at a different rate than the fluid, hence, the relative velocity between both (V_r) must be considered for skin shear stress assessment. The higher the Mach number (V_r/a_h) is, the greater the wall shear stress effects become (Ghidaoui *et al.*, 2005). Therefore, unsteady friction effects may be increased when fluid-structure interaction is important.

2.3.3 Dry damping

In the implementation of a four-equation model a major question may arise: is there movement in the pipe supports? Anchorages of pipelines aim to avoid the pipe-wall movement essentially by means of dry friction. However, pipe supports are never entirely stiff or entirely inert when loaded by impacts (Tijsseling, 1997). Thus, infinitesimal movements occur. In a system where the pipe is allowed to move, not only skin friction but also dry friction dissipation between the pipe-wall and its supports occur during fast hydraulic transients (Feeny *et al.*, 1998). This additional dissipation may affect all the pipe degrees-of-freedom involving the pipe-wall movement. Dry friction is proportional to the normal force, hence, for a high normal force, important energy might be dissipated from the structure to its supports/surroundings. Furthermore, in this context, it is crucial to define the stick-slip transitions.

For dry friction computation, the Coulomb's law is usually applied (Eq. 2.18), and it is assumed that the friction force F_{df} is proportional to the normal force N acting between the surfaces and opposite to the pipe-wall movement:

$$F_{df} = -\mu F_N \text{sign}(U) \quad (2.18)$$

in which μ is the friction coefficient, $sign()$ is a function that returns 1 or -1 according to the pipe-wall movement direction and N is the normal force corresponding to the weight of the pipe segment filled with water:

$$F_N = [\rho_p A_p + \rho_f A_f] \cdot \Delta z \cdot g \quad (2.19)$$

The friction coefficient increases from 0 until a maximum value is reached when the movement is imminent, and then it drops to a relatively constant value during motion for low velocities (Weaver Jr *et al.*, 1990).

Approximate values are given for Coulomb's friction coefficient for different materials, either for the static and the kinematic coefficients in Davis (1997). The static friction coefficient is used to conduct the stick-slip condition (Capone *et al.*, 1993) that balances the resultant force from axial stress in the pipe-wall section with the resultant force from dry friction.

Tijsseling & Vardy (1996a) included Coulomb's dry friction in a four-equation model with the goal to describe the behaviour of pipe racks, proposing a quantitative guideline equation aiming at assessing when dry friction forces may be relevant during hydraulic transients. As it can be observed in Fig. 2.7, the pipe-wall axial movement is clearly affected by the pipe rack and, although not that evident, as consequence fluid pressure is also affected. Hence, the dry friction occurring between the pipe and the supports affects, somewhat, the pressure transient wave amplitude.

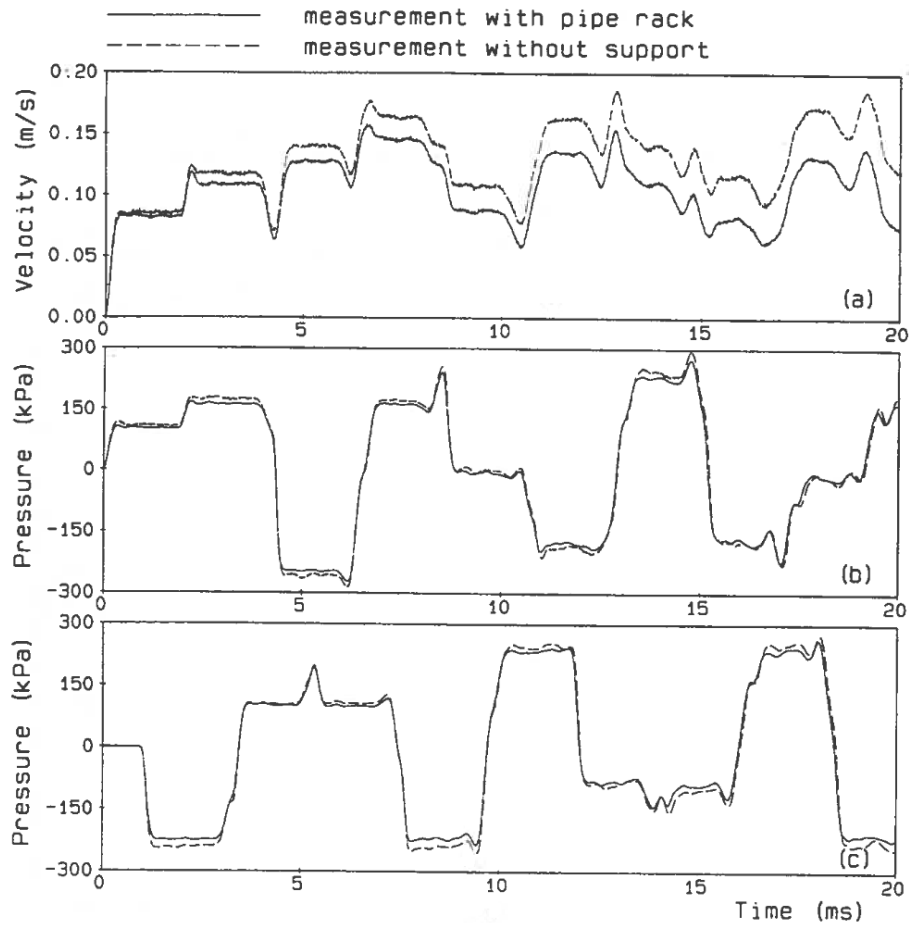


Figure 2.7 – Measured axial pipe velocity (a), and measured pressures at two different pipe locations (b,c) for a water-filled pipe excited by a steel rod impact (Tijsseling & Vardy, 1996a).

2.4 The most relevant experimental work programmes

2.4.1 Introduction and summary table

This section focuses on those experimental programmes that served waterhammer researchers to develop and validate their fluid-structure interaction models. Some of the presented publications form part of bigger projects that included both experimental and numerical research. The description of the laboratory pipe-rigs and the aim of their empirical outcome is explained hereby.

The fluid-structure interaction is difficult to isolate and frequently undesired FSI's occur in experimental facilities even when the target is the analysis of different phenomena. For instance, Holmboe & Rouleau (1967) decided to embed the pipe in concrete in order to avoid FSI in the pipe-rig, aiming to study frequency dependent wall shear stress. The following table 2.1 a summary of the main experimental research work related with fluid-structure

2.4. The most relevant experimental work programmes

interaction in pipe transient flow is depicted organized by research institutes, authors and dates.

Table 2.1 – Summary table of the most relevant experimental work in the research of fluid-structure interaction in hydraulic transients.

Research centre	Citations	Facility description and purpose
City University London, U.K.	Thorley (1969)	Aluminium alloy straight pipe. Experimental evidence of precursor waves is depicted.
University of Dundee, U.K.	Vardy & Fan (1986) Vardy & Fan (1987) Vardy & Fan (1989) Fan (1989) Fan & Vardy (1994) Vardy <i>et al.</i> (1996)	Suspended pipe rigs excited by the impact of a solid rod aiming at isolating FSI effects.
University of Karlsruhe, Germany	Bürmann (1975) Bürmann (1979) Bürmann & Thielen (1988c) Bürmann <i>et al.</i> (1985) Bürmann <i>et al.</i> (1986b) Bürmann <i>et al.</i> (1987) Bürmann <i>et al.</i> (1986a) Bürmann & Thielen (1988a)	Physical data from diverse case-studies: subterranean salt cavern, water-main bridge and tank-ship loading line. The aim was the development and validation of a four-equation model.
Delft Hydraulics, The Netherlands	Weijde (1985) Kruisbrink & Heinsbroek (1992) Heinsbroek & Kruisbrink (1993)	Complex apparatus hold by suspension wires and specially designed for FSI tests. Used for the development and verification of the FLUSTRIN code.
Michigan State University, U.S.A.	Wiggert (1983) Wiggert <i>et al.</i> (1985b) Wiggert <i>et al.</i> (1987) Lesmez <i>et al.</i> (1990)	U-bend and multi-plane copper pipe aiming at validating a fourteen-equation model.
Stanford Research Institute, U.S.A.	Regetz (1960) Blade <i>et al.</i> (1962) A-Moneim & Chang (1978) A-Moneim & Chang (1979)	Straight pipe extensively equipped with pressure and strain gauges in order to analyse pipe flexure during the transient events generated by a pulse gun.
University of Berkeley, U.S.A.	Krause <i>et al.</i> (1977) Barez <i>et al.</i> (1979)	Conduit excited by firing steel spheres onto the pipe ends with the goal to study axial stress waves.
In the University of Kentucky, U.S.A.	Wood (1968) Wood (1969)	Rigidly supported straight pipe terminated by a spring-mass device. Data used for model validation.
University of Guanajuato, Mexico.	Simão <i>et al.</i> (2015c) Simão <i>et al.</i> (2015b)	Pipe-rig assembled by concentric elbows aiming at validation of a CFD model.

2.4.2 Research in the U.K.

Thorley (1969) focused on the experimental analysis of tensile waves in the pipe-wall. He described the phenomenon of precursor waves and, in an aluminium alloy straight pipe, he was the first to observe precursor waves (*v.i.* Fig. 2.8), which are, at the same time, the evidence of Poisson coupling effect.

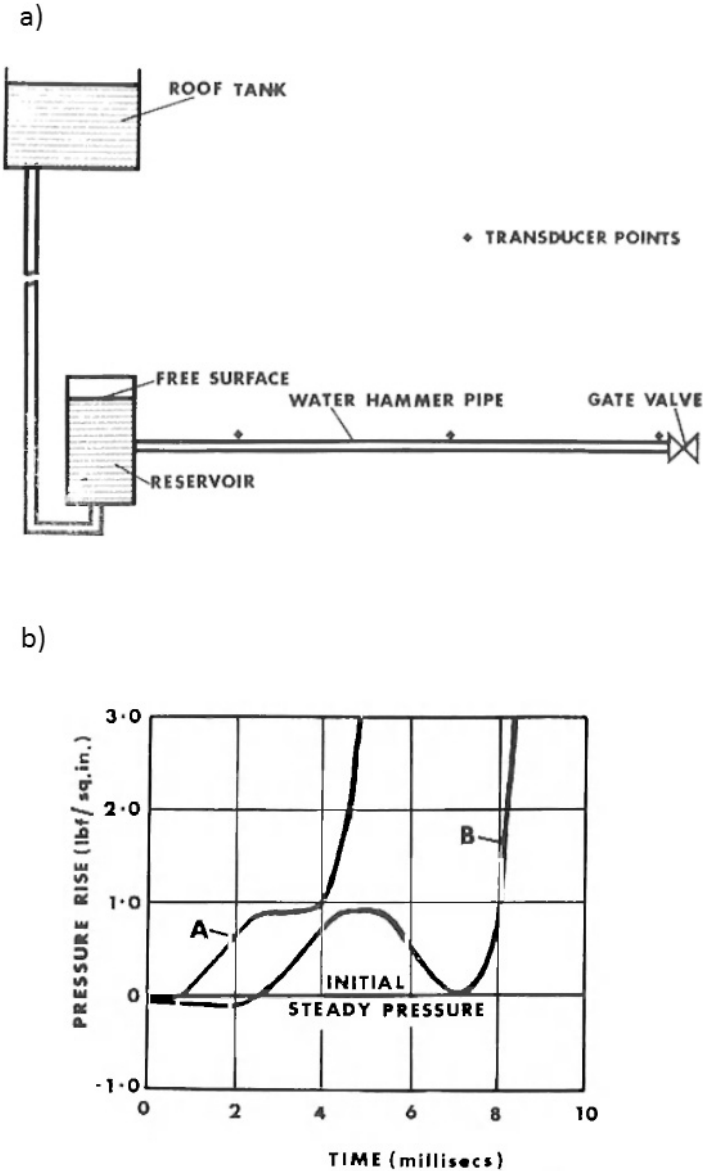


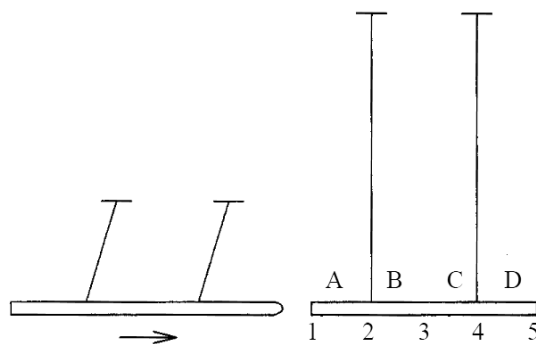
Figure 2.8 – Facility set-up used by Thorley (1969) (a); and measured precursor wave in different sections of the pipe (b).

In the University of Dundee, U.K., Vardy & Fan (1986, 1987, 1989) and Fan (1989) carried out experimental tests where FSI effects were specially well isolated by means of suspended

2.4. The most relevant experimental work programmes

pipe rigs which were excited by the impact of a solid rod. Fan & Vardy (1994) and Vardy *et al.* (1996) extended the work in the same experimental facility by including elbows and T-pieces (*vi.* Fig. 2.9 and 2.10). The tests were free of cavitation and other undesired dissipating phenomena. By means of striking the structure (and not the fluid) clean and steep wave fronts were achieved. This led to easily identifiable reflections and in general a good isolation of the targeted FSI mechanism, making these tests a good instrument for verification purposes. In combination with their numerical developments, they showed how FSI coupling changes the natural vibrating frequencies, which cannot be described in uncoupled approaches.

a)



b)

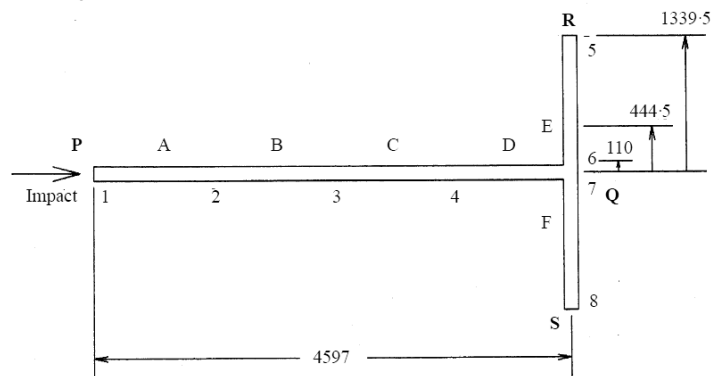


Figure 2.9 – Single pipe axial impact experiment set-up (a); and T-piece pipe impact experiment set-up (b) (Vardy *et al.*, 1996)

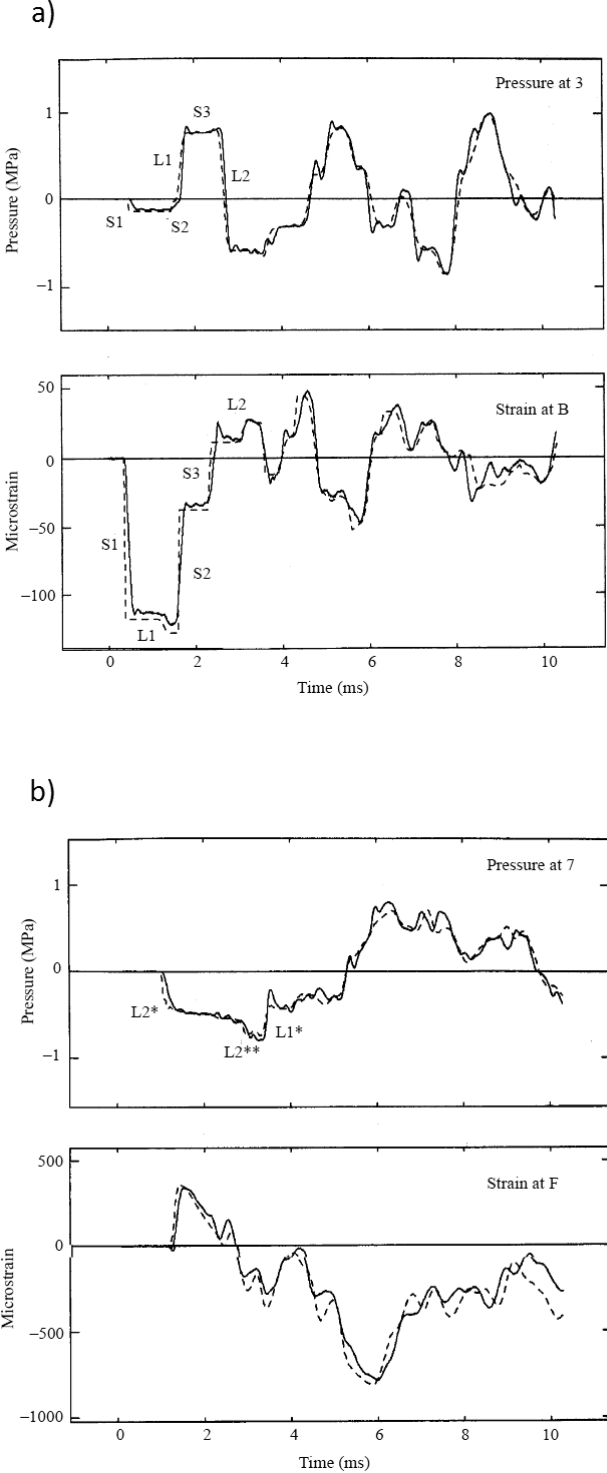


Figure 2.10 – Pressures and strains time series in the single pipe axial impact experiment (a) and in the T-piece pipe impact experiment (b). Solid lines correspond to experimental measurements and dashed lines to numerical output (Vardy *et al.*, 1996).

2.4.3 Research in Germany

In the University of Karlsruhe, Germany, interesting experimental programmes were carried out aiming at collecting physical data from particular pipe systems. Bürmann (1975, 1979) and Bürmann & Thielen (1988c) presented a series of tests carried out in a vertical pipe line located in a subterranean salt cavern (*v.i.* Fig. 2.11). In Bürmann *et al.* (1985, 1986b, 1987) measurements were shown from a water-main bridge, and in Bürmann *et al.* (1986a) and Bürmann & Thielen (1988a) from a loading line between tanks and ships. These measurements were used to develop and validate the four-equation model that was first presented in Skalak (1955).

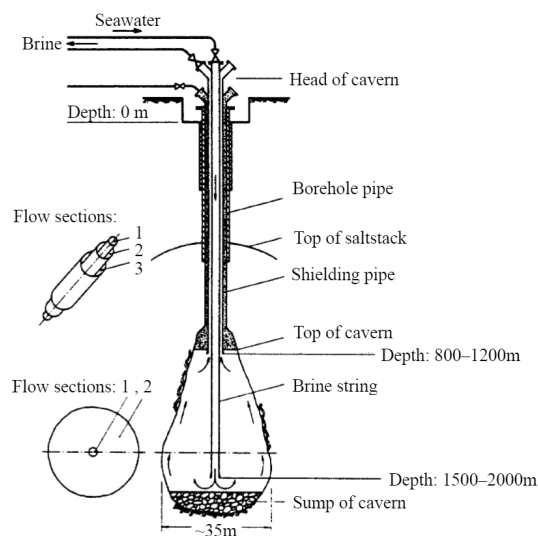


Figure 2.11 – Vertical pipe line located in a subterranean salt cavern for de-brining under direct circulation (Bürmann, 1975).

2.4.4 Research in The Netherlands

Weijde (1985) carried out experiments in a PVC pipe containing a U-shaped section at the laboratory of Delft Hydraulics, The Netherlands. He concluded that classic waterhammer theory was not accurate enough to describe the behaviour of the pipe-rig and, consequently, the FLUSTRIN project was launched. A complex apparatus (Fig. 2.12) held by suspension wires and specially designed for FSI tests was assembled at Delft Hydraulics laboratory and used for the development and verification of the FLUSTRIN code, which is based on a MOC-FEM approach. In this framework Kruisbrink & Heinsbroek (1992) and Heinsbroek & Kruisbrink (1993) carried out a series of numerical benchmark tests (*cf.* Figs. 2.16 and 2.20) which have been frequently used to verify FSI codes. They confirmed that classic and uncoupled calculations render unreliable results and emphasized the need of accounting for FSI effects.

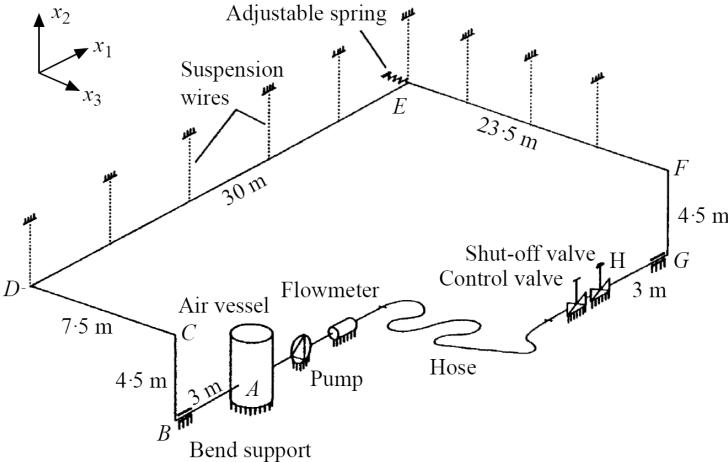


Figure 2.12 – FSI experimental set-up at Delft Hydraulics (Kruisbrink & Heinsbroek, 1992)

2.4.5 Research in the U.S.A.

Wiggert (1983) compiled the FSI research work carried out at Michigan State University, U.S.A., in the time and frequency-domain using, respectively, the MOC and the component-synthesis method for four-equation model solutions. Experimental data were used for the verification of the methods. In Wiggert *et al.* (1985b, 1987) a fourteen-equation solver was proposed and results compared with measurements in a multi-plane copper pipe (*u.i.* Fig. 2.13). A good fitting with measurements was obtained but the analysis concluded that further model developments were necessary. Lesmez *et al.* (1990) extended the work using an experimental set-up consisting of a copper pipe containing a U-bend free to move in an in-plane fashion.

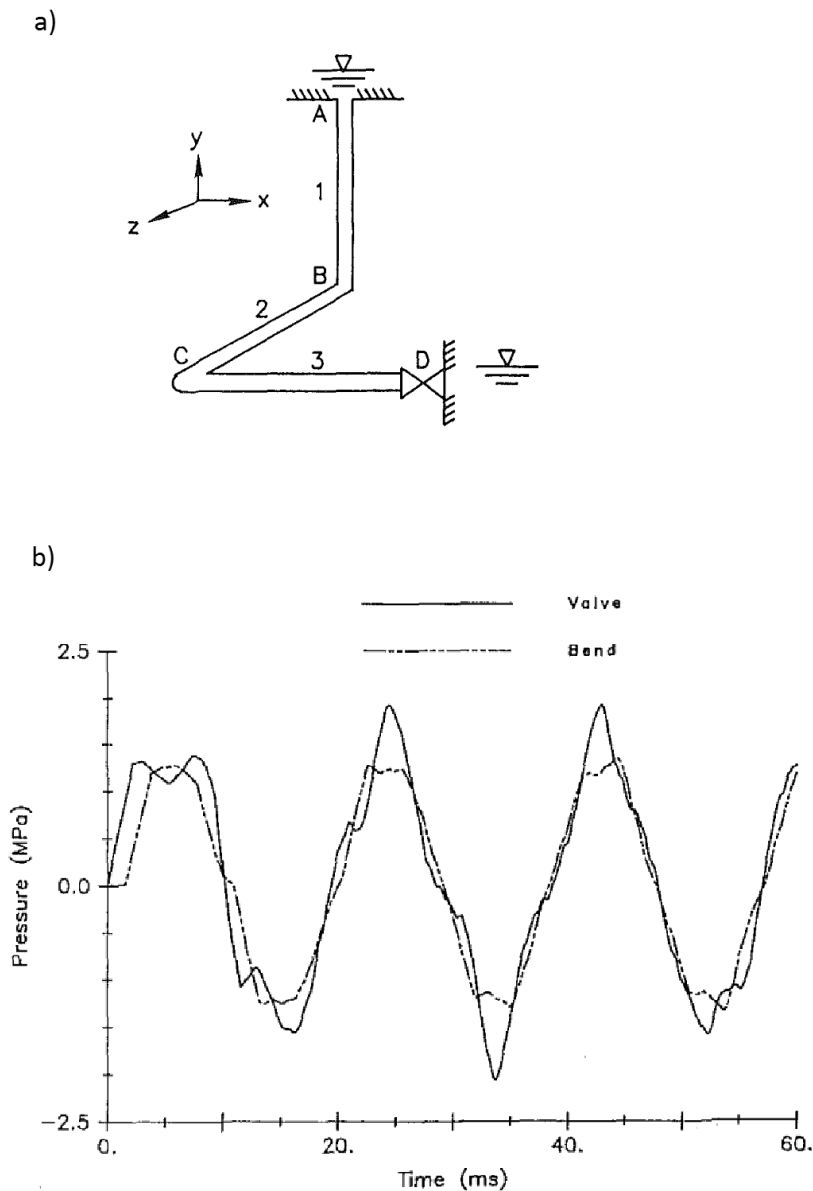


Figure 2.13 – Experimental set-up (a) and pressure measurements (b) next to the downstream valve and at the bend-C (Wiggert *et al.*, 1987).

At the Stanford Research Institute, U.S.A., Regetz (1960) investigated pressure and velocity fluctuations in a straight pipe filled with rocket fuel. His experimental apparatus allowed for axial pipe motion. Blade *et al.* (1962) extended the work by adding an elbow in the experimental pipe rig. Also A-Moneim & Chang (1978, 1979) followed the same line of research. As it can be observed in Fig. 2.14, the experimental facility consisted, first, of a straight pipe extensively equipped with pressure and strain gauges. Later on, an elbow was added in order to analyse pipe flexure during the transient events. The system was excited by a calibrated pulse gun.

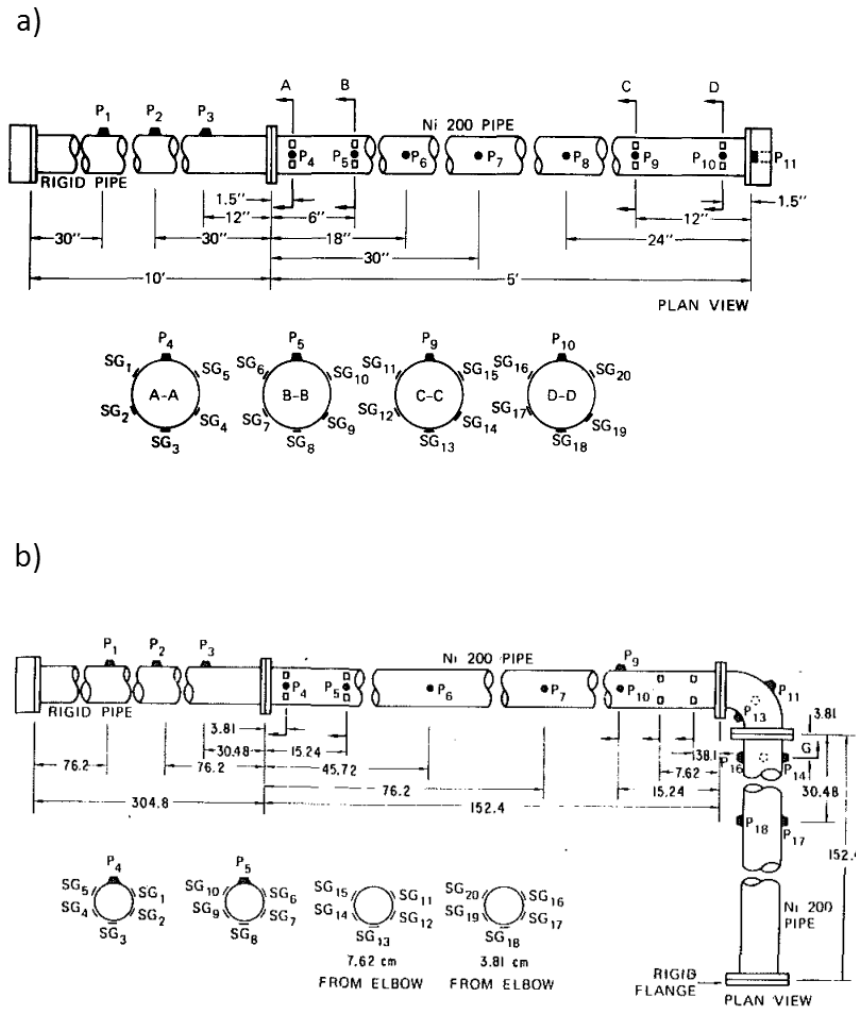


Figure 2.14 – Experimental straight pipe rig used in A-Moneim & Chang (1978) (a); and pipe equipped with an elbow used in A-Moneim & Chang (1979) (b).

In the University of California, Berkeley, U.S.A., Krause *et al.* (1977) studied axial stress waves in a closed conduit which was excited by firing steel spheres onto the tub ends. Barez *et al.* (1979) extended the work, experimentally and numerically.

In the University of Kentucky, U.S.A., Wood (1968, 1969) carried out experiments in a rigidly supported straight pipe terminated by a spring-mass device. Collected data were used for model development and validation in the time-domain. In Wood & Chao (1971) the work was extended by adding elbows and branches in the experimental set-up, concluding that if the elbows are anchored and do not, these do not affect much the transient wave and, when they move, their effect is considerable.

2.4. The most relevant experimental work programmes

2.4.6 Research in Mexico

In the University of Guanajuato, Mexico, Simão *et al.* (2015c,b) collected data from a pipe-rig assembled by concentric elbows of 90° (*v.i.* Fig. 2.15). The apparatus was equipped with pressure transducers and accelerometers. Waterhammer tests were carried out by a downstream valve manoeuvre. The aim of the experimental data collection was the validation of a numerical model which coupled CFD software for the fluid with FEM for the structure. The model was as well compared with a modified MOC approach which included damping coefficients to account for structural damping. The work highlighted the importance of integrated analyses including the description of both fluid and structure behaviours.

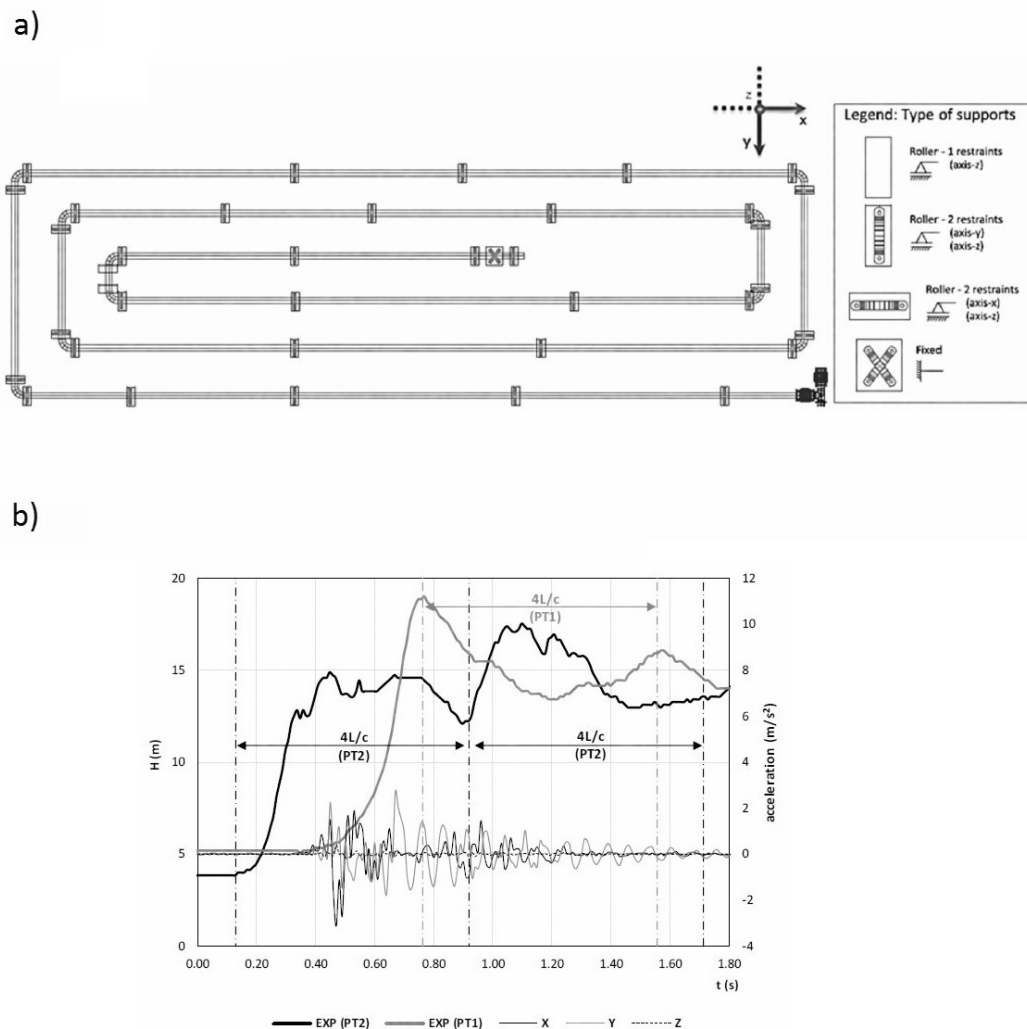


Figure 2.15 – Experimental set-up (a); and fluid pressure and pipe-wall acceleration measurements (b) in the x, y, z coordinates Simão *et al.* (2015c).

2.4.7 Research in other regions

Williams (1977) carried out experiments in steel, ABS and PVC pipes. The axial stress waves effect was depicted and the damping was attributed to FSI. In Davidson & Samsury (1969) and Davidson & Samsury (1972) fluid-structure interaction was analysed, respectively, in straight and curved pipes. Budny *et al.* (1990); Brown & Tentarelli (2001b) and Fan (1989) gave experimental evidence of Bourdon coupling (*cf.* Fig. 2.21). While, Gregory & Paidoussis (1966) and Jendrzejczyk & Chen (1985) focused their experimental research on describing the buckling and flutter effects in pipe systems.

2.5 Numerical research

2.5.1 One degree-of-freedom models

Two-equation model:

The classic waterhammer model (two-equation model) is a sophisticated version of the basic 1-DOF system (*cf.* Appendix A, Eqs. A.1 and A.2). Although the bulk modulus of compressibility and a finite acoustic wave speed are considered in the fluid, in terms of density variation the fluid is assumed to be incompressible and pressure changes are related to velocity changes somewhat by embedding fluid compressibility and pipe-wall extensibility into the wave celerity value, which is regarded as a constant parameter and is defined by Eq. 2.6.

On the one hand, the fundamental equations of classic waterhammer theory (*i.e.* mass and momentum conservation) can be derived from Navier-Stokes equations (Ghidaoui, 2004) or by directly applying the Reynolds Transport Theorem (Chaudhry, 2014) to a control volume of the pipe system. On the other hand, they can be also reached from the system of equations presented in Section 2.2, as, somewhat, classic theory considers a combination of the first two degrees-of-freedom. The fundamental momentum conservation equation is directly the one presented in 1-DOF (Eq. A.1). For mass conservation (continuity equation), the cross-sectional area of the control volume is assumed to vary and this variation is related to the fluid inner pressure by applying a quasi-static assumption in the 2-DOF. Establishing elastic stress-strain relations, and rearranging the system of equations composed of 1 and 2-DOF the continuity equation Eq. 2.21 is reached (*cf.* Appendix A).

The following system of PDE's (Eq. 2.21 and Eq. 2.20) represents the fundamental conservation equations of classic waterhammer theory.

$$\frac{\partial V}{\partial t} + \frac{1}{\rho_f} \frac{\partial p}{\partial z} = 0 \quad (2.20)$$

$$\frac{\partial V}{\partial z} + \frac{1}{\rho_f a_h} \frac{\partial p}{\partial t} = 0 \quad (2.21)$$

where a_h corresponds to the waterhammer wave celerity, which can be experimentally determined or theoretically computed by means of Eq. 2.5.

Usually the system of Eqs. 2.20 and 2.21 is solved by means of the Method of Characteristics (MOC), which is the most popular and extensively used method for waterhammer analysis thanks to its easy programming, computational efficiency and accuracy of the results (Vardy & Tijsseling, 2015).

CFD software

Computational-Fluid-Dynamics (CFD) refers to those models that solve the Navier-Stokes equations for a 3D fluid domain. Several numerical methods may be approached to solve the equations, such as $k - \epsilon$, Reynolds stress, SAS, DES, LES, etc. The former are the most suitable for parietal flows Anderson *et al.* (2001). Although the equations and the dimensions of the fluid domain are different in CFD models than in the proposed classification of Section 2.2, they are frequently used to yield information for the 1-DOF models, either for model development, verification or validation (Martins *et al.*, 2016). However, CFD models are still demanding both in computational time, pre-and post-processing time, as well as on input data, making their use for practical engineering purposes rarely justified.

In order to adapt CFD models for 1-DOF modelling, an important assumption has to be applied. If the pipe is rigid and does not deform, the hydraulic transient wave propagates at the acoustic speed in water (Eq. 2.1). To correct this, the bulk modulus of compressibility should be adapted (Martins *et al.*, 2016) in function of the a realistic wave celerity:

$$K^* = \rho_f a_h^2 \quad (2.22)$$

CFD software is being used in research on transient flows to assess unsteady skin friction models. Vardy & Hwang (1993) developed a weighting function unsteady friction model by means of using output data from a CFD model. In Ghidaoui *et al.* (2002) two different turbulence models were implemented and analysed for both quasi-steady and axisymmetric assumptions, suggestions for unsteady friction modelling were reported. Riedelmeier *et al.* (2014) compared skin friction rates in 1D and 3D for a pipe section with a 90° bend. Chung & Wang (2015) used direct numerical simulations (DNS) and identified a three-stage development of the mean wall shear stress for turbulent pipe flow at a constant acceleration rate. Martins *et al.* (2015b, 2016) has shown that the transient wall shear stress during waterhammer events in pipe flow has a strong dependence on the flow time history and the local velocity variation.

Simulation of multi-phase flow in pipes is also a stream where CFD models are contributing. Zhou *et al.* (2011), Zhou *et al.* (2013), Martins *et al.* (2015a) and Martins (2016) analysed the effect of entrapped and dissolved air during pipe flow transients. A state-of-the-art review in multi-phase transients in pipe flow for both 1D and 3D approaches is given by Tiselj (2015).

2.5.2 Models with up to three degrees-of-freedom

Four-equation models

The historical development of four-equation models can be traced back from Korteweg (1878) who already pointed out the need of considering axial stress waves. Gromeka (1883) and Lamb (1898), qualitatively, took into account pipe axial inertia and Poisson coupling in their analyses. Skalak (1955), who extended Lamb's work, presented the four basic fundamental equations and introduced the concept of precursor waves. Bürmann (1979), Thielen & Burmann (1980) and Bürmann & Thielen (1988b) presented a simplified version of Skalak's equations which represent the well-know four-equation system used in the standard four-equation models. Skalak's paper was revisited and analysed in Tijsseling *et al.* (2008).

For the description of pressure waves in pipe systems two or four-equation models are sufficient (Tijsseling, 1996). Four-equation models consider the combination of classic theory with the 3-DOF equations. Hence, four fundamental equations, two for the fluid and two for the pipe axial movement, are to be solved. The right-hand-side terms of the continuity equations of the 1-DOF and 3-DOF systems must be adapted in order to describe the Poisson coupling in terms of the dependent variables of the four-equation model (*i.e.*, respectively, σ_z and p). This derivation is explained in the Appendix A for which Eqs. 2.24 and 2.26 are obtained.

$$\frac{\partial V}{\partial t} + \frac{1}{\rho_f} \frac{\partial p}{\partial z} = 0 \quad (2.23)$$

$$\frac{\partial V}{\partial z} + \frac{1}{\rho_f a_h^2} \frac{\partial p}{\partial t} = \frac{2\nu}{E} \frac{\partial \sigma_z}{\partial t} \quad (2.24)$$

$$\frac{\partial U_z}{\partial t} - \frac{1}{\rho_p} \frac{\partial \sigma_z}{\partial z} = 0 \quad (2.25)$$

$$\frac{\partial U_z}{\partial z} - \frac{1}{\rho_p a_3^2} \frac{\partial \sigma_z}{\partial t} = -\frac{r\nu}{eE} \frac{\partial p}{\partial t} \quad (2.26)$$

Several numerical methods can be used to solve the previous system of equations, either integrating both the fluid and the structure in the same numerical scheme (*e.g.*, MOC-MOC) or by a combination between different schemes (*e.g.*, MOC-FEM). In Vardy & Alsarraj (1989) and Vardy & Alsarraj (1991) the Method of Characteristics for both the fluid and the structure (*i.e.*, MOC-MOC) was shown to have useful advantages. Schwarz (1978) used a FDM scheme in his four-equation model as a simplified version of a six-equation model which was solved by MOC. Ellis (1980) modelled fluid and axial stress waves in conduits by means of MOC, taking

into account only junction coupling (ignoring Poisson coupling). Kojima & Shinada (1988) also used a FDM approach which was validated by tests on a thin-walled straight pipe for Poisson coupling as well as junction coupling in a closed-free pipe end.

Wiggert *et al.* (1985a), Elansary & Contractor (1990), Elansary *et al.* (1994), Budny *et al.* (1991) and Elansary & Contractor (1994) explained how to solve the four-equation system considering Poisson coupling. They presented the characteristic equations from MOC transformation and how to integrate them into the same characteristic grid using time-line interpolations as explained in Goldberg & Benjamin Wylie (1983). The MOC transformation that allows hyperbolic partial differential equation systems to be converted to a set of ordinary differential equations was based on Forsythe *et al.* (1960). Zhang *et al.* (1994) used a FEM scheme for both, the fluid and the structure. In Bouabdallah & Massouh (1997) and Ghodhbani & Hadj-Taïeb (2013), time interpolation and wave adjustment methods are compared for MOC-MOC solutions. (Wiggert, 1983) used an hybrid MOC-FEM approach, MOC for the fluid and FEM for the structure. A FVM approach was presented in Gale & Tiselj (2005) to solve the four-equation model, which was successfully validated using the Delft Hydraulics Benchmark Problem A (Lavooij & Tijsseling, 1991; Tijsseling & Lavooij, 1990). In Lavooij & Tijsseling (1991) both approaches MOC-MOC and MOC-FEM are compared, concluding that for straight pipe problems the MOC procedure is more accurate and efficient.

The Delft Hydraulics Benchmark Problem A (20 m long, steel pipe, 0.4 m diameter) is a good approach for the verification of four-equation numerical codes (*v.i.* Fig. 2.16). In Li *et al.* (2003) and Tijsseling (2003), a theoretical development of an exact solution for the four-equation system by means of a recursion was presented. The drawback of the method is its exponential computational effort for longer simulation periods. Recently, in Loh & Tijsseling (2014), the computation for the exact solution was parallelized in order to increase computational efficiency and applicability. The analysis suggested to keep the scope of exact solutions to generate test cases and benchmark solutions for more conventional numerical methods.

Tijsseling (1997) has demonstrated the Poisson coupling beat, which is a phenomenon that arises from resonance between 1-DOF and 3-DOF (*v.i.* 2.17). Poisson coupling beat was already numerically observed by Wiggert (1986). So far, there is no experimental evidence about it as damping mechanisms tend to hide the oscillating resonance between the pipe-wall and the fluid vibrations.

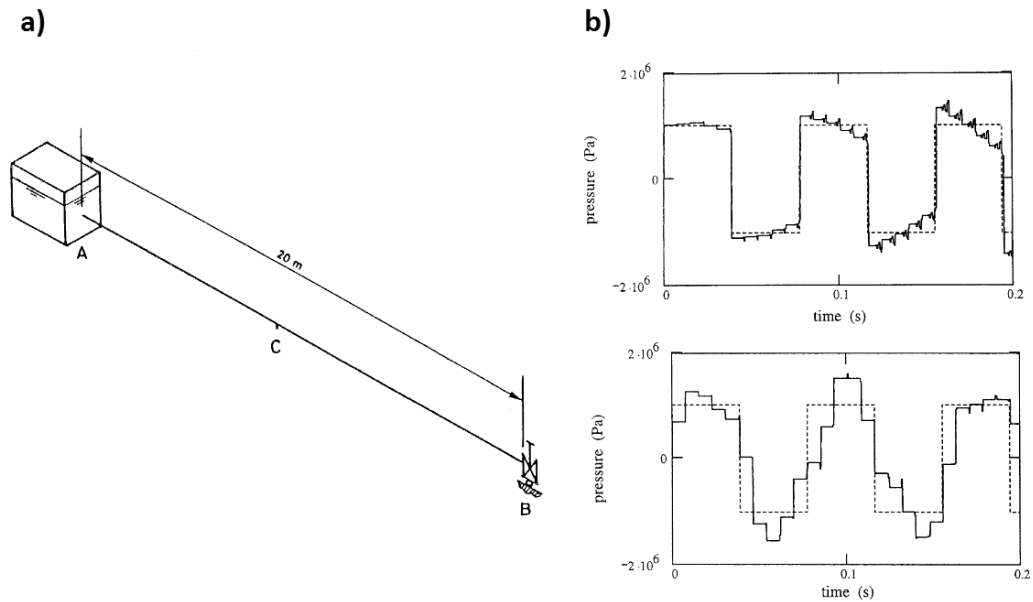


Figure 2.16 – Model set-up (a); and comparison between two-equation and four-equation models (b) for the Delft Hydraulics Benchmark Problem A, considering an anchored (top) or non-anchored valve (bottom) (Tijsseling, 2003).

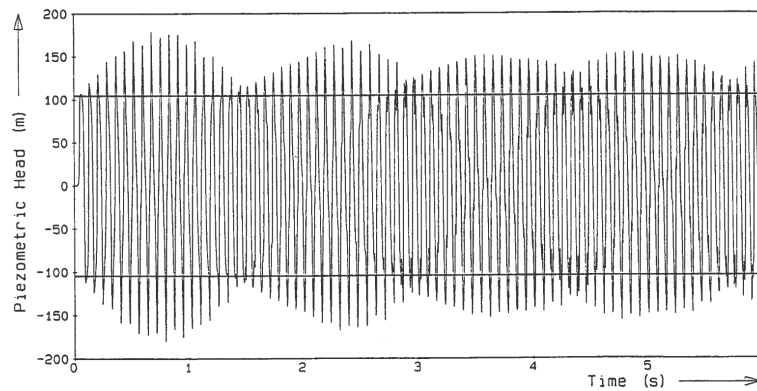


Figure 2.17 – Numerical evidence of the Poisson coupling beat (Tijsseling, 1997).

Six-equation models

Six-equation models aim at describing the 1,2,3-DOF's. As in the four-equation model, similar numerical schemes can be used for solving the six-equation system. However, the right-hand-sides of the three continuity equations are not expressed in differential terms. When integrating a first or second-order approximation can be applied.

Walker & Phillips (1977) was the first proposing, and solving by MOC, the six-equation model. These authors have compared results from the frequency and time-domains and carried out

its validation using experimental data collected from a water-filled copper pipe excited by hammering the pipe-end (*v.i.* Fig. 2.18).

With a similar MOC numerical scheme Schwarz (1978) solved the equations and compared them to a four-equation model solved by FDM, the effect of Poisson coupling in each case was also analysed. Kellner *et al.* (1983) extended the work of Walker & Phillips (1977) by proposing an added fluid mass term and solving the equations by a MOC-FEM approach. Gorman *et al.* (2000) used a MOC-FDM scheme in their numerical analysis, the effect of initial axial tensional stress was included in their derivation.

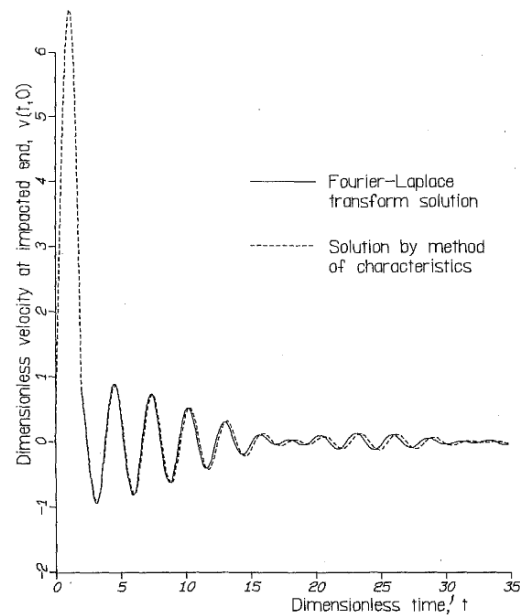


Figure 2.18 – Frequency and time-domain solutions of a six-equation model (Walker & Phillips, 1977).

From the six-equation system, Tijsseling (2007) derived a four-equation model which included correction terms and factors accounting for the wall thickness. The model was validated with exact solutions in the time-domain (Li *et al.*, 2003; Tijsseling, 2003). The authors concluded that a transient description of the 2-DOF is only important for very thick pipes ($r/e < 2$).

2.5.3 Models for more than three degree-of-freedom

Eight-equation model

According to the classification given in Subsection 2.2.3, eight-equation models solve the system of equations for either 1,3,4,6-DOF's or 1,3,5,7-DOF's. Hence, these kind of models are used to describe in-plane axial, torsional and flexural pipe displacements respectively in the \widehat{xz} or \widehat{yz} . Radial inertia is nested into the celerity of the 1-DOF as in the classic waterhammer theory.

Chapter 2. State-of-the-Art Review

Valentin *et al.* (1979) presented an eight-equation model for curved pipes for 1,3,4,6-DOF's. Hu & Phillips (1981) solved the same equations using MOC method and validated results using experimental data. Radial inertia was included in Joung & Shin (1987) solving a nine-equation model. Tijsseling *et al.* (1994, 1996) and Tijsseling & Heinsbroek (1999) used a MOC-MOC scheme in combination with cavitation, which was modelled by means of a lumped parameter model. In Gale & Tiselj (2006) a FVM method was used to solve the eight-equation model, which was tested for different set-ups (*v.i.* Fig. 2.19). In his analysis, Gale & Tiselj (2005) highlighted that a two-phase flow fluid model is needed for simulations of more universal FSI problems in pipelines.

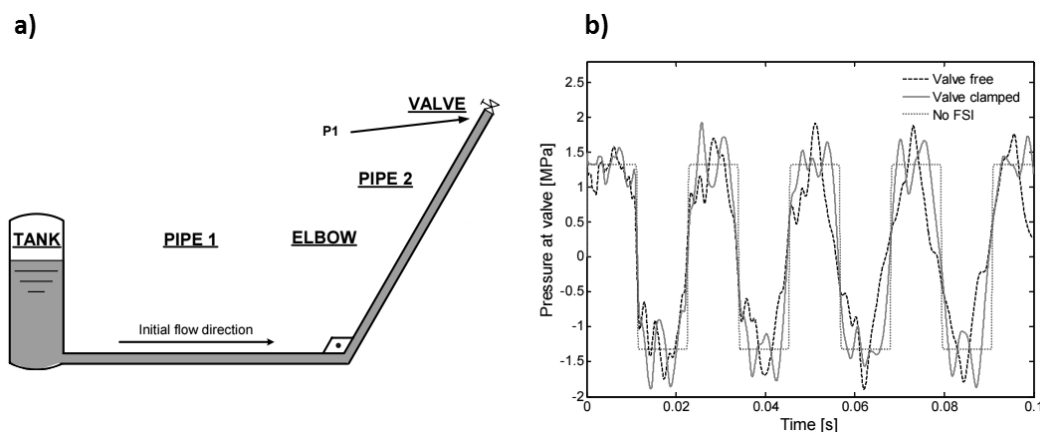


Figure 2.19 – Pipe rig set-up (a) and numerical output (b) for: a free moving valve (black dashed line), anchored (red solid line) and for classic waterhammer model (purple dotted line) (Gale & Tiselj, 2006).

Fourteen-equation model

The fourteen-equation model includes the degrees-of-freedom presented at Section 2.2 except the 2-DOF corresponding to the radial inertia of the pipe system, which is nested into the celerity of the 1-DOF like in the classic waterhammer theory.

Important work has been carried out for solving the fourteen-equation models in the frequency domain, to mention some: Wilkinson (1979), Kuiken (1988), Lesmez *et al.* (1990), Tentarelli (1990), De Jong (1994). Hatfield & Wiggert (1991) presented the component-synthesis method, which is an hybrid technique between frequency and time-domain. Time-domain solutions can be obtained from frequency domain analyses, however, Hatfield & Wiggert (1983) concluded that the time-domain solutions derived from frequency-domain are difficult and impractical.

Wilkinson (1977) introduced the fourteen-equation model in the time-domain, which was finally implemented by Wiggert *et al.* (1985a), Wiggert (1986) and Wiggert *et al.* (1987) with MOC approach, either in the fluid and in the structure. This method was used as well in

Obradović (1990), who simulated an accident. Tijsseling & Lavooij (1990) and Lavooij & Tijsseling (1989) implemented a code which solved the fourteen-equation system by means of a MOC-FEM scheme. The output was compared with a MOC-MOC when applied to a single straight pipe, corresponding to the Delft Hydraulics Benchmark Problem A (Lavooij, 1987). Coupled and uncoupled Poisson effect solutions were compared (*v.i.* Fig. 2.20) for the Delft Hydraulics Benchmark Problem F (Lavooij, 1987). Experimental measurements were used in this comparison and a guideline was provided suggesting when FSI is important. The same computer code was used by Kruisbrink (1990), Lavooij & Tijsseling (1991) and Heinsbroek (1997) with similar purposes of comparing with other modelling assumptions and using experimental tests for validation. Heinsbroek (1997) suggested that for four-equation modelling a MOC-MOC approach is more convenient, while for higher degrees-of-freedom a MOC-FEM scheme is preferable as higher grid resolution is required. Bettinali *et al.* (1991) presented a similar MOC-FEM code with differences on the implementation on the Poisson coupling mechanism.

The Delft Hydraulics Benchmark Problem F is a good approach for the verification of fourteen-equation numerical codes (*v.i.* Fig. 2.20).

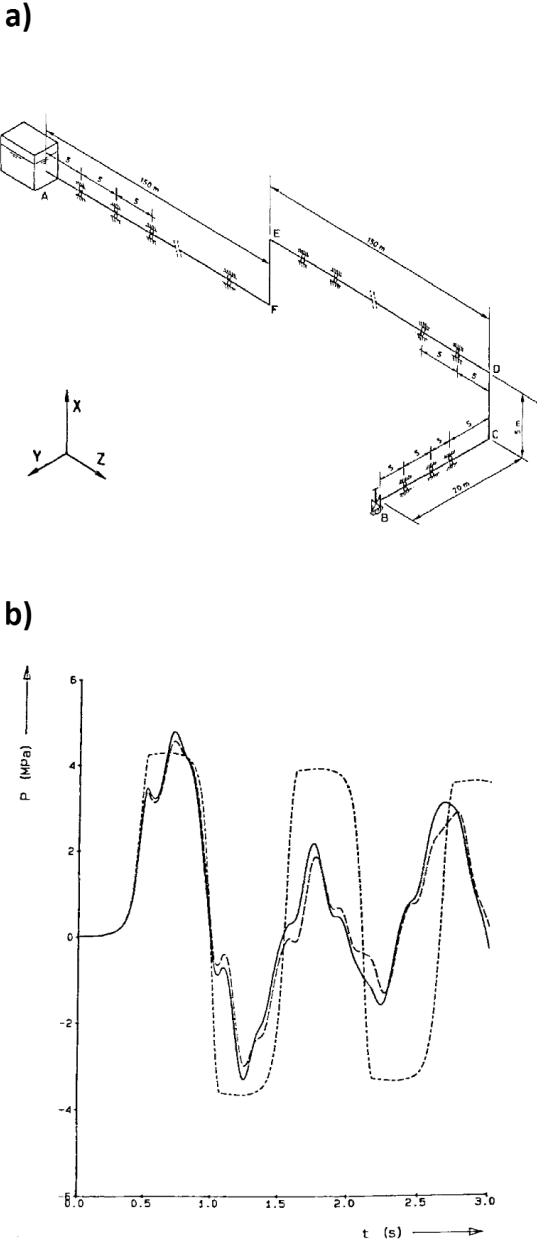


Figure 2.20 – Set-up of the Delft Hydraulics Benchmark Problem F (a); and numerical output (b) for: Poisson and junction coupling (solid line), only junction coupling (dashed line) and for classic waterhammer model (dash-dotted line) (Tijsseling & Lavooij, 1990).

Other FSI mechanisms

In curved pipes of non-circular cross-section an additional coupling mechanism, called Bourdon coupling, affects the pipe behaviour. This mechanism consists of the change of ovality of the pipe cross-section in function of the internal pressure loading. In Clark & Reissner (1950) and Reissner *et al.* (1952) the Bourdon tube deformation mechanism is explained and a methodology based on the Boltzmann superposition principle to describe stress-strain states in Bourdon tubes is presented. Bathe & Almeida (1980, 1982) studied Bourdon phenomena by means of a FEM approach. Bourdon effect was first dynamically coupled with the fluid response in Tentarelli (1990). The work was extended in Brown & Tentarelli (2001b) and Tentarelli & Brown (2001), experimental measurements were used for validation of the numerical output in the frequency domain (*v.i.* Fig. 2.21).

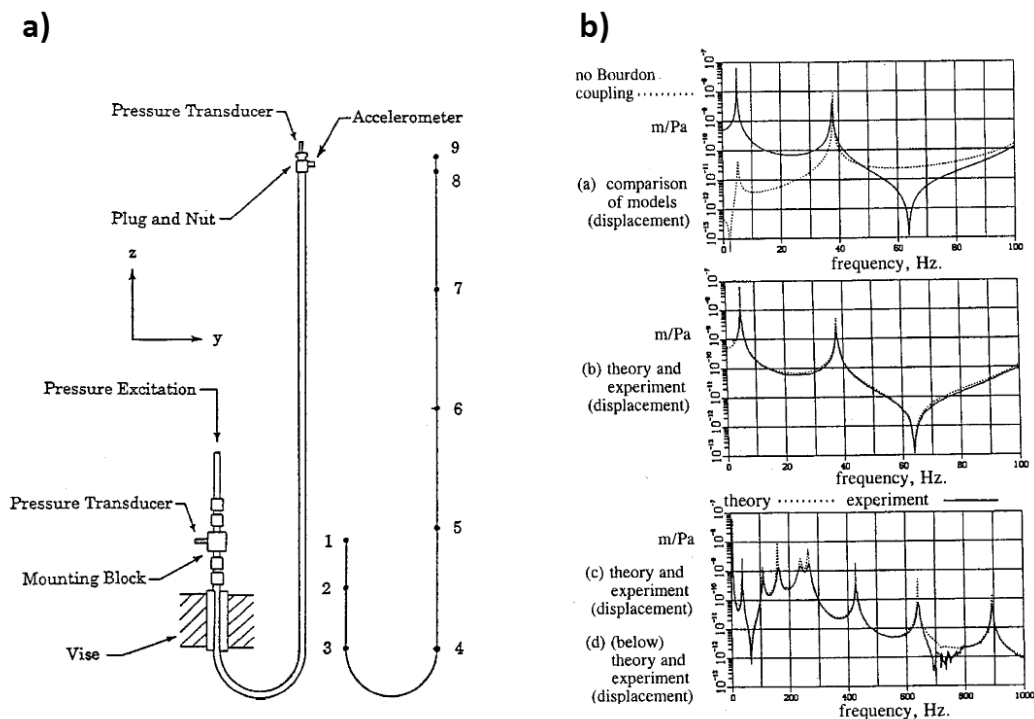


Figure 2.21 – Experimental set-up (a) and output in the frequency-domain (b) for Bourdon coupling analysis (Brown & Tentarelli, 2001b).

Other FSI mechanisms, not that common in regular engineering practices, are the buckling and flutter induced by centrifugal and Coriolis forces. Authors that have contributed on this matter are: Housner (1952), Gregory & Paidoussis (1966), Paidoussis & Issid (1974) and Paidoussis & Laithier (1976).

2.5.4 Coupling between different software

A different coupling approach consists of setting up an interaction between two different software, which is one specific for the fluid and another for the structure. In each time-step output information is transferred in both directions. There are contributions proposing methodologies to carry out this data transfer, such as Ware & Williamson (1982). However, the main challenge of this approach is the requirement of a huge computational effort (Belytschko *et al.*, 1986).

A-Moneim & Chang (1978) coupled a FDM software for the fluid and a FEM for the structure with the goal to simulate an interesting experimental research carried out at the Stanford Research Institute (SRI). Other authors who tried to simulate the same validating experiments are Romander *et al.* (1980) or Kulak (1982, 1985) who coupled FEM-FEM software. Also Erath *et al.* (1998) and Erath *et al.* (1999) used a FDM code for the fluid with a FEM for the structure with the goal to simulate field measurements from a pump shut-down and a closing valve from the nuclear power plant KRB II (Gundremmingen, Germany). Bietenbeck *et al.* (1985) and Mueller (1987) applied a MOC-FEM coupling aiming at describing the response of an experimental facility located at the Karlsruhe Nuclear Research Centre (KfK—Kernforschungszentrum Karlsruhe).

In Casadei *et al.* (2001) FEM and FVM are compared for the fluid domain simulation and coupling techniques are proposed. In Simão *et al.* (2015a,b) the traditional MOC approach for the fluid is compared with a CFD $k - \epsilon$ model, both are coupled with a FEM model for the structure.

2.6 Engineering applications

2.6.1 FSI consideration in codes and standards

In Moussou *et al.* (2004) several industrial cases of FSI generated by internal flows are analysed. The paper highlights the complexity of FSI problems and the need for guidelines and rules in international Codes and Standards. The following table 2.2 provides some of the Codes and Standards belonging to those engineering fields that frequently require waterhammer analyses. Certainly, none of the Standards consider any kind of FSI coupling.

Table 2.2 – Table of Codes and Standards in industries where waterhammer analyses are frequent.

Industry	Application	International standards
Hydropower energy	penstocks	ASME-B31, DIN-19704-1
Nuclear/thermal energy	cooling systems	ASME-BPV, NS-G-1.9
Oil/Gas transportation	oil/gas mains	ASME-B31, ISO-13628
Water distribution	water pipes	ANSI/ASSE-1010, PDI-WH 201
Aerospace	fuel pipes	ISO/FDIS-8575, NASA-STD-8719

2.6.2 Anchor and support forces

Fluid-structure interaction and specially the behaviour of pipe supports have a direct applicability in engineering pipe systems, such as hydropower systems, long oil and gas pipes, cooling systems of nuclear, thermal plants or any fluid distribution system in industrial compounds. However, only few authors investigated anchor and support behaviour in the context of waterhammer theory. Frequently, studies are based on qualitative discussions focused on post-accident analyses and mitigation measures case-by-case oriented. An example is Almeida & Pinto (1986) where recommendations for design criteria, operating rules and post accident analyses were given. Also Hamilton & Taylor (1996a,b) and Locher *et al.* (2000) presented qualitative discussions of the performance of different industrial piping systems, giving insights of pipe supports behaviour. The last one highlighted the case-by-case dependency of fluid-structure interaction and the high computational demand of including anchoring analyses, stating that the scope of such studies should be justifiable only for very critical systems, such as nuclear power plants.

Bürmann & Thielen (1988b) collected data from a firewater facility pipeline and carried out numerical analyses by means of MOC. Heinsbroek & Tijsseling (1994) studied the effect of support rigidity of pipe systems and discussed for what rigidity of the supports FSI becomes a dominant effect. In the analysis they applied both classic waterhammer theory and a MOC-FEM approach by means of FLUSTRIN code (Lavooij & Tijsseling, 1989; Kruisbrink & Heinsbroek, 1992). The simulated facility corresponded to the one from Delft Hydraulics laboratory (*cf.* Fig. 2.12). Fig. 2.22 shows the pressure histories computed by Heinsbroek & Tijsseling (1994) for different support rigidities at the downstream section of the pipe rig; classic and extended waterhammer theories are compared. The different responses of the system for each set-up point out the high sensitivity to the bend support rigidities when these are considered. The study concluded that classic theory computations are reliable for rigidly supported pipes but highly inaccurate for set-ups allowing pipe movement, underestimating overpressures.

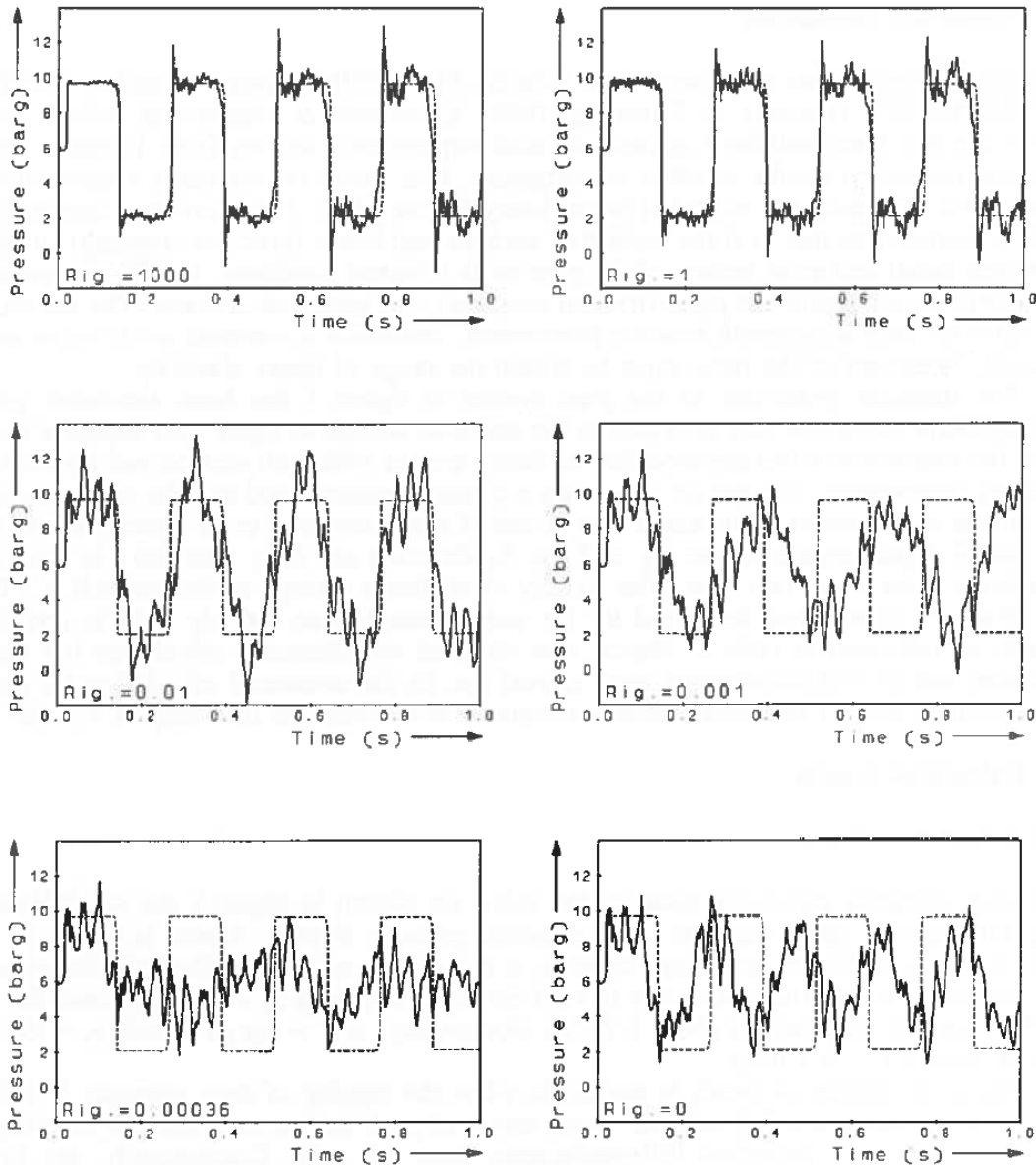


Figure 2.22 – System response to waterhammer tests varying bend rigidities. Pressure output at the downstream valve from classic and extended models (Heinsbroek & Tijsseling, 1994).

Tijsseling & Vardy (1996a) studied the effect of a pipe-rack considering the dry friction occurring between the rack and the pipe-wall (*cf.* Subsection 2.3.3). Recommendations were given in order to assess when dry friction must be considered. Different anchoring conditions were assessed in Simão *et al.* (2015c) using CFD software, which was validated by means of experimental data. The analysis pointed out the need of CFD simulations for the proper description of pipe supports behaviour. In Zanganeh *et al.* (2015) the aim was the simulation of hydraulic transients in a straight pipe anchored with axial supports using a MOC-FEM approach. Both pipe-wall and supports had a viscoelastic behaviour. The study concluded that the viscoelastic

supports significantly reduce displacements and stresses in the pipe and eliminate the high frequency fluctuations produced due to FSI. In Wu & Shih (2001) and Yang *et al.* (2004) a multi-span pipe system, with middle rigid constraints was analysed in the frequency-domain using the transfer matrix method, concluding that the middle rigid constraints have a much larger effect than the Poisson coupling. These type of multi-span pipes with middle rigid constraints set-ups are common in engineering practices and, so far, only a limited number of investigations has been carried out addressing this issue, specially in the time-domain.

2.6.3 Vibration damping and noise reduction

Tijsseling & Vardy (1996b) carried out experimental waterhammer tests on a steel pipe containing a short segment of ABS. MOC was successfully used to reproduce experiments and they concluded that the vibration could be adapted and modified in function of the segment material and geometry. Hachem & Schleiss (2012) reached a similar conclusion in an aluminium pipe set-up with a short segment of PVC. The analysis was carried out in the frequency-domain. Related with the previous subsection, Koo & Park (1998) proposed a methodology to reduce vibrations by the installation of intermediate supports.

Pipe vibration may induce audible noise and FSI analyses are required for the assessment of such noise. Moser *et al.* (1986) investigated the vibrating modes that produce sound. Kwong & Edge (1996) and Kwong & Edge (1998) carried out experimental analyses and developed a technique to reduce noise generation by the specific positioning of pipe clamps. De Jong (1994) suggested that for the full description of sound generation in pipe-systems, seven degrees-of-freedom are required. This statement was verified in Janssens *et al.* (1999). In Chen (2012) a pump-induced fluid-born noise is carried out by means of a distributed-parameter transfer-matrix model in the frequency-domain. It was claimed that the method could be used as well for structure-born noise as long as fluid-structure interaction was taken into account.

2.6.4 Earthquake engineering

Waterhammer waves can be produced by earthquake excitation on a pipe system. Fluid-structure interaction or soil-pipe interaction may be one of the potential damaging factors during earthquakes, specially for relatively low pressure and large diameter pipelines (Young & Hunter, 1979). Some authors have studied this kind of transients coupled with FSI. Hara (1988) analysed a Z-shaped piping system subjected to a one-directional seismic excitation. A numerical analysis of a 3D pipe system was carried out in Hatfield & Wiggert (1990). It was found that assuming the piping to be rigid produced an upper-bound estimate of pressure, but assuming the liquid to be incompressible resulted in underestimating the displacement of the piping. Coupled and uncoupled analyses applied to a single straight pipe were compared in Bettinali *et al.* (1991), who also concluded that coupled analyses accurately predicted lower wave amplitudes.

2.6.5 Aerospace engineering

Strong fluid transients occur in the filling up process of propulsion feedlines of satellites and launchers. In the experimental works of Regetz (1960), Blade *et al.* (1962), A-Moneim & Chang (1978) and A-Moneim & Chang (1979) (*cf.* Fig. 2.14) different configurations rocketed fuel-filled pipe rigs were tested. An overview of the main concerns experienced in the aerospace community with respect to fluid-hammer is reported in (Steelant, 2015). The study remarks the need of detailed investigation in fluid-structure interaction in combination with thermal heat transfer during fluid-hammer waves in satellites or launchers. Bombardieri *et al.* (2014) also highlights the importance of FSI in the filling of a pipelines during the start up of the propulsion systems of spacecrafts, claiming that more experimental research should be focused on this line.

2.6.6 Biomechanics

The disciplines of hydraulic transients and physiological flows share a good basis of the classic waterhammer theory as long as the assumptions of liquids with relatively low compressibility contained in thin-walled elastic cylindrical tubes are considered (Anderson & Johnson, 1990). Studies such as Lambossy (1950), McDonald (1974), Nakoryakov *et al.* (1976), Anderson & Johnson (1990) and Nichols *et al.* (2011) were focused on adapting classic waterhammer to the main factors that affect physiological flows. For instance, in Anderson & Johnson (1990), Helmholtz-Korteweg equation (Eq. 2.3) was reviewed in order to include pipe cross-section ovality effects. The study concluded that even for a low ovality of the pipe cross-section there may be significant reductions of the wave velocity due to bending-induced changes in the tube cross-section. Anderson & Johnson (1990) analysis serves also in the field of hydraulic transients for pipe bends and coils where the pipe cross-section is as well elliptic (*cf.* Section 2.5.3).

Nowadays, computational-fluid-dynamics tools are used to model the complexity of haemodynamics. Not just the pipe-wall viscoelasticity and the elliptic pipe cross-section, but the inner fluid defies as well classic waterhammer theory assumptions as blood is a non-Newtonian fluid, presenting shear-thinning, viscoelasticity and thixotropy. Wathen *et al.* (2009) presents a review of modern modelling approaches for haemodynamical flows. In Janela *et al.* (2010) a comparison of different physiological assumptions is carried out by means of a FEM-FEM approach. Newtonian and non-Newtonian assumptions are considered with fluid-structure interaction, highlighting their differences and the importance of good modelling criteria. More specific to blood flow diseases diagnoses, Simão *et al.* (2016a) also used CFD tools, including FSI, for modelling a vein blockage induced by a deep venous thrombosis and the occurrence of reverse flow in human veins.

2.7 Accidents and post-accident analyses related with FSI

FSI may generate overpressures higher than the provided by Joukowsky's equation and not only caused by waterhammer waves, but also by turbulence-induced vibrations, cavitation-induced vibrations or vortex shedding with lock-in. These phenomena are poorly understood (Moussou *et al.*, 2004), and are rarely taken into consideration in engineering designs, leading to accidents and service disruption of important infrastructure with large social relevance (*e.g.* industrial compounds, water and wastewater treatment plants, thermal plants, nuclear power plants, hydropower plants, hospitals).

Jaeger *et al.* (1948) reviewed a number of the most serious accidents due to waterhammer in pressure conduits. Many of the failures described were related to vibration, resonance and auto-oscillation (Bergant *et al.*, 2004). The Table 2.3 summarizes some of the accidents caused by strong hydraulic transients.

Normally accidents in hydraulic facilities are associated not only to a single phenomenon but to a series of enchainned events that make the system collapse. Although not all the accidents listed in Table 2.3 were caused by FSI, in many cases it is indirectly involved and its understanding is crucial in post-accident analyses, such as in Almeida & Pinto (1986); Wang *et al.* (1989); Obradović (1990); Simão *et al.* (2016b).

Chapter 2. State-of-the-Art Review

Table 2.3 – Summary table of historical accidents in pressurized pipe systems.

Location	Facility	Citation	Description
Oigawa, Japan	Penstock	Bonin (1960)	A waterhammer wave, caused by a fast valve-closure, split the penstock open and produced the pipe collapse upstream.
Big Creek, U.S.A.	Penstock	Trenkle (1979)	Burst turbine inlet valve caused by a fast closure.
Azambuja, Portugal	Pump station	Chaudhry (2014)	Collapse of water column separation causing the burst of the pump casing.
Lütschinen, Switzerland	Penstock	Chaudhry (2014)	Penstock failure during draining due to the buckling produced by a frozen vent at the upstream end.
Arequipa, Peru	Penstock	Chaudhry (2014)	The clogging of the control system of a valve resulted in buckling and the failure of the welding seams of the penstock due to fatigue.
Ok, Papua New Guinea	Power house	Chaudhry (2014)	The draft tube access doors were damaged and the power house flooded due to column separation in the system.
Lisbon, Portugal	Water main	Simão <i>et al.</i> (2016b)	Rupture of concrete support blocks during the slow closure of an isolation valve installed in a large suction pipe
New York, U.S.A.	Steam pipe	Veccio <i>et al.</i> (2015)	Condensation-induced-waterhammer caused the rupture of the steam pipe.
Lapino, Poland	Penstock	Adamkowski (2001)	Burst of the penstock caused by a rapid cut-off and low quality of the facility
Chernobyl, Ukraine	Nuclear reactor	Wang <i>et al.</i> (1989)	Fuel pin failure, fuel-coolant interaction and fluid-structure interaction were involved in the failure of the nuclear reactor
New York, U.S.A	Nuclear reactor	Meserve (1987)	Circumferential weld failure in one of the feedwater lines due to a steam generator waterhammer.

2.8 Motivation and gaps of knowledge

During this assessment several gaps of the state-of-the-art on FSI in 1D waterhammer theory have been identified. On the one hand, waterhammer research has provided supplementary upgrades to the basic two-equation model (classic waterhammer model) that are used as add-ons to suit the modelling purposes. On the other hand, the basic theory of FSI in 1D waterhammer seems quite consolidated, although improvements on the numerical approaches are still a focus of research. The author believes that all the knowledge around

classic waterhammer theory has not been transferred yet to the FSI models. The main idea to understand the need of this transfer of knowledge, from the classic model to the FSI models, is to perceive the last ones as sovereign theories that can hold themselves other subtheories. For instance, unsteady friction or viscoelastic models represent these kind of subtheories that have been designed to suit and upgrade the classic waterhammer model, but have not been adapted yet for the FSI models. Hence, not much research has been carried out so far, neither experimentally nor numerically, to understanding and distinguish unsteady friction, pipe-wall viscoelasticity or dry friction in the different FSI contexts.

The unsteadiness of skin friction has motivated waterhammer researchers during decades. As explained in Subsection 2.3.1, several theories for unsteady friction computation, based on varied assumptions, have been developed and are still under development for the classic two-equation model, but not for models including higher pipe degrees-of-freedom.

The effects of unsteady friction and pipe-wall viscoelasticity are hard to distinguish and, additionally, when combined with FSI, new interactions arise: the pipe-wall rheological behaviour affects the response of the movement of the pipe and this, at the same time affects the shear stress between the pipe-wall and the fluid. Only few researchers included pipe-wall viscoelasticity in FSI software, and, to the knowledge of the author, none included unsteady friction. The distinction of both phenomena, pipe-wall viscoelasticity and unsteady friction, in a FSI platform is appealing, challenging and novel.

Fluid-structure interaction offers a very suitable mean for the inclusion of a well known, but novel in waterhammer research, dissipation phenomena: dry friction. As pointed out in Subsection 2.3.3 very few research has been done in this subject. Movement of the pipe-wall is an output variable of FSI models. Using this output information, Coulomb's friction computation can be implemented either distributed throughout the pipe (friction coupling), or at the supports of the pipe (junction coupling). The last one, in combination with the description of thrust and anchoring blocks, could significantly upgrade simulation outcomes.

Anchor or thrust blocks are frequently used in straight pipelines to restrict and to avoid these movements so that the piping structure is stable and reliable. Anchor blocks absorb the axial stresses of the pipe-wall and transmit them to the surrounding ground by means of dry friction. Although its remarked engineering applicability, not much research has been carried out with respect to the understanding of pipe supports behaviour, neither experimentally nor numerically. Four-equation models are a convenient base for the representation of a straight pipe with middle anchors and thrust blocks, which can be embedded as internal conditions in the solver code. Moreover, the inclusion of Coulomb's dry friction into thrust blocks, allowing their movement conditioned to stick-slip criteria would enhance quantitative analyses of anchor and support forces.

All the proposed developments must be supported by reproducible and self-consistent empirical evidence. Structural damping, or pipe-wall visco-elasticity, can be assessed by the comparison of measured strain and pressure time histories in different pipe locations and

Chapter 2. State-of-the-Art Review

different set-ups. Dry friction and unsteady friction can be indirectly analysed by pressure history envelopes and wave amplitude decay ratios from different anchoring set-ups, allowing or constraining pipe-wall movements. These experiments would complement the development and validation of implementations describing pipe anchors and thrust blocks behaviours.

3 Experimental work

The present chapter is based on the following scientific publication:

- D. Ferras, P. Manso, D. Covas, A.J. Schleiss. Experimental distinction of damping mechanisms during hydraulic transients in pipe flow. *Accepted for publication at the Journal of Fluids and Structures (June 2016)*.

The work presented hereafter is original and was performed by the first author. The interpretation and discussion of results was carried out with the collaboration of the co-authors.

3.1 Introduction

The fundamental equations of classic waterhammer theory, *i.e.* mass and momentum conservation, can be derived from Navier-Stokes equations (Ghidaoui, 2004) or by directly applying the Reynolds Transport Theorem (Chaudhry, 2014) to a control volume of the pipe system. In their development, though, several mechanisms that may significantly affect pressure waveforms are neglected, such as unsteady friction (UF), cavitation (including column separation and trapped air pockets), a number of fluid-structure interaction (FSI) effects, viscoelasticity (VE) of the pipe-wall material, leakages and blockages. Depending on the field of work, and for each application, engineers should attempt to identify and to evaluate the influence of these mechanisms in order to decide whether to include or to neglect them. Firstly, these phenomena are not commonly included in standard waterhammer software packages and when they are, they often require the specification of blind parameters which the user is not sensitive to. Secondly, these effects tend to be often ‘hidden’ in real systems being therefore forgotten (Bergant *et al.*, 2008a,b). Consequently, the expertise of the modeller becomes crucial when add-ons are to be included into the classic waterhammer model.

The referred mechanisms have been largely studied by focusing on single phenomena. Though, several examples can be found in literature combining different mechanisms either in experimental or numerical analyses, such as: experiments in plastic and metallic pipes (Krause

Chapter 3. Experimental work

et al., 1977; Williams, 1977); development of numerical models incorporating both FSI and VE (Weijde, 1985; Walker & Phillips, 1977; Stuckenbruck & Wiggert, 1986); analysis of FSI and cavitation (Tijsseling, 1993; Tijsseling *et al.*, 1996; Tijsseling, 1996); analysis of VE in combination with UF (Covas *et al.*, 2004b); analysis of longitudinal stiffness heterogeneity by means of the combination of aluminium and PVC pipe reaches in an experimental set-up (Hachem & Schleiss, 2012); and analysis of FSI, column separation and UF in a viscoelastic pipe (Keramat & Tijsseling, 2012).

The purpose of the present research is to give experimental insight in the distinction and identification of the three phenomena that frequently affect the transient pressure wave, namely fluid-structure interaction, pipe-wall viscoelasticity and unsteady friction. These phenomena lead to increased damping and dispersion of the pressure transient wave. The aim is to highlight the features, from an empirical standpoint, in which way each mechanism affects the wave attenuation, shape and timing.

Experimental tests were carried out in three pipe rigs. The three experimental facilities, assembled at the Laboratory of Hydraulics and Environment of Instituto Superior Técnico (LHE/IST), Lisbon, Portugal, consist of: (i) a straight copper pipe, which is tested for different supporting set-ups; (ii) a coil copper pipe, whose response in transient conditions is strongly affected by the coil geometry; and (iii) a coil polyethylene pipe, clearly showing the dominant effect of the pipe-wall viscoelasticity.

The key innovative features of this chapter are: (i) the comparison of different pressure traces collected in pipe-rigs with different supporting conditions (moving or anchored pipe end), geometrical configurations (straight and coil) and pipe materials (metal and plastic), under similar initial conditions, complemented with (ii) the physically-based discussion, supported by bibliographic references, of different phenomena affecting and dominating waterhammer in each case. Finally, (iii) transient pressure measurements are complemented with axial and circumferential strain measurements to better understand the phenomena and to support conclusions.

The experimental evidence presented is used to develop, calibrate and validate numerical models to simulate hydraulic transients in the time-domain, including fluid-structure interaction, pipe-wall viscoelasticity and unsteady friction. The value and novelty of the actual research focus lies on the benefits of an integral assessment of the empirical distinction between different damping mechanisms affecting waterhammer tests carried out in varied experimental facilities.

3.2 Experimental data collection

3.2.1 Straight copper pipe

A straight copper pipe (SCP) rig was assembled at LHE/IST. The system is composed of a 15.49 m pipe, with an inner diameter $D = 0.020$ m and pipe-wall thickness $e = 0.0010$ m. Young's modulus of elasticity and Poisson ratio of the copper material were experimentally determined by measuring stress-strain states over a pipe sample for the experimental range of pressures. The obtained experimental values were the Young's modulus of elasticity $E = 105$ GPa and the Poisson ratio $\nu = 0.33$. At the upstream end, there is a storage tank followed by a pump and an air vessel, and at the downstream end, there is a ball valve pneumatically operated that allows the generation of fast transient events (*i.e.*, $t_v < 1/2 T$). The upstream air vessel has a volume of 60 l and its aim is to guarantee a constant pressure level at the upper pipe-end during the tests. The ball valve together with the actuator mechanisms and the supporting system have a mass of $m_v = 6$ kg. Downstream the valve there is a hose conveying the water to the water-tank, thus closing the pipe system circuit.

Three pressure transducers (WIKA S-10) were installed at the upstream, midstream and downstream positions of the pipe (PT1, PT2 and PT3). Strain gauges (TML FLA-2-11) disposed in the axial (SG1 and SG3) and circumferential (SG2 and SG4) directions were installed at the midstream and the downstream end of the pipe. The initial discharge was measured for steady state conditions by a rotameter located downstream of the valve. The sampling frequency was set to 1200 Hz after preliminary tests, in order to measure the FSI response of the pipe system during the waterhammer events, and 2400 Hz for wave celerity estimation (explained in Subsection 3.3.1). Fig. 3.1 shows an schematic of the experimental set-up, with the location of the pressure transducers and strain gauges, and pictures of a general view of the facility and details of the downstream valve and pipe supports are shown in Fig. 3.2.

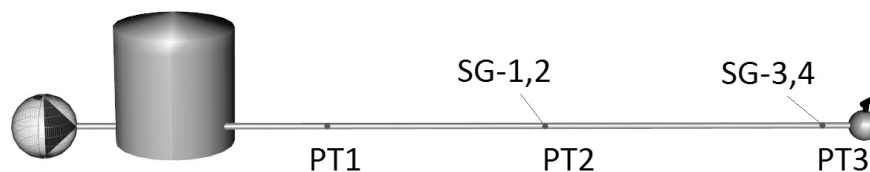


Figure 3.1 – Simplified schematic of the straight copper pipe set-up.

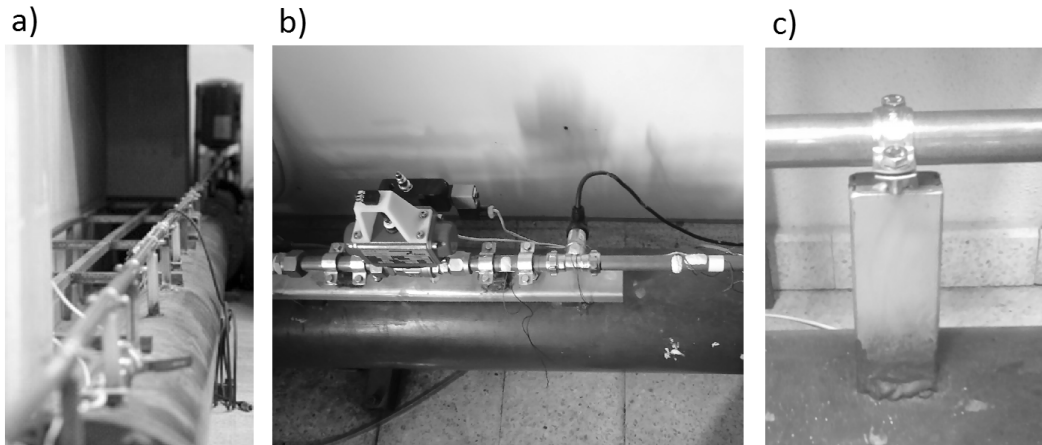


Figure 3.2 – View of the straight copper pipe set-up (a); detail of downstream valve (b); and detail of pipe support (c).

Two supporting configurations have been analysed (Fig. 3.3): a) the conduit anchored against longitudinal movement at both downstream and upstream ends; and b) the conduit only anchored against longitudinal movement at the upstream end. Rigidly fixed stainless steel clamps are used for the pipe anchoring. Table 3.1 summarizes the tests carried out in these experimental set-ups, displaying the initial flow velocity and Reynolds number, the initial piezometric head and the maximum and minimum piezometric heads measured immediately upstream of the valve. Figs. 3.4 and 3.5 depict the transient pressure traces at the downstream and the midstream pipe locations corresponding to the tests carried out in the straight copper pipe.

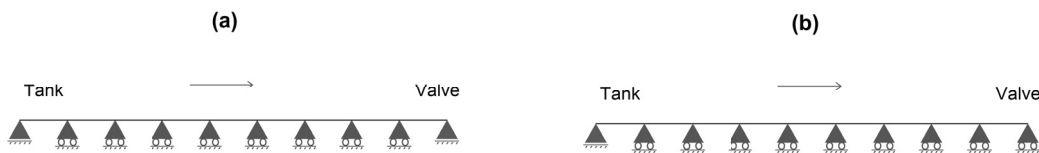


Figure 3.3 – Supporting configurations of the SCP facility with (a) valve anchored and (b) valve released.

Table 3.1 – Characteristics of the straight copper pipe (SCP) selected tests.

Test ID	V_0 (m/s)	Re_0	H_0 (m)	H_{max} (m)	H_{min} (m)	Valve
SCP01	0.26	5276	43.65	77.25	10.66	fixed
SCP02	0.36	7253	42.39	88.67	-2.95	fixed
SCP03	0.41	8206	42.87	94.88	-8.67	fixed
SCP04	0.26	5276	44.16	83.17	5.97	released
SCP05	0.36	7253	42.27	94.69	-8.34	released
SCP06	0.41	8206	42.55	100.04	-9.95	released

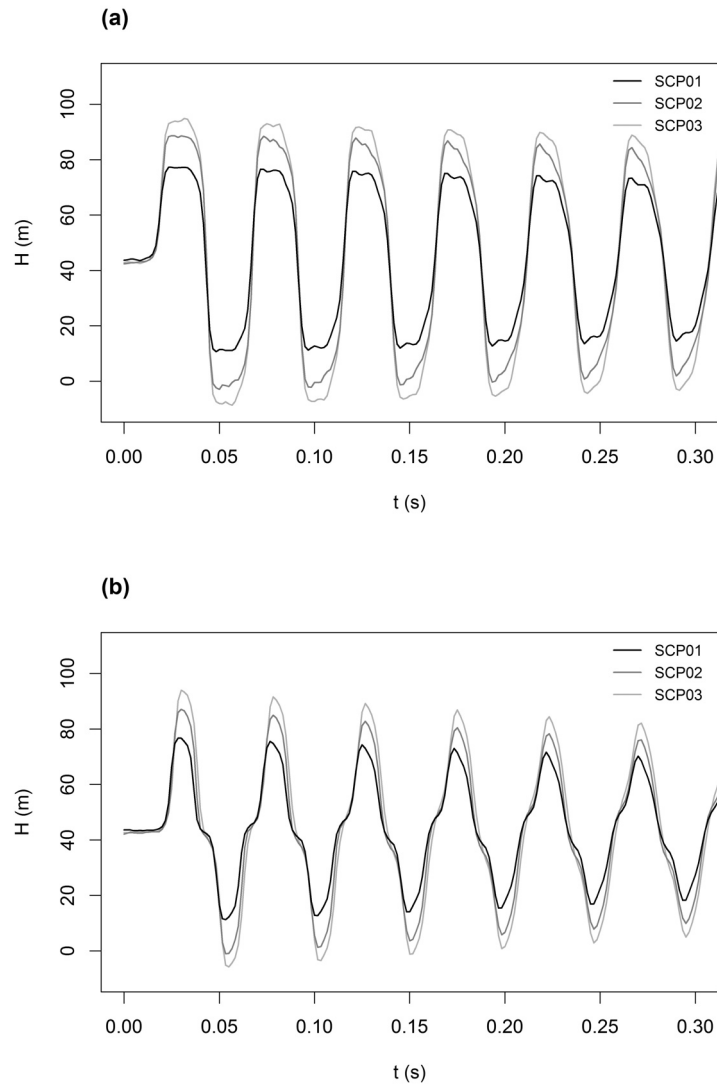


Figure 3.4 – Pressure data acquired at the straight copper pipe for an anchored downstream end: (a) at the **downstream** end (PT3); and (b) at the **midstream** section (PT2).

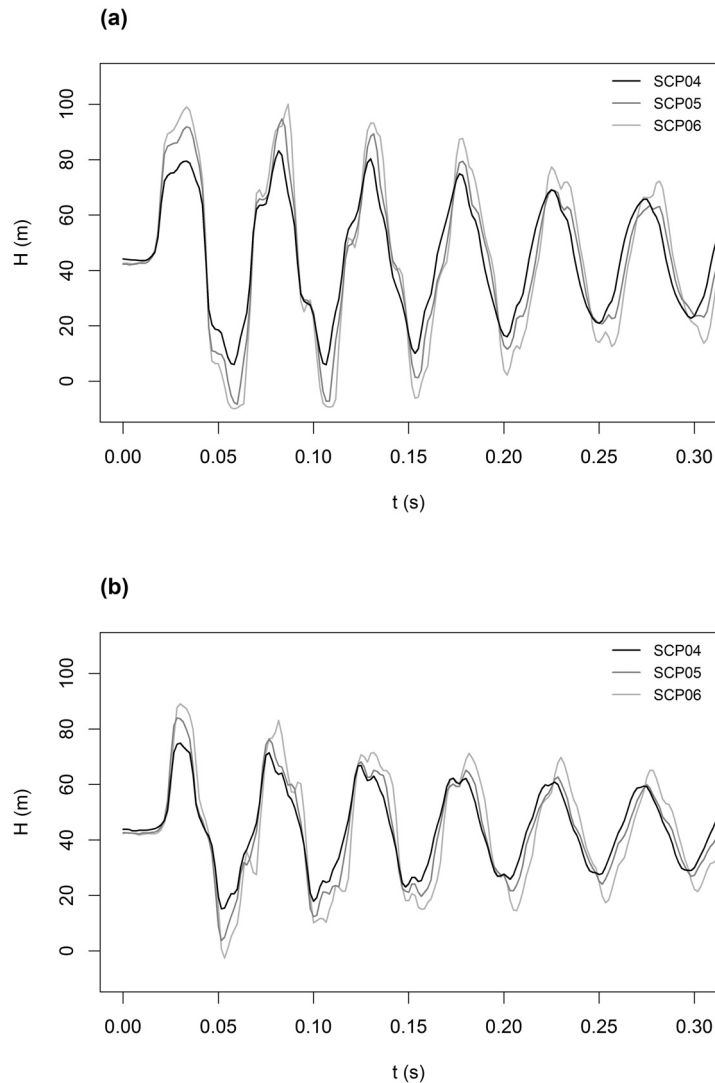


Figure 3.5 – Pressure data acquired at the straight copper pipe for an non-anchored downstream end: (a) at the **downstream** end (PT3); and (b) at the **midstream** section (PT2).

3.2.2 Coil copper pipe

The coil copper pipe (CCP), also assembled at LHE/IST, has an inner diameter $D = 0.020$ m, a pipe-wall thickness $e = 0.0010$ m and a pipe length, $L = 105$ m. The torus radius R is 0.45 m, thirty-six rings compose the entire coil and its total height is 1 m. Each coil ring is fixed by 4 anchoring points disposed every 90° and with rubber supports. Similarly to the straight copper pipe facility, the value of Young's modulus of elasticity is $E = 105$ GPa and Poisson ratio $\nu = 0.33$. Three pressure transducers (WIKA S-10) were located at the upstream, midstream and downstream positions of the pipe (PT1, PT2 and PT3). As depicted in Fig. 3.7, strain

3.2. Experimental data collection

gauges (TML FLA-2-11) disposed in the axial and circumferential directions (SG-1, SG-2 and SG-3) were installed in the midstream location. The sampling frequency was 1000 Hz. The upstream and downstream conditions are similar to the ones in the SCP: there is a tank, a pump and an air vessel at the upstream end and a ball valve to generate the transient events at the downstream end. The upstream air vessel has a volume of 60 l, assuring a constant pressure level at the upper pipe-end during the tests. Fig. 3.6 shows a schematic and an overall view of the facility.

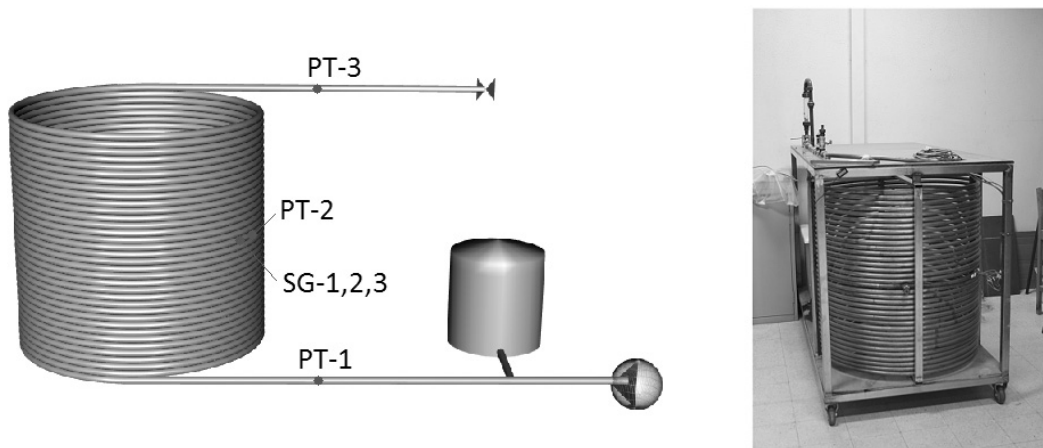


Figure 3.6 – Schematic and photograph of the coil copper pipe facility.

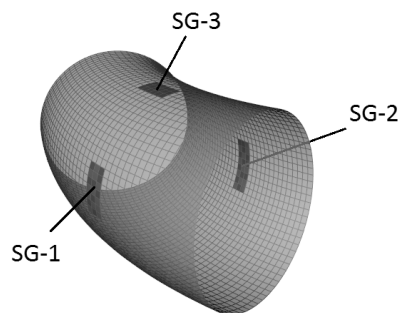


Figure 3.7 – Detail of the assembled strain-gauges.

Table 3.2 shows a summary of a set of tests carried out in this experimental set-up according to the initial flow velocity, Reynolds number and the initial piezometric head at the downstream boundary before the valve closure, and maximum and minimum piezometric heads measured during the tests. Transient events were generated by a manual ball valve closure.

Chapter 3. Experimental work

Table 3.2 – Characteristics of the coil copper pipe (CCP) selected tests.

Test ID	V_0 (m/s)	Re_0	H_0 (m)	H_{max} (m)	H_{min} (m)
CCP01	0.09	1765	40.71	49.56	32.18
CCP02	0.18	3530	39.62	57.94	23.02
CCP03	0.35	7059	38.31	74.39	5.18

Fig. 3.8 depicts the transient tests carried out in the coil copper pipe with transient pressures measured at the downstream and the midstream pipe locations.

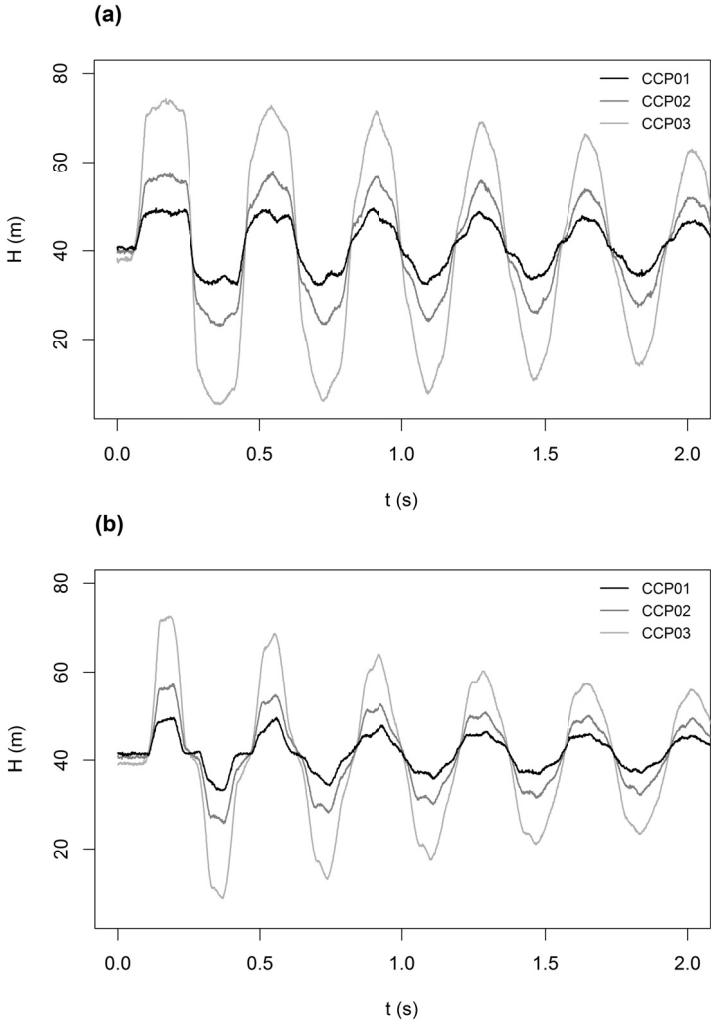


Figure 3.8 – Measured pressure data for the tests carried out at the coil copper pipe: (a) at the **downstream** end (PT3); and (b) at the **midstream** section (PT2).

3.2.3 Coil polyethylene pipe

The coil polyethylene pipe (CPP), assembled at LHE/IST, is composed of two irregular pipe coils of high density polyethylene (HDPE), with a total length $L = 203$ m, an inner diameter, $D = 0.043$ m, a pipe-wall thickness $e = 0.0030$ m and an average torus diameter $R = 0.70$ m. The coil structure is fixed by four braces disposed every 90° , linking the coil rings up and fixing them to the floor. The Young's modulus of elasticity and the wave speed were previously assessed for this set-up by Soares *et al.* (2009), who used an inverse method to estimate a Young's modulus of $E = 1.42$ GPa and a wave speed of $a = 315$ m/s. The nominal Poisson ratio for polyethylene is $\nu = 0.43$. An air vessel of a volume of 1000 l is connected in line at the upstream end and a manual ball valve allows the generation of transient events. Downstream the valve there is a tank collecting the water and closing the pipe system circuit. Two pressure transducers (WIKA S-10) were located at the midstream and downstream positions of the pipe (PT1 and PT2). Strain gauges (TML FLA-2-11) were disposed in the midstream section, in the axial and circumferential directions (SG1 and SG2). The sampling frequency was 50 Hz. Fig. 3.9 shows a schematic and an overall view of the facility.

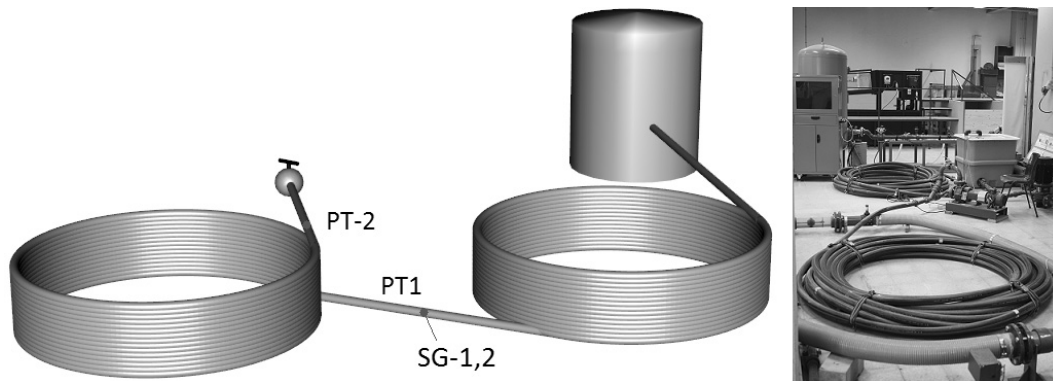


Figure 3.9 – Schematic and view of the coil polyethylene pipe facility.

Table 3.3 shows a summary of the tests carried out in the experimental set-up according to the initial flow velocity, Reynolds number and the initial piezometric head before the valve closure, and maximum and minimum piezometric heads measured at the valve during the assessed transient events.

Table 3.3 – Characteristics of the coil polyethylene pipe (CPP) selected tests.

Test ID	V_0 (m/s)	Re_0	H_0 (m)	H_{max} (m)	H_{min} (m)
CPP01	0.19	8664	31.08	36.21	27.31
CPP02	0.33	14440	30.09	38.56	24.43
CPP03	0.39	17324	30.50	40.01	24.33

Fig. 3.10 depicts the transient pressures at the downstream and midstream pipe sections measured during the tests carried out at the PE pipe coil.

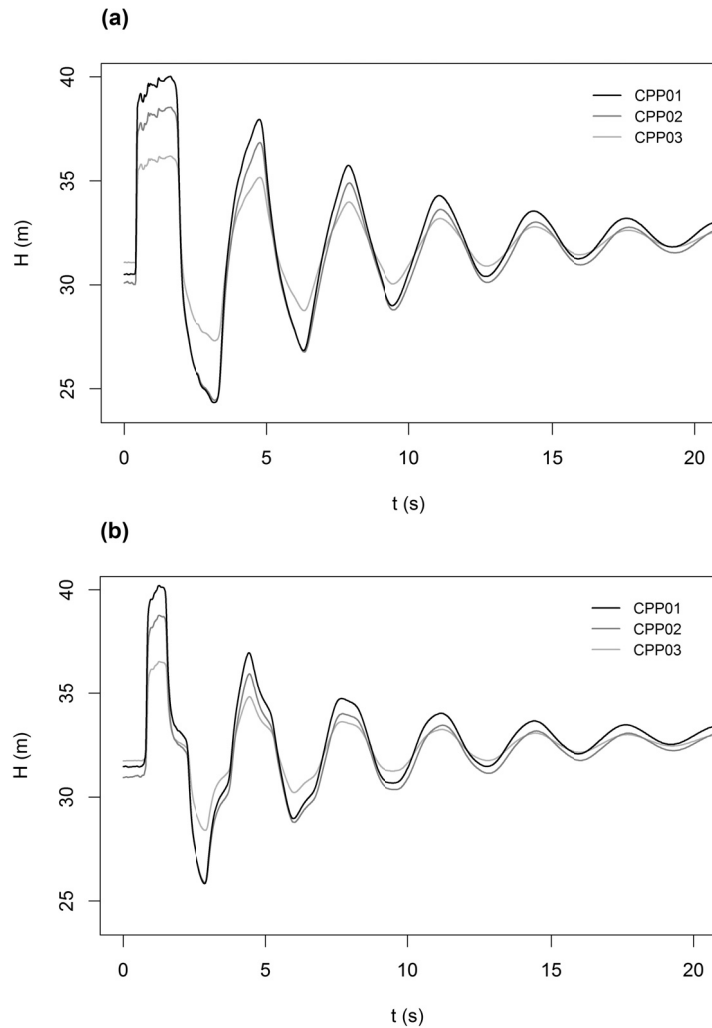


Figure 3.10 – Measured pressure data of the tests carried out at the coil PE pipe (PT2): (a) at the **downstream** end; and (b) at the **midstream** section (PT1).

3.3 Experimental analysis

3.3.1 Pressure data analysis

The figures presented in the Section 3.2 have already shown how differently transient events propagate throughout the three experimental set-ups, generated for similar steady state conditions (*i.e.*, similar initial velocities though different Re numbers) following fast valve manoeuvres. Differences of piezometric heads and time scales between the transient events measured in each rig hinder a straightforward comparison. To facilitate the comparison between system responses in terms of amplitude, dispersion and shape of the transient wave, dimensionless pressure traces have been prepared as described hereafter.

Observed transient pressure wave periods and amplitudes are mainly associated with two

main characteristics of the pipe system - the wave celerity, a , and the pipe length, L - and with the flow conditions - the initial steady state velocity, V_0 (Korteweg, 1878; Joukowsky, 1904).

The *pressure wave period* (T), in a reservoir-pipe-valve system, depends on the ratio between pipe length and wave celerity (Eq. 3.1) and is, therefore, independent of the initial conditions; it results from the combination of the pipe system characteristics (*i.e.* pipe elasticity, inner diameter, wall thickness and constraint conditions) with the fluid compressibility.

$$T = \frac{4L}{a_h} \quad (3.1)$$

The *pressure wave amplitude* for fast hydraulic transients, described by the Eq. 3.2 (Von Kries, 1883; Joukowsky, 1904), depends not only on the pipe and fluid physical properties, but also on the initial flow conditions, being proportional to the product between the velocity variation ΔV the wave celerity a_h and fluid density ρ_f .

$$\Delta p = -\rho_f a_h \Delta V \quad \text{or} \quad \Delta H_{JK} = -\frac{a_h \Delta V}{g} \quad (3.2)$$

Figures 3.11 and 3.12 depict the dimensionless plots of transient pressure traces for selected tests from each facility at the downstream and midstream pipe sections, respectively. The tests were selected with the aim to analyse transient flow free of cavitation but with sufficient pressure variation to depict the piping structural behaviour. These have been drawn by plotting a dimensionless hydraulic head (h) consisting of the difference between the transient and the initial pressure head and dividing by the maximum pressure wave amplitude like shown in Eq. 3.3:

$$h = \frac{H - H_0}{\Delta H_{JK}} \quad (3.3)$$

The time axis is made dimensionless using the wave periods computed by Eq. 3.1 and also presented in Table 3.4. Wave celerity values have been experimentally estimated by comparing the time lag between pressure measurements at the downstream and midstream pipe positions with sampling frequencies of up to 2400 Hz. Presented wave celerity and period values correspond to averages from all the runs carried out for each facility with different initial velocities; discrepancies between computed values for a given set of experimental runs are lower than 1%.

Table 3.4 – Main properties of the selected tests.

Test ID	a_h (m/s)	T (s)	V_0 (m/s)	ΔH_{JK} (m)	t_{valve} (s)
SCP02	1239	0.049	0.36	45.9	0.003
SCP05	1239	0.049	0.36	45.9	0.003
CCP03	1193	0.384	0.35	36.5	0.025
CPP03	315	2.88	0.40	12.7	0.050

Figs. 3.11 and 3.12 show different attenuation, shape and phase shift of transient pressure responses for each experimental set-up at both downstream and midstream pipe locations. These features are analysed in the following paragraphs.

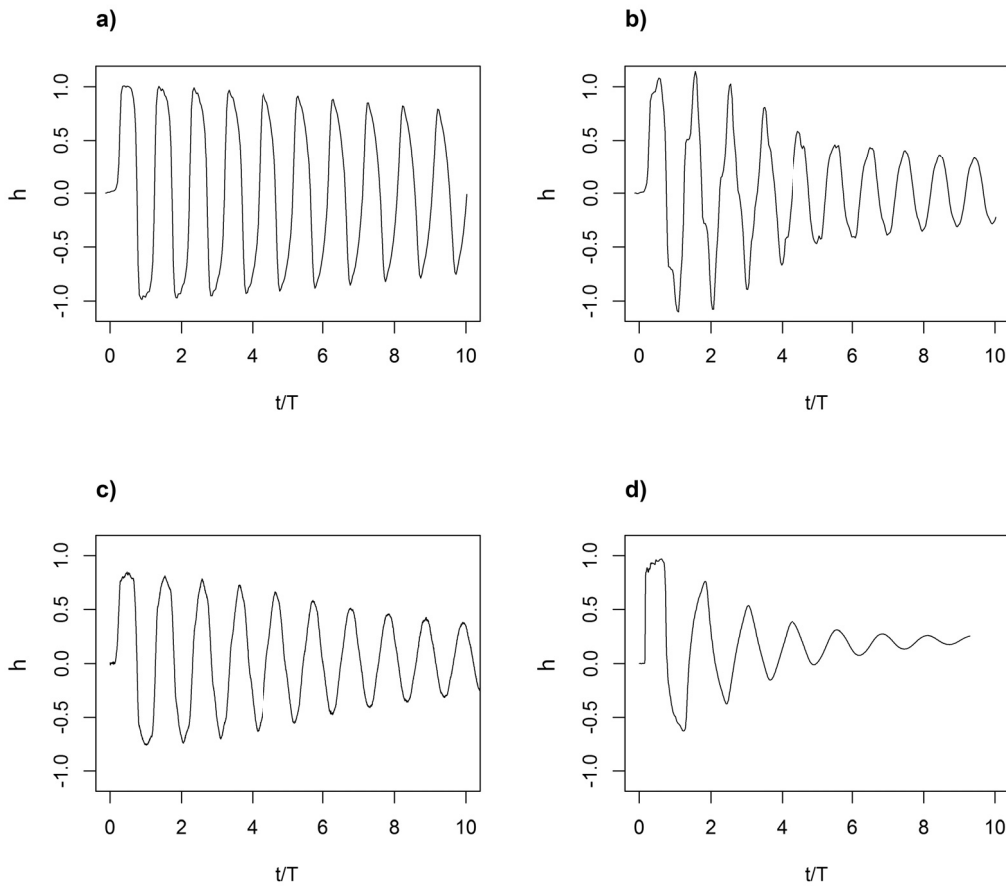


Figure 3.11 – Dimensionless transient pressures in the four assessed set-ups at the **downstream** pipe section. a) SCP02 test (anchored valve), b) SCP05 test (non-anchored valve), c) CCP03 test and d) CPP03 test.

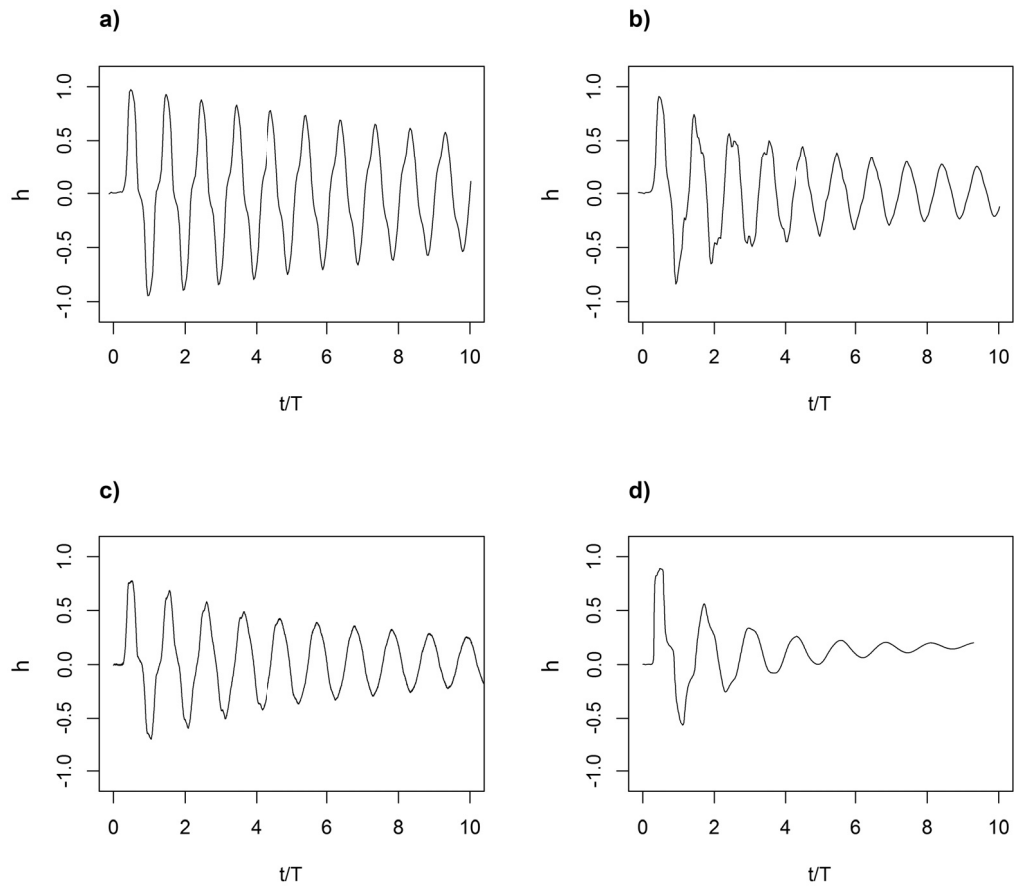


Figure 3.12 – Dimensionless transient pressures in the four assessed set-ups at the **midstream** pipe section. a) SCP02 test (anchored valve), b) SCP05 test (non-anchored valve), c) CCP03 test and d) CPP03 test.

Wave dissipation

The straight copper pipe set-up with anchored downstream end (SCP01, SCP02, SCP03) is the one with the lowest transient pressure wave damping. This is due to three main reasons. First, friction losses are less important in this pipe system due to its small length (*ca.* 15 m) in comparison with the other two pipe coils (copper coil $L = 105$ m and PE coil $L = 203$ m); the less the pressure wave travels, the lower the frictional damping is during the transient event per wave cycle. Second, the pipe has a linear elastic behaviour, deforming almost instantaneously with pressure changes, without a retarded response, unlike the PE pipe. Third, the downstream valve is well-fixed to the supporting anchors.

Much higher damping exhibits the same facility but with the released valve set-up (*i.e.* the downstream pipe end is free to move). The dimensionless damping after 10 wave cycles is of similar order of magnitude to the coil copper pipe facility, which has much longer wave length

(*cf.* Figs. 3.11-b and -c). The reason of such high damping is associated with the pipe-wall deformation and movement in the axial direction at the downstream end. In the released valve tests there is much higher transfer of momentum from the fluid to the pipe-wall than in the ones with fixed valve, and this higher momentum is dissipated through shear between the pipe and its supports. In addition, the vibration of the pipe also increases the shear between the inner fluid and the pipe-wall, increasing as well the momentum dissipation.

In the copper pipe coil, the first pressure peak is 15 to 20% lower than the Joukowsky maximum wave amplitude (see Figs. 3.11-c and 3.12-c), which, in the dimensionless plot, corresponds to the unit. The main reason for this reduction is the characteristic FSI occurring in the pipe coil: during the transient propagation, coil rings have a 'breathing effect' as they expand axially for positive pressures increasing the pipe inner volume and, consequently, attenuating the pressure peaks, and vice-versa for negative pressures; this attenuation is particularly evident in the first pressure rise. This phenomenon has been comprehensively analysed by Ferràs *et al.* (2014, 2015a).

In the coil PE pipe, wave damping is the most significant of all tested set-ups (*e.g.* pressure peaks are more than halved already after the second cycle). According to previous research (Covas *et al.*, 2004c, 2005) wave dissipation in PE pipes is dominated by the viscoelastic behaviour of the pipe wall characterised by an instantaneous elastic response followed by a retarded viscous response. Other effects like fluid-structure interaction and unsteady friction although existing, have minor contributions.

Fig. 3.13 shows the pressure time-series at the downstream section for the tests SCP02, SCP05, CCP03 and CPP03 with the time-envelops of extreme envelops and regression curves of the maximum envelops. The waterhammer waves of the tests SCP02 and CCP03 (respectively Fig. 3.13-a and Fig. 3.13-c) present a linear damping, steeper in the case of the CCP03 because of the longer length of the pipe. In SCP05 test, the damping is only linear after the fifth wave cycle. This is because at the beginning of the transient the pipe has a considerable movement and FSI is dominant. After some waves cycles the oscillating loading cannot overcome dry friction, the pipe stops moving and a similar linear damping as the one in SCP02 occurs. In CPP03 test (Fig. 3.13-d), there is a major damping during the whole pressure history, described by a logarithmic law, viscoelasticity of the polyethylene material is the cause of such a damping, significantly higher than the one created by unsteady friction, with a linear trend. This behaviour has already been observed by Ramos *et al.* (2004). The characteristics of the damping laws are summarized in Table 3.5.

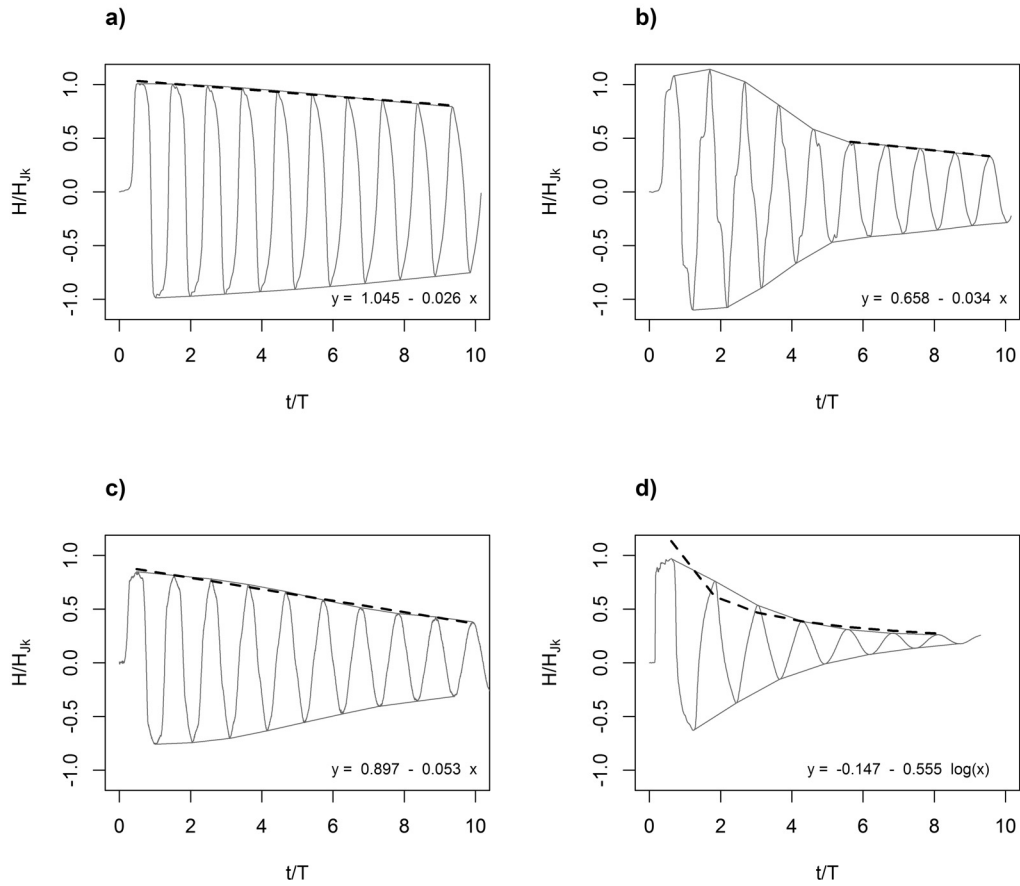


Figure 3.13 – Dimensionless transient pressures, time-envelopes and regression curves (dashed lines) in the four assessed set-ups at the downstream pipe section. a) SCP02 test (anchored valve), b) SCP05 test (non-anchored valve), c) CCP03 test and d) CPP03 test.

Table 3.5 – Characteristics of the damping laws in the four assessed set-ups

Test ID	regression law	trend
SCP02	$y = 1.045 - 0.026x$	linear
SCP05	$y = 0.658 - 0.034x$	linear after 5 cycles
CCP03	$y = 0.897 - 0.053x$	linear
CPP03	$y = -0.147 - 0.555 \log(x)$	logarithmic

Wave shape

The waterhammer wave in the straight copper pipe with fixed valve is the closest to the theoretical ‘squared’ wave described by the classic waterhammer theory. However, a clear development smoothing the wave peaks can be observed in the first pressure rise and, afterwards, during the wave propagation. The rounded slope in the first pressure rise is due

to the closure manoeuvre of the ball valve, the subsequent smoothing is caused by both FSI and UF. Although the pipe is well anchored at its extreme ends, in between supports the pipe is allowed to displace due to the elastic deformation in the circumferential direction and its respective axial deformation due to the Poisson effect. During the transient loading, the fluid pressure generates circumferential stresses in the pipe-wall which, at the same time, induce axial strain due to Poisson effect. This phenomenon is known as Poisson coupling, as it causes transient axial stresses throughout the pipe coupled with the transient fluid pressure. Poisson coupling was first analysed by Skalak (1955) and, later, extensively studied by Tijsseling (1996, 1997, 2003); Lavooij & Tijsseling (1991); Elansary *et al.* (1994). UF is added to this effect and is visible after several pressure cycles (Fig. 3.11-a).

On the other side, for exactly the same initial flow rates, a different transient wave shape is observed in the same facility with the released valve set-up. When the pipe is released at the downstream end, the free valve is excited by the transient pressure generating axial stress waves throughout the pipe. The first pressure peak shows three main stages (Figs. 3.11-b and 3.14): Stage-1 in which the pressure is lower than the expected pressure rise; Stage-2 with higher pressure; and, finally, Stage-3 with a pressure drop. This characteristic wave shape change is described, from a numerical standpoint in Bergant *et al.* (2008b). The coupling mechanism is known as junction coupling and is normally generated due to unbalanced pressure forces acting at singular points of the pipe, such as unrestrained dead-ends, elbows and tees (Tijsseling, 1996). This phenomenon dominates the transient response over UF, whose effect is hardly noticeable in the first pressure cycles.

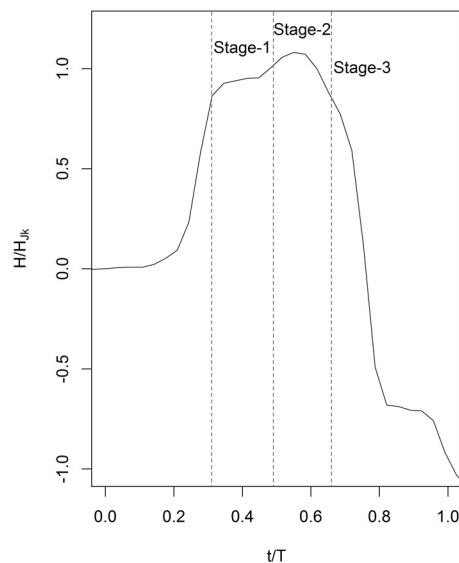


Figure 3.14 – First pressure peak corresponding to SCP05 test at the downstream section.

In the coil copper pipe, a different wave shape is observed (Figs. 3.11-c and 3.12-c), which is associated to two phenomena. The first is friction (steady and unsteady) that, as explained, is more evident in the coil system due to a higher length and a larger inertia of the water column, as unsteady friction depends on the time history of the velocity profile. Contributions analysing the flow time history dependency of unsteady skin friction can be found, for instance, in Zielke (1968); Vardy & Brown (2003, 2004); Martins *et al.* (2016, 2015b). The second phenomenon is the coil rings movement that directly induces FSI, despite the existing four fixing supports at 90° spacing. The FSI behaviour in pipe coils has been analysed in Ferràs *et al.* (2014, 2015a).

Regarding the PE pipe, an evident shape change is noticed, both in the first pressure peak and throughout the wave propagation (Figs. 3.11-d and 3.12-d). The pressure rise in the first peak is associated to the line packing effect, which is more evident in the PE pipe; this effect is dependent on the head losses gradient during the initial steady state, which is higher in the test carried out in this pipe. The wave shape changes during its propagation are herein associated with a retarded response of the HDPE material which has a viscoelastic rheological behaviour (Covas *et al.*, 2004c, 2005). Additionally, a relatively faster reaction to the valve manoeuvre is observed (see detail in Fig. 3.15-b), as the slope of the first pressure rise is steeper in the polyethylene case.

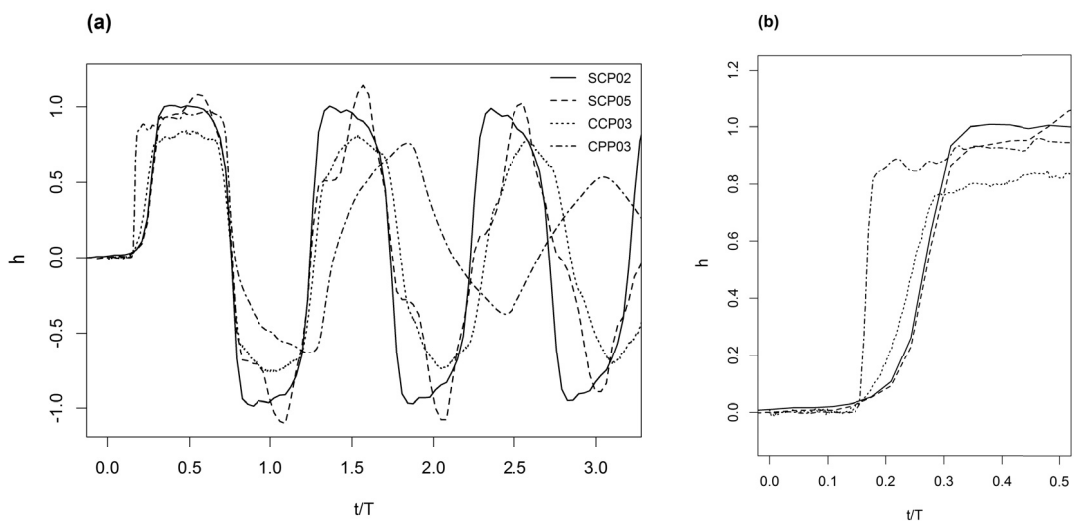


Figure 3.15 – (a) Dimensionless pressure time series at the downstream pipe-end; and (b) detail of the valve manoeuvres of the selected tests.

Wave delay

Regarding the wave timing, a smooth delay can be observed in the tests carried out in the straight copper pipe with released valve in comparison to the tests with fixed valve (see Fig. 3.16). The reason is associated to the dispersive effect of junction coupling, which leads to

Chapter 3. Experimental work

two different periodic phenomena oscillating and interacting at different frequencies, with the ultimate effect of an increase of the overall dissipation when the valve is released.

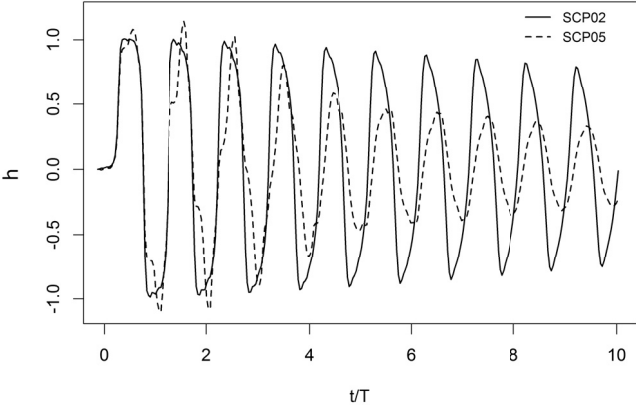


Figure 3.16 – Dimensionless pressure time series at the downstream pipe-end for tests SCP02 (anchored end) and SCP05 (released end).

The coil copper system also presents a time delay with regard to the straight copper pipe tests (see Fig. 3.17), which suggests that both steady and unsteady friction affect the pressure signal more than in the straight copper pipe. The reason is the higher pipe length of the coil copper pipe in comparison with the straight copper pipe.

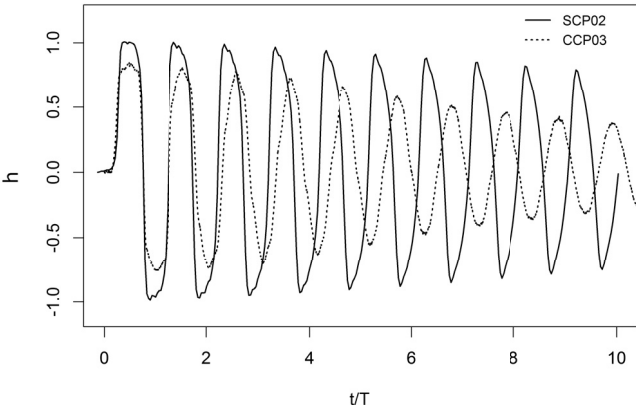


Figure 3.17 – Dimensionless pressure time series at the downstream pipe-end for tests SCP02 and CCP03.

Regarding the polyethylene set-up, the reason of such delay is mainly attributed to the retarded response of the pipe-wall (see Fig. 3.18). In viscoelastic pipes, maximum or minimum pressure fluctuations are rapidly attenuated and the overall transient pressure wave is delayed in time due to the retarded deformation of the pipe-wall (Covas *et al.*, 2004c).

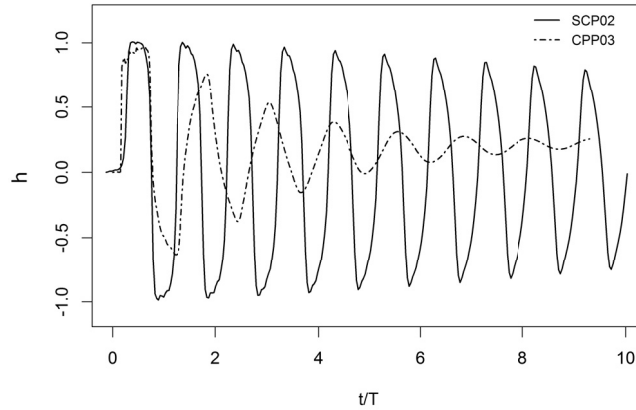


Figure 3.18 – Dimensionless pressure time series at the downstream pipe-end for tests SCP02 and CPP03.

3.3.2 Strain data analysis

The collected strain data allows the analysis of the circumferential and axial strains in a similar manner as in the previous Subsection 3.3.1. Hence, the approach followed to compare the collected strain data consisted, as well, of normalizing measurements by means of the waterhammer wave amplitude and period. Although in the pipe system exists several pipe vibration modes, the first mode is the dominant, therefore the periods used to get dimensionless time scales are the fluid ones (see Table 3.4). On the other side, the strain signal has been normalized by the theoretical maximum circumferential strain (Eq. 3.4) resulting from hoop stress in pipes due to inner pressure loads, both in straight and coil pipes (Ferràs *et al.*, 2014), using as input the pressure wave amplitudes from Table 3.4. Both circumferential and axial strain signals have been normalized using the same values with the goal to get comparable time-series.

$$\Delta\epsilon_{\theta} = \frac{\sigma_{\theta}}{E} = \frac{1}{E} \frac{D\Delta p}{2e} \quad (3.4)$$

Fig. 3.19 presents the dimensionless strain data collected in the four assessed set-ups, at the midstream pipe sections, depicting very different pipe behaviours.

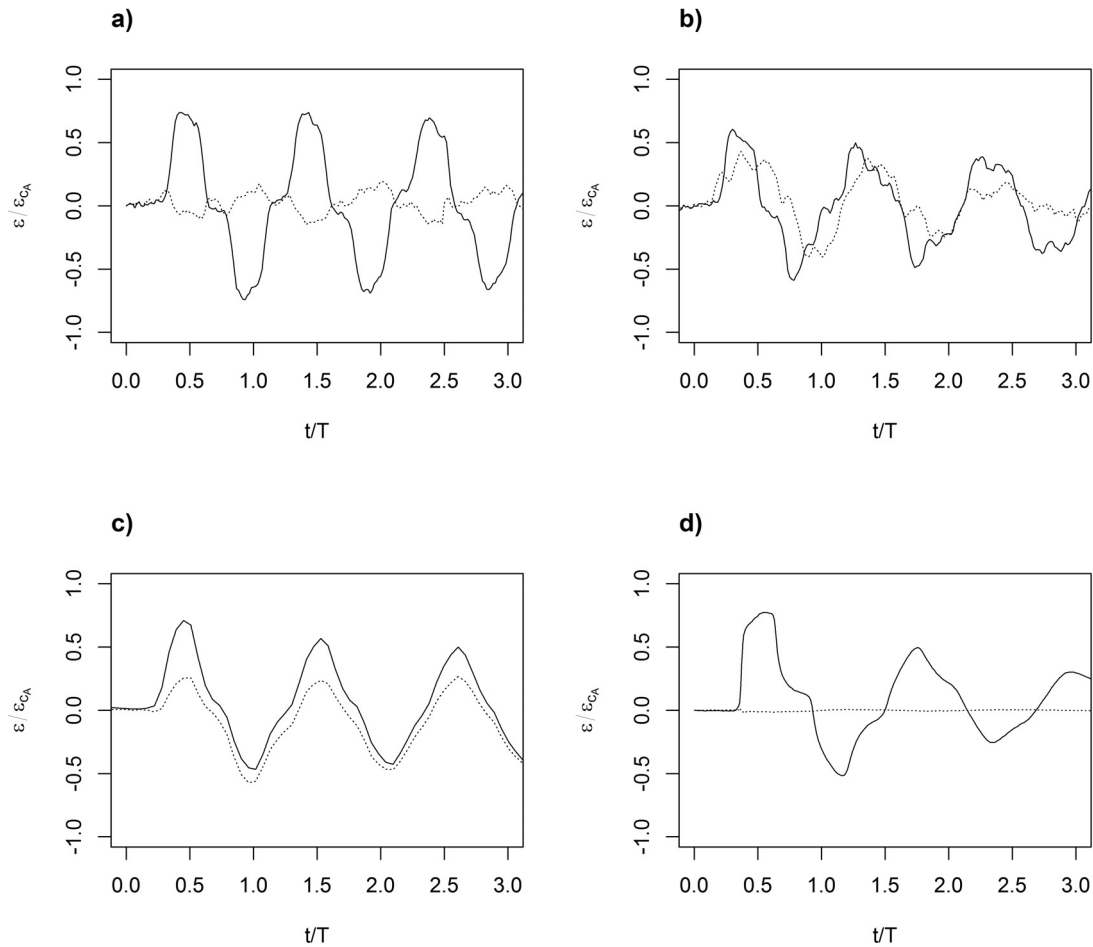


Figure 3.19 – Dimensionless transient circumferential strain (solid lines) and axial strain (dotted lines) at the *midstream* pipe sections for: a) SCP02 (anchored end), b) SCP05 (released end), c) CCP03 and d) CPP03.

In the straight copper pipe facility, strain measurements significantly differ according to the different supporting conditions. In the first case (Fig. 3.19-a), due to the Poisson effect, axial strain presents a phase shift of π with respect to the circumferential strain. Nonetheless, the Poisson relation is not fulfilled ($\epsilon_z \neq -\nu\epsilon_\theta$), this is because of the generation of axial stress waves following the pressure wave propagation. The Poisson effect induces a first positive axial strain spike (precursor wave) before the first circumferential strain rise (see detail in Fig.3.20). Precursor waves were first theoretically studied by Skalak (1955) and experimentally observed, indirectly from pressure measurements, by Thorley (1969).

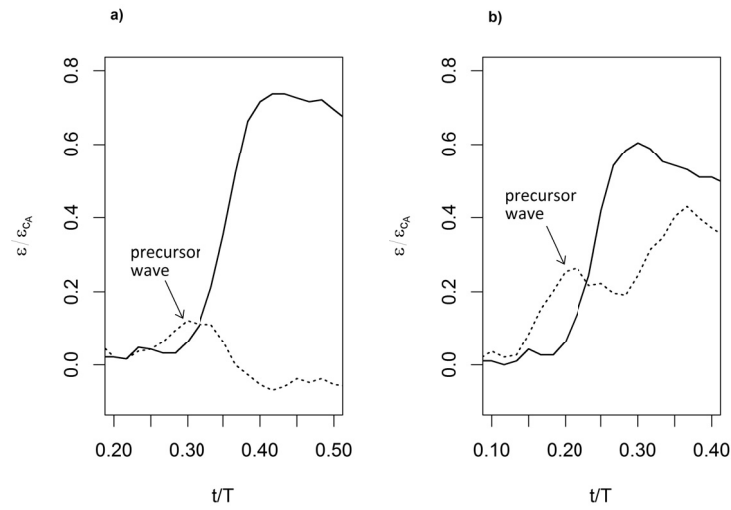


Figure 3.20 – Precursor stress waves during the tests SCP02 (a) and SCP05 (b). Solid lines: circumferential strain; and dashed lines: axial strain.

In Fig.3.20 (right) a clear precursor wave can also be observed in the SCP with released valve set-up; moreover, three axial strain sub-peaks (Fig.3.21) can be distinguished during the first half period, these sub-peaks result from the first axial stress wave, the first impact propagating back and forth throughout the system. After the first wave period, axial and circumferential strains are affected by the dispersion from the interaction of the two pipe vibrating modes.

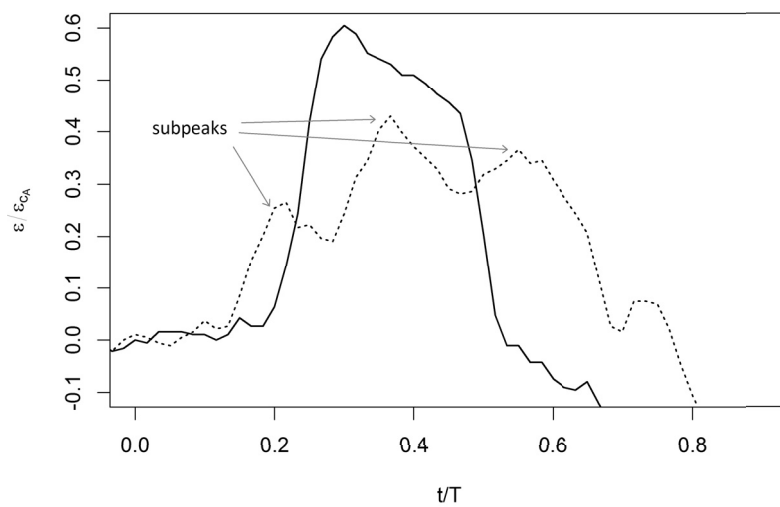


Figure 3.21 – Axial strain sub-peaks observed in the straight copper pipe facility for a free valve.

Chapter 3. Experimental work

The strain measurements obtained in the coil copper facility (Fig.3.19-c) have been corrected according to Ferràs *et al.* (2014), who proposed a methodology for assessing axial and circumferential strains in oval pipes. Both axial and circumferential strains are in phase, following the pattern of the inner pressure wave. It is interesting to point out that, specially during the first wave period, positive axial strain values are lower than negative strain values and *vice versa* for circumferential strains. The coil supports partially constrain the expansion of the coil rings so the pipe-wall is not fully free to deform and develop in the axial direction. Circumferential strain is inversely affected due to the Poisson effect.

Finally, axial strain does not show sensitivity to waterhammer excitation in the coil PE pipe (Fig. 3.19-d), nonetheless the circumferential strain clearly follows the pressure wave pattern. Fig. 3.22 depicts axial and circumferential strains for the different tests carried out in the PE facility, being the axial strain almost null for all the tests and showing that the PE is not influenced by the Poisson effect. As shown in Fig. 3.9, the strain gauges were installed in the straight section between the two coils. It cannot be excluded at this stage that FSI may occur between the two coils cancelling the Poisson effect.

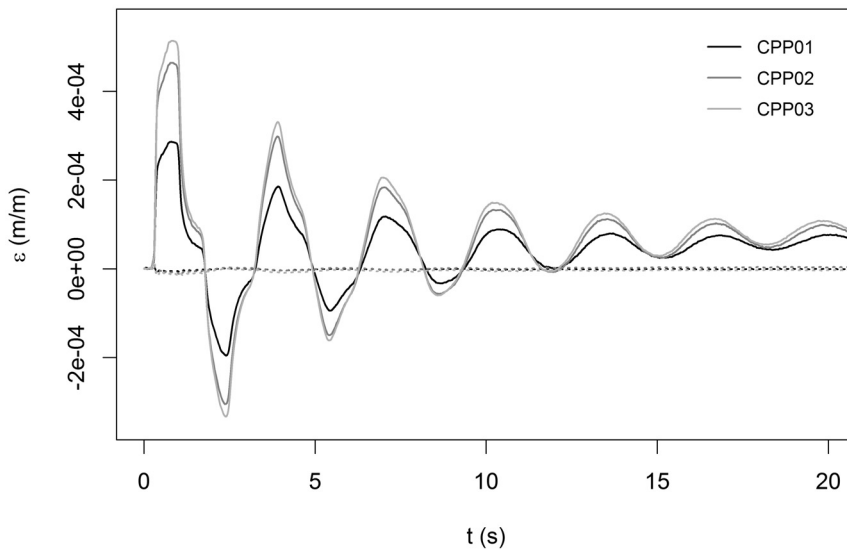


Figure 3.22 – Circumferential (solid lines) and axial (dashed lines) strains measured in the coil PE pipe facility for the different tests carried out.

3.4 Discussion of results

3.4.1 Fluid structure interaction

FSI according to pipe anchoring conditions

The most notable FSI effect can be observed from the comparison between the tests carried out in the straight copper pipe with anchored and released valve (Figs. 3.11-a and -b). Just the fact of setting an anchored or non-anchored valve significantly changes the system response. Fig. 3.11-a shows that the measured pressure during the first wave cycle resembles the expected ‘squared’ wave shape and magnitude of classic theory, being very close to the Joukowsky pressure rise. Nonetheless, the wave shape develops in a characteristic shape typical of Poisson coupling by damping the tail of the pressure peaks and troughs.

Different behaviour can be observed in Fig. 3.11-b. The inertial valve system in this case is released and, consequently, at the downstream boundary there is an imbalance of forces between fluid inner pressure and pipe-wall stresses that makes the valve move (junction coupling). The valve movement generates a characteristic wave shape subdividing the first pressure peak into three stages (*cf.* Fig. 3.14) (Ferràs *et al.*, 2015a): Stage-1 in which the pressure is lower than the expected in classic theory; Stage-2 with higher pressure and; finally, Stage-3 with a pressure drop. The first pressure rise is reduced by the movement of the valve in the downstream direction after the first pressure surge. Afterwards, as the solid axial stress wave travels approximately three times faster than the fluid pressure wave, at around one third of the pressure peak, there is an increase of pressure resulting from the negative axial stress which is pulling the pipe upwards, producing a ‘pumping’ effect. Finally, the axial stress wave, which travels faster than the main pressure wave, bounces back pushing again the valve and producing the last pressure drop over the pressure surge.

Appendix E deepens on the effect of valve movement, where new formulae are presented with the aim of correcting the Joukowsky equation and better predicting the expected maximum pressure rise in a straight pipe with a non-anchored downstream end. Eq. 3.5 is derived from this analysis.

$$\Delta H_{max} = \Psi_{JK} \frac{a_h V_0}{g} \quad (3.5)$$

where Ψ_{JK} is a correcting factor for Joukowsky overpressure and is defined in Table E.1. The result of applying Eq. 3.5 to SCP05 test is depicted in Fig. 3.23, where the grey solid line corresponds to Joukowsky pressure (Eq. 3.2 of classic theory) and black dashed line is the predicted maximum pressure rise by means of Eq. 3.5. The maximum overpressure (ΔH_{max}) observed in the SCP05 test is 10% higher than Joukowsky overpressure. This is accurately predicted by the Joukowsky correction factor (Ψ) presented in Table E.1.

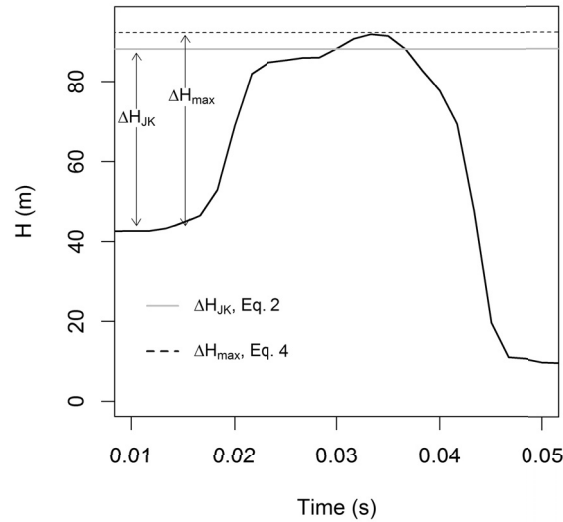


Figure 3.23 – Corrected Joukowski overpressure for the test SCP05.

It is also important to highlight the higher wave damping observed in the test SCP05, where the valve is released, in comparison with SCP02, where the valve is fixed (*cf.* Fig. 3.16). FSI does not introduce a direct wave damping, though, there are additional frictional losses through shear between the fluid and the pipe-wall and between the pipe-wall and the structure supports. UF is significantly affected by the different vibrating frequency of the pipe-wall axial stress wave and the fluid pressure wave.

FSI according to pipe geometry

The coil copper pipe facility also presents a characteristic FSI behaviour which was analysed in Ferràs *et al.* (2015a). The ‘breathing’ effect of the coil introduces a systematic wave amplitude reduction. In steady conditions an analogy can be established between a coil pipe and a straight pipe with a moving end for the computation of axial stresses due to inner pressure loads (Ferràs *et al.*, 2014). However, in transient conditions, axial stress waves are originated in the coil rings when these are excited by the inner pressure load, hence the origin and consequent propagation of the axial stress waves significantly differs from the FSI phenomenon occurring in the straight copper pipe with released end.

A similar wave amplitude reduction is observed also in the polyethylene facility. However, it is more likely that such attenuation is dominated by the viscoelasticity of the pipe-wall material rather than FSI, as further discussed in Subsection 3.4.2.

3.4.2 Pipe-wall rheological behaviour

Collected strain data allows the analysis of the rheology and of the structural displacements of the pipe systems during the transient tests. Fig. 3.24 depicts measured pressures *versus* measured circumferential and axial strains for the selected transient tests of Table 3.4. The theoretical circumferential strain expected from a linear-elastic pipe-wall behaviour given by Eq. 3.4 is also shown in dashed line.

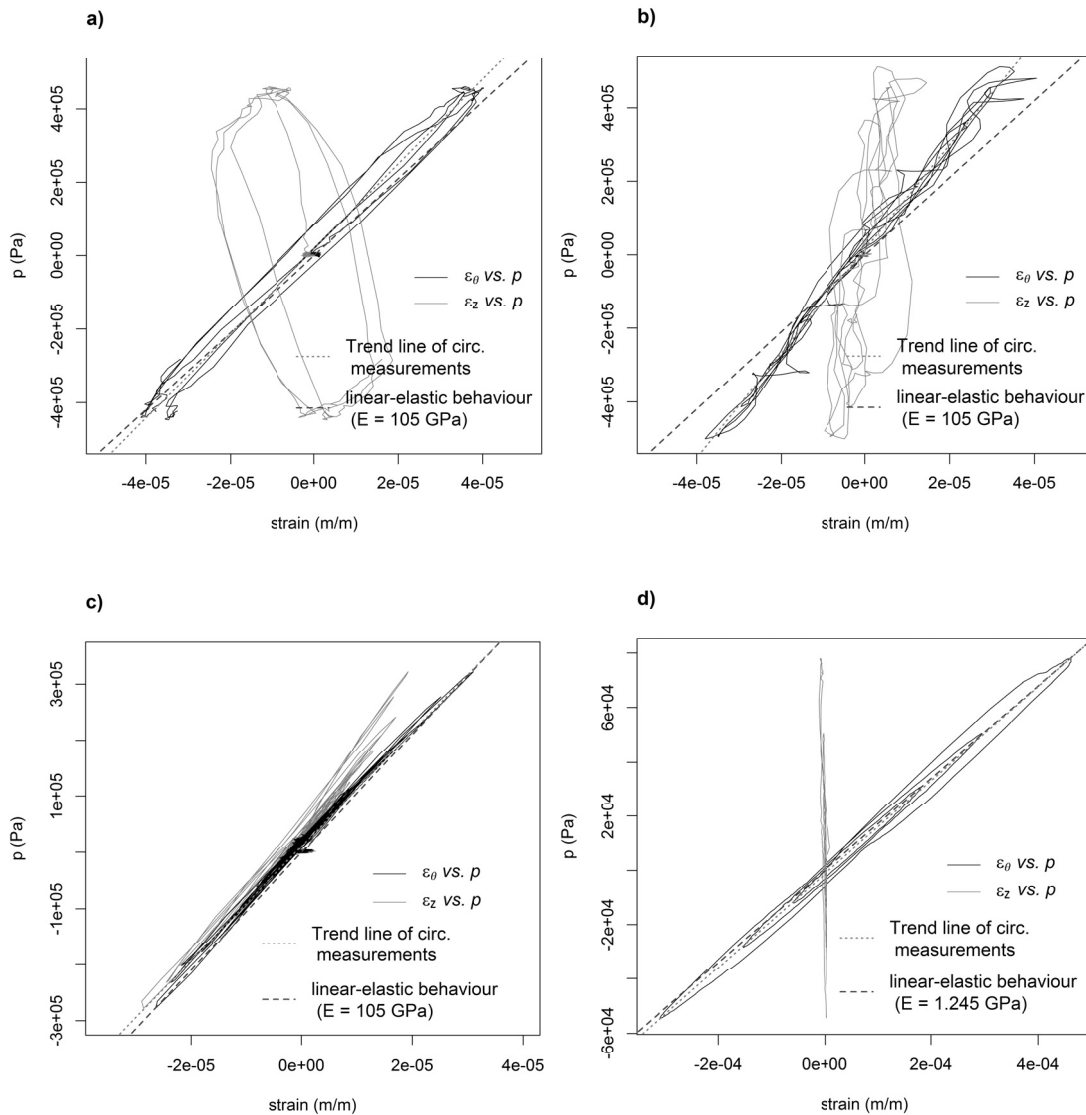


Figure 3.24 – Measured pressures *vs.* measured axial (grey solid line) and circumferential (black solid line) strains during the transient tests carried out at a) SCP02 (fixed valve set-up), b) SCP05 (released valve set-up), c) CCP03 and d) CPP03.

Loading-unloading behaviours significantly depend on the valve anchoring conditions. In the

case of the straight copper pipe with anchored valve (Fig. 3.24-a), a clear pattern is observed: the loading-unloading slope of circumferential strain is quite close to the theoretical linear-elastic behaviour and the axial strain is opposed to the circumferential strain due to Poisson effect. However, loading paths significantly differ from unloading ones, specially in the case of axial measurements. The reason is the FSI interaction occurring due to Poisson coupling as it has a direct effect on the axial direction and an indirect effect on the circumferential. For a non-anchored downstream pipe-end more erratic loading-unloading lines are observed: (Fig. 3.24-b) axial strain measurements for such anchored conditions are affected by junction coupling at the valve section and, consequently, the vibrating pipe produces a breathing-pumping effect. This effect can be observed through the horizontal spikes of the loading-unloading curves in the circumferential direction of (Fig. 3.24-b).

The coil copper facility shows a clear linear-elastic behaviour of the pipe-wall material, as the measurements in the stress-strain space are presented in a straight line (Fig. 3.24-c).

Finally, for the polyethylene facility (Fig. 3.24-d), different loading-unloading paths can be distinguished (see Fig. 3.25) in the strain-pressure plot, typical of the *hysteresis* of the PE pipe-wall material (Covas *et al.*, 2004c, 2005). Also, axial strain measurements in the polyethylene facility show low sensitivity to the transient inner pressure, as depicted by the almost vertical loading-unloading curves.

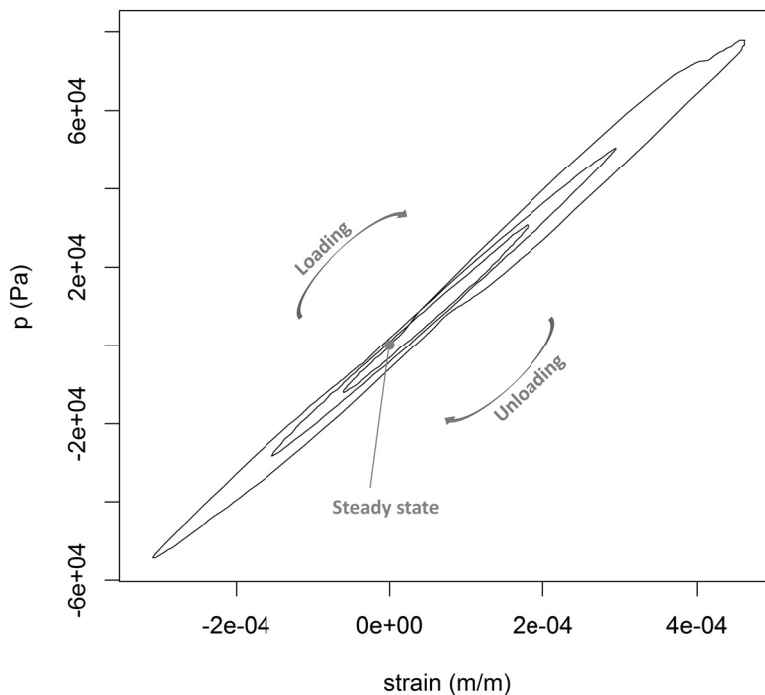


Figure 3.25 – Measured pressures *vs.* circumferential strains during the transient test CPP03.

The ratio between stress and strain (Eq. 3.4), the Young's modulus of elasticity, is an intrinsic

property of the pipe material that is affected by its molecular structure, temperature, stress-strain history and material aging (Jones & Ashby, 2005; Ward & Sweeney, 2012). In this context, the main slope of the trend-lines fitted to collected data in the circumferential direction (dot lines in Fig. 3.24) give some insight about the Young's modulus of the respective pipes. For instance, the slope of the straight copper pipe (Fig. 3.24-a) is quite close to the theoretical linear-elastic behaviour for a Young's modulus of the copper material $E = 105$ GPa. However, the slope of stress-strain is not related to the rheological behaviour of the pipe material but also to the anchoring conditions: in Fig. 3.24-b, circumferential strain presents a higher slope which means the pipe has a stiffer response. This effect is actually produced due to the influence of FSI and junction coupling in this particular anchoring set-up: for positive pressures the pipe is axially stretched and through the Poisson effect this positive axial strain produces a negative circumferential strain reducing the radial expansion of the pipe; and *vice versa* for negative pressures. On the other side, experiments in the copper and PE coil pipes follow clearly the expected trend of the theoretical Young's modulus of elasticity.

3.5 Overview and concluding summary

This chapter summarises physical observations of transient pressures in three different experimental set-ups: a straight copper pipe (SCP) with anchored and non-anchored downstream pipe-end, a coil copper pipe (CCP) and a coil polyethylene pipe (CPP). Hydraulic transient tests were generated by fast downstream valve closures for different initial steady state conditions. Both transient pressures and circumferential and axial strains were measured at the downstream and at the midstream pipe positions.

Two main dissipating phenomena have been identified which affect the attenuation, shape and timing of the pressure wave, namely, fluid-structure interaction and pipe-wall viscoelasticity. Unsteady friction is certainly always present but its effect could not be isolated in the first pressure cycles. For similar initial steady state conditions the experimental set-ups present very different mechanical behaviours.

Different system responses have been compared by means of dimensionless plots of pressure and strain. Experimental pressure and strain measurements in the straight copper pipe with anchored valve are the least affected by the dissipating phenomena, being the closest to the theoretical waterhammer waves expected from classic theory, and with UF the dominant damping mechanism. Releasing the pipe end generates an important wave shape change, higher pressure peaks and higher wave damping. The coil copper pipe, with a similar damping rate, shows a systematic wave amplitude reduction.

Fluid-structure interaction has been identified as being the dominant dissipating phenomenon in straight and coil copper pipes. Formulae have been developed (Appendix E) to more accurately predict the Joukowsky overpressure taking into account FSI. On the other side, the pipe rheological behaviour has been analysed by means of strain-pressure plots. The copper facilities (SCP and CCP) present a clear linear-elastic behaviour; the PE facility (CPP) presents

Chapter 3. Experimental work

different loading and unloading paths across the strain-pressure space, indicating a retarded response (hysteresis) between the inner pressure loading and the circumferential strain response. This viscoelastic behaviour of the polyethylene material is the dominant damping mechanism in the CPP piping system.

Table 3.6 qualitatively summarizes the relative importance of the analysed damping mechanisms during hydraulic transients in the different experimental set-ups.

Table 3.6 – Summary of the qualitative importance of damping mechanisms in the analysed experimental set-ups.

Set-up ID	FSI-supports	FSI-coil	UF	VE
SCP _{anchored}	+	–	+++	–
SCP _{released}	+++	–	+	–
CCP	–	+++	+	–
CPP	–	+	+	+++

Note: +++ strong effect; + medium effect; – low effect.

In polyethylene pipes the structural damping produced by the viscoelasticity of the pipe-wall is crucial and it has to be included in those waterhammer analyses aiming for an accurate model output of the entire pressure time-series. Nonetheless, pipe-wall viscoelasticity does not increase maximum pressures, hence the use of the classic waterhammer model for the design of plastic pipes does not imply a threat on the reliability of the pipe system. Similar phenomena occurs in coil pipes, where the fluid-structure interaction implies the reduction of the wave amplitude. Damping rates though are much lower in the metallic pipe, where the pipe-wall presents an elastic behaviour. The fluid-structure interaction occurring in the straight copper pipe has shown to be highly dependent on the anchoring conditions, specially at the valve section. The pressure loads might be significantly underestimated if the classic waterhammer model, or Joukowsky equation, is used in the design of straight pipe lines without considering the fluid-structure interaction and the structural behaviour of the pipe supports. For instance, in the test SCP05 (free valve) classic waterhammer theory showed a 10% of underestimation of the maximum pressure rise, and this could be worsen for different mass valve configurations. The proposed Eq. 3.5 aims at correcting such discrepancy.

4 Fluid-structure interaction in coils

The present chapter is based on the following scientific publications:

- D. Ferras, D. Covas, A.J. Schleiss. Stress-strain analysis of a toric pipe for inner pressure loads. *Journal of Fluids and Structures*, 51:68-84, 2014.
- D. Ferras, P. Manso, D. Covas, A.J. Schleiss. Comparison of conceptual models for fluid-structure interaction in pipe coils during hydraulic transients. *Submitted at the Journal of Hydraulic Research (July 2014)*.

The work presented hereafter is original and was performed by the first author. The interpretation and discussion of results was carried out with the collaboration of the co-authors.

4.1 Introduction

The aim of the present chapter is to achieve a better understanding of the stress-strain states of a coil pipe during hydraulic transient events. Classic theory of waterhammer assumes that the pipe does not move and that the circumferential deformation is incorporated, together with pipe deformability and fluid (liquid) compressibility, in the elastic wave speed. However, several physical phenomena not taken into account in classic waterhammer theory affect transient pressure wave attenuation, shape and timing (Bergant *et al.*, 2008a,b). One of these effects, Fluid-Structure Interaction analysis (FSI), can be important depending on the set up of the piping system. Consequently, a FSI analysis has to be carried out in order to determine the effect of the structural inertia over the transient pressure wave. Pipe systems experience severe dynamic forces during waterhammer events. When these forces make the system move, significant FSI may occur, so that liquid and pipe systems cannot be treated separately and interaction mechanisms must be taken into account (Tijsseling, 2007). Recommendations by means of some dimensionless parameters and with the aim to analyse when FSI must be taken into account are drawn in Tijsseling (1996).

Pipe coils have many industrial engineering applications, being typically used in most heat

exchange systems, like cooling systems in power plants, industrial and commercial refrigerators, solar water heaters or radiators for automotive industry. Although work has been done in the experimental characterization of the transient flow occurring in pipe coils (Brito *et al.*, 2014), according to the knowledge of the authors, the incorporation of the pipe coil behaviour in hydraulic transient analyses through FSI has never been carried out.

The current chapter gives thereby a novel contribution for the numerical and experimental investigation of pipe coil behaviour during hydraulic transients. First a static analysis is carried out with the goal to understand the stress-strain states for inner pressure loads. Then the coil system is assessed for dynamic conditions allowing the characterization of the fluid-structure interaction (FSI) phenomena, which is the two-way coupling occurring between the pipe structure and the inner pressurized fluid.

4.2 Stress-strain analysis

4.2.1 Introduction and background theory

A stress-strain analysis is a first step for FSI, the goal is to determine the pipe deformation equations. Torsion, bending, shear and axial stresses and strains are the structural responses that a piping system may experience during waterhammer events. In classic waterhammer theory the effect of pipe-wall distensibility is implicitly included in the wave celerity (Chaudhry, 2014). Although radial expansion of the pipe-wall is taken into account, axial strains are not considered in classic waterhammer theory. Skalak (1955) extended classic waterhammer theory aiming to include axial stress and movement of the pipe. Circumferential strain in straight pipes is described by the following relation and included in the conservation equations:

$$\epsilon_{\theta} = \frac{1}{E} \frac{pr}{e} \quad (4.1)$$

where ϵ_{θ} is the circumferential strain, E the Young's modulus of elasticity of the pipe, p the inner pipe pressure, r the pipe radius, and e the pipe-wall thickness.

However, in coil systems, the structural behaviour considerably differs from that of a straight pipe, either in axial and circumferential directions, due to the toroid geometry and the cross-section shape, which becomes oval when the pipe is curved. Consequently, when classic waterhammer theory is applied in coil pipes discrepancies generally arise changing the wave shape and overshooting computed pressures during peak transitions. Anderson & Johnson (1990) analysed the effect of tube ovaling on pressure wave propagation speed in the context of physiological flows, reaching to the conclusion that transient pressure waves are very sensitive to the eccentricity of an ovalled cross-section.

A toroid can be described as a surface of revolution, i.e. by rotation a plane curve through 360° over a straight line (axis of revolution) in the plane of the curve. A coil pipe can be

geometrically defined in the same manner but adding a constant slope in the direction of the axis of revolution, and the number of coil rings will depend on the angle of rotation. Therefore, the helical system of a coil can be considered as a composition of toroids and described as a thin shell of revolution. Membrane theory of shells of revolution is a suitable approach to solve circumferential and axial strains in an axisymmetrically loaded torus. However, in a torus with ovalled or elliptic cross-section, when it is pressurized, loads are not axisymmetric and bending moments are generated. Membrane theory of shells of revolution assumes that no bending moments, twisting moments and transverse shearing forces that exist in the shell (Zingoni, 1997). Bending theory of shells must be applied to account for bending effects and to describe the complete state of stress and strains. However, such theory is more general and, consequently, its main equations are more difficult to be solved for complex geometries.

Clark & Reissner (1950) proposed a methodology based on the Boltzmann superposition principle to describe stress-strain states in Bourdon tubes. Such approach consisted essentially of the computation of axial and circumferential strains using the thin-walled assumption and describing the bending effects using the thick-walled assumption and applying bending theory. In the context of hydraulic transients, Brown & Tentarelli (2001b) and Brown & Tentarelli (2001a) carried out FSI coupling in order to account for the Bourdon effect during waterhammer events. The structural constraint conditions of the pipe coil, though, do not comply with the Bourdon tube theory, as Bourdon tube is a disconnected torus with closed ends, while the pipe coil analysed must be considered as a connected torus. However, a similar approach can be applied in order to determine its stress-strain states, combining thin and thick-walled assumptions by the Boltzmann superposition principle as a function of the applied loads. The current research approaches the stress-strain states problem in pipe coils by computing circumferential and axial strains using membrane theory of shells of revolution and the bending effects by applying an inverse approach based on thick-walled assumption.

4.2.2 Data collection

The experimental data used in the present stress-strain analysis was acquired from the copper coil pipe rig (CCP) assembled at the Laboratory of Hydraulics and Environment of Instituto Superior Técnico (LHE/IST), Lisbon, Portugal, and described in the Subsection 3.2.2.

When the pipe is bended to get the curved shape of the pipe coil, the cross-section is changed from circular to slightly elliptic (as shown in Subsections 4.2.3 and 4.2.4). This ellipticity of the cross-section has important consequences in the structural behaviour of the system.

Two different kinds of experiments were carried out in the coil facility. Firstly, circumferential and axial strains were measured for different quasi-steady pressure loads, and secondly dynamic loading was applied by producing waterhammer events for different flow rates. The results presented in Subsection 4.2.4 correspond to a steady pressure test of $6 \times 10^5 \text{ Pa}$ and results in Subsection 4.2.5 correspond to a waterhammer wave produced for an initial flow rate of $1.4 \times 10^{-4} \text{ m}^3/\text{s}$. Fig. 4.1 shows the measurements obtained for static pressure tests,

namely axial and circumferential strains of the pipe-wall, and fluid pressures.

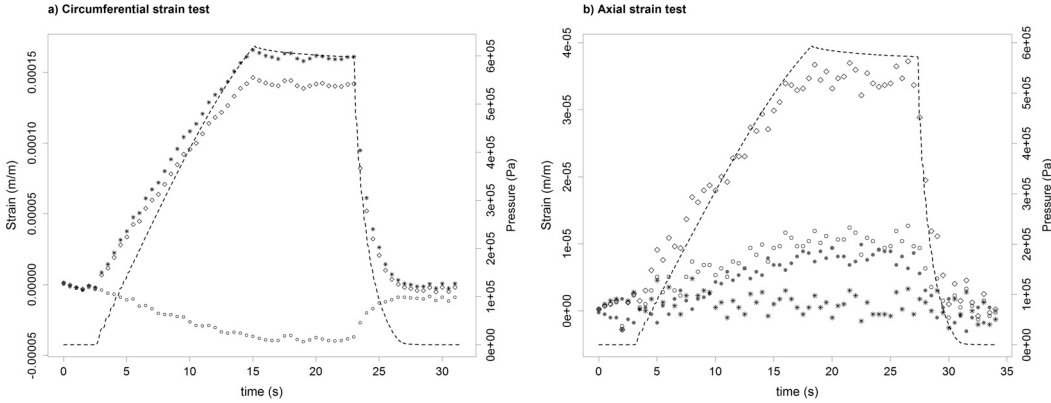


Figure 4.1 – Strain and pressure measurements: (a) circumferential strain test and (b) axial strain test. \circ strain at top side (SG-1 and SG-4); \diamond strain at outer side (SG-2 and SG-5); $*$ strain at bottom side (SG-6); \bullet strain at inner side (SG-3 and SG-7). Pressure measurements in dashed lines (PT-2).

4.2.3 Model development

Membrane theory of shells of revolution: stress-strain models

A shell of revolution is a three-dimensional structure bounded primarily by two arbitrary curved surfaces a relatively small distance apart (Seide, 1975). In the present section the membrane theory of shells of revolution, assuming thin wall and axisymmetrical load, has been considered for the computation of axial and circumferential stresses. Nonetheless, the membrane theory of shells of revolution assumes momentless shells, thus, this theory does not consider the bending of the cross-section.

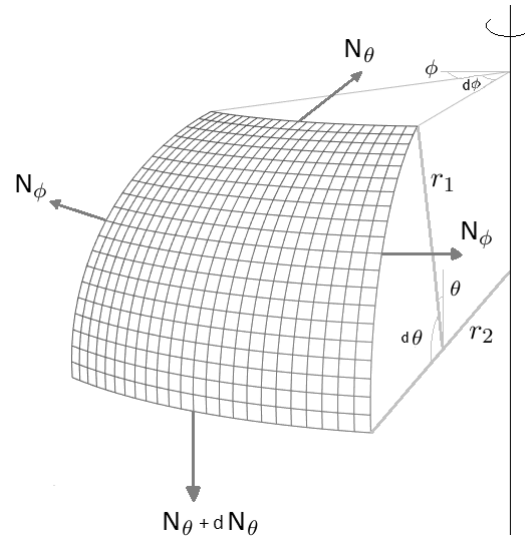


Figure 4.2 – Element of the axisymmetrically loaded shell of revolution

The starting point to derive stress-strain models is the general solution of the membrane theory of shells of revolution for axisymmetric loads (Zingoni, 1997), which outcome is an expression for axial and circumferential stresses:

$$N_{\theta} = \frac{1}{r_2 \sin^2 \theta} \left[\int r_1 r_2 (p_r \cos \theta - p_{\theta} \sin \theta) \sin \theta \, d\theta + j \right] \quad (4.2)$$

$$N_{\phi} = r_2 p_r - \frac{r_2}{r_1} N_{\theta} \quad (4.3)$$

where N_{θ} is the circumferential unit force and N_{ϕ} the axial unit force; p_r is the load applied in the normal direction of the shell midsurface, p_{θ} the load in the tangential direction of the shell midsurface; r_1 and r_2 correspond to different radii of curvature (see Fig 4.2); θ and ϕ are respectively the angles corresponding to the parallel and meridional directions; and j is a constant of integration to be obtained from appropriate boundary conditions.

Adapting the general solution with regard to the coil geometry, two stress-strain models, one for the torus with elliptic cross-section (elliptic torus model) and the other for the circular cross-section (circular torus model), were implemented following the development explained in Zingoni (1997).

Torus with elliptic cross-section: After determining the radius of curvature r_1 and r_2 for an elliptic cross-section, and introducing them in Eq. 4.2, the definite integral can be solved fixing a finite j constant for $\theta = 0$ and $\theta = \pi$, for which $\sin \theta = 0$. Expressing the unitary force in terms

of stress, the expression obtained for circumferential stress is:

$$\sigma_{\theta} = \frac{p a^2}{e \sqrt{a^2 \sin^2 \theta + b^2 \cos^2 \theta}} \left[\frac{R \sqrt{a^2 \sin^2 \theta + b^2 \cos^2 \theta} + \frac{a^2}{2} \sin \theta}{R \sqrt{a^2 \sin^2 \theta + b^2 \cos^2 \theta} + a^2 \sin \theta} \right] \quad (4.4)$$

where σ_{θ} is the circumferential stress, p the inner pressure, e the pipe-wall thickness, a the minor semi-axis length of the elliptic cross-section, b the major semi-axis length and R is the torus radius from the centre of the toroid to the pipe axis.

Substituting the previous Eq. 4.4 into Eq. 4.3 and rearranging terms the expression for axial stress is obtained:

$$\sigma_z = \frac{p a^2}{e b^2} \left[R \left(\frac{b^2 - a^2}{a^2} \right) \sin \theta + \frac{b^2 - \frac{1}{2}(a^2 \sin^2 \theta + b^2 \cos^2 \theta)}{\sqrt{a^2 \sin^2 \theta + b^2 \cos^2 \theta}} \right] \quad (4.5)$$

For $R \gg a$ & b , the term $\left[\left(\frac{b^2 - a^2}{a^2} \right) \sin \theta \right]$ in Eq. 4.5 becomes very sensitive to ellipse eccentricity. This high sensitivity and the uncertainty associated to the accuracy of the measurement of the ellipticity are the main reasons why eccentricity value is calibrated in an *a posteriori* analysis from axial strain measurements.

Torus with circular cross-section: Circular torus equations are straightforwardly derived by simplifying Eq. 4.4 and 4.5 for $a = b = r$, resulting the following expression for circumferential over the outer surface

$$\sigma_{\theta} = \frac{p r}{e} \left(\frac{R + \frac{r}{2} \sin \theta}{R + r \sin \theta} \right) \quad (4.6)$$

and over the inner surface the circumferential stress is

$$\sigma_{\theta} = \frac{p r}{e} \left(\frac{R - \frac{r}{2} \sin \theta}{R - r \sin \theta} \right) \quad (4.7)$$

$$\sigma_z = \frac{p r}{2e} \quad (4.8)$$

For $R \gg r$, Eqs. 4.6 and 4.7 can be further simplified, cancelling the second term and reaching the expression for straight pipes (Eq. 4.1) used in classic waterhammer theory. For instance, in the case of the copper coil facility analysed where $R = 0.5 \text{ m}$ and $r = 0.02 \text{ m}$ the circumferential stress at $\theta = \pi/2$ will be $\sigma_{\theta} = \frac{p r}{e} \cdot (0.981)$. Hence, applying straight pipe equation for circumferential stress only, a 2% error will be produced as much in the most unfavourable location within the cross-section. Eq. 4.8 shows that axial stress is independent of the coil radius R and of the position angle θ . Hence, contrary to an elliptic torus, axial stress is constant along the pipe wall for the circular cross-section, like a straight pipe with closed ends.

Once stresses are computed by the previous equations, either using elliptic torus or circular torus assumptions, strains can be obtained by Hooke's law for isotropic elastic materials:

$$\epsilon_{\theta} = \frac{1}{E}(\sigma_{\theta} - \nu\sigma_z) \tag{4.9}$$

$$\epsilon_z = \frac{1}{E}(\sigma_z - \nu\sigma_{\theta}) \tag{4.10}$$

where ϵ_{θ} and ϵ_z are the circumferential and axial strains, respectively, and ν is the Poisson ratio.

Cross-sectional bending analysis: inverse method

Membrane theory of shells of revolution assumes thin-walled shells, that is no bending moments are transmitted along the shell. However, due to the elliptic geometry of the pipe cross-section, when the fluid pressure changes, radial loads are not balanced in the coil (they are not axisymmetric any more) as its projection on the minor axis of the ellipse will not be equal to the projection on the major axis (see Fig. 4.3). This unbalance of forces generates bending moments that for positive pressures will tend to reduce the eccentricity of the ellipse and vice versa for negative pressures. Hence, in the case of positive pressures, the outer fibres of the upper and lower generatrices of the cross-section will be compressed and the outer fibres of the lateral generatrices stretched. For negative pressures, the effect will be the opposite.

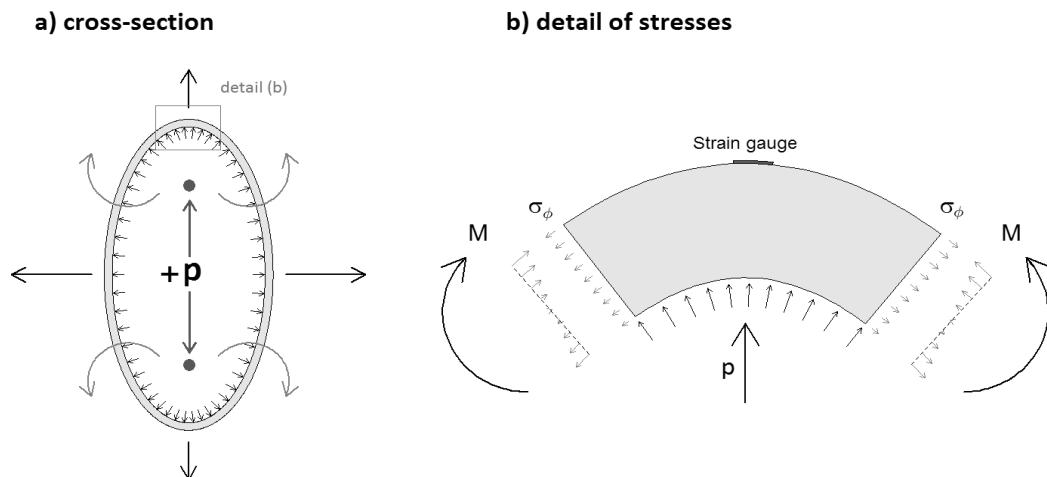


Figure 4.3 – Schematics of radial loads balance in (a) an elliptic cross-section and (b) detail of stresses over the upper generatrice

Strain-gauges measurements give information from these outer fibres, so the real measurements will be actually a combination of circumferential strain (obtained by membrane theory of shells of revolution) plus the extra deformation at the outer fibres due to bending. Therefore, the effect of bending can be analysed by an inverse method from computed circumferential strains in the central fibres of the pipe-wall and measured strains in the circumferential direction at the external fibres.

The assessment of this bending effect has two goals: firstly, it will allow the comparison between measured and computed circumferential strains, and secondly, it will provide information about the cross-sectional shape change, which is important for fluid-structure coupling during hydraulic transients in coils.

Derivation of the bending moment M : The pressurized elliptic cross-section is a hyperstatic system, i.e. internal forces such as the bending moment $M(\theta)$ cannot be obtained explicitly from the static equilibrium equations. Therefore, $M(\theta)$ can only be obtained numerically. The derivation carried out is based on Fig. 4.4:

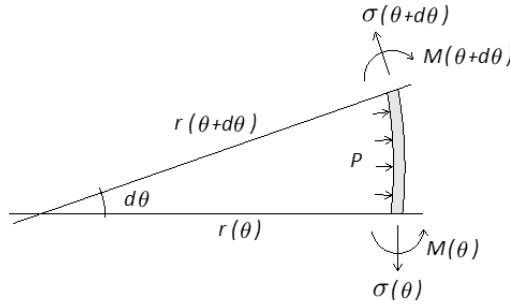


Figure 4.4 – Schematic for bending moment $M(\theta)$ derivation

Applying equilibrium of moments at point $(\theta + d\theta)$ and assuming some simplifications the following expression can be obtained:

$$M(\theta + d\theta) = M(\theta) - \sigma(\theta) [r(\theta) - r(\theta + d\theta)] + P \frac{(d\theta r(\theta))^2}{2} \quad (4.11)$$

By rearranging terms in the previous equation, it yields:

$$\frac{M(\theta + d\theta) - M(\theta)}{d\theta} = -\sigma(\theta) \frac{r(\theta) - r(\theta + d\theta)}{d\theta} + P \frac{(d\theta r(\theta))^2}{2d\theta} \quad (4.12)$$

that is

$$\frac{dM(\theta)}{d\theta} = \sigma(\theta) \frac{dr(\theta)}{d\theta} + P \frac{d\theta r(\theta)^2}{2} \quad (4.13)$$

As the elliptic cross-section is a closed system, Eq. 4.13 has to be solved by imposing some internal conditions. From measurements and applying the inverse approach explained in the previous section, bending moments can be obtained at convenient points of the cross-section and, then, be used as internal conditions. Though, as the inverse method must be applied in any case, the implementation of the stress-strain models was carried out by using the inverse approach all over the cross-section.

Centrifugal force throughout the coil pipe

Another effect that may contradict the axi-symmetrical loading assumption is the inertial force generated by the rotation of the flow along the coil. The centrifugal force produced by an infinitesimal control-volume of the fluid on the coil may be defined as:

$$dN_{\theta} = \rho dV \frac{V^2}{R} = \rho A_f \frac{dx}{R} V^2 = \rho A_f d\phi V^2 \quad (4.14)$$

where N_{θ} is the centrifugal force, ρ is the fluid density, dV is the volume of the control-volume, V is the average flow velocity and A_f the fluid cross-sectional area.

Applying the balance of forces shown in Fig. 4.5 between the axial stress of the pipe-wall and the centrifugal force N_{θ} :

$$dN_{\theta} = 2N_{\phi} \sin \frac{d\phi}{2} \approx N_{\phi} d\phi \quad (4.15)$$

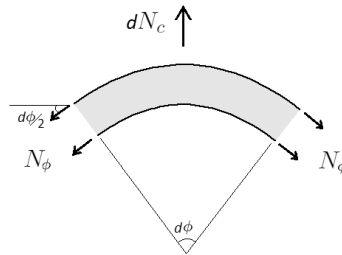


Figure 4.5 – Balance of forces of a control volume, pipe-wall stress forces versus centrifugal force

By combining Eqs. 4.14 and 4.15, the following expression can be obtained for the axial unit force due to centrifugal effect:

$$N_z = \rho A_f V^2 \quad (4.16)$$

which, in terms of stress, is

$$\sigma_{z_c} = \frac{N_z}{A_s} = \rho \frac{A_f}{A_s} V^2 = \rho \frac{\pi r^2}{e 2 \pi r} V^2 = \rho \frac{r}{2e} V^2 \quad (4.17)$$

where A_s is the solid cross-sectional area.

The ratio between the axial stress due to the fluid centrifugal force σ_{z_c} (Eq. 4.17) and the axial stress due to inner pressure σ_{z_p} (Eq. 4.8) is:

$$\frac{\sigma_{z_c}}{\sigma_{z_p}} = \rho \frac{V^2}{p} \quad (4.18)$$

Considering maximum effects during waterhammer events, p_{max} can be computed using Joukowsky expression ($p = \rho a V$). Substituting in Eq. 4.18:

$$\frac{\sigma_{z_{cmax}}}{\sigma_{z_{pmax}}} = \frac{V}{a} \quad (4.19)$$

where a is the waterhammer wave speed. In most engineering applications $a \gg V$, so the non-dimensional number presented in Eq. 4.19 will be very low (in the case of the copper facility $\approx 10^{-4}$) and, consequently, the axial stress due to inertia of the fluid flow throughout the coil can be neglected.

4.2.4 Model application

Forward approach for circumferential and axial strains

Torus with elliptic cross-section: States of stresses and strains were computed by Eqs. 4.4, 4.5, 4.9 and 4.10 for the static loading test for a pressure of $6 \times 10^5 Pa$ (i.e., 60 mH_2O) and obtained results are shown in Fig. 4.6.

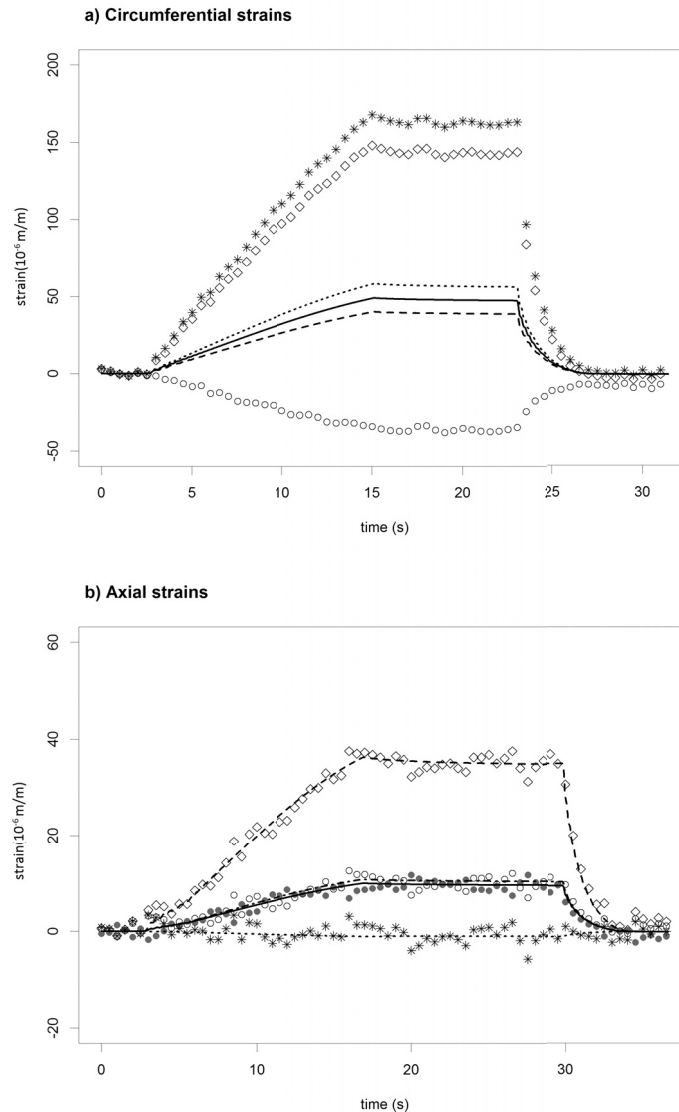


Figure 4.6 – Measured versus computed circumferential and axial strains using elliptic torus. \circ measured strain at top side; \diamond measured strain at outer side; $*$ measured strain at bottom side; \bullet measured strain at inner side. Computed strain at top side in solid line (SG-1 and SG-4); computed strain at outer side in dashed line (SG-2 and SG-5); computed strain at bottom side in dash-dot line (SG-6); and computed strain at inner side in dotted line (SG-3 and SG-7).

After adjusting ellipse eccentricity $\sqrt{\frac{b^2 - a^2}{b^2}} = 0.094$, a good agreement between the computed axial strains and the measurements is obtained. The consistency between the different positions in the cross-section strengthens the reliability of membrane theory of shells of revolution in regard to axial strains. Nevertheless, circumferential strain results do not present the same accuracy, as major discrepancies arise between circumferential strains in the different positions of the cross-section. The main reason of such discrepancies is the bending effect over

Chapter 4. Fluid-structure interaction in coils

the cross-sectional plane due to non-axisymmetry of loads (Fig. 4.3), which at this stage has not been taken into account.

Torus with circular cross-section: Stress-strain states were also solved by applying the model of the torus with circular cross-section and for the same pressure loads as in the previous section. Deformations were computed by using Eqs. 4.6, 4.7, 4.8, 4.9 and 4.10 and the results are presented in Fig. 4.7.

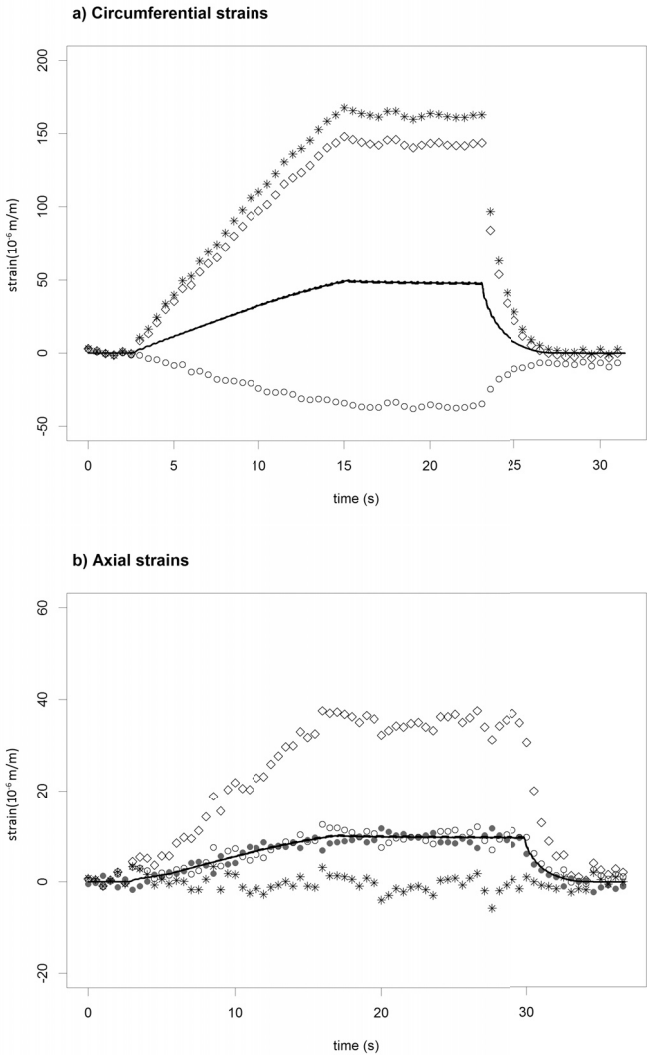


Figure 4.7 – Measured versus computed circumferential and axial strains for a circular torus. \circ measured strain at top side; \diamond measured strain at outer side; $*$ measured strain at bottom side; \bullet measured strain at inner side. Computed strain at top side in solid line (SG-1 and SG-4); computed strain at outer side in dashed line (SG-2 and SG-5); computed strain at bottom side in dash-dot line (SG-6); and computed strain at inner side in dotted line (SG-3 and SG-7).

In Fig. 4.7 it can be seen that both circumferential and axial computed strains from a circular torus hardly vary with their relative position in the cross-section (see all dashed lines overlapped). This is in agreement with the assumption that $R \gg r$, indicating that circumferential strains computed by classic theory do not vary much in comparison to the model for a circular torus. However, as in the case of elliptic torus, discrepancies with measurements are evident. On the other side, axial strains are constant over the cross-section, and their magnitude is close to the measured axial strain in the top and in the bottom sides of the cross-section.

In general, the circular torus model can describe quite well average circumferential and axial strains. However, the capacity of elliptic torus to adjust *a posteriori* elliptic eccentricity of the pipe cross-section and its reliability shown in axial strains (Fig. 4.6) justify a good basis to carry out the bending analysis of the cross-section. The analysis will allow the correction of circumferential strains at the outer fibres of the pipe-wall.

It should be highlighted that the differences between measurements and computed circumferential strains by the membrane theory of shells of revolution, either considering elliptic or circular cross-section, are coherent with the phenomena explained in Subsection 4.2.3. The bending of the cross-section when pressure is increased produces a compression of the external fibres of the top side of the cross-section and stretches the external fibres in the lateral sides. Hence, computed results overestimate circumferential strains in the top side and underestimate circumferential strains in the lateral sides in comparison to measurements.

Inverse approach for bending effects

The inverse approach is used to correct the bending effect not described by the previous models. First of all, the relation between strains and the *focal distance* (from this point on d_F , i.e. distance between the two foci of the ellipse; cf. Fig.4.3) is determined. After a geometrical development, the deformation at any point of the external side of the pipe wall has to be analytically found for any change in ellipse eccentricity. Fig. 4.8 shows the deformation from circumferential cross-section (i.e. $d_F = 0$) to any d_F up to a maximum value of $d_F = 6.77 \text{ mm}$. The relation between d_F and strains at the external sides of the pipe wall for the upper and lateral generatrices of the cross-section is presented in Fig. 4.9. Although the general law is not linear, as the experimental strains are located in a very small range, the expression can be approximated to a linear relationship.

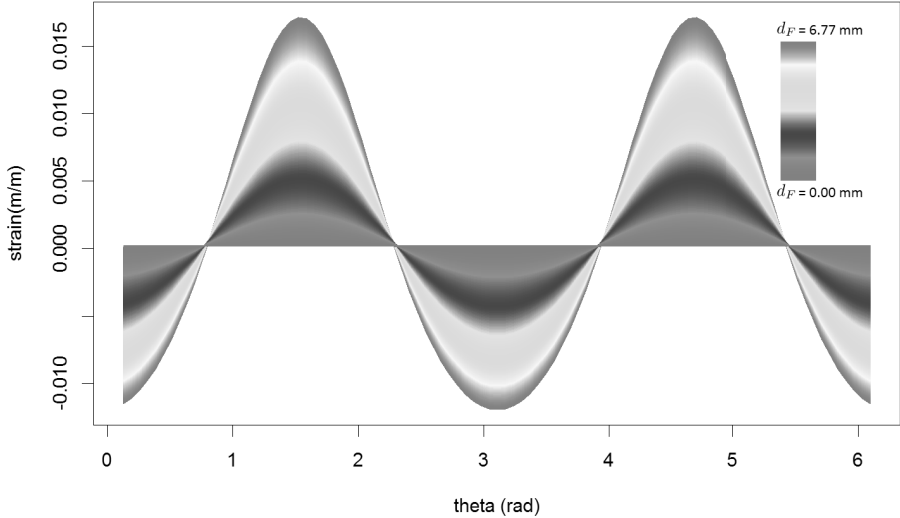


Figure 4.8 – Circumferential strains over the cross-section when focal distance d_F is changed

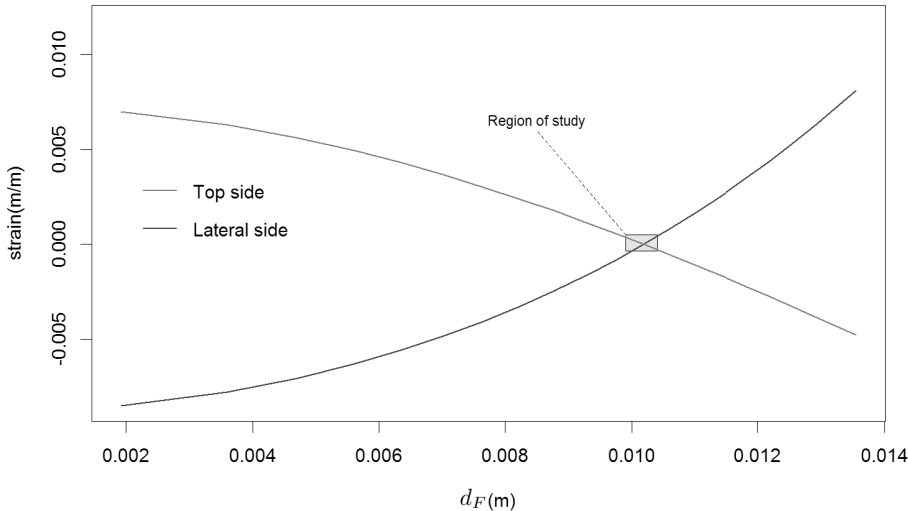


Figure 4.9 – Circumferential strains as a function of focal distance d_F

In a second stage, as time-series relating pressures and strains could be obtained from measurements, with the combination of the previous relations depicted in Fig. 4.9, an empirical relation between pressure and d_F could be found (Fig. 4.10).

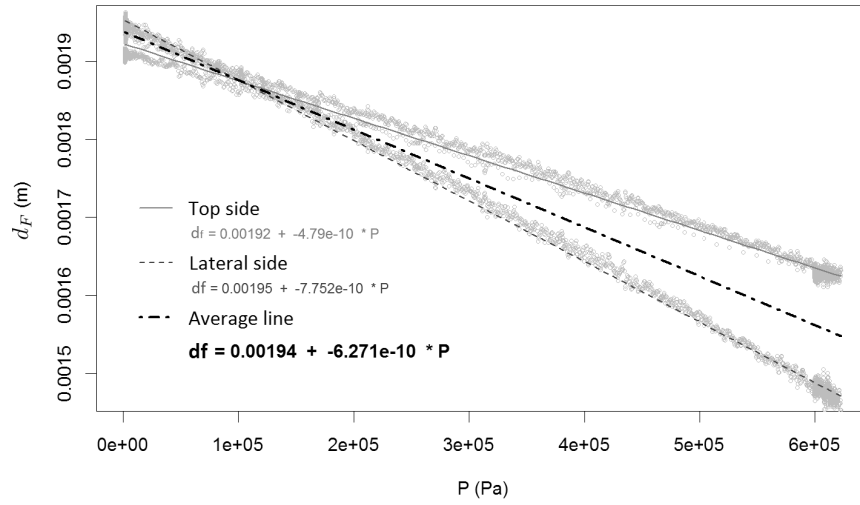


Figure 4.10 – Empirical laws relating pressure p and focal distance d_F

In Fig. 4.10 three empirical relationships between pressure p and the focal distance d_F are shown: the solid red line represents this relation obtained according to strains measured on the top side of the cross-section, the blue dash line according to strains measured on the lateral side and the black dash-dot line represents the average line obtained between the previous relationships. The relationship between d_F and p should be equal over the whole cross-section, consequently, the solid and dashed lines, ideally, should be overlapping. This graph allows the validation of the method: the closer the solid and dash lines are, the more accurate the method is. Notice that before this stage no calibration had been carried out, only ellipse eccentricity had been initially adjusted in order to get the best fitting for axial strains. This small discrepancy over the solid and dash lines is due to uncertainty arisen from strain measurements, experimental Young's modulus, ellipse eccentricity and other possible secondary effects, like torsion and shear along the coil due to its structural constraints. A better fitting of both lines could be achieved calibrating the mentioned parameters. Notwithstanding, obtained linear laws are quite similar, therefore for the purpose of the analysis both relationships are considered accurate enough and the dash-dot interpolated line will be used in next steps as the relationship between pressure and focal distance (Eq. 4.20). No further calibration is applied.

$$d_F[m] = 0.00194 - 6.27 \cdot 10^{-10} * p[Pa] \quad (4.20)$$

Eq. 4.20 allows, therefore, the estimation of 'an average' focal distance of elliptic cross-section for all pressures within the experimental pressures range. Consequently, the volume change in the coil due to cross-section shape change can be analysed, and circumferential strains computed from membrane theory of shells of revolution can be corrected. Fig. 4.11 presents the strains computed and corrected with this approach (elliptic torus with bending effect), the previous strains obtained with the basic models (elliptic and circular torus) and the

experimental data.

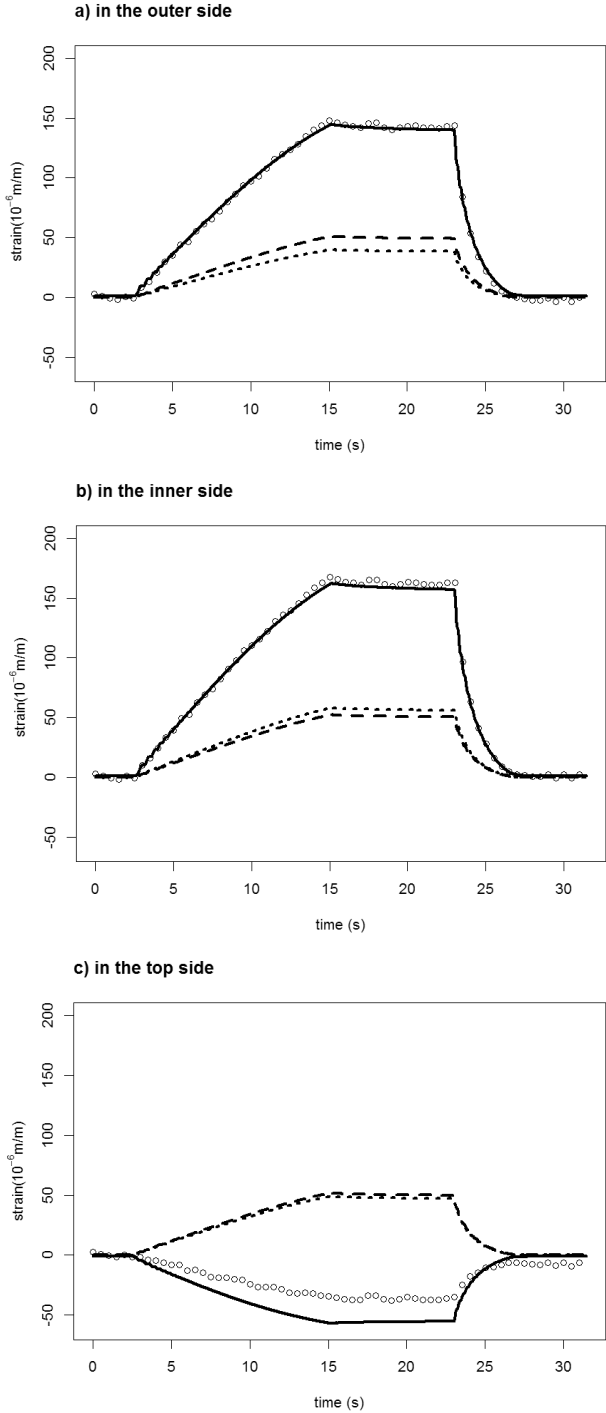


Figure 4.11 – Circumferential strains corrected and not corrected versus experimental data: a) in the outer side, b) in the inner side, and c) in the top side of the pipe. \circ measured data; output from elliptic torus model in dotted lines; from circular torus model in dashed lines; and from elliptic torus model taking into account bending effect in solid lines.

Fig. 4.11 shows that once circumferential strains are corrected by taking into account the bending effect, there is good agreement between measured and computed strains, particularly in the inner and outer sides of the cross-section. Discrepancies are observed in the top position of the cross-section where computed strains seem to be more sensitive to the inaccuracy of the method already depicted in the Fig. 4.10. However, the overall performance of the model after the bending correction is quite satisfactory, allowing the assessment of pipe-wall displacements for the analysed range of static loadings.

4.2.5 Model validation

Dynamic loading tests were carried out in order to assess whether the calibrated stress-strain model can accurately describe pipe-wall displacements during hydraulic transients. A hydraulic transient is characterized by fast loading-unloading cycles over the pipe wall. Consequently, other physical phenomena such as non-elastic behaviour of the copper material may arise, which are not taken into account in a static analysis.

For this purpose, once the stress-strain model was defined, strains were computed from measured pressure during a hydraulic transient test and compared with measurements. Axial strains were determined by using the elliptic model developed by membrane theory of shells of revolution approach (Eq. 4.5). Circumferential strains were computed by the superposition of membrane theory (Eq. 4.4) and the correction for the bending effect presented in Subsection 4.2.4.

A hydraulic transient was generated by the fast closure of a valve (in 0.1 s) located at the downstream end of the pipe and for an initial discharge of $1.4 \times 10^{-4} \text{ m}^3/\text{s}$. With a frequency of data sampling of 100 Hz the measured wave speed was 1120 m/s. Fig. 4.12 presents the numerical results versus measurements of circumferential and axial strains on the outer side of the coil cross-section.

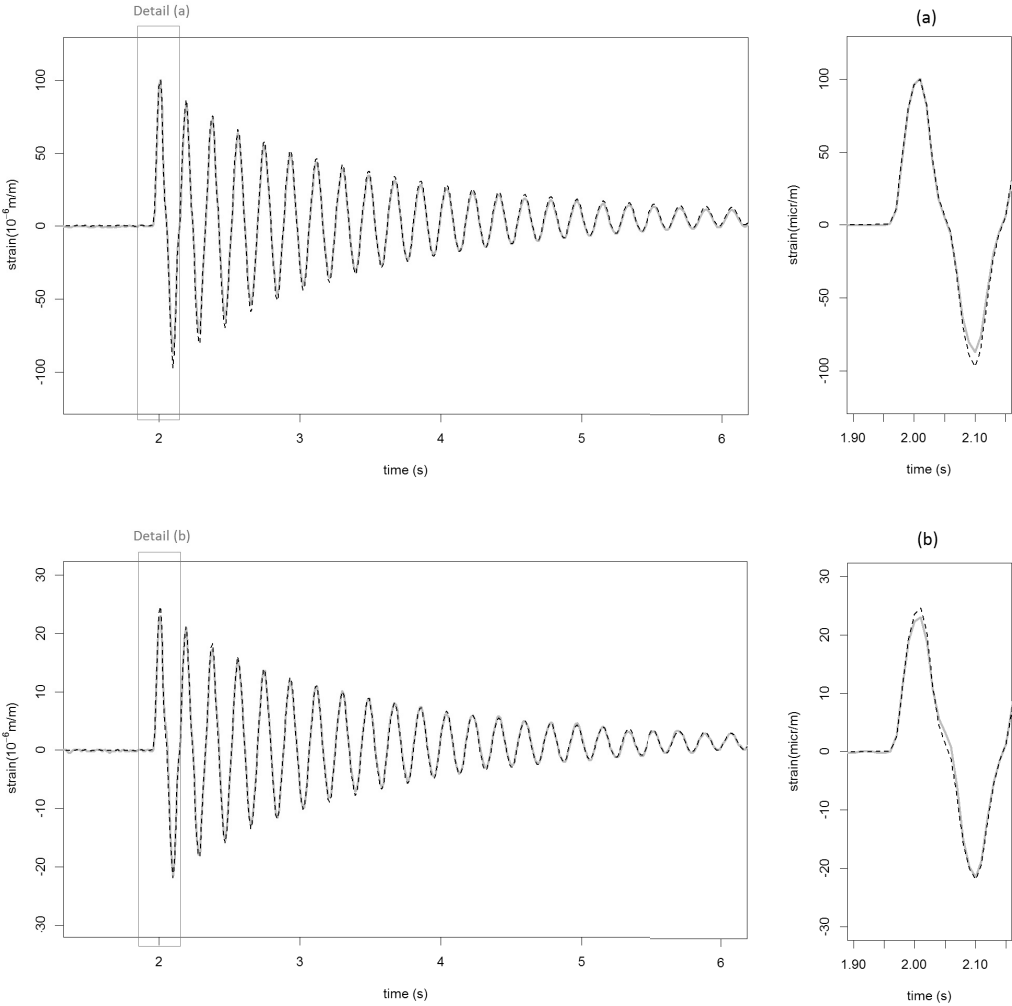


Figure 4.12 – Circumferential (top) and axial (down) strains (in $\mu m/m$) in the outer side of the cross-section during transient test at the middle section of the pipe and detail of the first peaks (right). Measured data in grey solid lines and computed data in black dashed lines.

Strains computed in the circumferential direction have a Mean Squared Error equal to $2.1 \frac{\mu m}{m}$, while strains in axial direction have $0.25 \frac{\mu m}{m}$. The stress-strain model has a better performance in the axial direction because the computed strains in this direction have not to be corrected, since assumptions from membrane theory of shells of revolution are consistent with the physical phenomena. This is because bending is only occurring over the cross-sectional plane, and not over the horizontal plane. However, strains in the circumferential direction are affected by the bending of the elliptic cross-section (Fig. 4.3), and therefore uncertainty arises from the introduced correction.

Simplification of pipe stress-strain equations for FSI coupling

In FSI implementation for the analysed coil pipe system, membrane theory of shells of revolution have to be applied for circumferential and axial strains computation, while the bending effect has to be considered by the empirical relationship from Fig. 4.10. Coupling will be performed for 1D hydraulic transient equations. Hence, for the sake of FSI implementation, the stress-strain equations are simplified with the aim to consider only averaged values over the entire cross-section.

Simplification for circumferential stress: The circumferential stress equation for elliptic torus can be simplified by assuming quasi-circular cross-section ($a \simeq b \simeq r$) and quasi-straight pipe ($R \gg r$). Hence, substituting a and b by r in Eq. 4.4:

$$\begin{aligned} \sigma_{\theta_1} &= \frac{pr^2}{e \underbrace{\sqrt{r^2 \sin^2 \theta + r^2 \cos^2 \theta}}_r} \left[\frac{R \sqrt{r^2 \sin^2 \theta + r^2 \cos^2 \theta} + \frac{r^2}{2} \sin \theta}{R \sqrt{r^2 \sin^2 \theta + r^2 \cos^2 \theta} + r^2 \sin \theta} \right] = \\ &= \frac{pr}{e} \underbrace{\frac{Rr + \frac{r^2}{2} \sin \theta}{Rr + r^2 \sin \theta}}_{1 \text{ for } R \gg r} \\ \sigma_{\theta_1} &= \frac{pr}{e} \end{aligned} \tag{4.21}$$

obtaining the same expression corresponding to circumferential stress in straight pipes used in classic waterhammer theory.

Simplification for axial stress: Though, regarding axial stress the term $R \left(\frac{b^2 - a^2}{a^2} \right) \sin \theta$ from Eq. 4.5 can not be simplified. Using the same assumptions, as for the quasi-straight pipe assumption ($R \gg r$) the term tends to $\pm \infty$ while for the quasi-circular section assumption ($a \simeq b$) it will tend to 0, thus the term is undefined. Hence, substituting in the other terms a and b by r it yields:

$$\sigma_{\theta} = \frac{p}{er} \left[R \left(\frac{b^2 - a^2}{a^2} \right) \sin\theta + \frac{r^2 - \frac{1}{2}(r^2 \sin^2 \theta + r^2 \cos^2 \theta)}{\sqrt{r^2 \sin^2 \theta + r^2 \cos^2 \theta}} \right]$$

$$\sigma_{\theta} = \frac{pr}{2e} + \frac{pR}{e} \left(\frac{b^2 - a^2}{a^2} \sin\theta \right) \quad (4.22)$$

The first term of the obtained Eq. 4.22 is equivalent to the axial stress for circular torus, which actually is the result of the structural constraint of closed torus (same expression would be obtained for a straight pipe with frequent expansion joints and closed ends). The second term is composed of the product of two factors. The first factor (pR/e) is equivalent to an average circumferential stress computed over the horizontal plane instead of the vertical (R instead of r). The last factor can be seen as a term dependent on the eccentricity of the elliptic cross-section and the position angle θ . Hence, axial stress, with an averaged value of $\sigma_z = \frac{pr}{2e}$ varies, depending on the position over the cross-section, according to the product of the equivalent average circumferential stress over the horizontal plane multiplied by the ellipse eccentricity and projected over the horizontal plane. Accordingly, for FSI, averaged axial stress can be described by:

$$\sigma_z = \frac{pr}{2e} \quad (4.23)$$

which is the same expression as for torus with circular cross-section (see Eq. 4.8)

Simplification for bending effect: As mentioned before, axial and circumferential stresses can be simplified to average values using reasonable assumptions according to the geometry of the coil system. To get average strain values from the bending effect, a different approach has to be chosen. The aim is to represent the increase of cross-section area when ellipticity is changed due to pressure changes. For this purpose, an equivalent radial expansion of the cross-section can be assumed and related with the $d_F - P$ expression determined in Subsection 4.2.4.

First of all, d_F must be related to the ellipse area for a fixed ellipse perimeter, secondly, the ellipse area can be related to an equivalent radius for a circular section and, finally, the empirical $d_F - P$ law can be embedded.

The ellipse properties are defined as follows:

$$\begin{aligned}
 d_F &= 2\sqrt{b^2 - a^2} \\
 A_{ellipse} &= \pi ab \\
 P_{ellipse} &= 2\pi\sqrt{\frac{b^2 + a^2}{2}}
 \end{aligned}
 \tag{4.24}$$

For known values of d_F and of the initial perimeter (P_0), the previous system of equations can be simplified obtaining the following expression:

$$A_{ellipse} = \pi\sqrt{\left(\frac{P_0}{2\pi}\right)^4 - \frac{1}{4}\left(\frac{d_F}{2}\right)^4}
 \tag{4.25}$$

Assuming the equivalent area for a circular section, the previous expression can be expressed in terms of radius:

$$r = \sqrt[4]{\left(\frac{P_0}{2\pi}\right)^4 - \frac{1}{4}\left(\frac{d_F}{2}\right)^4}
 \tag{4.26}$$

Eq. 4.26 can be further simplified applying a linearisation via Taylor series¹ with a centre point at d_F corresponding, in the case of the dynamic test, to the initial steady state before closing the valve:

$$r = 0.01 - 1.0567 \times 10^{-4} \cdot d_F
 \tag{4.27}$$

In terms of circumferential strain:

$$\epsilon_{\theta_2} = \frac{0.01 - 1.0567 \times 10^{-4} \cdot d_F}{r_0} - 1
 \tag{4.28}$$

¹ Taylor series:

$$f(x) = \sum_{n=0}^{\infty} \frac{f^{(n)}(a)}{n!} (x-a)^n$$

and for the analysed case:

$$f(d_F) = f(d_{F_0}) + \frac{f'(d_{F_0})}{1!} (d_F - d_{F_0}) + \frac{f''(d_{F_0})}{2!} (d_F - d_{F_0})^2 + \frac{f'''(d_{F_0})}{3!} (d_F - d_{F_0})^3 + \dots$$

Chapter 4. Fluid-structure interaction in coils

Finally, substituting the empirical expression found for d_F (Eq. 4.20) in Eq. 4.28, it yields:

$$\epsilon_{\theta_2} = -6.169 \times 10^{-7} + 6.626 \times 10^{-12} \cdot p \quad (4.29)$$

Simplified strain equations: Applying Hooke's law for isotropic materials (Eqs. 4.9 and 4.10) and the Boltzman superposition principle for circumferential strains, the final simplified equations, in terms of strain, are:

$$\epsilon_z = \frac{1}{E} \left(\frac{pr}{2e} - \nu \frac{pr}{e} \right) \quad (4.30)$$

$$\epsilon_{\theta} = \frac{1}{E} \left(\frac{pr}{e} - \nu \frac{pr}{2e} \right) - 6.169 \times 10^{-7} + 6.626 \times 10^{-12} p \quad (4.31)$$

Fluid wave celerity in a coil pipe: The fluid wave celerity inside of a coil with no anchorages can be obtained by deriving the basic conservation waterhammer equations, starting by Reynolds Transport Theorem and applying the specific stress-strain equations for a coil pipe.

Developing the mass conservation equation as explained at Chaudhry (2014) and with the update of the new circumferential strain equation (Eq. 4.31), the expression reached is:

$$\frac{\partial V}{\partial z} + \left(\frac{1}{K} + (2 - \nu) \frac{r}{Ee} + 1.3252 \cdot 10^{-11} \right) \frac{dp}{dt} = 0 \quad (4.32)$$

where K is the bulk modulus of elasticity of the fluid and z represents space in the axial direction.

and with the following definition

$$\frac{1}{\rho_f a_h} = \left(\frac{1}{K} + (2 - \nu) \frac{r}{Ee} + 1.3252 \cdot 10^{-11} \right) \quad (4.33)$$

the fluid wave celerity can be obtained:

$$a_h = \sqrt{\left[\left(\frac{1}{K} + (2 - \nu) \frac{r}{Ee} + 1.3252 \cdot 10^{-11} \right) \rho_f \right]^{-1}} \quad (4.34)$$

It should be highlighted that, in the previous Eq. 4.34, the constant value associated to the bending effect ($1.3252 \cdot 10^{-11} \frac{m}{Pa \cdot s}$) is specific of this case study and cannot be generalized for other pipe systems with different sizes, coil radii and pipe materials. The remaining terms can

be generalized to any pipe coil.

Finally substituting values according to the coil parameters the wave celerity obtained is 1261 m/s , while omitting the cross-sectional bending term the wave celerity would be 1274.5 m/s . For instance, for a rigid conduit, the celerity is 1480 m/s , for an elastic straight thin-walled pipe anchored against longitudinal movement in its upper end, $a = 1292 \text{ m/s}$ and, finally, allowing the movement in both boundaries, the celerity is 1260 m/s .

4.2.6 Validation of the simplified equations

4.2.7 Pipe displacements using the elliptic torus model and the simplified equations

In order to assess the effect of circumferential, axial and bending deformations in the context of hydraulic transients, pipe-wall displacements were first computed from the stress-strain model for the static pressure test. Fig. 4.13 depicts such displacements either over the cross-sectional and horizontal planes of the torus for a static pressure of $6 \times 10^5 \text{ Pa}$. For the sake of visual representation, strains have been amplified by a scale factor of 10 in regard to bending, 100 for circumferential strains and 10000 for axial strains.

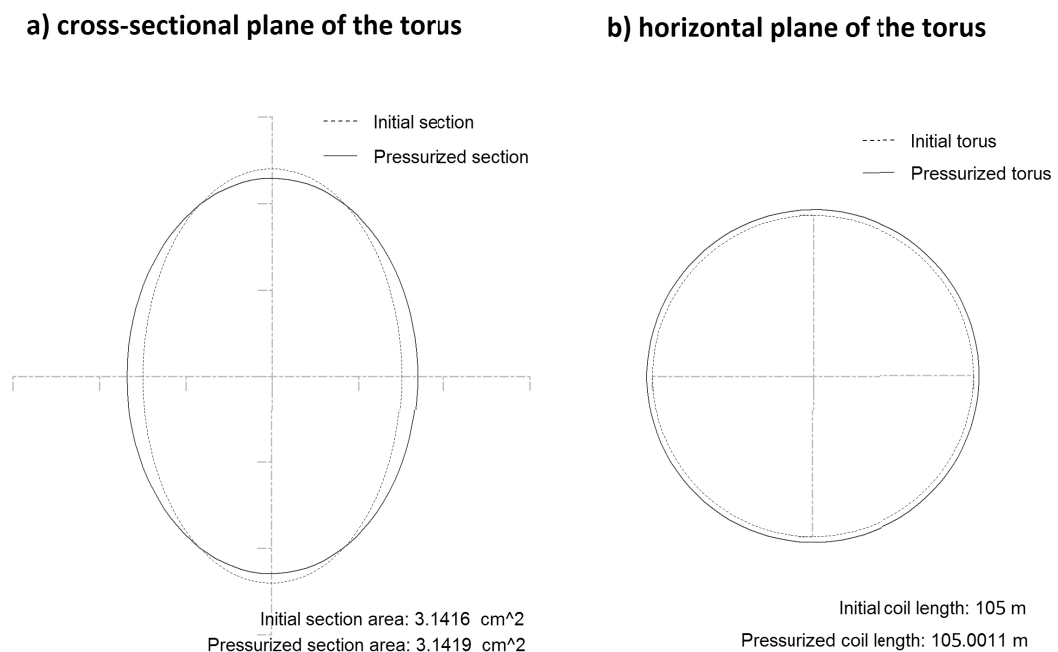


Figure 4.13 – Computed displacements of the pipe wall over the coil cross-section (left) and in the horizontal plane(right)

The total deformation of the pipe section and pipe length for the pressurized system has been

Chapter 4. Fluid-structure interaction in coils

computed in order to get an idea of the magnitude of circumferential and axial strain effects and also the cross-sectional shape change due to bending. The computation has been carried out for both, elliptic torus before and after simplification. Eqs. 4.35, 4.36 and 4.37 describe the volume variation either by circumferential, axial and bending deformations:

$$\Delta V_{\theta} = L \cdot \int_{\theta=0}^{\theta=2\pi} \epsilon_{\theta} \cdot \frac{1}{k^2(\theta)} d\theta \quad (4.35)$$

$$\Delta V_z = L \cdot \bar{\epsilon}_z|_{cs} \quad (4.36)$$

$$\Delta V_{d_F} = L \cdot \left(\pi \sqrt{\left(\frac{P_0}{2\pi}\right)^4 - \frac{1}{4} \left(\frac{d_F}{2}\right)^4} - A_0 \right) \quad (4.37)$$

where ΔV_{θ} is the volume change due to circumferential strain, ΔV_z due to axial strain, and ΔV_{d_F} due to bending effect, k is the curvature of the ellipse which is dependent on the angle θ , L is the total pipe length, P_0 is the initial perimeter of the cross-section and A_0 the initial area.

Results of the application of previous equations are shown in Table 4.1:

Table 4.1 – Volume change for a steady pressure of $6 \times 10^5 Pa$ (i.e. 60m)

	Non-simplified equations	Simplified equations	error
ΔV_{θ}	3.24×10^{-6}	3.11×10^{-6}	-4%
ΔV_z	3.60×10^{-7}	3.16×10^{-7}	-12%
ΔV_{d_F}	1.64×10^{-7}	2.19×10^{-7}	33%
<i>total</i> ΔV	3.76×10^{-6}	3.70×10^{-6}	-3%

In both cases, approximately 85% of the total volume variation when the pipe is pressurized corresponds to circumferential expansion of the conduit, 8 – 10% to the axial deformation and 4 – 6% to the bending of the cross-section. The volume variation inside the pipe is more sensitive to circumferential strain effect than to axial strain or bending effects, even though, these minor effects cannot be neglected. The simplified equations give similar results in comparison to the original elliptic torus equations.

Range of application

The first criterion to determine the range of application of the presented equations is the consideration of the limit between thin and thick pipe-wall. In the current study, Goldberg *et al.* (1974) criteria are assumed, in which thin and thick pipe-wall theories were compared for

circular cylinders submitted to inner pressure loads, concluding that for ratios $\frac{l}{e} > 10$ results using thin-walled assumption were satisfactory.

In the simplification of the equations in Subsection 4.2.5, two extra assumptions are taken: quasi-circular cross-section and quasi-straight pipe. As it was shown in Fig. 4.7, the circular torus assumption presents good average values of axial strains, while the quasi-straight pipe assumption only affects distribution of circumferential stresses over the cross-section, but not its average value. Therefore, in the context of 1D hydraulic transient modelling, where only averaged strain values are concerned, the elliptic eccentricity of the cross-section does not represent any constraint in regard to the range of validity of the proposed equations for axial and circumferential strains.

Additionally, the bending analysis carried out is only valid for the coil system analysed. The empirical relation between d_F and P (Eq. 4.20) must be redefined if structural conditions are changed. The presented equation for equivalent circumferential strain due to bending (Eq. 4.29) is valid only for the tested range of pressures (approx. 0 to 10^6 Pa), as the linearisation via Taylor series is centred in d_F corresponding to a non-pressurized system; consequently, the greater the amplitude of pressure range is, the greater the error will be.

4.2.8 Research outcome

Two stress strain models based on the theory of shells of revolution are presented to describe the stress-strain relationships in the cross-section of a coil pipe. A semi-empiric bending analysis has been carried out in order to improve the accuracy of the models.

Membrane theory of shells of revolution applied to an elliptic torus has been proven to be a good approach for the axial strain description but inaccurate with regard to circumferential strain. The main reason is that circumferential strains are strongly affected by a common singularity of coil pipes: the cross-section is slightly elliptic and bending moments are generated over the cross-sectional plane. In order to assess the bending effect and correct circumferential strains, a semi-empiric method has been proposed to determine an empiric law relating the ellipse focal distance with pipe inner pressure. The method enables the assessment of cross-sectional shape change and the correction of circumferential strains. The effect of the centrifugal force produced by the rotating flow within the coil has been also assessed, concluding that its effect is negligible in comparison to the inner pressure effect. Validation has been carried out for dynamic loading with the aim to ensure the final purpose of the research, FSI during hydraulic transients. Finally, for the sake of FSI implementation, a simplification of the proposed model is presented.

Displacement volumes have been computed for the static pressure concluding that the impact of the three effects (circumferential, axial and bending strains) are important to describe hydraulic transients in pipe-coils and they should be distinguished for FSI assessment. Circumferential and axial strains have to be described by Eqs. 4.4, 4.5, 4.9 and 4.10. Displacements

due to bending (i.e. cross-sectional shape change) can be directly obtained from the empirical law relating ellipse focal distance with pressure depicted in Eq. 4.20. The simplified version of the equations for FSI implementation is given in Eqs. 4.31 and 4.30. The range of validity of these equations, according to the membrane theory of shells of revolution, is subjected to thin-wall criteria (i.e. $\frac{t}{e} > 10$), while the presented bending analysis, due to its empirical nature, is only valid for the test facility and range of pressures assessed.

4.3 Fluid-structure interaction

4.3.1 Introduction and background theory

The present section focuses on the analysis of hydraulic transient flow in coil pipe systems. The aim is the characterization of the fluid-structure interaction (FSI) phenomena occurring between the pipe structure and the inner pressurized fluid. Three interaction mechanisms are analysed: the shear-stresses generated between the fluid and the pipe-wall, the axial movement of the pipe induced by its radial deformation during pressure surges and the pipe movement generated by an imbalance of forces at junctions and boundaries.

Although FSI occurs in any structure, it is important to have the right criteria in order to decide when and which FSI effects are actually relevant. For this purpose, the main FSI dimensionless parameters are (Tijsseling, 1996): the Poisson ratio of the pipe material (ν), the ratio between the pipe radius and the pipe-wall thickness ($\frac{t}{e}$), ratio between the solid and the fluid densities ($\frac{\rho_p}{\rho_f}$) and the ratio between the pipe Young's modulus and the fluid bulk modulus ($\frac{E}{K}$). Also Tijsseling (1996) stated that FSI may be of importance when fluid and solid wave celerities are of the same order of magnitude, provided that the transient excitation is sufficiently rapid. Therefore, the ratio between fluid pressure wave and solid stress wave celerities ($\frac{a_h}{a_3}$) must be considered as well. In the specific case of coil systems the ratio between coil radius and pipe radius ($\frac{R}{r}$) and the ratio between flow velocity and fluid wave celerity ($\frac{V_0}{a_h}$) have to be also taken into account (Ferràs *et al.*, 2014).

Fluid-structure interaction is a complex problem that is highly dependent on the pipe layout. Generalization is not presently possible, and FSI calculations have to be treated on a case-by-case basis (Wiggert & Tijsseling, 2001). Pipe coils deform in a three-dimensional space with several degrees-of-freedom: deformation in the circumferential and axial directions, flexion in the cross-sectional plane and along the pipe axis, torsion, shear, etc. Hence, for a full description of the FSI of a pipe coil during hydraulic transients a multi-mode model is required.

Tentarelli (1990) carried out FSI coupling in order to account for the Bourdon effect during waterhammer events, which occurs in curved fluid-filled tubes of non-circular cross-section (Tijsseling, 1996). The structural constraint conditions of the pipe coil, though, do not comply with the Bourdon tube theory, as Bourdon tube is a disconnected torus with closed ends,

while the pipe coil analysed herein must be considered as a connected torus (Ferràs *et al.*, 2014). Also, Anderson & Johnson (1990) analysed the effect of tube ovaling on pressure wave propagation speed in the context of physiological flows, though, Ferràs *et al.* (2014) showed that, for the coil case of study, the slight ovality of the cross-section is negligible.

Radial inertia, flexure and torsion are neglected in the present research and the fluid-structure interaction in the coil system is described by a four-equation model. Such assumption is based on a previous study (Ferràs *et al.*, 2014) where stress-strain laws were derived for coils loaded by static inner pressure. It could be shown that torsional and bending movements in a pipe coil are negligible in comparison to axial or circumferential displacements. Moreover, Ferràs *et al.* (2014) also concluded that the axial stress generated for the inner pressure load is equivalent to the axial stress produced in a free moving straight pipe with closed ends. Additionally the numerical solutions analysed include Brunone's unsteady skin friction computation and Coulomb's dry friction.

The novelty of this study is the description, analysis and discussion of the FSI occurring in pipe coils by three one-dimensional conceptual models using a four-equation solver: the first model simplifies the problem to a straight pipe with a moving end; the second is an analogue mechanical model composed of a straight pipe with moving side pipe segments describing the independent movement of each ring; finally, a third model is similar to the second but assuming the vibrating rings are fully damped at each time-step. Unsteady skin friction and dry friction have been included in the last model as dissipating mechanisms.

4.3.2 Data collection

The downstream boundary of the copper coil pipe facility (CCP) is equipped with a spherical valve that allows the generation of waterhammer events by a fast manual valve closure, with an effective closing time $t_v = 0.025$ s, much lower than the half of the experimental wave period ($T = 4L/a_h = 0.35$ s) for an experimental wave celerity $a_h = 1193$ m/s.

Several dimensionless parameters indicate when FSI effects might be important as referred in Subsection 4.3.1. The values of these parameters for the copper coil facility are presented in Table 4.2:

Table 4.2 – Dimensionless parameters for the experimental facility

ν	a_h/a_3	r/e	ρ_p/ρ_f	E/K	R/r	V_0/a_h
0.33	0.368	10	8.96	47.95	50	0.00028

The pressure histories at the downstream and midstream pipe sections for the experimental tests carried out in the coil facility are presented in Fig. 4.14.

Fig. 4.15 depicts measured piezometric head immediately upstream the valve in comparison with the numerical results obtained by the classic waterhammer model for an initial flow rate

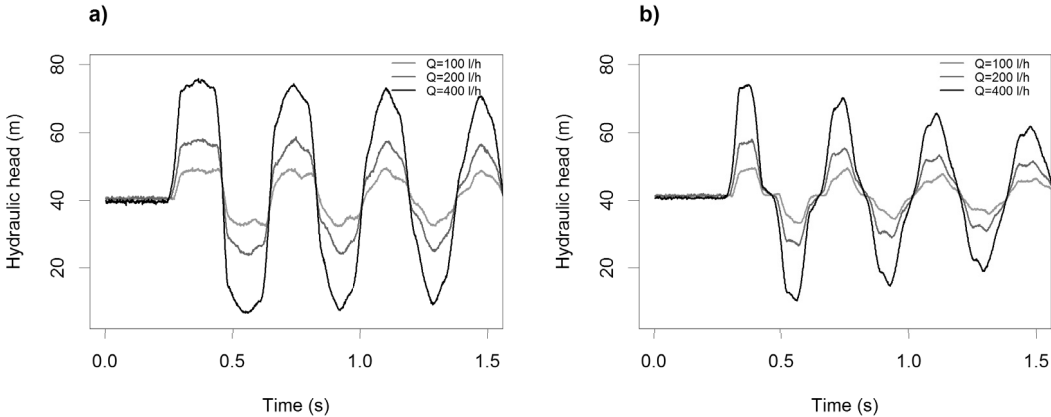


Figure 4.14 – Measured hydraulic head at the downstream (a) and midstream (b) pipe positions for the transient tests carried out in the experimental facility.

$Q_0 = 400 \text{ l/h}$. The wave amplitude is significantly overestimated by the classic model. The present study tries to reduce this overestimation by assuming that its source is the structural behaviour of the coil pipe system as well as the movement of the downstream end valve.

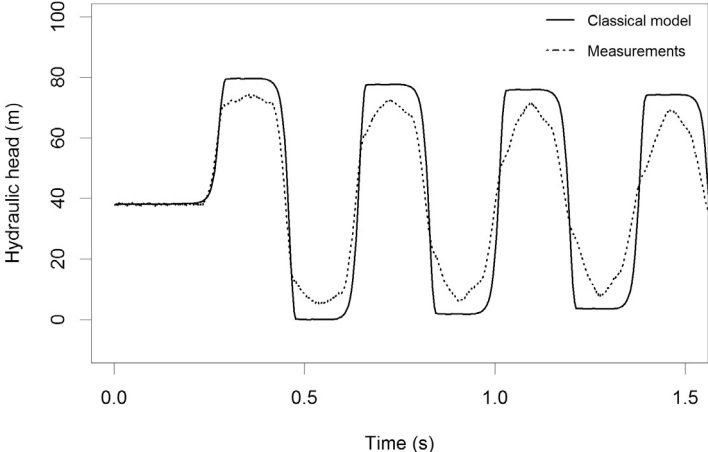


Figure 4.15 – Measured hydraulic head at the downstream boundary in comparison with the classic waterhammer theory solution for a fast hydraulic transient generated after an initial discharge $Q_0 = 400 \text{ l/h}$.

4.3.3 Model development

Characteristic grid in a four-equation model

The set of partial differential (Eqs. A.47) are transformed to ordinary differential equations (compatibility equations) by applying the method of characteristics (MOC). Resulting equations can be easily integrated over a characteristic grid.

However, in a four-equation model two different waves propagate with different celerities over the same characteristic grid: fluid pressure wave and solid stress wave. Two main approaches can be used: wave celerity adjustment in order to keep Courant numbers equal to one by achieving a ratio between celerities of integer numbers, as suggested by Schwarz (1978), Wiggert (1986) or Bergant *et al.* (2008b); or by applying either temporal or spatial interpolation over the grid, as followed, for example, by Fan (1989), Elansary & Contractor (1990), Bouabdallah & Massouh (1997) or Ghodhbani & Hadj-Taïeb (2013). Tijsseling (2003) proposed a third approach, namely the resolution of an exact solution by means of a mathematical recursion. Methods based on interpolations introduce numerical dispersion and diffusion, while the exact solution is feasible only for verification and validation, since for large simulation times it is time consuming. The method applied herein is based on the celerities adjustment, though, special attention was given on validation, as this method introduces phase shift in the transient pressure wave.

For instance, when computing the theoretical wave celerities in the copper facility (see characteristics in Table 4.2), the celerities obtained are 3423 *m/s* for the solid stress wave and 1261 *m/s* for the fluid pressure wave. To adjust the characteristic lines in the numerical grid two different integer numbers ratio were tested $\frac{a_f^*}{a_s^*} = \frac{1}{3}$ (being $a_f^* = 1141$ *m/s* for $a_s^* = 3423$ *m/s*) and a more accurate $\frac{a_h^*}{a_p^*} = \frac{4}{11}$ (being $a_h^* = 1245$ *m/s* for $a_p^* = 3423$ *m/s*). Inevitably such adjustment leads to a small phase error resulting from the adjusted fluid wave celerity. To minimize the error with respect to the theoretical wave celerity the ratio retained for the model application was $\frac{a_h^*}{a_p^*} = \frac{4}{11}$.

Fluid and solid densities were corrected according to the modified celerities applying the following equations (Lavooij & Tijsseling, 1991):

$$\rho_p^* = k_1 \frac{(a_h^{*2} + a_p^{*2}) + \sqrt{(a_h^{*2} + a_p^{*2})^2 - 4(1 + k_1 \frac{k_3}{k_2} a_h^{*2} a_p^{*2})}}{2(1 + k_1 \frac{k_3}{k_2}) a_h^{*2} a_p^{*2}} \quad (4.38)$$

$$\rho_p^* = k_2 \frac{(a_h^{*2} + a_p^{*2}) - \sqrt{(a_h^{*2} + a_p^{*2})^2 - 4(1 + k_1 \frac{k_3}{k_2} a_h^{*2} a_p^{*2})}}{2a_h^{*2} a_p^{*2}} \quad (4.39)$$

Chapter 4. Fluid-structure interaction in coils

where ρ_f^* is the adjusted fluid density and ρ_p^* the adjusted solid density, a_h^* and a_p^* the modified wave celerities, and k_i are parameters given by: $k_1 = (\frac{1}{K_f} + \frac{2R}{e} \frac{(1-\nu^2)}{E})^{-1}$, $k_2 = E$ and $k_3 = 2\nu^2 \frac{R}{e}$.

The adjustment of wave speeds allows calculations to lie in the grid points. However, in the boundaries and in their vicinities, temporal or spatial interpolations are unavoidable. Temporal interpolations were carried out herein as shown in Fig 4.16.

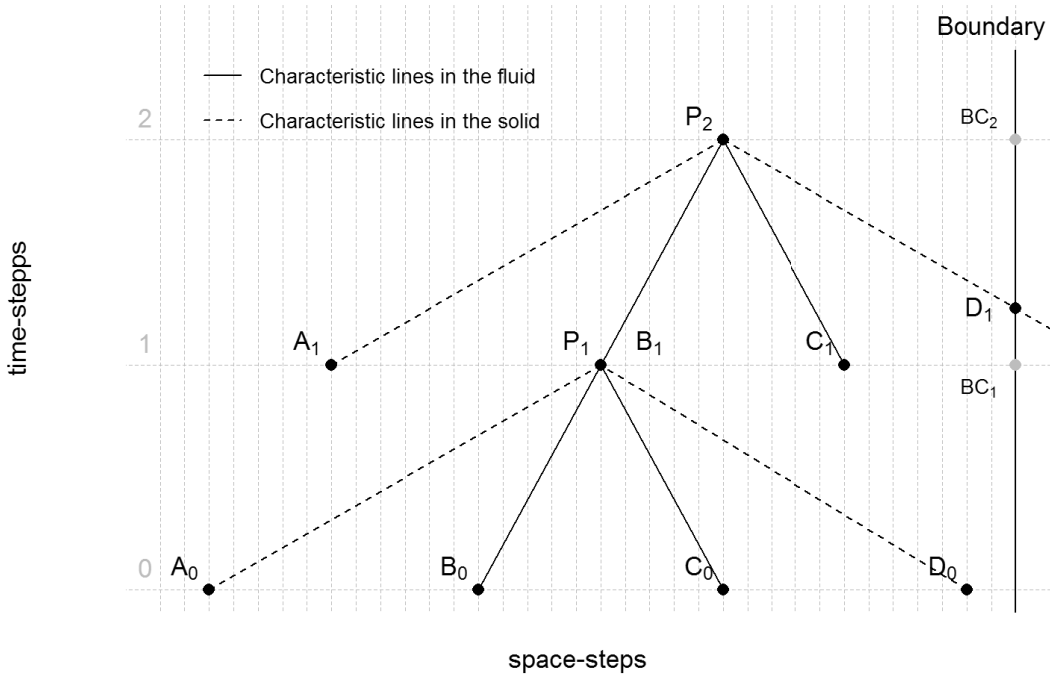


Figure 4.16 – Scheme of the characteristic lines for the wave celerities adjustment $\frac{a_h^*}{a_p^*} = \frac{4}{11}$.

Boundary conditions and junction coupling

For a reservoir-pipe-system, the boundary conditions for the fixed infinite reservoir at the upstream boundary are

$$\begin{cases} p[0, j] = p_{res} \\ U_z[0, j] = 0 \end{cases} \quad (4.40)$$

while for a fixed valve at the downstream boundary they are

$$\begin{cases} U_z[l, j] = 0 \\ V[l, j] = \tau(t) \sqrt{\frac{\Delta p}{\rho_f g}} \end{cases} \quad (4.41)$$

where $\tau(t)$ is a function describing the valve closure, the coefficients in the squared brackets correspond to space and time coordinate, 0 stands for the upstream boundary and l for the downstream boundary, j for the time-step, and p_{res} is the pressure in the reservoir.

For a boundary condition of a moving valve, the balance of forces must take into account the movement of the valve. Hence, the second law of Newton is applied, describing the rate of change of momentum at the valve as the unbalance of forces over the valve between the fluid pressure and the pipe-wall stress:

$$\Delta p A_f - \sigma_z[l, j] A_p = m_v \dot{U}_z[l, j] \quad (4.42)$$

The resulting movement of the pipe induces an axial stress wave that propagates throughout the pipe (junction coupling). Nevertheless, assuming static conditions, Ferràs *et al.* (2014) showed that the axial stress in a toroidal pipe due to inner pressure is equivalent to the axial stress of a non-anchored straight pipe with closed ends, being $\sigma_z[l, j] = \frac{p r}{2e}$, which corresponds to Equation 4.42 considering a massless valve. However, in dynamic conditions, the inertia of the moving element must be taken into account. By rearranging Equation 4.42 and considering the change of flow rate due to valve closure, the following boundary conditions are obtained:

$$\begin{cases} \sigma_z[l, j] = \frac{A_f \Delta p}{A_p} - \frac{m_v}{A_p} \dot{U}_z[l, j] \\ V[l, j] - U_z[l, j] = \tau(t) \sqrt{\frac{\Delta p}{\rho_f g}} \end{cases} \quad (4.43)$$

The implemented four-equation solver is successfully verified at Appendix C by means of Delft Hydraulics FSI benchmark problems from Tijsseling & Lavooij (1990) and Lavooij & Tijsseling (1989).

4.3.4 Modelling approaches

Modelling assumptions

The coil pipe system, when pressurized, increases the fluid volume due to both the axial and the circumferential deformation of the pipe-wall. Conversely, for negative pressures, the pipe reduces its fluid volume. In coil-pipes, due to the axial deformation, this effect is stronger than in straight pipes with anchored boundaries. The consequent response of such "breathing" effect of the coil over the hydraulic transient wave is a smoothing of the pressure peaks, resulting on a reduction of the wave amplitude.

Axial strains of a pipe coil for inner pressure loads in static conditions can be assumed to be equivalent to the ones of a straight pipe with closed ends, though, with a modified wave celerity (Ferràs *et al.*, 2014). In the cited paper also the additional axial stress produced by the centrifugal force of the rotating inner fluid throughout the coil was assessed concluding that it is negligible for the given ratio between the torus radius and the pipe radius (R/r)

Chapter 4. Fluid-structure interaction in coils

(Ferràs *et al.*, 2014). Also the curvature in the coil pipe affects the velocity profile and consequently the friction losses. Based on Blasius formulation Di Liberto *et al.* (2013) proposed a formula to compute Darcy friction factor taking into account the curvature in serpentine pipes ($f = 0.304Re^{-0.25} + 0.029\sqrt{r/R}$). As in the copper coil facility $0.304Re^{-0.25} \gg 0.029\sqrt{r/R}$, the additional friction losses due to the pipe curvature can be neglected and friction factor computed by Blasius formulation for both facilities. In the present study the interaction between the pipe and the supporting structure is as well neglected, *i.e.* there is no transfer of momentum or friction between the pipe-wall and the pipe-supports.

Three models have been developed for describing the pipe coil behaviour. Basic assumptions for model conceptualization and discretization are depicted in Table 4.3.

Table 4.3 – Main modelling assumptions for the simulation of the coil system.

Model parameter	Model-1	Model-2	Model-3
Solver	four-equation	two and four-equation	two-equation adjusted
Geometry	Single straight pipe	Multi-pipe system	Single straight pipe
Moving elements	Valve	Coil rings	–
Celerities ratio (a_h/a_3)	4/11	4/11	–
Modified fluid celerity (a_h^*)	1245 m/s	1245 m/s	1141 m/s
Modified solid celerity (a_3^*)	3423 m/s	3423 m/s	–
Time-step (dt)	0.0025 s	0.0025 s	0.0025
Space-step (dx)	2.83 m	2.83 m	2.83 m

Model-1: straight pipe with moving valve

Model-1 corresponds to a four-equation model presented in Subsection 4.2.3, in the present section it is used to describe the transient pressures in the coil copper facility. A reservoir-pipe-valve system with a free moving valve was considered, describing the “breathing” effect of the coil through the axial deformation of the straight pipe.

Model-1 has the following characteristics: pipe length of $L = 105\text{ m}$, pipe inner diameter $D = 2\text{ cm}$, pipe-wall thickness $e = 1\text{ mm}$, modulus of elasticity $E = 105\text{ GPa}$, fluid bulk modulus $K = 2,19\text{ GPa}$, fluid density $\rho_f = 1000\text{ kg/m}^3$, solid density $\rho_p = 8960\text{ kg/m}^3$, Poisson ratio $\nu = 0.33$, initial flow velocity $V_0 = 0.354\text{ m/s}$ and initial Darcy friction factor $f = 0.035$ (smooth wall pipe). Brunone’s unsteady friction computation has been taken into account during the transient state using a reynolds dependent decay coefficient k .

Fig. 4.17 depicts the model results for a moving massless valve in comparison with the classic waterhammer solution.

Piezometric head obtained by the four-equation model, although being smoothed due to the non-instantaneous closure of the valve, is subdivided into three stages (see Fig. 4.17b): Stage-1 in which the pressure is lower than the classic two-equation model; Stage-2 with higher pressure and; finally, Stage-3 with a pressure decrease. The first pressure drop is caused by the

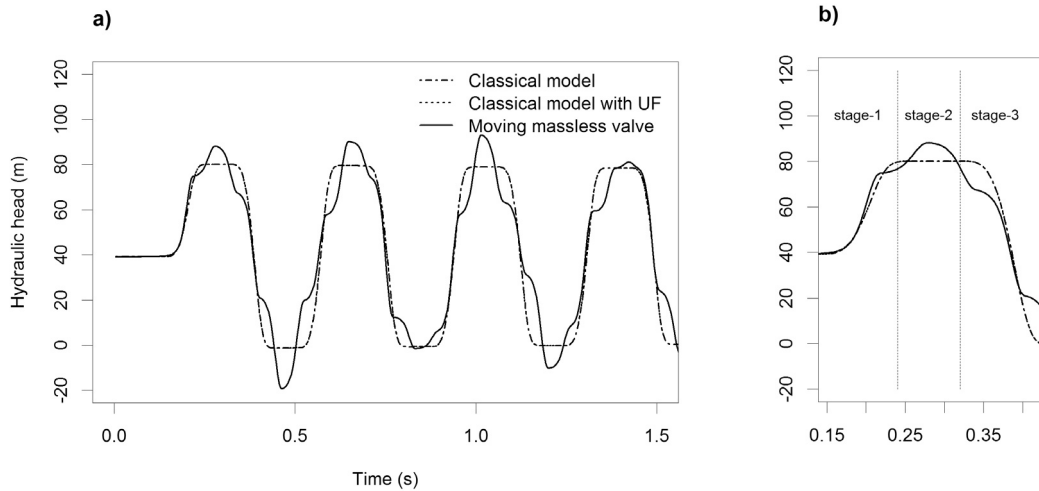


Figure 4.17 – Results of Model-1: a) simulated piezometric head at the pipe downstream end for a free moving massless valve versus results of classic waterhammer solver; b) detail of the first peak. Notice that the pressure traces corresponding to the classic model with steady and unsteady friction are almost overlapped.

movement of the valve in the downstream direction after the first pressure surge. Afterwards, as the solid axial stress wave travels approximately 3 times faster than the fluid pressure wave, at around one third of the pressure peak there is an increase of pressure resulting from the negative axial stress which is pulling the pipe upwards, producing this “pumping” effect. Finally, the axial stress wave bounces back pushing again the valve and producing the last pressure drop over the pressure surge. Unsteady friction hardly affect pressure traces in the one-mode model (as shown in Fig. 4.17), and the transient is highly dominated by FSI.

In order to assess the effect of the moving valve, a sensitivity analysis has been carried out for the valve mass (m_v). A set of 100 simulations from $m_v = 0$ kg until $m_v = 1000$ kg was carried out.

The range of possible solutions of the four-equation model for a free moving valve of variable mass are shown in Fig. 4.18. The bold dashed line indicates the solution for the minimum valve mass threshold modelled, which is equal to the already presented massless valve solution. The dotted line depicts the output for the maximum valve mass threshold modelled, which is $m_v = 1000$ kg. As the mass valve increases, results tend to the solution of Poisson coupling with a fixed valve. It is interesting to point out that, due to the dispersion effect of the mass valve, the maximum pressure peak does not occur for an infinite mass valve (fixed valve) nor for a massless valve, but for a solution in-between.

In order to determine the best simulation, the Mean Squared Error (MSE) was computed for the first pressure peak (within the time slot 0.2 to 0.5 s, see Fig. 4.18-b) as a function of the mass valve variation. The lowest MSE corresponds to a valve mass $m_v = 121$ kg, which does not

Chapter 4. Fluid-structure interaction in coils

correspond to the valve actual weight (as the valve is quite small, weighting 300 *gr*), however it represents the valve constraints as the valve and the pipe at the downstream end are fixed to a metal frame (not rigidly anchored).

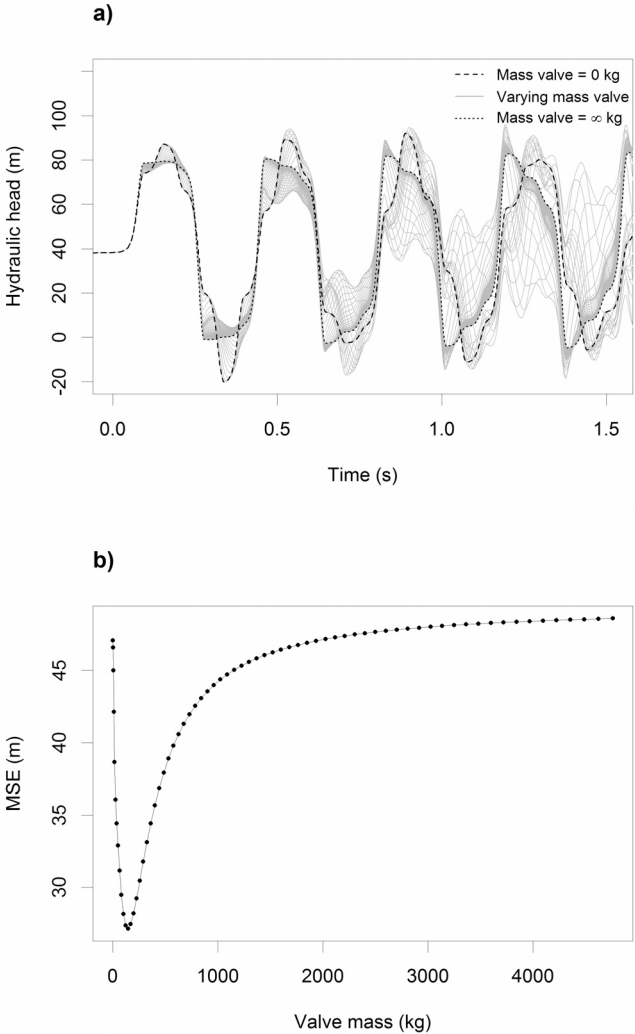


Figure 4.18 – Feasible solution region of Model-1 output for a free moving valve with variable mass (a); and Mean Square Error (MSE) values computed for the first pressure peak taking as reference experimental observations (b).

Model-2: analogue mechanical model

In order to better describe the observed structural behaviour of the pipe coil during the transient pressure wave propagation, an analogue mechanical model was build using the four-equation FSI model. The approach applies the concept that the rings of the coil vibrate independently from each other according to their inner pressure load in each time-step.

To describe these independent vibrating rings two sorts of models were combined: 1) a main two equation model representing a straight pipe with a total length of $L = 105\text{ m}$, discretized by 38 nodes with each inner node representing a coil ring; and 2) 36 four-equation sub-models describing the rings behaviour. These FSI sub-models were built as straight pipes of length equal to the ring perimeter (i.e., 2.83 m) and with closed free moving ends. The valve in the main pipe is fixed. The model is schematically shown in Fig. 4.19.

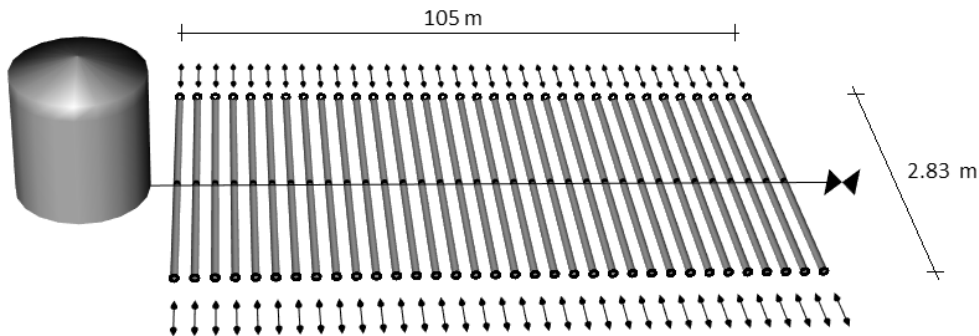


Figure 4.19 – Model-2: independent vibrating rings described by FSI sub-models which assume straight pipes with closed free moving ends.

The coupling is carried out by considering the centre node of the ring models as the inner node of the main system. In each time-step, the pressure of the rings is equal to the pressure of the entire submodels, consequently the free moving ends stretch or shrink the pipes and describe such ring behaviour. This effect produces an increase or decrease of pressure which is transferred to the main pipe. The effect of the moving closed ends can be calibrated by adding inertia to the pipe boundaries (i.e. varying the mass of the extreme ends of the pipe segments representing the coil rings). Finally, velocity must be recomputed in each time-step and each node of the main system.

A calibration sequence is carried out in Model-2 by a three steps procedure. First, the overall mass of the coil rings is analysed considering the mass is homogeneously distributed throughout the coil. Then a sensitivity analysis allows the understanding of the effect of the mass distribution on the coil rings. Finally a manual calibration was carried out with the goal to fix the best mass distribution.

Sensitivity analysis: First, a set of simulations was carried out by equally varying the mass of all rings, from $m_r = 0\text{ kg}$ to $m_r = 40\text{ kg}$ with the aim of assessing the sensitivity of model output to the rings inertia. For this set of simulations Fig. 4.20 show the solution band for the varying mass in the rings. As it can be observed, the proposed mechanical model allows a good adjustment of the pressure peaks by considering the independent expansion and contraction of the rings. The simulation with the best fitting to measurements (i.e. lowest MSE) was selected from the sequence presented above. The calibration process consisted of distributing

Chapter 4. Fluid-structure interaction in coils

a varying mass throughout the coil rings in order to get the best fitting for the first pressure peak. For this purpose, in a second step, a sensitivity analysis of the mass distribution in the rings was carried out (Fig. 4.20-b). The analysis consisted of a set of simulations by enabling the free movement of massless rings throughout the coil except one fixed ring. Each ring was assessed. A total of 36 simulations was carried out. The output allowed the analysis of the effect of the fixed ring over the pressure output. Fig. 4.21 depicts hydraulic head during the first peak for the mentioned set of simulations.

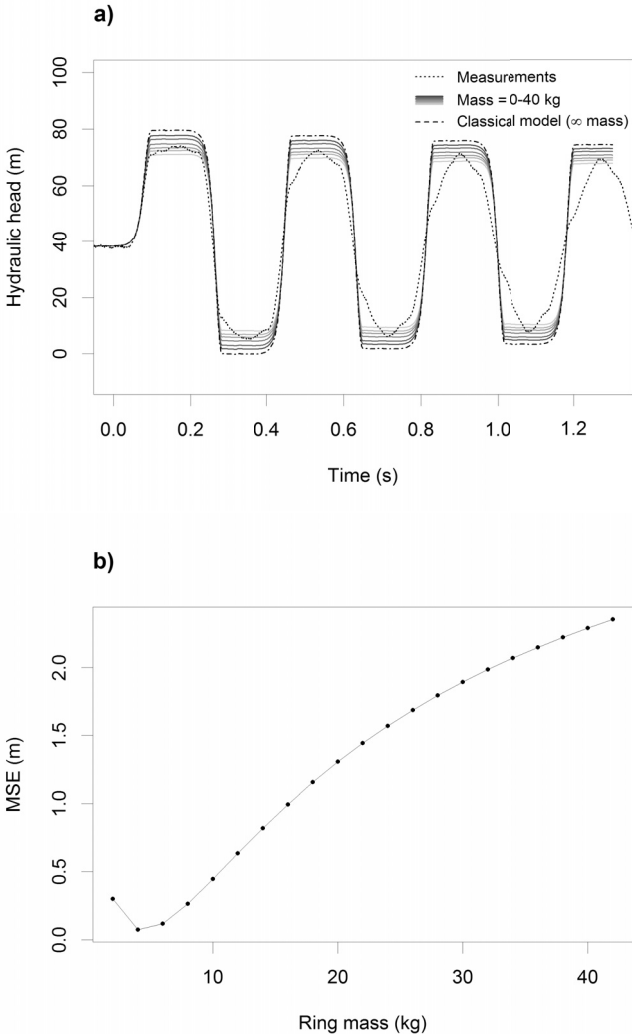


Figure 4.20 – Model-2 output considering a varying mass of the rings in comparison with measured pressure data at the downstream end (a); and Mean Square Error (MSE) values as a function of ring mass variation computed for the first pressure peak taking as reference experimental observations (b).

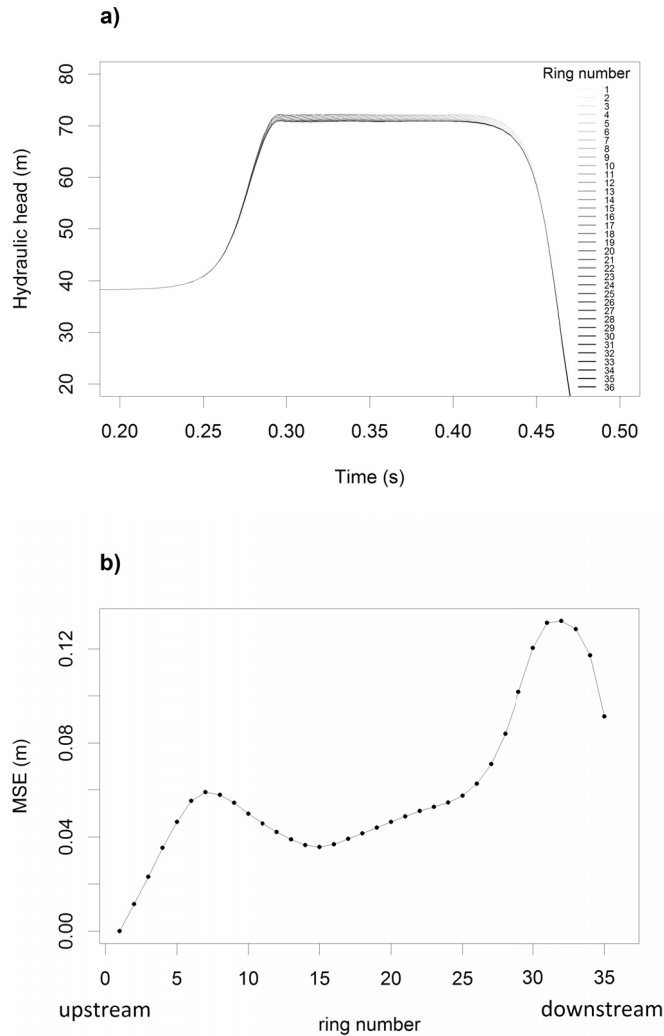


Figure 4.21 – Model-2 output (a) of the first pressure peak for a set of simulations by allowing the free movement of the rings except one. The position of the fixed ring is changed in each simulation (1 = upstream ring; 36 = downstream ring). Mean Squared Error (b) computed taking as reference the massless rings solution.

The sensitivity of the model to the mass ring distribution is shown in Fig. 4.21-b presenting the computed MSE by taking as reference the solution of massless rings throughout the coil. Thereby, the lower MSE is, the closer the model output is to the massless rings solution, and consequently, the lower is the sensitivity of the model to the fixed ring.

Calibration: Fig. 4.21-b depicts the closer to the upstream boundary the rings are, the less sensitive is the model to the ring movement. Finally, taking into account this sensitivity analysis and based on the best ring mass of Fig 4.20-b (*i.e.* 2.9 kg), a manual calibration was

Chapter 4. Fluid-structure interaction in coils

carried out by distributing the mass over the rings with the purpose to get the best fit for the first pressure peak. Fig. 4.22 shows the distribution of mass over the rings after calibration. Calibrated mass rings aim to describe different supporting stiffness and the consequent independent movement.

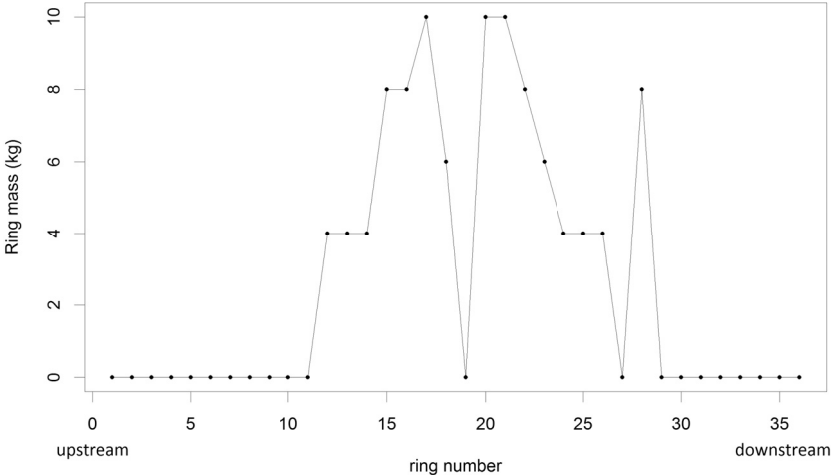


Figure 4.22 – Mass distribution of the rings throughout the coil after calibration.

As it can be seen in Fig. 4.23, results from the simulation with homogeneous mass load are quite accurate in regard to the wave amplitude and phase, however this simulation does not describe the wave shape, being quite similar to the classic theory.

On the other hand, the model calibration by distributing the mass loads allows a very good fitting in the first pressure peak. However, the achieved wave shape remains quite stable over the propagated pressure peaks.

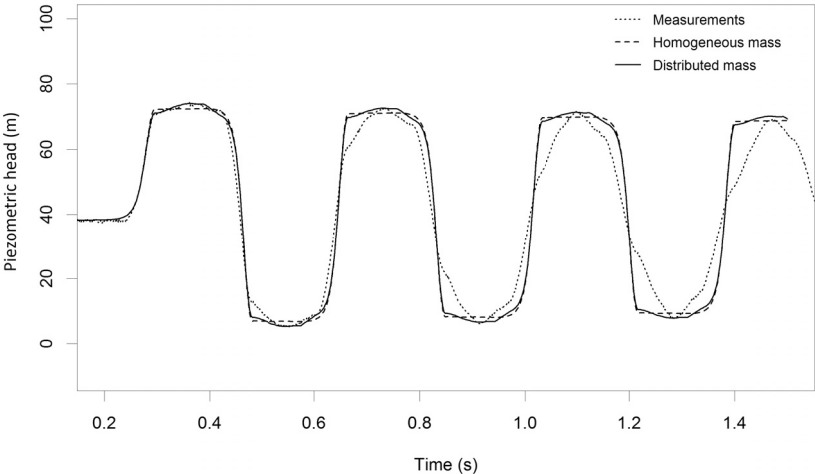


Figure 4.23 – Model-2 output after calibration, either with homogeneous rings mass or distributed, and in comparison with measured pressure data at the downstream end.

Model-3: 1-mode adjusted model

A third model has been developed considering that the vibration of the coil rings is highly damped by the dry friction between the pipe and its supports, their viscoelastic behaviour, and the transfer of momentum between the pipe and its supporting structure. As defined by Chaudhry (2014): “a transient-state is that intermediate-stage when the conditions are change from one steady-state condition to another steady-state”. In the coil pipe system the transient flow is coupled with the transient vibration of the rings. The first vibrates at a frequency of 2.7 Hz while the latest at 272.4 Hz. Considering this higher vibration of the coil rings and the aforementioned damping mechanisms it is legitimate to assume that at the vibration of the coil rings fully develop their final steady-state at each fluid wave cycle. Therefore, in Model-3 implementation the pipe rings deform following the inner pressure loading by means of a quasi-steady assumption and applying stress-strain relations. At each time-step, the two-mode vibration of the coil rings is assumed to reach the final steady-state.

According to Model-2, the final steady-state of the second pipe vibrating mode corresponds to null flow and pipe-wall movement. Hence, to compute the pressure variation caused by the coil breathing effect, the following conditions are imposed for the second oscillation mode, at every node and time-step:

$$V_i^j = 0 \tag{4.44}$$

$$U_{z_i}^j = 0 \tag{4.45}$$

A third condition is added to the model, coming from the stress-strains relations given by the balance of forces of inner pressure, axial stress and dry friction at the pipe supports. The model domain is discretized in 36 nodes, each node represents a coil ring and the pipe supports are embedded at each node. Fig 4.24 depicts the balance of forces carried out at each node.

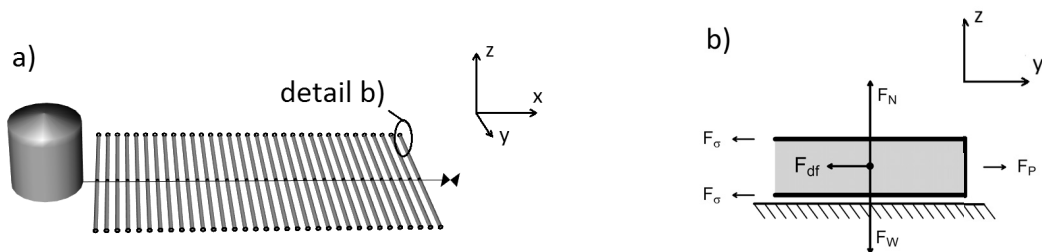


Figure 4.24 – Schematic of Model-3: (a) general overview and (b) detail of balance of forces carried out at the end of the pipe-segments.

Chapter 4. Fluid-structure interaction in coils

From this balance the axial stress in the coil rings is obtained as a function of the inner pressure increment:

$$\sigma_{z_i}^j = \frac{A_f}{A_p} (p_i^j - p_i^{j-1}) - \frac{\mu \cdot g \cdot m_r}{A_p} \quad (4.46)$$

Substituting Eqs. 4.44, 4.45 and 4.46 into the compatibility equations of the two-mode solver, the updated pressure is obtained by means of the following implicit equation:

$$p_{i_{k+1}}^j = p_{i_k}^j + \frac{\frac{2 \cdot v \cdot \frac{a_h^2}{a_3^2}}{\rho_p \cdot a_f \left(1 - \frac{a_h^2}{a_3^2}\right)} \left[\frac{A_f}{A_p} (p_{i_k}^j - p_i^{j-1}) - \frac{\mu \cdot g \cdot m_r}{A_p} \right] + C_{n_f}}{\frac{1}{\rho_f \cdot a_h} + v^2 \frac{D}{e} \frac{1}{a_h \cdot \rho_p} \frac{\frac{a_h^2}{a_3^2}}{1 - \frac{a_h^2}{a_p^2}}} \quad (4.47)$$

where the term C_{n_f} is known and depends on the values of the dependent variables at the previous time-step (Lavooij & Tijsseling, 1991). After few iterations the correction of pressure due to the breathing effect of the coil rings, at every node and for each time-step, is obtained by means of Eq. 4.47.

The setting up of the model consists of fixing the mass of the coil rings, which is calculated according to pipe geometry and material densities, and assuming variable Coulomb's static (μ_s) and kinetic (μ_k) dry friction coefficients. These coefficients represent the anchoring conditions of the coil rings. The coil rings are allowed to move if the static dry friction force is exceeded; when this happens, the pressure at a node is corrected using Eq. 4.47 and considering the kinetic Coulomb's coefficient.

Fig. 4.25 depicts a sensitivity analysis carried out by modifying, homogeneously, the dry friction coefficient, and considering it constant at every dead-end node.

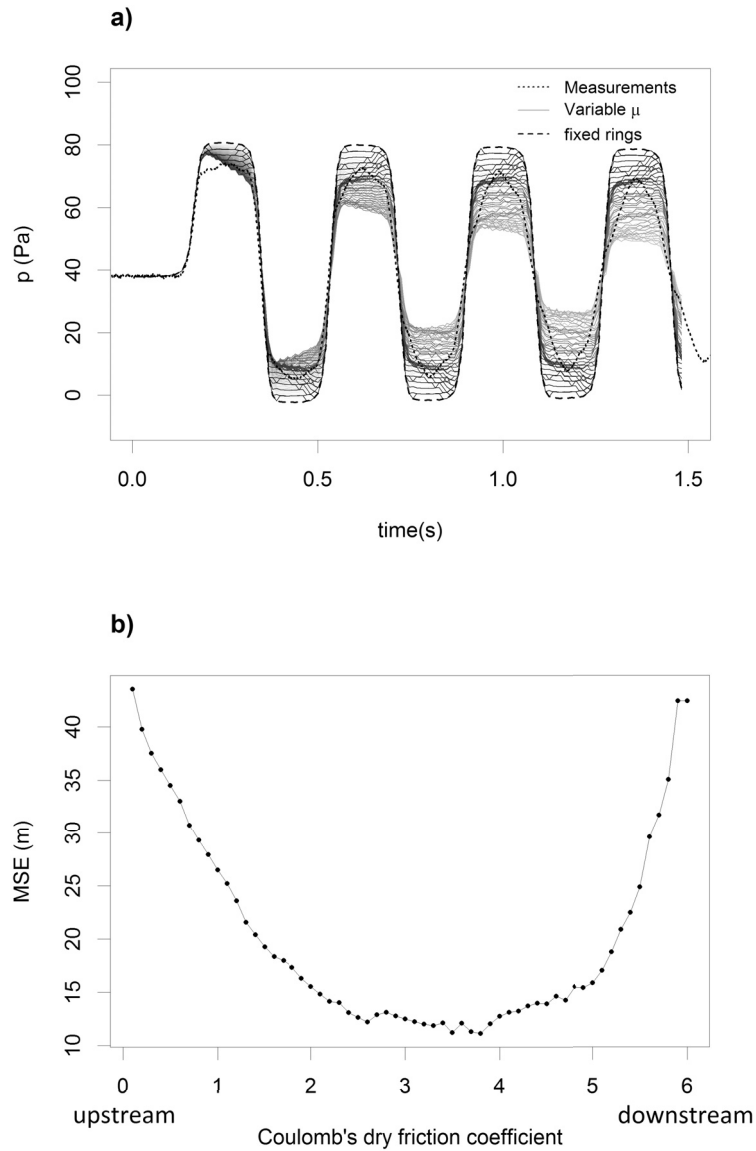


Figure 4.25 – Model-3 output (a) for a set of simulations varying the Coulomb’s dry friction coefficient. (b) Mean Squared Error computed taking as reference the measurements.

Finally, a manual calibration by adjusting, node by node, static and kinetic dry friction coefficients is carried out. Fig. 4.26 depicts the value of the calibrated parameters along the pipe and Fig. 4.27 shows the respective model output. Note that node-1 is the closest to the upstream and node 35 to the downstream. As expected, calibrated coefficients closer to the downstream boundary are higher as transient pressures increase to downstream and consequently, the breathing effect of the coil and dry friction are higher as well. The sensitivity of the model to the friction coefficient values located from midsection to upstream is very low, hence the

linear variation is not representative of any law in the dry friction distribution.

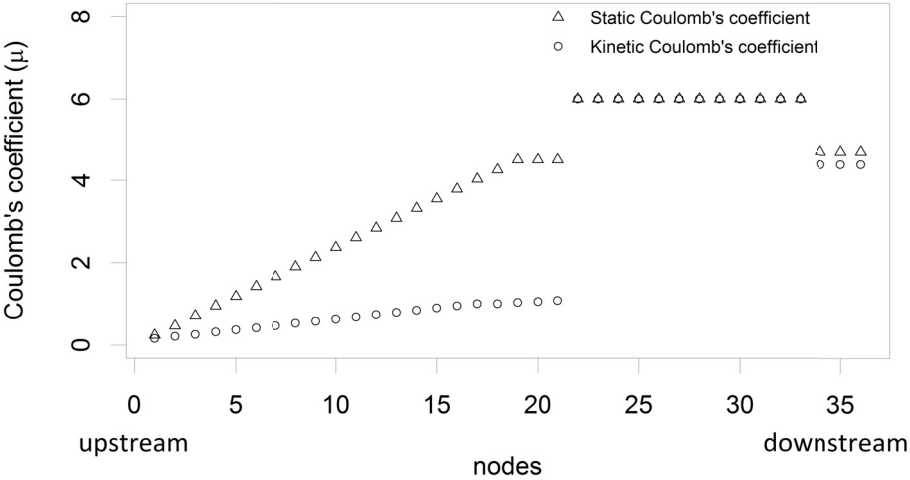


Figure 4.26 – Distribution of Coulomb's friction coefficients, kinematic and static, along the pipe rig.

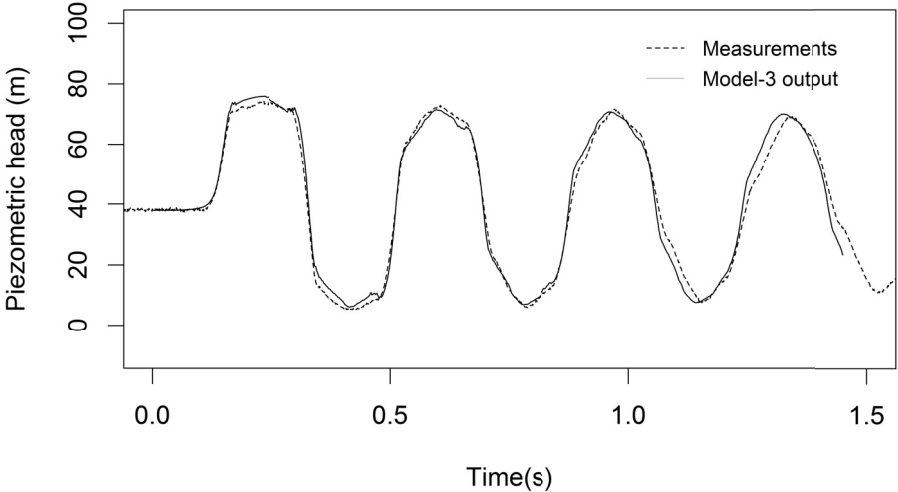


Figure 4.27 – Model-3 output after calibration (according Fig 4.26) *v.s.* experimental data at the downstream end section.

As result of the simplification of the model and the inclusion of dry friction dissipation an accurate fitting can be observed in Fig. 4.27. The coil breathing effect is well described, not only by the systematic reduction of the wave amplitude but also by the wave shape during the transient event.

4.3.5 Results discussion

The three implemented models, assuming different modelling assumptions, lead as well to different numerical results. Figs. 4.28 and 4.29 show the results of the best simulations of the three models respectively at the downstream and midstream pipe sections. The best simulation of Model-1 corresponds to a valve mass of $m_v = 121 \text{ kg}$, with a $MSE = 127.31 \text{ m}^2$ at the downstream section and for the simulation period of 1.5 s. The best simulation of Model-2, with a $MSE = 32.73 \text{ m}^2$, corresponds to the mass distribution over rings presented in Fig. 4.22 (total mass of 100.8 kg over the entire coil). Both mass values are of the same order of magnitude and are in accordance with the real mass of the coil system, which is 95 kg ; this represents actually the real inertia that both models aim to simulate. Finally, the best simulation of Model-3 corresponds to the real mass of the system with the calibrated Coulomb's dry friction coefficients of Fig. 4.26. The much lower MSE of Model-3 suggests its modelling assumptions are more faithful to the physics of the real system.

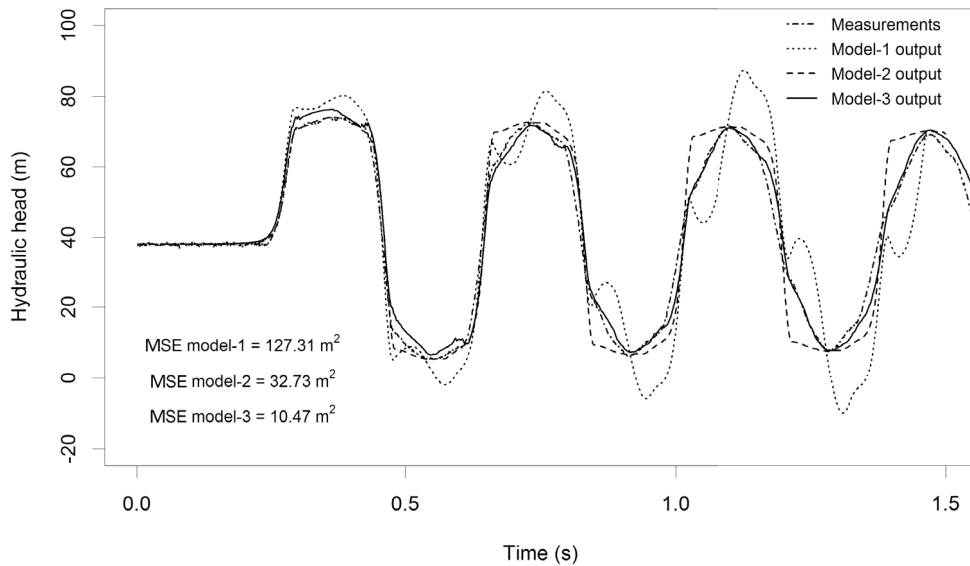


Figure 4.28 – Pressure outputs at the **downstream section** of the pipe from the best simulations of Model-1 and Model-2 in comparison with measurements. Computed MSE are shown for both models.

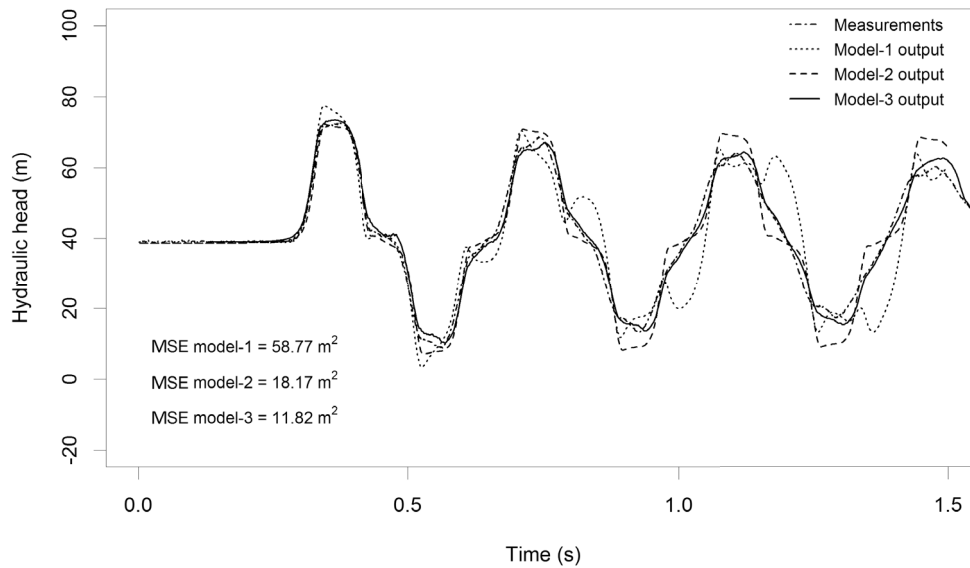


Figure 4.29 – Pressure outputs at the **middle section** of the pipe from the best simulations of Model-1 and Model-2 in comparison with measurements. Computed MSE are shown for both models.

Although Model-1 enables the description of the pressure variation according to pipe-wall axial deformation, the model does not describe with accuracy the shape of the pressure wave. Consequently, the mean squared error is quite high in comparison to Model-2 for both measuring points. Model-2 presents very good agreement with measured data for the first pressure peak, since the distributed mass of the rings allows an accurate calibration of the pressure wave shape. However, the calibrated wave shape in the first pressure peak does not evolve according to the observed propagation of the transient event. Finally, thanks to the incorporation of dry friction dissipation, the computed waterhammer wave of Model-3 evolves in terms of shape and damping showing a very good fitting to measurements.

The main difference between Model-1 and Model-2 is on how junction coupling is considered. In Model-1 the junction coupling is focused on the balance of forces over the valve (boundary condition). In Model-2, junction coupling results from the balance of forces in each coil ring (internal conditions). In the experimental coil system, the moving elements are the rings and not the valve, hence Model-2 is more faithful to the real phenomenon. However, the mechanical model proposed does not entirely solve the FSI problem, as variables related to the structure are only partially solved in the pipe segments representing the coil rings and unsteady friction and dry friction are not taken into account. Model-3, corresponds to a simplification of Model-2, where, additionally unsteady skin and dry friction dissipation have been included. Unsteady skin friction does not significantly affect the transient wave (see Fig. 4.17)

Finally, in order to validate and to show the reliability of Model-3, different time-series are

displayed in Figs. 4.30 and 4.31, where a consistent fitting between observations and numerical output can be observed for different initial discharges and along the waterhammer wave propagation, on space and time. The values of the calibrated dry friction coefficients were adjusted proportionally to the initial discharge, as consequence of the variability of the normal anchoring force against the pipe-supports.

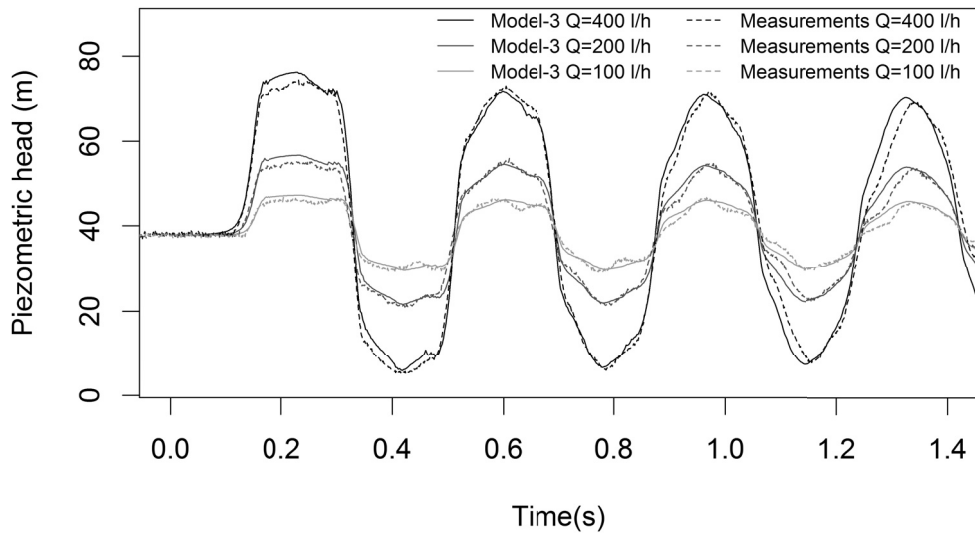


Figure 4.30 – Pressure outputs for initial discharges $Q_0 = 100 \text{ l/h}$, $Q_0 = 200 \text{ l/h}$ and $Q_0 = 400 \text{ l/h}$ at the **downstream section** of the pipe from the selected solution of Model-2 in comparison with measurements.

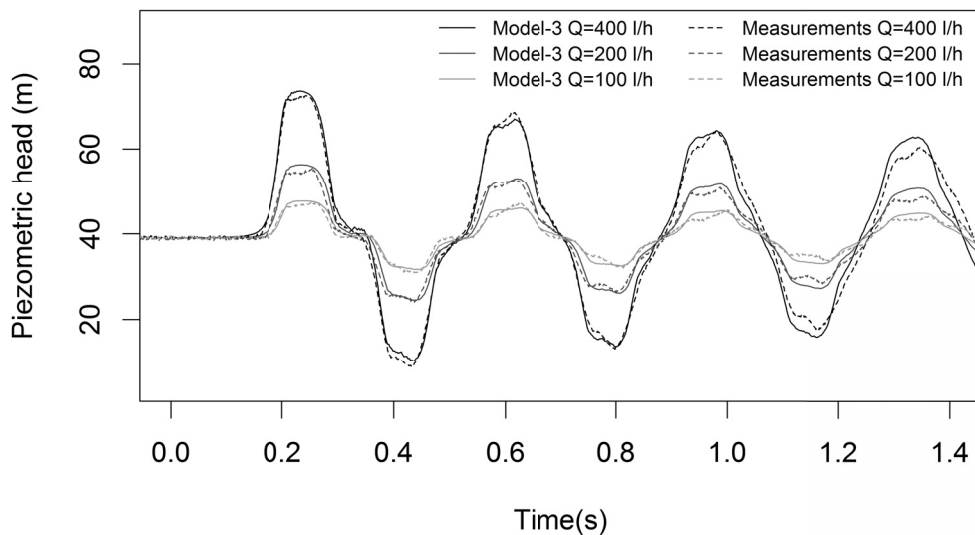


Figure 4.31 – Pressure outputs for initial discharges $Q_0 = 100 \text{ l/h}$, $Q_0 = 200 \text{ l/h}$ and $Q_0 = 400 \text{ l/h}$ at the **middle section** of the pipe from the selected solution of Model-2 in comparison with measurements.

4.3.6 Research outcome

A mathematical model that describes the fluid-structure interaction occurring in a coil pipe system during hydraulic transient events has been developed. The followed approach is based on the implementation of a four-equation model, which takes into account the effect of axial stress waves throughout the pipe-wall. The research novelty is the identification and description of the FSI phenomenon occurring in pipe-coils systems.

After the implementation of a basic FSI four-equation model and its verification by means of the Delft Hydraulics benchmark Problem A (Tijsseling & Lavooij, 1990; Lavooij & Tijsseling, 1989), three models were built up with the goal to adapt to the coil singularities. Model-1 simplifies the coil pipe system to a straight pipe with a moving valve at its downstream end. In Model-2 the independent vibrating rings are described by assuming an analogue mechanical model. In Model-3, only the first vibration mode of the pipe is solved and pressures are corrected by adding internal conditions that take into account the movement of the pipe and the dry friction against the pipe supports. The main difference between Model-1 and Model-2 is how junction coupling is considered. Model-3 considers additional dissipating phenomena, namely unsteady skin friction and dry friction.

In Model-1, the generation of axial stress waves due to junction coupling is localized in the valve, while in Model-2 is rather distributed throughout the ring bends. In a static analysis this fact does not make any difference as both models would return equal stresses for equal pressure loads. The present study shows that when fluid variables are dynamically interacted with solid variables, the source of the axial stress wave does matter. Contrarily to Model-1 where the valve mass was object of calibration, in Model-2 it is the mass of each individual ring that is calibrated. Detailed calibration is also allowed in Model-3 by means of dry friction adjustment. Instead of the system inertia, in Model-3 dry friction dissipation occurring between the pipe-wall and the pipe supports is taken into account.

The three models confirm the hypothesis that the cause of the discrepancy between the experimental measurements and the output from the classic waterhammer model, stated in Subsection 4.2.2, stems from the interaction between the fluid and the coil structural behaviour. As shown, this can be corrected by means of a four-equation model, which covers the coupling of the fluid pressure wave with the solid axial stress wave, hence describing the "breathing" effect of the coil due to the longitudinal movement of the pipe-wall. Model-1 is a good first approximation to tackle the FSI problem. However, it does not allow an accurate description of all the physical phenomenon. Model-2, using the analogue mechanical model, attempts to describe the movement of the coil rings that are not rigidly fixed. This behaviour is case-dependent and must be calibrated based on collected data. The same comment stands for Model-3. The inclusion of dry friction dissipation allows a much greater accuracy during the wave propagation, and, after calibration, Model-3 shows a good performance and it allows a more precise description of the dynamics of the FSI occurring in the coil facility. Model-3 has been successfully validated for three different experimental tests at different initial flow

rates. The model output showed a good agreement with the experimental observations, either on time and space.

4.4 Overview and concluding summary

In a first stage, a stress-strain analysis is carried out aiming at the description of the static structural behaviour of a coil pipe system exposed to inner pressure loads. For this purpose theory of shells of revolution is applied and effects such as the ellipticity of the pipe cross-section or the centrifugal force generated by a steady flow in the coil pipe are considered. Finally the stress-strain model is applied for dynamic waterhammer tests giving accurate results for a quasi-static uncoupled approach. This first stress-strain analysis concludes that the static deformations of the pipe coil system are equivalent to those of a straight pipe with closed ends. Hence, according to the classification presented at Section 2.2, the pipe response can be described by focusing on the 3-DOF.

In a second stage, a 1D waterhammer model describing the fluid-structure interaction in pipe coils is developed. Based on the conclusions from the stress-strain analysis three conceptual models engined by a four-equation solver are used. The different models are compared with experimental data concluding that the dynamic response of the coil system differs from that of a straight pipe. The independent vibrating coil rings must be considered, converting FSI in coils a case-dependent problem difficult to be approached by a general solution.

Finally, a 1-DOF model adjusted to account for the pipe-wall movement is proposed. Internal conditions, considering a quasi-steady pipe-wall deformation of the coil rings, are applied accordingly to the stress-strain analysis. Unsteady skin friction and dry friction dissipation were also included, allowing a much greater accuracy during the wave propagation. The model was successfully validated for different flow rates showing a good performance of the dynamics of the coil behaviour during hydraulic transients.

5 Fluid-structure interaction in straight pipelines

The present chapter is based on the following scientific publications:

- D. Ferras, P. Manso, D. Covas, A.J. Schleiss. Fluid-structure interaction in straight pipelines: friction coupling mechanisms. *Accepted for publication at the Journal of Computers and Structures (June 2016)*
- D. Ferras, P. Manso, D. Covas, A.J. Schleiss. Fluid-structure interaction in straight pipelines anchored against longitudinal movement. *Submitted at the Journal of Sound and Vibration (March 2016)*

The work presented hereafter is original and was performed by the first author. The interpretation and discussion of results was carried out with the collaboration of the co-authors.

5.1 Introduction

In straight pipelines all the interaction mechanisms between the fluid and the structure (*i.e.* Poisson, junction and friction coupling) act alongside the pipe axial direction. Hence, 1,2,3-DOF's are the main degrees-of-freedom excited in straight pipelines during waterhammer waves. For thin pipe-wall conduits, where the inertia of the pipe 2-DOF is negligible a four-equation model is sufficient for accurately describing hydraulic transients in straight pipelines. However, depending on the pipe configuration, reactions like the pipe anchoring, valve movement or dry friction between the pipe-wall and the outer surrounding may affect the waterhammer wave shape, damping and timing. In the present chapter these effects are analysed by the incorporation of several add-ons in the basic four-equation solver. Experimental validation is carried out by collected data from the experimental set-up described in Subsection 3.2.1.

A first approach is carried out by considering no anchors along the pipe-rig and friction coupling is analysed. Both dissipation mechanisms unsteady skin friction and dry friction are

considered and two different experimental set-ups are assessed: (a) the conduit anchored in both pipe-ends; and (b) the downstream pipe-end is free to move. The aim of this first stage is to learn the importance of the different friction mechanisms in the dissipation of hydraulic transients in straight pipelines.

A second assessment is performed aiming at describing the behaviour of the pipe supports and their effect in the transient wave. For this purpose internal conditions are added in the four-equation solver. These internal conditions represent the pipe supports and they are defined by considering the inertia and the dry friction of the anchoring block, which is their resistance to movement. Hence, junction coupling is applied at each anchoring node by means of a balance of forces in the second law of Newton. For model validation three basic anchoring configurations are assessed: (a) the conduit anchored in both pipe-ends; (b) the downstream pipe-end is free to move; and (c) the conduit is anchored in the midstream section. After this second stage, the goal is to achieve a four-equation model capable of describing with accuracy the behaviour of the straight pipelines most common engineering practices.

5.2 Friction coupling mechanisms

5.2.1 Introduction and background theory

Fluid-structure interaction (FSI) in pressurized hydraulic transients analyses is frequently approached by considering the first two pipe vibration modes (*i.e.*, pressure wave propagation in the fluid and axial stress wave propagation in the pipe-wall). For the description of pressure waves in pipe systems, one-mode or two-mode solutions are sufficient (Tijsseling, 1996). Two-mode models can be implemented either by using MOC-FEM procedure (*i.e.*, the method of characteristics for the fluid and finite element method for the structure) (Wiggert, 1983) or MOC procedure (*i.e.*, the method of characteristics for both the fluid and the structure) (Wiggert *et al.*, 1985a). Lavooij & Tijsseling (1991) applied the two approaches to solve the four basic conservation equations in the time domain, concluding that for straight pipe problems the MOC procedure is more accurate. Thus, a four-equation model represents a suited tool to describe the ideal reservoir-pipe-valve system in its basic FSI configurations, namely either considering an anchored or non-anchored downstream valve.

Several authors combined FSI with other wave dissipating phenomena, such as: FSI and pipe-wall viscoelasticity (Weijde, 1985; Walker & Phillips, 1977; Stuckenbruck & Wiggert, 1986); FSI and cavitation (Tijsseling, 1993; Tijsseling *et al.*, 1996; Tijsseling, 1996); and the most complete including FSI, column separation and unsteady friction (UF) in a viscoelastic pipe (Keramat & Tijsseling, 2012). However, the effects of unsteady friction and pipe-wall viscoelasticity are hard to distinguish (Covas *et al.*, 2004b) and, to the knowledge of the authors, unsteady friction effect has never been separately assessed in a two-mode FSI model. Due to FSI, the pipe-wall vibrates axially at a different rate than the fluid, hence, the relative velocity between both (V_r) must be considered for skin shear stress assessment. The higher the Mach number (V_r/a_h) is,

the greater the wall shear stress effects are (Ghidaoui *et al.*, 2005). Therefore, unsteady friction effects may be increased when fluid-structure interaction is important.

Besides, in the implementation of a four-equation model a major question may arise: Is there movement in the pipe supports? Anchorages of pipelines aim to avoid the pipe-wall movement essentially by means of dry friction (Feeny *et al.*, 1998). However, from Newton principles, when a system is loaded, null deformation/displacement by means of only resistance is not possible. Pipe supports are never entirely stiff or entirely inert when loaded by impacts (Tijsseling, 1997). Thus, movement occurs. Dry friction is proportional to the normal force, hence, for a high normal force, important energy might be dissipated from the structure to its supports/surroundings. Furthermore, in this context, it is crucial to define with good criteria the stick-slip transitions.

Tijsseling & Vardy (1996a) included Coulomb's dry friction in a four-equation model with the goal to describe the behaviour of pipe racks, proposing a quantitative guideline equation aiming at assessing when dry friction forces may be relevant during hydraulic transients. In the present work dry friction is approached differently not at a single point but distributed all throughout the pipeline. For this purpose, a new right-hand-side term in the momentum equation of the pipe-wall axial movement was incorporated.

This research aims at assessing firstly the effect of different skin friction models during hydraulic transients in a FSI 4-equation solver. For this purpose, three skin friction models are assessed: (i) quasi-steady friction; (ii) Brunone's unsteady friction formulation, which is based on instantaneous local and convective accelerations; and (iii) Trikha's unsteady friction model, which is based on weights of past velocity changes. Secondly, dry friction is implemented, nesting its computation into the friction coupling mechanism, and its dissipation effect over the transient wave is assessed. The theoretical background of these implementations is explained in Chapter 2 and the respective Appendices A to D.

The aim of this section is the assessment of different friction dissipation assumptions in a FSI two-mode model. A four-equation solver is implemented including the three basic coupling mechanisms: Poisson, junction and friction coupling; and the last one nests the skin friction models (*i.e.* quasi-steady, Brunone's and Trikha's) and the dry friction model (*i.e.* Coulomb's friction). The innovation of this research is the incorporation of dry friction computation in the fundamental equations of the two-mode (four-equation) waterhammer model. This implies a modification of the pipe-wall momentum equation in the axial direction. The effect of dry friction is compared with skin friction and results are assessed by means of experimental data in a straight copper pipe rig.

5.2.2 Experimental data collection

The experimental data used in the present study was acquired from the straight copper pipe rig (SCP) assembled at the Laboratory of Hydraulics and Environment of Instituto Superior

Chapter 5. Fluid-structure interaction in straight pipelines

Técnico (LHE/IST), Lisbon, Portugal, and described in the Subsection 3.2.1. Two supporting configurations have been analysed: (a) the conduit anchored against longitudinal movement at both downstream and upstream ends; and (b) the conduit only anchored against longitudinal movement at the upstream end. Throughout the pipe there were no anchorages nor supports; the pipe layed directly over the floor of the laboratory.

Table 5.1 summarizes the tests carried out in these experimental configurations, displaying the initial flow velocity and Reynolds number, the initial piezometric head and the maximum and minimum piezometric heads measured immediately upstream the valve.

Table 5.1 – Characteristics of the experimental tests.

Test ID	V_0 (m/s)	Re_0	H_0 (m)	H_{max} (m)	H_{min} (m)	Valve
SCP01	0.26	5276	43.65	77.25	10.66	fixed
SCP02	0.36	7253	42.39	88.67	-2.95	fixed
SCP03	0.41	8206	42.87	94.88	-8.67	fixed
SCP04	0.26	5276	44.16	83.17	5.97	released
SCP05	0.36	7253	42.27	94.69	-8.34	released
SCP06	0.41	8206	42.55	100.04	-9.95	released

Figs. 5.1-a and 5.1-b depict the transient pressure traces at the downstream section for both anchoring conditions. Figs. 5.2-a and 5.2-b depict the transient circumferential and axial strain traces, respectively, at the downstream pipe section for both anchoring conditions. As it can be observed, strain and pressure traces present a similar response during the waterhammer wave being in phase and circumferential strains in phase, and axial strains following the expected behaviour according to Poisson effect. Either in terms of pressure (Fig. 5.1) or strain, (Fig. 5.2), the system response is very different when the downstream pipe-end is released, presenting greater maximum pressures and a noticeable wave shape change.

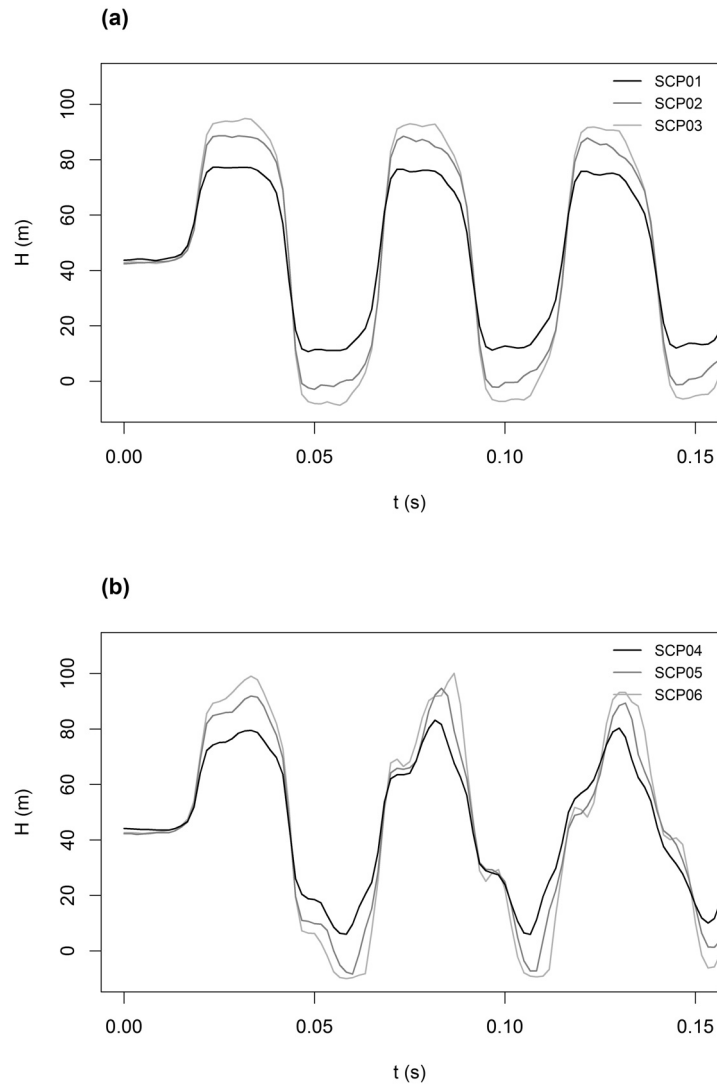


Figure 5.1 – Pressure data acquired at the downstream end (PT3) of the straight copper pipe for an *anchored* (a) and for a *non-anchored* (b) downstream end.

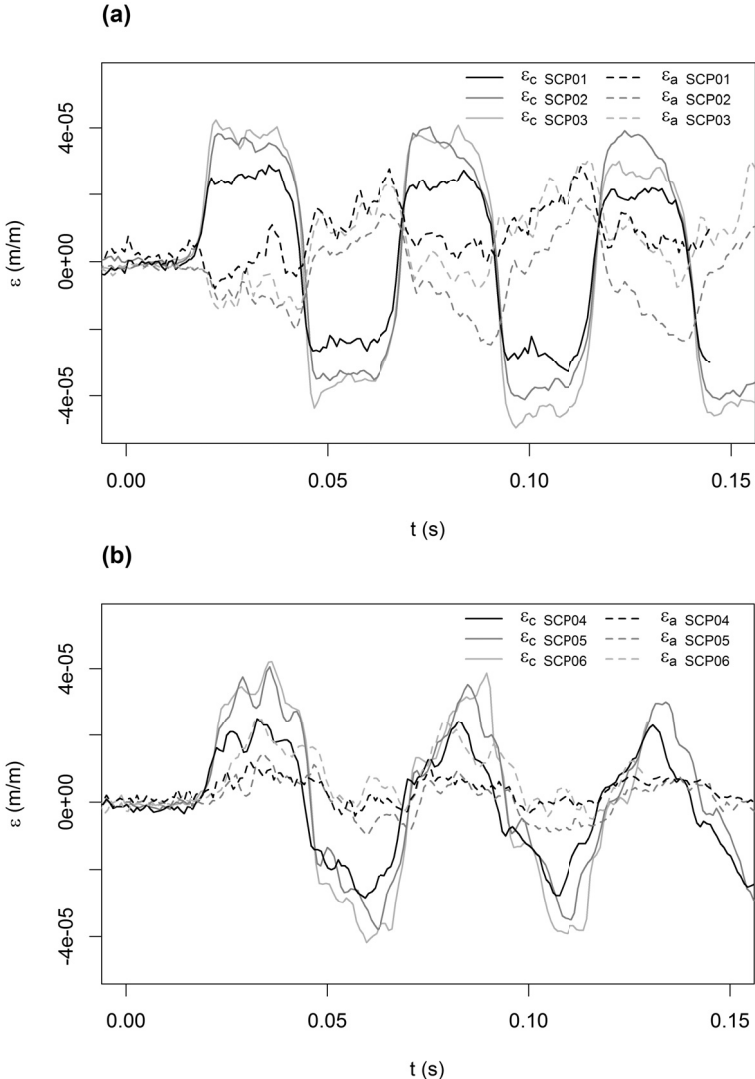


Figure 5.2 – Circumferential (solid lines) and axial (dashed lines) strain data acquired at the downstream section of the straight copper pipe for an *anchored* (a) and for a *non-anchored* (b) downstream end.

5.2.3 Numerical model development

Fundamental equations

The following set of equations (Eqs. 5.1 to 5.4) is based on Lavooij & Tijsseling (1991) four fundamental conservation equations with the momentum equation (Eq. 5.3) of the pipe-wall in the axial direction adapted in order to include dry friction (*v.i.* ★). Their derivation is

presented in Appendices A and D.

$$\frac{\partial V}{\partial t} + \frac{1}{\rho_f} \frac{\partial p}{\partial z} = -\frac{f}{4r} (V_r) |V_r| \quad (5.1)$$

$$\frac{\partial V}{\partial z} + \frac{1}{\rho_f a_h^2} \frac{\partial p}{\partial t} = \frac{2\nu}{E} \frac{\partial \sigma}{\partial t} \quad (5.2)$$

$$\frac{\partial U}{\partial t} - \frac{1}{\rho_p} \frac{\partial \sigma}{\partial z} = \frac{\rho_f A_f}{\rho_p A_p} \frac{f}{4r} V_r |V_r| + \underbrace{\left(1 + \frac{\rho_f A_f}{\rho_p A_p}\right)}_{\star} g \mu \operatorname{sign}(U) \quad (5.3)$$

$$\frac{\partial U}{\partial z} - \frac{1}{\rho_p a_p^2} \frac{\partial \sigma}{\partial t} = -\frac{r\nu}{eE} \frac{\partial p}{\partial t} \quad (5.4)$$

It is the right-hand-side terms of Eqs. 5.1 to 5.4 that make the system of equations nonlinear. The right-hand-side term of the fluid continuity equation (Eq. 5.2) describes the interaction with the pipe-wall by means of Poisson coupling mechanism. Similarly, the right-hand-side of the pipe-wall continuity equation (Eq. 5.4) describes the interaction with the fluid. On the other side, the right-hand-side terms of the momentum equations (Eqs. 5.1 and 5.3) represent the friction losses. Skin friction loss affects oppositely the fluid and the pipe-wall, while dry friction (*v.s.* \star) only affects the pipe-wall momentum equation, as this occurs between the pipe and the outer surrounding.

Compatibility equations

Eqs. 5.1, 5.2, 5.3 and 5.4 represent a linear hyperbolic system of four first-order partial differential equations. Due to its hyperbolic nature, the system can be converted into a set of four ordinary differential equations (Eqs. 5.5) by the MOC method (Forsythe *et al.*, 1960; Lavooij & Tijsseling, 1991). The derivation of the compatibility equations is explained in Appendices B and D. The ξ coefficients are presented in Table B.3, while the SF_f and DF_s coefficients correspond, respectively, to the skin and the dry friction losses terms and they can be found in Table D.2.

$$\begin{pmatrix} \xi_{fV} & \xi_{fp} & \xi_{fU} & -\xi_{f\sigma} \\ \xi_{fV} & -\xi_{fp} & \xi_{fU} & \xi_{f\sigma} \\ -\xi_{sV} & -\xi_{sp} & \xi_{sU} & -\xi_{s\sigma} \\ -\xi_{sV} & \xi_{sp} & \xi_{sU} & \xi_{s\sigma} \end{pmatrix} \frac{d}{dt} \begin{pmatrix} V \\ p \\ U \\ \sigma \end{pmatrix} = \begin{pmatrix} SF_f + DF_f \\ SF_f + DF_f \\ SF_s + DF_s \\ SF_s + DF_s \end{pmatrix} \quad (5.5)$$

The compatibility equations are only valid along the characteristic lines with slopes: $\pm 1/a_f$ for the characteristics associated with the fluid, and $\pm 1/a_s$ for the characteristics associated with the pipe-wall. Fig. 5.3 depicts the adopted numerical scheme at the interior nodes and the domain boundaries, where: 'P' represents the space and time coordinates in the grid where the computation is carried out, 'A' represents the information source brought by the positive characteristic line in the pipe-wall, 'B' the information source brought by the positive characteristic line in the fluid, 'C' the information source brought by the negative characteristic line in the fluid and 'D' the information source brought by the negative characteristic line in the pipe-wall. Notice that time interpolations are necessary in the nodes close to the extreme-end boundaries.

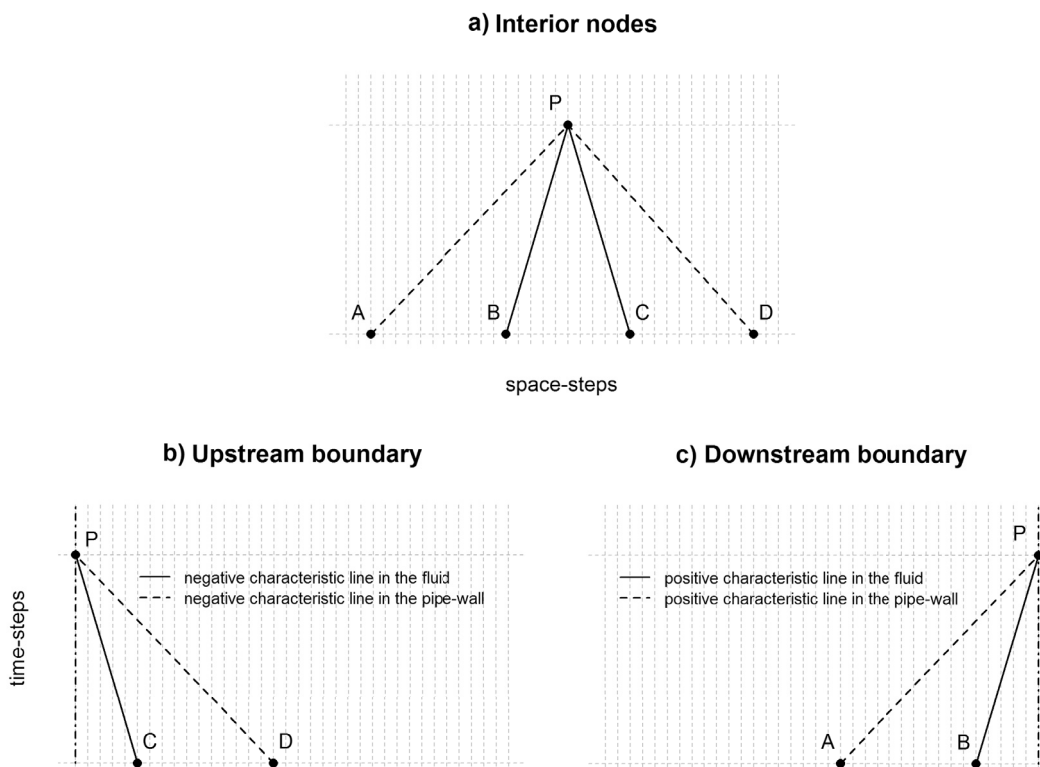


Figure 5.3 – Numerical scheme of the four-equation model. Characteristic lines at different sections of the pipe.

The previous ordinary differential equations (Eqs. 5.5) can be integrated according to the schemes presented in Fig. 5.3

$$\xi_{f_V} \int_B^P \frac{dV}{dt} + \xi_{f_p} \int_B^P \frac{dp}{dt} + \xi_{f_U} \int_B^P \frac{dU}{dt} - \xi_{f_\sigma} \int_B^P \frac{d\sigma}{dt} = \int_B^P (SF_f + DF_f) \quad (5.6)$$

$$\xi_{f_V} \int_C^P \frac{dV}{dt} - \xi_{f_p} \int_C^P \frac{dp}{dt} + \xi_{f_U} \int_C^P \frac{dU}{dt} + \xi_{f_\sigma} \int_C^P \frac{d\sigma}{dt} = \int_C^P (SF_f + DF_f) \quad (5.7)$$

$$-\xi_{s_V} \int_A^P \frac{dV}{dt} - \xi_{s_p} \int_A^P \frac{dp}{dt} + \xi_{s_U} \int_A^P \frac{dU}{dt} - \xi_{s_\sigma} \int_A^P \frac{d\sigma}{dt} = \int_A^P (SF_s + DF_s) \quad (5.8)$$

$$-\xi_{s_V} \int_D^P \frac{dV}{dt} + \xi_{s_p} \int_D^P \frac{dp}{dt} + \xi_{s_U} \int_D^P \frac{dU}{dt} + \xi_{s_\sigma} \int_D^P \frac{d\sigma}{dt} = \int_D^P (SF_s + DF_s) \quad (5.9)$$

$$(5.10)$$

reaching the following discrete linear explicit system of equations:

$$\xi_{f_V} V_P + \xi_{f_p} p_P + \xi_{f_U} U_P - \xi_{f_\sigma} \sigma_P + Cp_f = 0 \quad (5.11)$$

$$\xi_{f_V} V_P - \xi_{f_p} p_P + \xi_{f_U} U_P + \xi_{f_\sigma} \sigma_P + Cn_f = 0 \quad (5.12)$$

$$-\xi_{s_V} V_P - \xi_{s_p} p_P + \xi_{s_U} U_P - \xi_{s_\sigma} \sigma_P + Cp_s = 0 \quad (5.13)$$

$$-\xi_{s_V} V_P + \xi_{s_p} p_P + \xi_{s_U} U_P + \xi_{s_\sigma} \sigma_P + Cn_s = 0 \quad (5.14)$$

where Eqs. 5.11 and 5.12 correspond to the positive and negative characteristic equations of the fluid pressure wave and Eqs. 5.13 and 5.14 correspond to the positive and negative characteristic equations of the axial stress wave. The values Cp_f , Cn_f , Cp_s and Cn_s enclose the information from the previous time-step:

$$Cp_f = -\xi_{f_V} V_B - \xi_{f_p} p_B - \xi_{f_U} U_B + \xi_{f_\sigma} \sigma_B + SF_{f_B} + DF_{f_B} \quad (5.15)$$

$$Cn_f = -\xi_{f_V} V_C + \xi_{f_p} p_C - \xi_{f_U} U_C - \xi_{f_\sigma} \sigma_C + SF_{f_C} + DF_{f_C} \quad (5.16)$$

$$Cp_s = \xi_{s_V} V_A + \xi_{s_p} p_A - \xi_{s_U} U_A + \xi_{s_\sigma} \sigma_A + SF_{s_A} + DF_{s_A} \quad (5.17)$$

$$Cn_s = \xi_{s_V} V_D - \xi_{s_p} p_D - \xi_{s_U} U_D - \xi_{s_\sigma} \sigma_D + SF_{s_D} + DF_{s_D} \quad (5.18)$$

Interior nodes

From the linear system of equations (Eqs. 5.11, 5.12, 5.13 and 5.14) the following expressions are obtained determining the dependent variables along the interior nodes:

$$p_P = -\frac{\frac{Cp_f - Cn_f}{\xi_{f_\sigma}} - \frac{Cp_s - Cn_s}{\xi_{s_\sigma}}}{2\left(\frac{\xi_{f_p}}{\xi_{f_\sigma}} + \frac{\xi_{s_p}}{\xi_{s_\sigma}}\right)} \quad (5.19)$$

$$V_P = -\frac{\frac{Cp_f + Cn_f}{\xi_{fU}} - \frac{Cp_s + Cn_s}{\xi_{sU}}}{2\left(\frac{\xi_{fV}}{\xi_{fU}} + \frac{\xi_{sV}}{\xi_{sU}}\right)} \quad (5.20)$$

$$\sigma_P = \frac{\frac{Cp_f - Cn_f}{\xi_{fp}} + \frac{Cp_s - Cn_s}{\xi_{sp}}}{2\left(\frac{\xi_{f\sigma}}{\xi_{fp}} + \frac{\xi_{s\sigma}}{\xi_{sp}}\right)} \quad (5.21)$$

$$U_P = -\frac{\frac{Cp_f + Cn_f}{\xi_{fV}} + \frac{Cp_s + Cn_s}{\xi_{sV}}}{2\left(\frac{\xi_{fU}}{\xi_{fV}} + \frac{\xi_{sU}}{\xi_{sV}}\right)} \quad (5.22)$$

Boundary conditions

Upstream reservoir: As shown in Fig. 5.3-a only the negative characteristic lines reach the upstream boundary. The boundary condition for a constant level reservoir in the upstream pipe-end is given by:

$$p_P = p_{res} \quad (5.23)$$

$$U_P = 0 \quad (5.24)$$

Substituting the Eqs. 5.23 and 5.24 into Eqs. 5.12 and 5.14 expressions for V_P and σ_P are obtained.

$$V_P = \frac{\left(\frac{\xi_{fp}}{\xi_{f\sigma}} + \frac{\xi_{sp}}{\xi_{s\sigma}}\right) p_{res} - \frac{Cn_f}{\xi_{f\sigma}} + \frac{Cn_s}{\xi_{s\sigma}}}{\frac{\xi_{fV}}{\xi_{f\sigma}} + \frac{\xi_{sV}}{\xi_{s\sigma}}} \quad (5.25)$$

$$\sigma_P = \frac{\left(\frac{\xi_{fp}}{\xi_{fV}} - \frac{\xi_{sp}}{\xi_{sV}}\right) p_{res} - \frac{Cn_f}{\xi_{fV}} - \frac{Cn_s}{\xi_{sV}}}{\frac{\xi_{f\sigma}}{\xi_{fV}} + \frac{\xi_{s\sigma}}{\xi_{sV}}} \quad (5.26)$$

Downstream valve: A solution is derived for a non-instantaneous valve closure, with a non-anchored pipe-end and taking into account the valve inertia. As shown in Fig. 5.3-b only the positive characteristic lines reach the downstream boundary. The boundary conditions for

such assumptions are expressed in Eqs. 5.27 and 5.28, where the first determines the discharge rate through the valve and the second the balance of forces at the valve section by means of Newton's second law of motion.

$$V_P = \tau(t) \sqrt{\frac{\Delta p}{\rho_f g}} + U_P \quad (5.27)$$

$$\sigma_P = \frac{1}{A_p} \left(A_f (1 - \tau(t)) (p_P - p_0) - m_v \frac{\Delta U}{\Delta t} \right) \quad (5.28)$$

A non-linear dependency arises between the valve displacement and the valve closure, yet, it is a second degree relation. Substituting the Eqs. 5.27 and 5.28 into Eqs. 5.11 and 5.13 expressions for p_P and U_P are obtained.

$$p_P = \left(\frac{-b^* + \sqrt{b^{*2} - 4a^*c^*}}{2a^*} \right)^2 + p_0 \quad (5.29)$$

where

$$a^* = \left(\frac{\xi_{f_p} - \xi_{f_\sigma} \frac{A_f(1-\tau(t))}{A_p}}{\xi_{f_v} + \xi_{f_\sigma} \frac{m_v}{A_p \Delta t} + \xi_{f_u}} - \frac{\xi_{s_p} + \xi_{s_\sigma} \frac{A_f(1-\tau(t))}{A_p}}{\xi_{s_v} - \xi_{s_\sigma} \frac{m_v}{A_p \Delta t} - \xi_{s_u}} \right)$$

$$b^* = \left(\frac{\xi_{f_v} \frac{\tau(t)}{\sqrt{\rho_f g}}}{\xi_{f_v} + \xi_{f_\sigma} \frac{m_v}{A_p \Delta t} + \xi_{f_u}} - \frac{\xi_{s_v} \frac{\tau(t)}{\sqrt{\rho_f g}}}{\xi_{s_v} - \xi_{s_\sigma} \frac{m_v}{A_p \Delta t} - \xi_{s_u}} \right)$$

$$c^* = \left(\frac{\xi_{f_p} p_0 - \xi_{f_\sigma} \frac{m_v}{A_p \Delta t} U_{P-1} + C p_f}{\xi_{f_v} + \xi_{f_\sigma} \frac{m_v}{A_p \Delta t} + \xi_{f_u}} - \frac{\xi_{s_p} p_0 + \xi_{s_\sigma} \frac{m_v}{A_p \Delta t} U_{P-1} - C p_s}{\xi_{s_v} - \xi_{s_\sigma} \frac{m_v}{A_p \Delta t} - \xi_{s_u}} \right)$$

and

$$U_P = - \frac{\left(\xi_{f_p} - \xi_{f_\sigma} \frac{A_f(1-\tau(t))}{A_p} \right) (p_P - p_0) + \xi_{f_v} \frac{\tau(t)}{\sqrt{\rho_f g}} \sqrt{p_P - p_0} + \xi_{f_p} p_0 - \xi_{f_\sigma} \frac{m_v}{A_p \Delta t} U_{P-1} + C p_f}{\xi_{f_v} + \xi_{f_\sigma} \frac{m_v}{A_p \Delta t} + \xi_{f_u}} \quad (5.30)$$

For the anchored valve condition a very high fictitious mass value is considered so the downstream section becomes motionless.

Notice that, as it can be inferred from Figs. 5.3-a and 5.3-c, temporal interpolation have to be carried out at the nodes located in the vicinity of the computational domain boundaries as a consequence of the leaps adopted in the numerical scheme.

5.2.4 Model testing

Introduction

The implemented model describes three physical phenomena occurring during hydraulic transients in pipe-flow: fluid-structure interaction, skin friction and dry friction. To ensure and verify the implemented code outputs according with the modelling assumptions, the three phenomena are assessed one at a time by deactivating their functionality in the code; afterwards they are combined two at a time. Table 5.2 summarizes how this verification tests have been carried out according to the combination of each one of the modelled phenomena. The geometry of the simulated pipe corresponds to the experimental facility described in Subsection 5.2.2.

Table 5.2 – Summary of simulations carried out for model verification. (✓) activated mechanism, (–) deactivated mechanism.

Test ID	Fluid-structure interaction		Skin friction			Dry friction
	Poisson coupling	Junction coupling	Steady	Brunone	Trikha	Coulomb
CI-1	–	–	–	–	–	–
FSI-1	✓	–	–	–	–	–
FSI-2	–	✓	–	–	–	–
SF-1	–	–	✓	–	–	–
SF-2	–	–	–	✓	–	–
SF-3	–	–	–	–	✓	–
DF-1	–	–	–	–	–	✓
DF-2	✓	–	–	–	–	✓
DF-3	–	✓	–	–	–	✓

Note: CI = classic model; FSI = fluid-structure interaction; SF = skin friction; DF = dry friction.

Thereafter, in the following subsections fluid-structure interaction, skin friction models and Coulomb's dry friction are separately verified and assessed. The aim is not only to show the right performance of the implemented code but also the sensitivity of the numerical output to each phenomenon in terms of wave shape, timing and damping.

Fluid-structure interaction verification

With skin and dry friction deactivated a verification of the fluid-structure interaction was carried out for the two basic configurations: anchored (FSI-1) and non-anchored (FSI-2) pipe-ends. The first allows the assessment of *Poisson coupling*, as the Poisson's effect throughout the pipe-wall generates axial displacements. The second allows the assessment of *Junction coupling* due to the valve movement. Figures 5.4-a and 5.4-b depict the numerical outputs from these simulations. Both show the effect of the axial stress waves propagating at a celerity three times faster than the waterhammer wave.

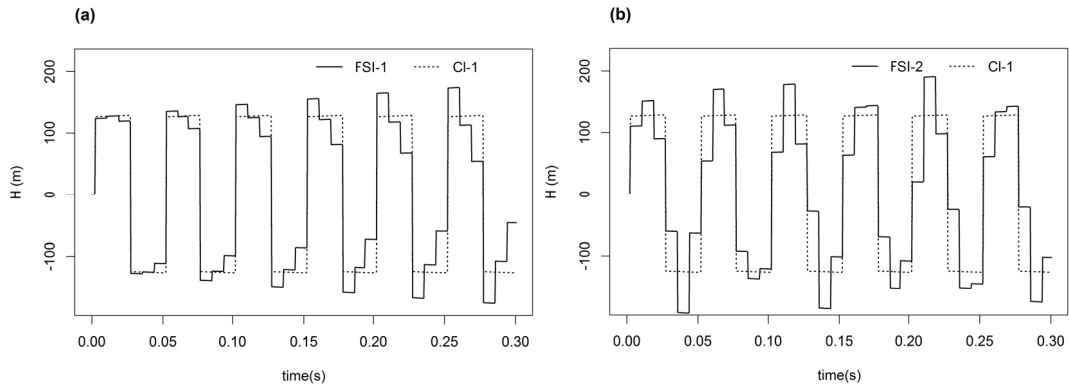


Figure 5.4 – Frictionless four-equation FSI model output for (a) anchored and (b) non-anchored downstream pipe-end *vs.* classic theory. Simulation period of 0.3 s

The apparent amplification of the transient pressure of Fig. 5.4 can be further analysed by longer simulation periods. For this purpose simulation periods of 3 s were launched. Results are shown in Fig. 5.5.

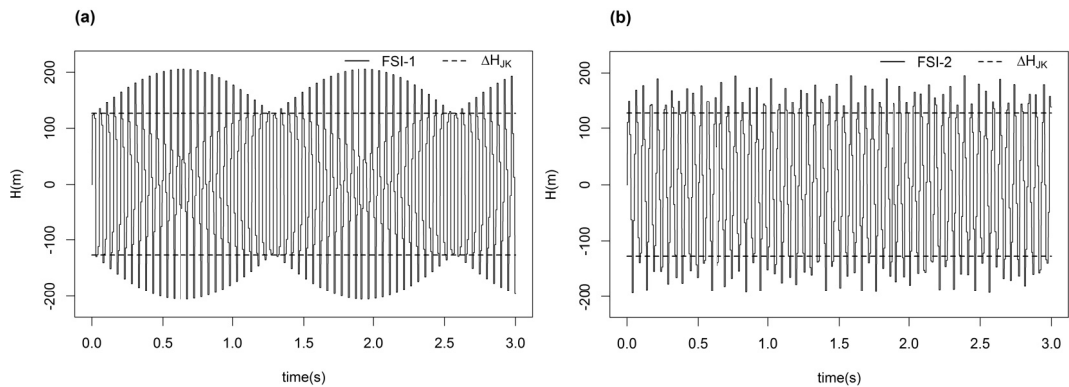


Figure 5.5 – Frictionless four-equation FSI model output for (a) anchored and (b) non-anchored downstream pipe-ends *vs.* Joukowski overpressure. Simulation period of 3 s.

Fig.5.5-a depicts a phenomenon called the Poisson-coupling beat, which was already documented and described by Tijsseling (1997). The phenomenon is not present for a non-anchored pipe end as shown in Fig. 5.5-b. Comparing with Joukowski overpressure ($\Delta H_{JK} = a_h \Delta V / g$) both simulations show that FSI does not introduce directly damping into the pipe system and the maximum pressure may be much higher than Joukowski overpressure.

Skin friction verification

The verification of the skin friction models was carried out by activating and deactivating Poisson coupling, according to Table B.3, the different skin friction computations once at a time: (i) quasi-steady friction (SF-1), (ii) Brunone’s unsteady friction (SF-2), and (iii) Trikha’s

unsteady friction (SF-3).

Fig. 5.6 compares both unsteady friction models with quasi-steady friction at the downstream end of the pipe; Joukowski overpressure (ΔH_{JK}) is also presented in this figure. Brunone's unsteady friction model introduces a higher damping and delay on the transient wave, while Trikha's model affects rather the wave shape.

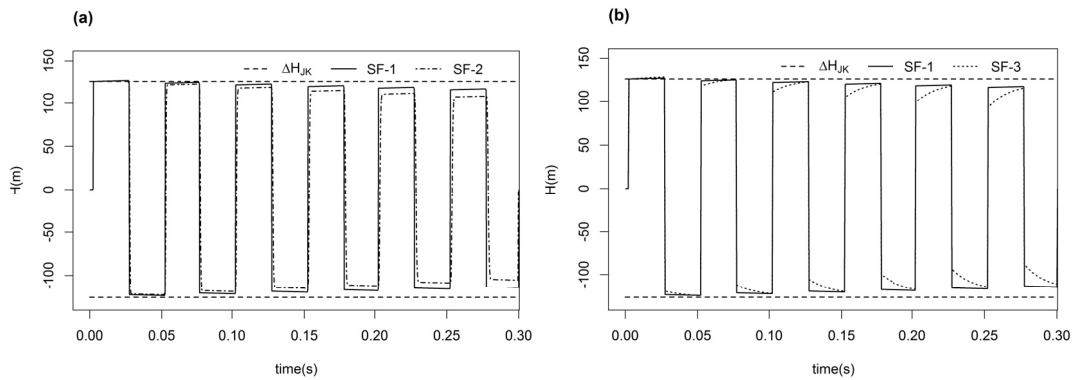


Figure 5.6 – Quasi-steady friction (SF-1) vs. (a) Brunone's (SF-2) and (b) Trikha's (SF-3) unsteady friction. The horizontal dashed line represents Joukowski overpressure.

To analyse the overall dissipation effect of skin friction in the pipe system, a longer simulation period of 3 s was run. Figure 5.7 shows the output for the three different skin friction models. Unsteady friction models significantly increase the pressure wave damping, specially Brunone's model with the k coefficient calculated according to Eq. 2.12. A small phase shift is also observed in the pressure wave.

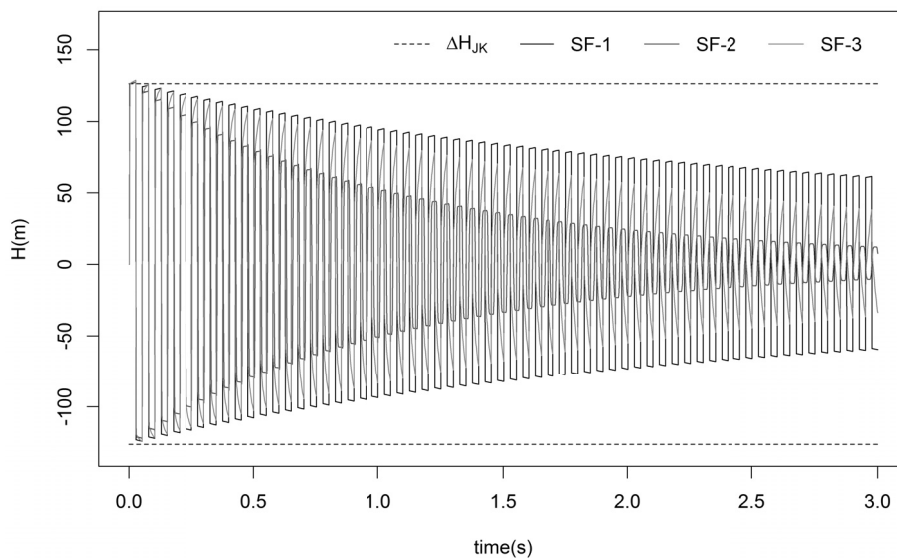


Figure 5.7 – Quasi-steady friction (SF-1) vs. Brunone's (SF-2) and Trikha's (SF-3) unsteady friction models. Simulation period of 3 s.

Dry friction models verification

Decoupling Poisson effect as depicted in Table B.3 allows cutting out the interaction between the pressure wave in the fluid and the axial stress wave in the pipe-wall, yet the system is still composed of four equations: the two classic mass and momentum conservation equations of waterhammer theory and the beam equations for the pipe axial vibration.

In the real system dry friction directly affects the momentum dissipation of the pipe-wall and indirectly the fluid, and *vice versa*. Hence, in order to isolate, and simplify, the assessment of the dry friction phenomenon a different transient simulation is performed. FSI and skin friction are deactivated, fluid density is set to $\rho_f = 0$, and only the structure is excited (DF-1), so the pipe vibrates unaffected by the inner fluid (as if it was empty) but affected by the dry friction between the pipe-wall and the outer media (*i.e.* pipe supports). As explained in Subsection 2.3.3, the Coulomb's dry friction coefficient value used corresponds to the one for copper sliding over cast iron, which is $\mu_k = 0.29$. In this analysis no stick-slip condition is considered. Notice that in this set-up the normal force N is reduced as only the mass of the pipe-wall affects dry friction computation. The transient is generated by hammering the pipe at the upstream boundary, which is set fixed after the impact while the downstream boundary is free to move. Fig. 5.8 shows the output of this simulation compared with the Young solution ($\Delta\sigma = \rho_p a_3 \Delta U$), which is equivalent to Joukowski's expression but for axial stress transients. A linear decrease in the wave amplitude can be observed in Fig. 5.8. Unlike the traditional logarithmic decrement associated to viscous dissipation, dry dissipation involves a rather linear damping (Feeny & Liang, 1996).

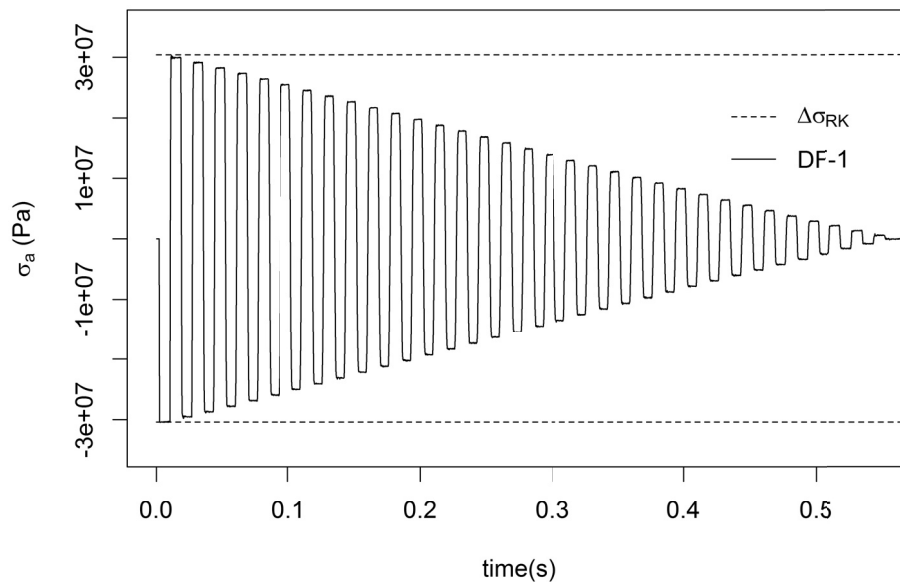


Figure 5.8 – Axial stress of a vibrating fluid-emptied conduit excited by hammering and damped by dry friction. The horizontal dashed line represent Rankine axial stress rise.

Chapter 5. Fluid-structure interaction in straight pipelines

The effect of dry friction on pressure head for a fluid-filled conduit is depicted in Fig.5.9 for the two anchoring conditions. In both simulations the dry friction dissipation affects the pressure transient wave in a similar manner, by smoothing the edges of the stepped transitions caused by the pipe-wall axial movement. This effect is much more evident when the valve is released, as pipe-wall displacements are higher.

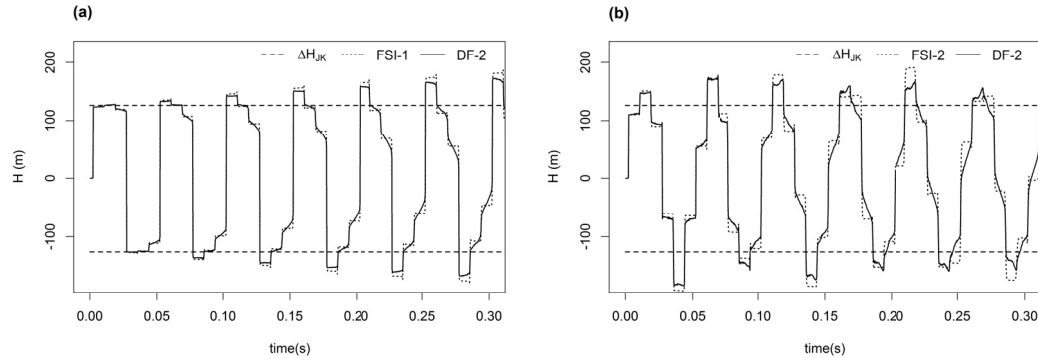


Figure 5.9 – Four-equation FSI model output for (a) anchored and (b) non-anchored downstream pipe-ends; for a frictionless systems (FSI-1,2) and taking into account only dry friction (DF-1,2).

5.2.5 Model application

Simulation of combined effects

In the present analysis the experimental tests presented in Subsection 5.2.2 are simulated using the numerical model developed. Fluid-structure interaction is considered in the numerical simulations and the main input parameters are presented in Table 5.3.

Table 5.3 – Input parameters for the simulation of combined effects.

Parameters for pipe system:							
L (m)	D (m)	e (m)	m_v (kg)	t_v (s)			
15.49	0.02	0.001	6	0.003			
Parameters for fluid and pipe-wall materials:							
ρ_f (kgm^{-3})	ρ_p (kgm^{-3})	E (Pa)	K (Pa)	g (ms^{-2})	ν	μ_s	μ_k
1000	7900	$1.17 \cdot 10^{11}$	$2.2 \cdot 10^9$	9.81	0.33	1.05	0.29
Wave celerities and domain discretization:							
a_h (ms^{-2})	a_3 (ms^{-2})	Δx (m)	Δt (s)				
1239	3717	0.304	$2.45 \cdot 10^{-4}$				

A preliminary analysis has been carried out to identify which of the two UF models described better the observed dynamic behaviour combined with FSI effects. The simulations considering anchored (a) and non-anchored (b) pipe-ends are depicted in Fig. 5.10. Both Brunone's (blue lines) and Trikha's (red lines) unsteady skin friction losses are analysed and dry friction omitted. Results are compared with pressure measurements (black lines) at the downstream end section for a simulation period of 3 s. First, the overall wave dissipation is underestimated in both simulations, with Brunone's results being slightly closer to measurements in terms of damping and wave timing. Second, in the first 10 pressure wave cycles UF has hardly any effect being indifferent the use on any of the models.

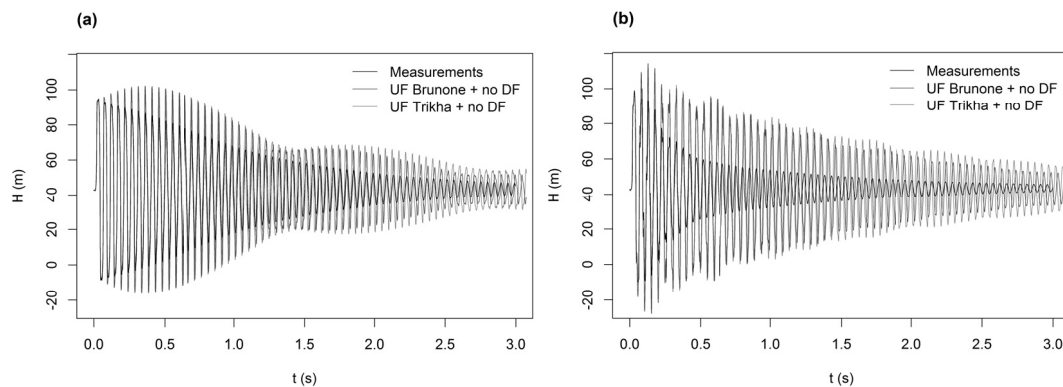


Figure 5.10 – Numerical output considering Brunone's and Trikha's unsteady friction *vs.* measurements for: (a) test SCP03 with anchored pipe-end; and (b) test SCP06 with non-anchored pipe-end. Output from the downstream end section. Dry friction is not considered.

A similar analysis has been carried out combining dry friction with FSI effects and using Brunone's unsteady friction model; results are presented in Fig. 5.11. A much higher damping effect due to dry friction can be observed in the released set-up, specially for a long simulation period. The reason is the higher energy dissipation caused by the higher axial pipe-wall displacements in the released set-up. Coulomb's dry friction is a force affecting the momentum of the pipe-wall. Dry friction force times pipe-wall displacement is the energy dissipated by the pipe system to its surroundings.

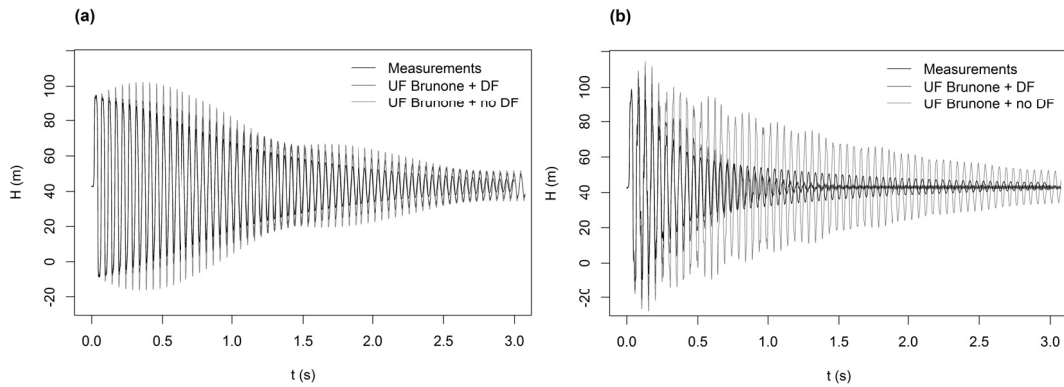


Figure 5.11 – Experimental measurements *vs.* numerical output considering Brunone’s unsteady and including and excluding dry friction for: (a) test SCP03 with anchored pipe-end; and (b) test SCP06 with non-anchored pipe-end. Output from the downstream end section.

In Fig. 5.12 the numerical output, considering the combination of the three phenomena, is compared with the experimental data for all the assessed discharges and for (a) anchored pipe-end and (b) non-anchored pipe-end. Skin friction losses are computed using Brunone’s model and dry friction by Coulomb’s law. The simulation period of 0.15 s allows the assessment of the wave shape. As it can be observed, during the first wave cycles FSI is the dominant effect, specially in the case of the released set-up.

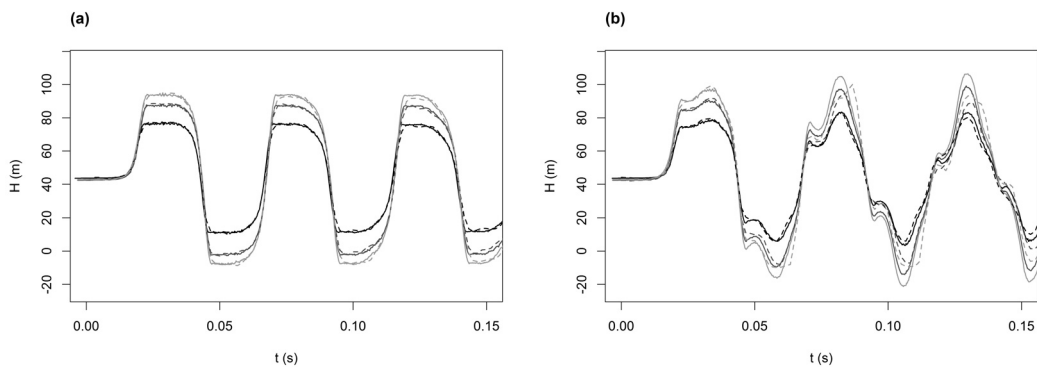


Figure 5.12 – Numerical output (solid lines) considering FSI, Brunone’s unsteady friction and dry friction *vs.* experimental measurements (dashed lines) for the tests SCP01 and SCP04 (black), SCP02 and SCP05 (dark grey), SCP03 and SCP06 (light grey). (a) for anchored pipe-end, (b) for non-anchored pipe-end. Pressure history at the downstream pipe-end.

Discussion of results

The results shown in Subsection 5.2.5 enable the analysis of the reliability of the modelling assumptions concerning fluid-structure interaction, skin friction and dry friction. Notice the coherent pattern followed by all the assessed time series (*vs.* Fig. 5.12): for the different initial

flow velocities (0.26, 0.36, and 0.41 m/s), and for both anchoring set-ups (fixed and moving downstream valve).

The accurate fitting of the first pressure cycle, either in the tests with anchored pipe-end (Fig. 5.12-a) or, specially, in the ones with non-anchored pipe-end (Fig. 5.12-b), indicate the good performance of the four-equation model in describing the pipe system structural behaviour and its rebound on the pressure transient wave. Hence the rightness of the hypothesis of considering the pipe-wall axial vibration is confirmed, being FSI dominant over UF and DF at the beginning of the transient. However, as the wave propagates (second and third wave cycles) the numerical output, in the case of non-anchored pipe-end, tends to detach from the measured data revealing that modelling assumptions can be further improved.

Moreover, the long term simulations (*v.s.* Fig. 5.10) show that Brunone's unsteady friction computation outputs slightly higher wave damping as compared with the experimental tests. However, if dry friction is not considered in the numerical model, such damping is even further from the one observed in the real pipe system. When dry friction is included (*v.s.* Fig. 5.11) the wave damping rate is improved, yet remains insufficient in the set-up with anchored pipe-end and overestimated in the released pipe-end.

Anchoring conditions are deeper analysed in the following Fig. 5.13 for the tests SCP03 (anchored pipe-end) and SCP06 (non-anchored pipe-end), revealing the different FSI behaviour dependent on the anchoring conditions for longer simulation periods.

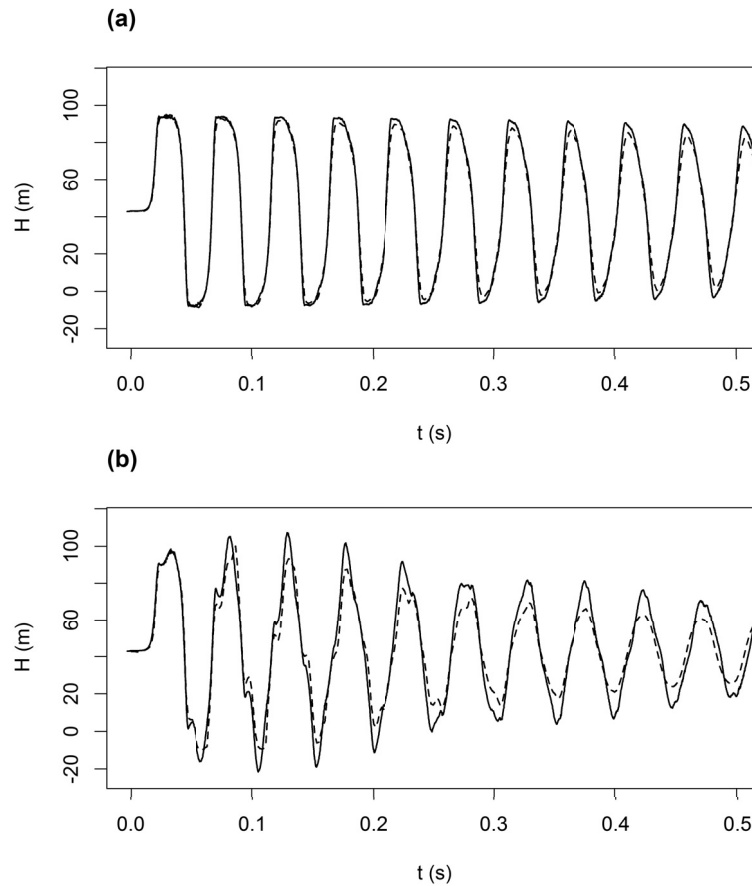


Figure 5.13 – Numerical output (solid lines) considering FSI, Brunone’s unsteady and Coulomb’s dry friction losses *vs.* experimental measurements (dashed lines) for: (a) test SCP03, with anchored downstream end; and (b) test SCP06, with non-anchored downstream end.

Junction coupling at the downstream pipe-end section plays a very important role in the system response (*e.g.* Fig. 5.13-b). The evident wave shape change is a result from the interaction between the two first pipe vibration modes, related with the fluid pressure and the axial pipe movement. This characteristic wave shape change due to the pipe vibration mode for a released downstream valve was described by Bergant *et al.* (2008b) from a numerical point of view and by Ferràs *et al.* (2015b) from an experimental standpoint.

In addition, in the case of a non-anchored pipe-end a clear wave delay can be observed with respect to the anchored set-up (*cp.* Fig. 5.13-a and 5.13-b). This wave delay occurs due to the vibration of the pipe when this is released, and it can be observed straight from the comparison of experimental time series. However, after some wave cycles ($t \gtrsim 0.4$), numerical output tends to overestimate this delay (*cp.* time series SCP06, solid and dashed lines from Fig. 5.13-b).

FSI does not directly affect the wave dissipation; momentum is transferred from the fluid to the structure but also the other way around. Hence it is by means of dry friction that the

momentum transferred to the structure is finally dissipated. Consequently, the reason why the numerical output mismatches wave dissipation and phase after some wave cycles lies in the dry friction modelling, specially in the stick-slip condition, which is distributed throughout the pipe and is not treated differently at the valve section. The valve is heavier and, consequently, dry friction losses should be higher and the stick-slip effect more intensive. In the case of the released pipe-end set-up, dry friction is underestimated in the first wave cycles and subsequently overestimated during further propagation. FSI should be diminished according to stick-slip condition in a way that junction coupling would be dominant only during the firsts oscillations. Additionally, the hose connected downstream the valve could affect as well the experimental pipe rig behaviour, increasing the inertia of the pipe downstream end.

With regard to skin friction head losses, Fig. 5.10 depicts the numerical output considering Brunone's and Trikha's unsteady friction model in comparison with measurements from the test SCP03 (anchored pipe-end) and SCP06 (non-anchored pipe-end). Both unsteady friction models are in agreement as they offer a pretty similar wave damping. In terms of wave timing, Brunone's adds more wave delay than Trikha's. In the case of anchored pipe-end this delay matches with good accuracy the wave propagation. In the test SCP03 fluid-structure interaction is highly constrained and unsteady skin friction rather isolated as being the only damping mechanisms. Observing a zoom between $t = 1$ s and $t = 1.5$ s, depicted in Fig. 5.14, Brunone's model seems to be more faithful to the real system behaviour than Trikha's.

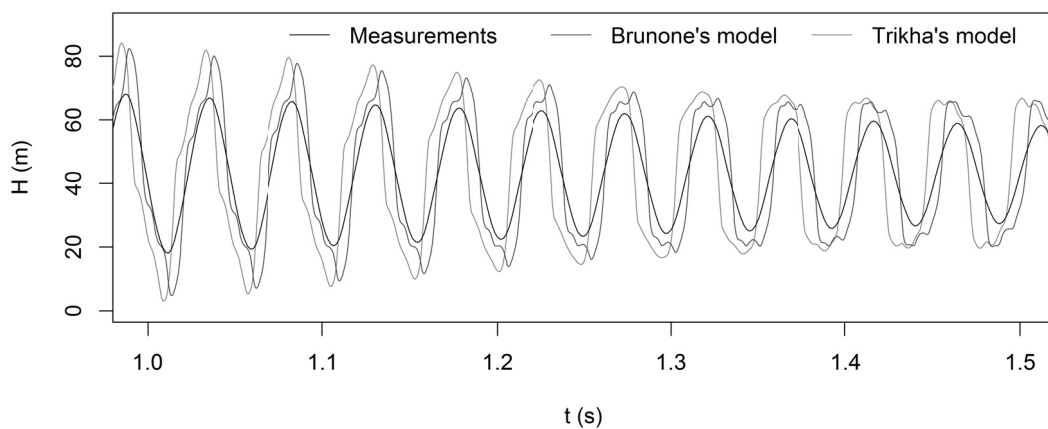


Figure 5.14 – Numerical output for Brunone's and Trikha's friction losses *vs.* experimental measurements for the test with anchored downstream end (SCP03). Time window between $t = 1$ s and $t = 1.5$ s.

With regard to dry friction, Fig. 5.11 confronts the numerical output either including or excluding dry friction losses. For anchored pipe-end, the dry friction affects the wave shape (*v.i.* Fig.5.15-a) and the additional damping adjusts and develops in a closer manner to the real wave, though, this is still underestimated for the fixed valve set-up, as lower momentum is transferred from the fluid to the structure. On the contrary, in the case of a non-anchored pipe-end the effect of Coulomb friction is much more evident, where the dry dissipation

fully dampens the wave in a long term simulation (*vi.* Fig. 5.15-b). At this stage the model overestimates wave damping because it fails on describing the stick-slip phenomenon. The reason is that the implemented distributed dry friction does not allow to locally adjust dry friction dissipation at the valve section. It is also important to highlight that in both anchoring conditions dry friction does not directly influence the wave timing but only shape and amplitude.

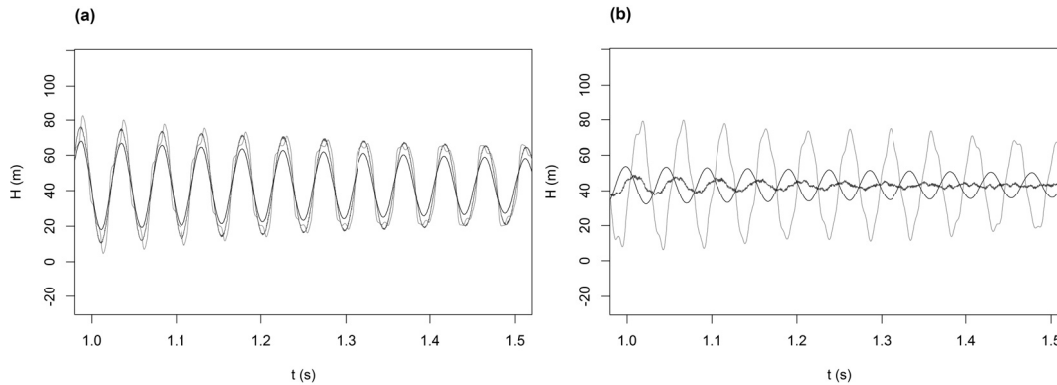


Figure 5.15 – Experimental measurements (black lines) *vs.* numerical output considering Brunone's friction losses and with (blue lines) or without (red lines) dry friction for the tests: SCP03, with anchored downstream end (a); and SCP06, with non-anchored downstream end (b). Time window between $t = 1$ s and $t = 1.5$ s.

An adjustment of the static dry friction coefficient would either enhance the output for the anchored valve set-up (Fig.5.15-a) and worsen the non-anchored one (Fig.5.15-b), or the other way around. This is a sign that stick-slip condition merits further improvement by means of imposing null pipe movement when stick condition is true. Though, this would involve the implementation of internal conditions and describing dry friction as junction coupling rather than friction coupling, which is out of the scope of the present research.

5.2.6 Research outcome

The present section is based on the implementation of a 1D four-equation MOC solver. Experimental data collected from a straight copper pipe-rig are used for the model validation of the main modelling assumptions in terms of wave shape, timing and damping. Fluid-structure interaction, skin friction and dry friction are the main phenomena to be assessed. Essentially, the implemented FSI code includes three coupling mechanisms: Poisson, junction and friction coupling. The last one nests the skin friction models (*i.e.* quasi-steady, Brunone's and Trikha's) and the dry friction model (*i.e.* Coulomb's friction).

Two different experimental set-ups are assessed: (i) anchored downstream pipe-end, and (ii) non-anchored downstream pipe-end. In both cases the pipe is lying over the floor of the laboratory. In the first set-up Poisson coupling dominates the FSI physical phenomenon (*cf.*

5.3. Pipelines anchored against longitudinal movement

Fig. 5.12-a), while in the second set-up junction coupling at the downstream valve section strongly affects the transient wave (*cf.* Fig. 5.12-b). Numerical results satisfactorily fit measured pressure head at the downstream section for the first wave cycle, when FSI phenomenon is dominant. However, numerical output tends to detach for a long term simulation, specially in the set-up for a non-anchored downstream pipe-end (*cf.* Fig. 5.13). Skin and dry friction dissipation are the dominant damping phenomena in the long term simulation.

Unsteady friction effects are rather isolated in the anchored set-up as less momentum is transferred to the structure and consequently FSI and dry friction effects are much lower. For this set-up Brunone's unsteady friction model gives a better performance in the account of both wave timing and damping (*cf.* Fig. 5.10). However, without the incorporation of dry friction, a clear additional wave damping is missing.

The implementation of Coulomb's dry friction model aims at describing this additional wave damping. Dry friction arises from the shear between the pipe-wall and its surroundings. Consequently, its effect is strongly related with the FSI occurring during the transient event. The higher momentum is transferred to the pipe-wall, the greater the effect of dry friction is (*c.p.* Figs. 5.11-a and 5.11-b). The inclusion of dry friction allowed a clear improvement of the numerical model output, proving the importance of considering such phenomenon in hydraulic transient analyses. Nonetheless, the present approach of nesting the Coulomb model in the FSI friction coupling does not allow for a fully satisfactory description of the observed pressure signal (Fig. 5.13 and 5.15), specially in the case of released downstream pipe-end. The dry friction dissipation occurring at the valve section is crucial for the accurate description of the pipe system behaviour, and this should be treated differently for two main reasons. First, the valve section is heavier and pipe-wall displacements are higher than any other section, hence kinematic dry friction dissipation is greater at the downstream section. Second, fluid-structure interaction effect is more intensive at the downstream end, and consequently more sensitive to stick-slip condition.

At this stage of research the authors conclude that a more satisfactory means to represent junction coupling merits being investigated. In fact, assumptions on dry friction computation need a further upgrade as, in the present work, Coulomb's model was nested in the FSI friction coupling but not considered in junction coupling. Junction coupling arises from a balance of forces at pipe junctions, tees, elbows, boundaries, etc. Dry friction force can be as well considered in such a balance. Using this approach stick-slip condition could be as well improved by imposing null pipe-wall movement when stick criterion is met.

5.3 Pipelines anchored against longitudinal movement

5.3.1 Introduction and background theory

In simple reservoir-pipe-valve systems, FSI occurs mainly due to the Poisson effect and the movement of the downstream valve. These mechanisms excite the second pipe vibration

Chapter 5. Fluid-structure interaction in straight pipelines

mode, which is the corresponding to the axial movement of the pipe. Anchor or thrust blocks are frequently used in straight pipelines to restrict and to avoid these movements so that the piping structure is stable and reliable. Anchor blocks absorb the axial stresses of the pipe-wall, which are transmitted to the surrounding ground by means of dry friction (Feeny *et al.*, 1998). The present research aims at describing the behaviour of straight pipelines fixed to anchor blocks by means of a four-equation model.

A four-equation model solved by the Method of Characteristics (MOC) represents a suitable tool to describe FSI in straight pipes (Tijsseling, 1996; Wiggert, 1983; Wiggert *et al.*, 1985a; Lavooij & Tijsseling, 1991). However, to the knowledge of the authors, hardly any work has been carried out to describe the pipe supporting conditions, often not well defined (Tijsseling & Vardy, 1996a). A fluid-structure interaction analysis for anchor blocks taking into account the block inertia and the dry friction with the surrounding ground would fill this gap in literature.

From one side, Heinsbroek & Tijsseling Heinsbroek & Tijsseling (1994) worked on the assessment of the influence of the pipe-supports stiffness, concluding that the stiffness of the supports affects waterhammer pressure amplitude and phase, and pointed out to the need of more detailed analyses. Tijsseling & Vardy Tijsseling & Vardy (1996a) investigated the effect of pipe racks on waterhammer waves considering the dry friction occurring between the pipe-wall and the rack; accurate numerical results were compared with measurements; quantitative criteria to assess when dry friction forces are relevant during hydraulic transients were proposed. On the other side, Lavooij & Tijsseling Lavooij & Tijsseling (1991) analysed the effect of the inertia of a downstream moving valve during a waterhammer event. An anchor block located at the downstream pipe-end would behave in a very similar manner to a moving valve but likely with a heavier mass. Yang & Zhang Yang *et al.* (2004) analysed in the frequency domain the effect of rigid constraints in multi-span pipes, concluding that the junction coupling has a larger effect on the transient wave than the Poisson coupling.

The novelty of the present study consists of the development and validation of a four-equation model capable of accurately describing anchor blocks behaviour located at any section of the pipe, moving rigidly with the pipe-wall, taking into account the block inertia and the dry friction between the blocks and the ground. For model validation, experimental waterhammer tests were carried out in a straight copper pipe-rig for three different basic set-ups consisting of, alternatively, releasing or anchoring the downstream valve or a midstream anchor block. Additionally, a sequence of tests was run in which the pipe supports were systematically released from the downstream to the upstream end.

5.3.2 Experimental data collection

For the present study different supporting configurations of the SCP pipe rig have been analysed (*u.i.* Fig.5.16): (a) setup-1 where the conduit is anchored against longitudinal movement at both downstream and upstream ends; (b) setup-2 where the conduit is only anchored against longitudinal movement at the upstream end; and (c) setup-3 where the conduit is

5.3. Pipelines anchored against longitudinal movement

anchored against longitudinal movement at the midstream and the upstream sections.

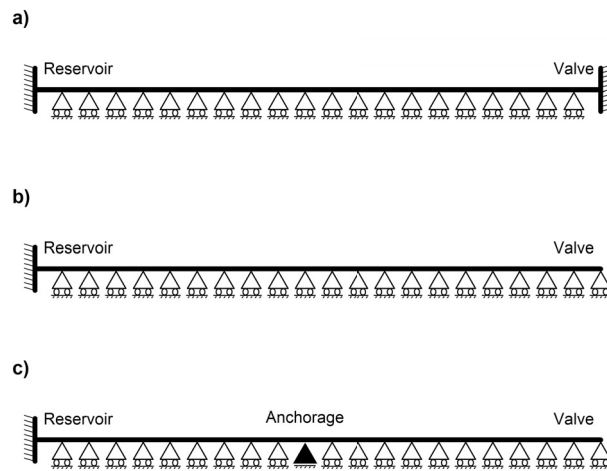


Figure 5.16 – Different tested configurations: (a) setup-1 where the conduit is anchored at both pipe ends; (b) setup-2 where the conduit is only anchored at the upstream end; and (c) setup-3 where the conduit is anchored at the midstream and upstream sections of the pipe.

The experimental tests carried out for the three different set-ups and for an initial discharge of $Q = 300 \text{ l/h}$ are depicted in Fig 5.17.

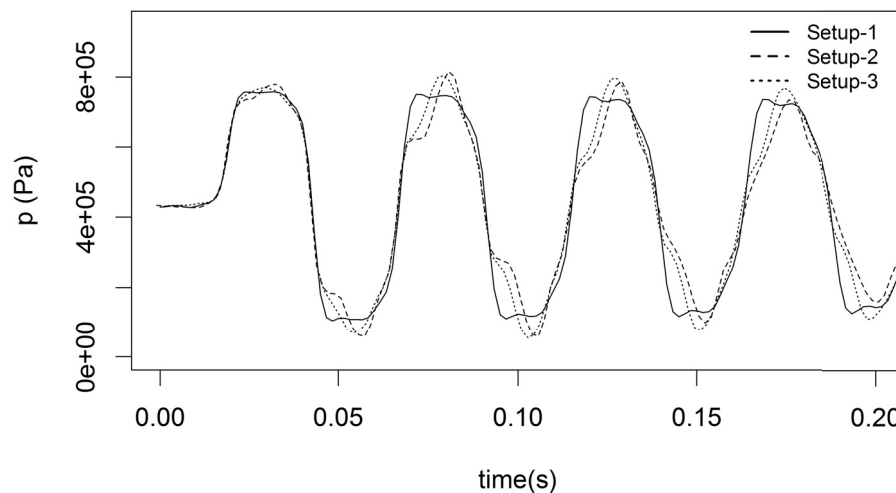


Figure 5.17 – Waterhammer tests carried out for a conduit anchored at the upstream and downstream pipe-ends (setup-1); anchored only at the upstream end (setup-2); and anchored at the upstream and midstream pipe sections (setup-3), for $Q = 300 \text{ l/h}$.

Additionally, a set of tests was carried out consisting of first fixing the facility against longitudinal movement all throughout the pipe and then, sequentially, releasing the supports one by one, from the downstream valve to the upstream end reservoir, and carrying out water-

hammer tests one at a time. Fig 5.18 shows the results of these tests for an initial discharge of $Q = 426 \text{ l/h}$.

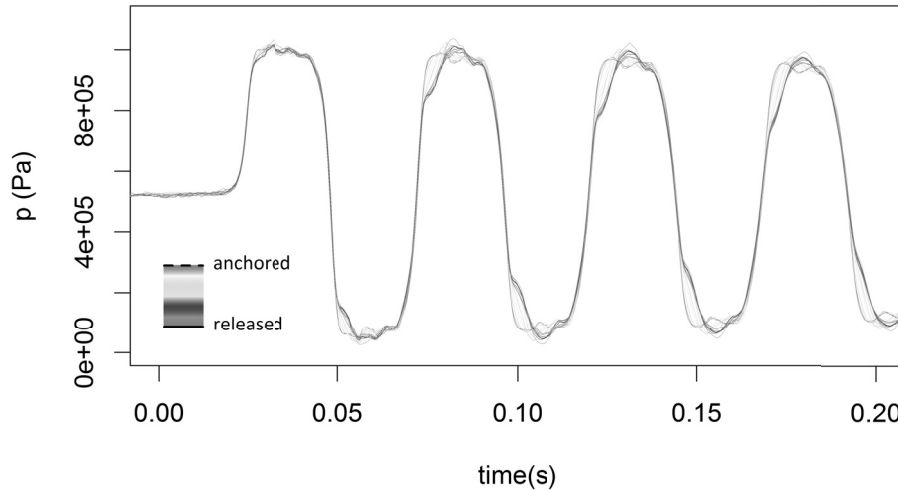


Figure 5.18 – Set of waterhammer tests consisting of releasing one support at a time, from the downstream to the upstream pipe-end, starting from a fully anchored pipe against longitudinal movement, for $Q = 426 \text{ l/h}$ and 23 tests in total.

5.3.3 Numerical model development

Numerical scheme

By assuming that the ratio between the wave celerity in the fluid and in the pipe-wall can be expressed by the ratio of two natural numbers ($a_h/a_3 \approx \mathbb{N}_f/\mathbb{N}_s$), leaps can be applied in both characteristic lines and these can be fitted in a regular grid (Tijsseling & Lavooij, 1990; Lavooij & Tijsseling, 1991).

Fig. 5.19 depicts the adopted numerical scheme at the interior nodes and the domain boundaries, where: 'P' represents the space and time coordinates in the grid where the computation is carried out, 'A' represents the information source brought by the positive characteristic line in the pipe-wall, 'B' the information source brought by the positive characteristic line in the fluid, 'C' the information source brought by the negative characteristic line in the fluid and 'D' the information source brought by the negative characteristic line in the pipe-wall.

5.3. Pipelines anchored against longitudinal movement

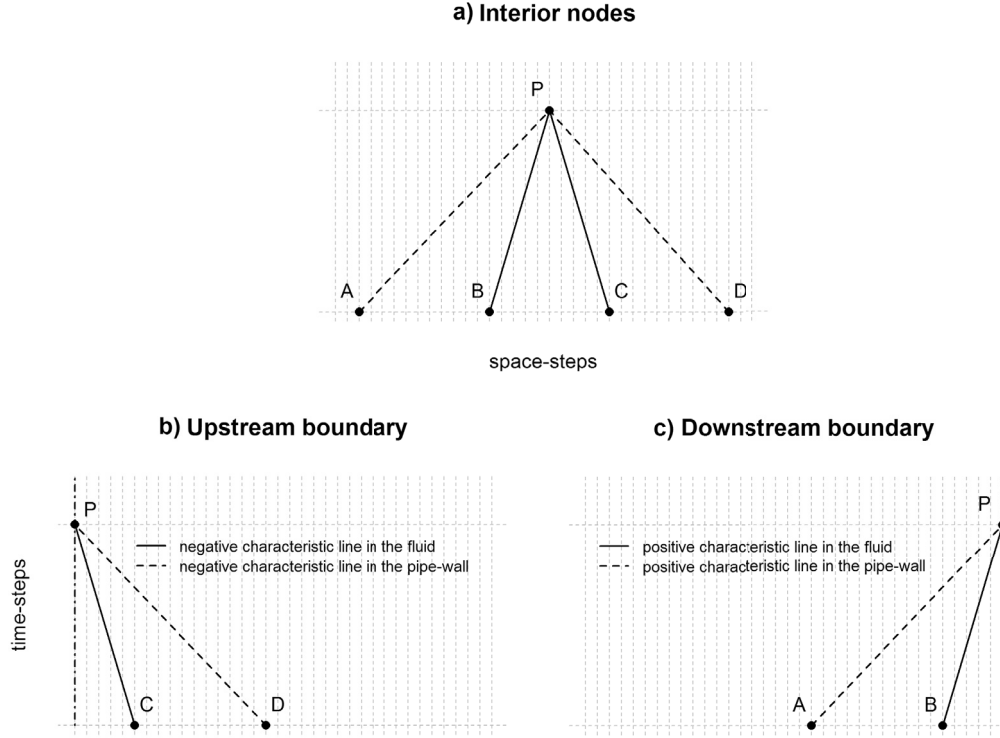


Figure 5.19 – Numerical scheme of the four-equation model. Characteristic lines at different sections of the pipe: (a) at the interior nodes; (b) at the upstream boundary; and (c) at the downstream boundary.

After the MOC transformation the set of partial differential equations (Eqs. A.47) can be expressed in terms of compatibility equations by means of time integration, using p_P , V_P , σ_P and U_P as dependent variables. The ξ coefficients are presented in Table B.3.

$$\xi_{f_V} V_P + \xi_{f_p} p_P + \xi_{f_U} U_P - \xi_{f_\sigma} \sigma_P + C p_f = 0 \quad (5.31)$$

$$\xi_{f_V} V_P - \xi_{f_p} p_P + \xi_{f_U} U_P + \xi_{f_\sigma} \sigma_P + C n_f = 0 \quad (5.32)$$

$$-\xi_{s_V} V_P - \xi_{s_p} p_P + \xi_{s_U} U_P - \xi_{s_\sigma} \sigma_P + C p_s = 0 \quad (5.33)$$

$$-\xi_{s_V} V_P + \xi_{s_p} p_P + \xi_{s_U} U_P + \xi_{s_\sigma} \sigma_P + C n_s = 0 \quad (5.34)$$

where Eqs. (5.31) and (5.32) correspond to the positive and negative characteristic equations of the fluid pressure wave and Eqs. (5.33) and (5.34) correspond to the positive and negative characteristic equations of the axial stress wave. The values $C p_f$, $C n_f$, $C p_s$ and $C n_s$ enclose the information from the previous time-step:

$$Cp_f = -\xi_{fV} V_B - \xi_{fp} p_B - \xi_{fU} U_B + \xi_{f\sigma} \sigma_B + SF_{fB} \quad (5.35)$$

$$Cn_f = -\xi_{fV} V_C + \xi_{fp} p_C - \xi_{fU} U_C - \xi_{f\sigma} \sigma_C + SF_{fC} \quad (5.36)$$

$$Cp_s = \xi_{sV} V_A + \xi_{sp} p_A - \xi_{sU} U_A + \xi_{s\sigma} \sigma_A + SF_{sA} \quad (5.37)$$

$$Cn_s = \xi_{sV} V_D - \xi_{sp} p_D - \xi_{sU} U_D - \xi_{s\sigma} \sigma_D + SF_{sD} \quad (5.38)$$

where SF terms correspond to the skin friction losses which in the current research have been computed using Brunonone's unsteady skin friction model (*cf.* Table D.2).

Interior nodes

The dependent variables along the interior nodes are obtained from sorting out the linear system of equations, Eqs. (5.31), (5.32), (5.33) and (5.34), and are defined as follows:

$$p_P = -\frac{\frac{Cp_f - Cn_f}{\xi_{f\sigma}} - \frac{Cp_s - Cn_s}{\xi_{s\sigma}}}{2\left(\frac{\xi_{fp}}{\xi_{f\sigma}} + \frac{\xi_{sp}}{\xi_{s\sigma}}\right)} \quad (5.39)$$

$$V_P = -\frac{\frac{Cp_f + Cn_f}{\xi_{fU}} - \frac{Cp_s + Cn_s}{\xi_{sU}}}{2\left(\frac{\xi_{fV}}{\xi_{fU}} + \frac{\xi_{sV}}{\xi_{sU}}\right)} \quad (5.40)$$

$$\sigma_P = \frac{\frac{Cp_f - Cn_f}{\xi_{fp}} + \frac{Cp_s - Cn_s}{\xi_{sp}}}{2\left(\frac{\xi_{f\sigma}}{\xi_{fp}} + \frac{\xi_{s\sigma}}{\xi_{sp}}\right)} \quad (5.41)$$

$$U_P = -\frac{\frac{Cp_f + Cn_f}{\xi_{fV}} + \frac{Cp_s + Cn_s}{\xi_{sV}}}{2\left(\frac{\xi_{fU}}{\xi_{fV}} + \frac{\xi_{sU}}{\xi_{sV}}\right)} \quad (5.42)$$

Boundary conditions

Upstream reservoir: Only the negative characteristic lines reach the upstream boundary as shown in Fig. 5.19. The boundary condition for a constant level reservoir in the upstream

5.3. Pipelines anchored against longitudinal movement

pipe-end is given by:

$$p_P = p_{res} \quad (5.43)$$

$$U_P = 0 \quad (5.44)$$

Substituting the Eqs. (5.43) and (5.44) into Eqs. (5.32) and (5.34) expressions for V_P and σ_P are obtained.

$$V_P = \frac{\left(\frac{\xi_{fp}}{\xi_{fs}} + \frac{\xi_{sp}}{\xi_{ss}}\right) p_{res} - \frac{Cn_f}{\xi_{fs}} + \frac{Cn_s}{\xi_{ss}}}{\frac{\xi_{fv}}{\xi_{fs}} + \frac{\xi_{sv}}{\xi_{ss}}} \quad (5.45)$$

$$\sigma_P = \frac{\left(\frac{\xi_{fp}}{\xi_{fv}} - \frac{\xi_{sp}}{\xi_{sv}}\right) p_{res} - \frac{Cn_f}{\xi_{fv}} - \frac{Cn_s}{\xi_{sv}}}{\frac{\xi_{fs}}{\xi_{fv}} + \frac{\xi_{ss}}{\xi_{sv}}} \quad (5.46)$$

Downstream valve: A solution is derived for a non-anchored downstream valve taking into account the valve inertia and the dry friction between the valve and the supporting structure. Only the positive characteristic lines reach the downstream boundary as shown in Fig. 5.19. The boundary conditions for such assumptions are expressed in Eqs. (5.47) and (5.48), where the first determines a closed valve and the second the balance of forces at the valve section by means of Newton's second law of motion.

$$V_P = U_P \quad (5.47)$$

$$\sigma_P = \frac{1}{A_s} \left(A_f (1 - \tau(t)) (p_P - p_0) - \mu F_N \text{sign}(U) - Mv \frac{\Delta U}{\Delta t} \right) \quad (5.48)$$

Substituting the Eqs. (5.47) and (5.48) into Eqs. (5.31) and (5.33) expressions for p_P and U_P are obtained.

$$p_P = \frac{\frac{-\frac{A_f}{A_p} p_0 \xi_{fs} + \frac{m_v}{A_p \Delta t} U_{p-1} \xi_{fs} - \xi_{fs} \frac{\mu F_N}{A_p} \text{sign}(U) - Cpf}{\xi_{fv} + \frac{m_v}{A_p \Delta t} \xi_{fs} + \xi_{fu}} - \frac{-\frac{A_f}{A_p} p_0 \xi_{ss} + \frac{m_v}{A_p \Delta t} U_{p-1} \xi_{ss} - \xi_{ss} \frac{\mu F_N}{A_p} \text{sign}(U) - Cps}{-\xi_{sv} + \frac{m_v}{A_p \Delta t} \xi_{ss} + \xi_{su}}}{\frac{\xi_{fp} - \frac{A_f}{A_p} \xi_{fs}}{\xi_{fv} + \frac{m_v}{A_p \Delta t} \xi_{fs} + \xi_{fu}} - \frac{-\xi_{sp} - \frac{A_f}{A_p} \xi_{ss}}{-\xi_{sv} + \frac{m_v}{A_p \Delta t} \xi_{ss} + \xi_{su}}} \quad (5.49)$$

$$U_p = \frac{-\frac{A_f}{A_p} p_0 \xi_{f\sigma} + \frac{m\nu}{A_p \Delta t} U_{p-1} \xi_{f\sigma} - \xi_{f\sigma} \frac{\mu FN}{A_p} \text{sign}(U) - Cpf}{\xi_{fp} - \frac{A_f}{A_p} \xi_{f\sigma}} - \frac{-\frac{A_f}{A_p} p_0 \xi_{s\sigma} + \frac{m\nu}{A_p \Delta t} U_{p-1} \xi_{s\sigma} - \xi_{s\sigma} \frac{\mu FN}{A_p} \text{sign}(U) - Cps}{-\xi_{sp} - \frac{A_f}{A_p} \xi_{s\sigma}} \quad (5.50)$$

$$\frac{\xi_{fv} + \frac{m\nu}{A_p \Delta t} \xi_{fv} + \xi_{fU}}{\xi_{fp} - \frac{A_f}{A_p} \xi_{f\sigma}} - \frac{-\xi_{sv} + \frac{m\nu}{A_p \Delta t} \xi_{sv} \xi_{sU}}{-\xi_{sp} - \frac{A_f}{A_p} \xi_{s\sigma}}$$

As consequence of the leaps adopted in the numerical scheme (*v.s.* Fig. 5.19), time-line interpolations have to be carried out at the nodes located in the vicinity of the computational domain boundaries.

Internal conditions, anchor blocks

The usual approach in FSI junction coupling consists of splitting the pipe into segments and then establishing relations (boundary conditions) between these segments (Wiggert & Tijsseling, 2001). In this subsection, a general solution is derived that allows conducting junction coupling of anchor blocks as internal conditions, without the need of dividing the pipe in segments.

For this purpose, special attention is focused on how the anchor blocks affect the characteristic lines in the numerical scheme. The blocks are considered non-deformable and moving jointly with the pipe-wall. Fig 5.20 depicts these assumptions both in the nodes containing anchor blocks and in their vicinities. The vicinity is defined as a group of computational nodes to the side of the anchor block node for which computations are made with a particular set-up.

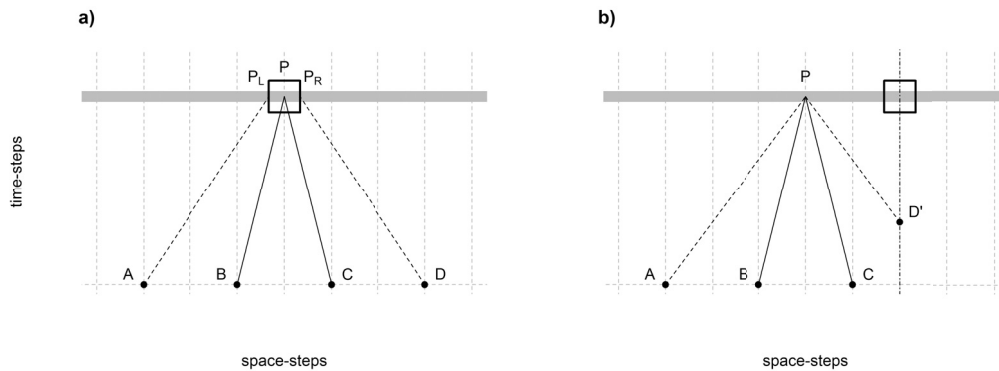


Figure 5.20 – Numerical scheme of the four-equation model. Characteristic lines at (a) anchor block nodes and (b) in their vicinity. The dashed and continuous lines represent characteristic lines in the pipe-wall and in the fluid, respectively.

As shown in Fig. 5.20 characteristic lines in fluid are not disrupted. Time-line interpolation of the variables must be carried out at the anchor block node and the normal equations for inner nodes are applied, Eqs. (5.39) to (5.42), to solve the dependent variables of the system at

5.3. Pipelines anchored against longitudinal movement

the vicinity nodes. Space discretization has to be fine enough to get sufficient computational nodes between pipe supports but coarse enough to avoid numerical diffusion as consequence of too intensive time-line interpolation in their vicinities.

However, the resistance of the anchor block to move produces a discontinuity on the axial stresses in the pipe-wall, which become different upstream and downstream (*i.e.* left and right sides) of the anchor block. Therefore, an imbalance of forces occurs. Fig. 5.21 depicts the forces acting at the anchor block, including: the dry friction force (F_{df}), the weight (F_W), the normal force (F_N) and the force due to the axial stress in the pipe-wall at the left (F_{σ^L}) and at the right of the pipe segment (F_{σ^R}).

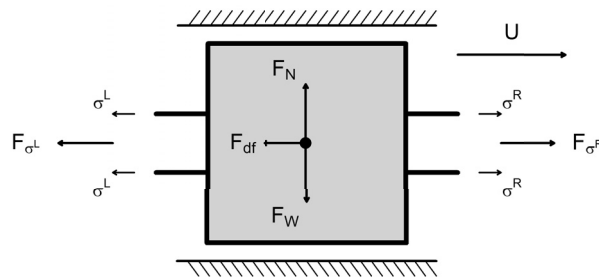


Figure 5.21 – Balance of forces at anchor blocks.

The internal conditions at the nodes containing anchor blocks are defined in Eqs. (5.51) to (5.54).

$$p^L = p^R \quad (5.51)$$

$$V^L = V^R \quad (5.52)$$

$$\sigma^L \neq \sigma^R \quad (5.53)$$

$$U^L = U^R \quad (5.54)$$

The second law of Newton can be applied using the balance of forces at the anchor block from Fig. 5.21:

$$F_{\sigma^R} - F_{\sigma^L} - F_{df} = m_b \dot{U} \quad (5.55)$$

which is the same as:

$$(\sigma_P^R - \sigma_P^L) A_p - \mu g m_b \text{sign}(U) = m_b \frac{\Delta U_P}{\Delta t} \quad (5.56)$$

Chapter 5. Fluid-structure interaction in straight pipelines

On the other hand, the positive characteristic lines in the pipe-wall reach the left side of the anchor block but do not go through it, while in the right side only the negative characteristic lines reach the block. Hence, using respectively the positive and negative characteristic lines in the pipe-wall, left and right axial stresses can be expressed in function of the remaining dependent variables, as shown in Eqs. (5.57) and (5.58).

$$\sigma_P^L = \frac{-\xi_{s_p} p_P - \xi_{s_v} V_P + \xi_{s_U} U_P + C p_s}{\xi_{s_\sigma}} \quad (5.57)$$

$$\sigma_P^R = \frac{-\xi_{s_p} p_P + \xi_{s_v} V_P - \xi_{s_U} U_P - C n_s}{\xi_{s_\sigma}} \quad (5.58)$$

Substituting Eqs. (5.57) and (5.58) into Eq. (5.56) the displacement of the anchor block U can be expressed in function of flow variables (*e.g.*, flow velocity V):

$$U_P = \frac{\frac{2\xi_{s_v} V_P}{\xi_{s_\sigma}} - \frac{C p_s + C n_s}{\xi_{s_\sigma}} + \frac{m_b U_{P-1}}{A_p \Delta t} - g\mu \frac{m_b}{A_p} \text{sign}(U)}{\frac{m_b}{A_p \Delta t} + \frac{2\xi_{s_U}}{\xi_{s_\sigma}}} \quad (5.59)$$

The characteristic lines in the fluid, both positive and negative, go through and reach the centre of the block, hence characteristic equations of the fluid are valid inside the block and allow to express the flow velocity V in function of the block (or pipe-wall) velocity U . Combining Eqs. (5.32) and (5.31) the following expression is obtained:

$$2\xi_{f_v} V_P + 2\xi_{f_U} U_P + C p_f + C n_f = 0 \quad (5.60)$$

and substituting Eq. (5.59) into Eq. (5.60) the solution for the flow velocity V is obtained.

$$V_P = \frac{-C p_f - C n_f - 2\xi_{f_U} \frac{\frac{m_b U_{P-1}}{A_p \Delta t} - g\mu \frac{m_b}{A_p} \text{sign}(U) - \frac{C p_s + C n_s}{\xi_{s_\sigma}}}{\frac{m_b}{A_p \Delta t} + \frac{2\xi_{s_U}}{\xi_{s_\sigma}}}}{2\xi_{f_v} + 2\xi_{f_U} \frac{\frac{2\xi_{s_v}}{\xi_{s_\sigma}}}{\frac{m_b}{A_p \Delta t} + \frac{2\xi_{s_U}}{\xi_{s_\sigma}}}} \quad (5.61)$$

Once V_P is obtained by Eq. (5.61), U_P can be calculated by applying Eq. (5.59), and the remaining dependent variables (*i.e.* p and σ) are calculated by means of Eqs. (5.32) and (5.31).

5.3.4 Model testing

Modal analysis for an empty pipe

If the fluid density is negligible compared to the pipe-wall density (empty pipe assumption) and the mass of the pipe-wall is negligible compared to the mass of the anchor blocks, the piping system can be described as mass-spring systems. If, additionally, the anchor blocks displacement is very small compared to the space discretization of the numerical scheme, this analogy can be described by the method of characteristics (Vardy & Fan, 1986, 1987). Hence, the implemented model can be tested in a way to verify if it enables the description of such mass-spring systems.

For this purpose, simulations have been carried out for different pipe set-ups considering single and multiple degrees-of-freedom. The piping system modelled corresponds to the one described in section 5.3.2 but frictionless, without fluid and incorporating heavy anchor blocks (with $M_a = 1000 \text{ kg}$). The system is excited by imposing initial velocities at the anchor block of $U = 1 \text{ m/s}$. (*v.i.* Figs. 5.22 and 5.23). The number of degrees-of-freedom depends on the number of anchor blocks throughout the pipe, or what is the same, the number of masses in the mass-spring system (Sinha, 2010).

Single degree-of-freedom: There is only one natural mode of oscillation for a one degree-of-freedom of a pipe system with one anchor block. A simple harmonic oscillator, like the one depicted in Fig. 5.22, vibrates at a frequency $f r = \frac{1}{2\pi} \sqrt{\frac{4s}{M_a}}$, where s stands for the ‘spring’ constant and it is directly proportional to the area of the pipe-wall cross section, to the Young’s modulus of elasticity, and inversely proportional to its length. This is the case of a pipe anchored at both ends with an anchor block located at the middle section. Fig. 5.22 shows a scheme of the pipe-block-pipe system under the imposed initial conditions and the respective output from the 4-equation model, showing the resultant natural frequency for a Young’s modulus of elasticity $E = 105 \text{ GPa}$ and $s = 4EAs/L = 518047 \text{ kg/s}^2$.

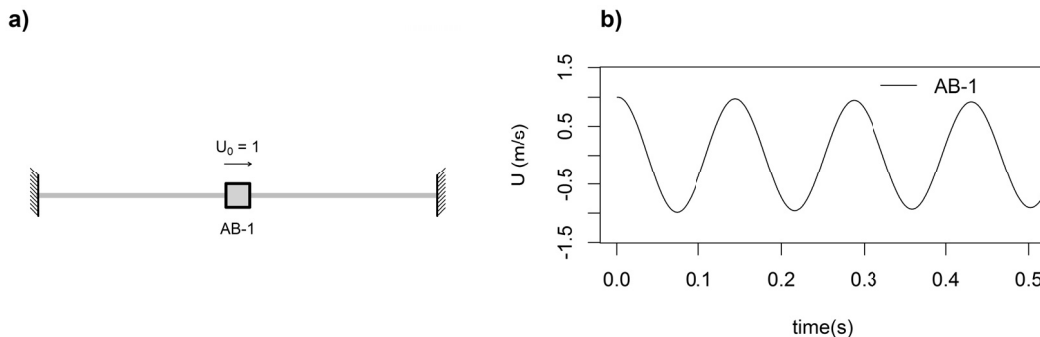


Figure 5.22 – Pipe-block system for one degree-of-freedom. (a) schematic of the modelled system; (b) velocity of the anchor block U .

Multiple degree-of-freedom: Multiple degree-of-freedom systems have more than one natural vibration mode with more than one resonance frequency. The example analysed consists of a 3-DOF system with three identical anchor blocks connected with four identical pipe segments. The system has, therefore, three distinct natural vibration modes that can be observed depending on the initial conditions. Fig. 5.23 presents the second natural vibration mode of this system, for which the initial velocities of the anchor blocks are opposite at the outer blocks and zero at the one in the middle. At this vibration mode the central block does not move (*i.e.* a node), and the outer ones have a symmetrical behaviour. The natural frequency of this vibration mode is $f r = \frac{1}{2\pi} \sqrt{\frac{8s}{M_a}}$, as the aligned ‘springs’ are two times stiffer because four times shorter than the basic system.

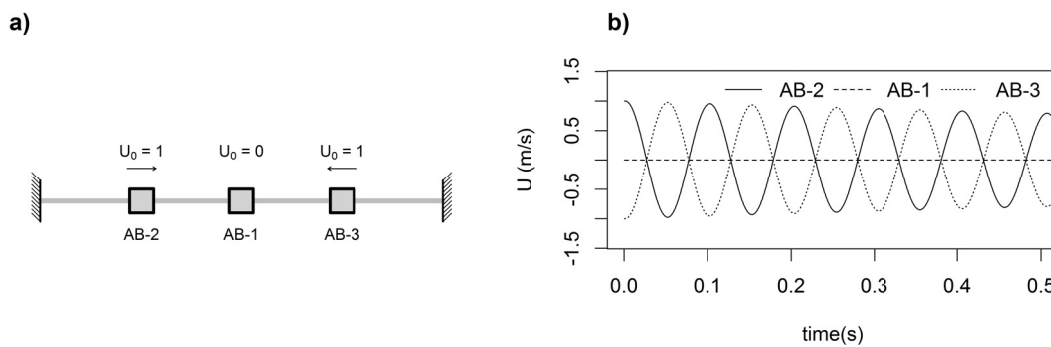


Figure 5.23 – Pipe-block system for three degrees of freedom and second vibration mode: (a) schematic of the modelled system; (b) velocity of the anchor block U .

Modal analysis for a fluid-filled pipe

A similar analysis to the one in the previous subsection is carried out for a fluid-filled conduit. The fluid density is set up to the water density $\rho_f = 1000 \text{ kg/m}^3$ and the fluid elasticity $K = 2.2 \text{ GPa}$ so the numerical model not only describes the transient vibrating pipe but also its interaction with the contained fluid. Due to the high weight of the anchor blocks with respect to the pipe, the transient is dominated by their movement and the interaction is rather from the structure to the fluid, and not the other way around. So the analysis essentially depicts the dominant effect of different pipe vibrating modes on the fluid.

Single-degree-of-freedom: In this simulation two fixed reservoirs at both ends with constant pressure levels and an anchor block in the middle are considered. Like previously, the system is excited by imposing an initial pipe-wall velocity at the anchor-block of $U = 1 \text{ m/s}$. Figure 5.24 depicts the transient velocities at the anchor block section, both of the pipe-wall U and of the fluid V . As it can be seen in Fig. 5.24 the initial longitudinal motion of the anchor block generates an opposite movement in the fluid. Both fluid and pipe-wall oscillate in phase, however the flow velocities remain negative during the whole transient event; the anchor block movement is pumping the fluid from one reservoir to another.

5.3. Pipelines anchored against longitudinal movement

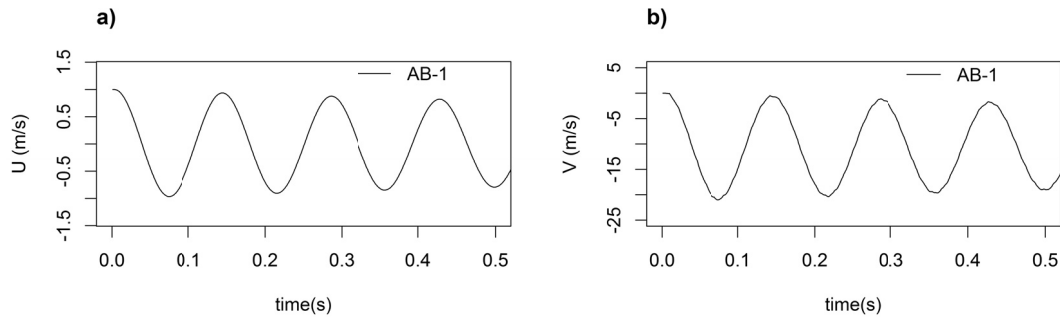


Figure 5.24 – Pipe-block-pipe fluid-filled system for one degree of freedom: (a) velocity of the anchor block U .; and (b) velocity of the fluid V at the anchor block section.

The pumping effect depicted in Fig. 5.24 can be explained by Poisson coupling, which is the interacting mechanisms that transforms the motion of the block to flow change. The vibrating block, with such a heavy mass, generates important oscillating pipe-wall axial deformations, oppositely in both sides of the block, and launching axial stress waves that propagate throughout the pipe. These axial deformations, by means of Poisson effect (Poisson coupling), induce circumferential deformations that affect the fluid flow. The result is a strong oscillating negative flow velocity pumping the fluid from one reservoir to the other.

This effect is similar and could be considered as special case of the Liebau effect, which is object of study in the field of physiological flows and is defined as (Borzi & Propst, 2003): the occurrence of valveless pumping through the application of a periodic force at a place which lies asymmetric with respect to the system configuration. Although the anchor block is located symmetrically, the asymmetry in the case presented hereby lies on the opposite signs of the axial stress waves released in both sides of the anchor block. The flow direction of a Liebau pump is dependent to the frequency of the forced oscillation, while in the phenomenon described hereby the flow direction depends on the initial conditions (*i.e.* U_0). To the knowledge of the authors a Liebau pump based on Poisson coupling has never been described and may be object of further research.

Multiple-degrees-of-freedom: Fig. 5.25 shows, for the fluid-filled 3-DOF set-up, a very similar behaviour regarding the piping structure and a symmetrical behaviour as well regarding the fluid. Flow velocity at the central block section is 0, while antiphase oscillating velocities are observed at the outer blocks' sections.

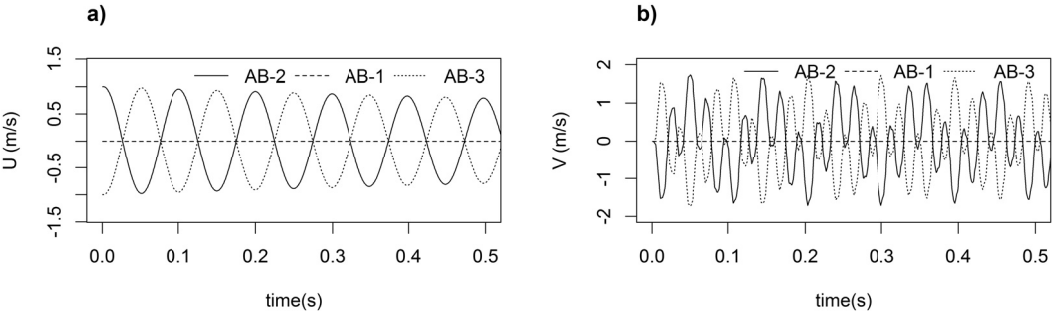


Figure 5.25 – Fluid-filled system for three degrees-of-freedom and second vibration mode: (a) velocity of the anchor block U .; and (b) velocity of the fluid V at the anchor block section.

The vibration mode corresponding to the fluid can be seen in Fig. 5.25-b. Due to the symmetrical transient flow generated by the movement of the structure, the pipe could be split in two identical symmetrical reservoir-pipe-block-pipe-valve systems, with anchored valves. The resultant transients due to the block movements would be exactly the same. From this standpoint it is straightforward to figure out, from classic waterhammer theory, that the frequency of both transient flows is $f r = \frac{a_f}{4L/2} \approx 43 \text{ Hz}$.

The following spectral density plot (*v.i.* Fig. 5.26) confirms the aforementioned statement, where the two dominant frequencies, corresponding to the fluid and the pipe-wall, can be clearly depicted from flow velocity V output data.

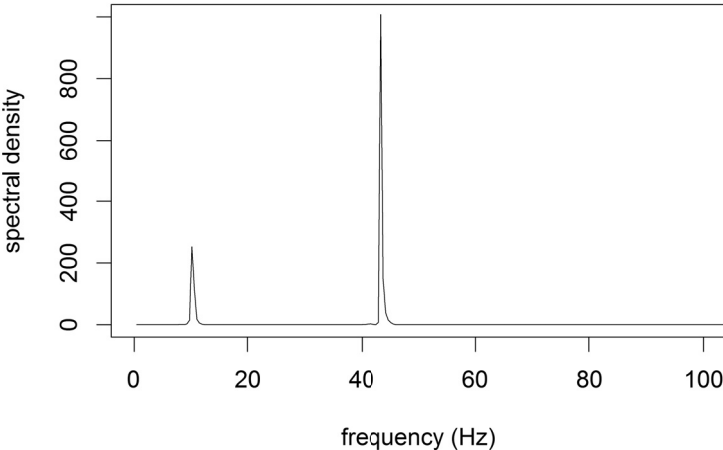


Figure 5.26 – Spectral density plot corresponding to flow velocity output data V from the three degrees-of-freedom set-up.

5.3.5 Model application

Sensitivity analysis

A sensitivity analysis is carried out with the aim to assess how the output is affected by model parameters associated to the resistance of movement of the valve and the anchor blocks due to both inertial and dry friction forces. The numerical model is set up according to the geometry and characteristics of the facility described in Subsection 5.3.2 and kinetic dry friction coefficient μ_k , valve mass and anchor block mass are modified for a wide range of values. Brunone’s unsteady friction model is applied for skin friction computation. All the tests are carried out for an initial discharge of $Q_0 = 426 \text{ l/h}$. Table 5.4 presents a summary of the sensitivity analysis to valve and anchor blocks inertia and dry friction.

Table 5.4 – Tests carried out for the sensitivity analysis.

Phenomenon	parameter	values	simulations	Valve anchorage
Valve inertia	m_v	0 – 12000 kg	100	released
Blocks inertia	m_b	0 – 12000 kg	100	released and fixed
Dry friction at valve	μ_k	0 – 3.3	100	released
Dry friction at blocks	μ_k	0 – 10	100	released and fixed

Sensitivity to valve inertia: With the aim to analyse the sensitivity of the system to the valve inertia, a set of 100 simulations was carried out varying the valve mass from 0 to 12000 kg. During these simulations the valve is released and no dry friction is considered between the valve and its supports. No pipe supports or anchor blocks are considered throughout the pipe, which is free to move in the longitudinal direction. The model output from this analysis is depicted in Fig. 5.27, showing the range of possible solutions of the four-equation model for a frictionless moving valve of variable mass.

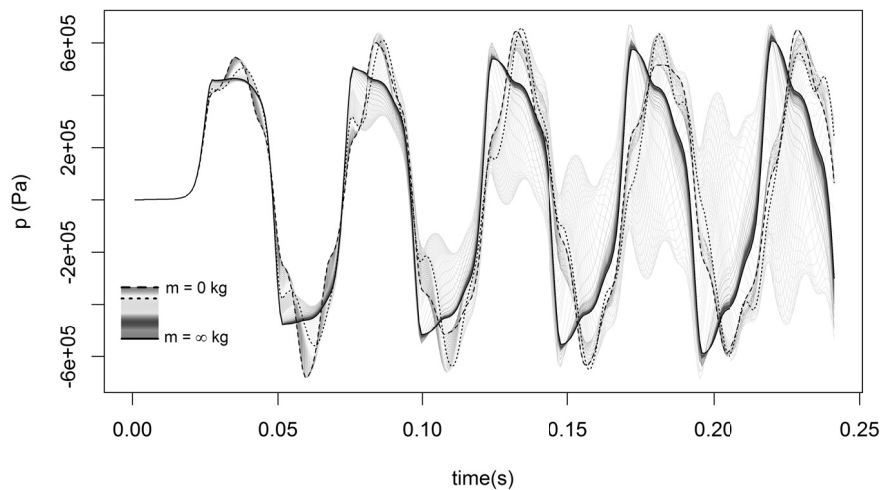


Figure 5.27 – Transient pressures at the downstream pipe-end for a variable valve mass.

Chapter 5. Fluid-structure interaction in straight pipelines

The bold dashed line of Fig. 5.27 indicates the solution for a massless valve, while the solid line depicts the output for the maximum valve mass threshold modelled, which can be considered equivalent to the results for an infinite valve mass or fixed valve. Between this range the progress of model output can be observed according to the mass valve variation. The bold dotted line corresponds to a 6 kg valve mass, which is actually the real mass of the system described in Subsection 5.3.2.

Sensitivity to anchor block inertia: The same kind of analysis is carried out for an anchor block located at the midstream section of the pipe. A number of 100 simulations was launched varying the mass of the anchor block from 0 to 12000 kg. Two different anchoring conditions are assessed: (a) fixing the valve and (b) letting the valve free to move, massless and frictionless. The model output from this analysis is depicted in Fig. 5.28, showing the range of possible solutions of the four-equation model for a frictionless moving anchor block of variable mass at the midstream section of the pipe.

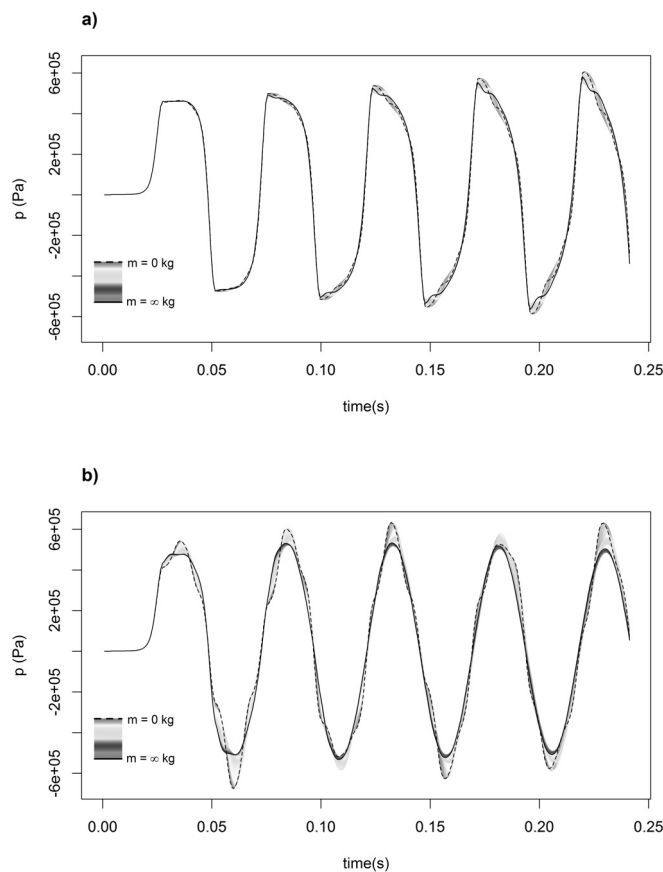


Figure 5.28 – Transient pressures at the downstream pipe-end for the varying mass of an anchor block located at the midstream section of the pipe: (a) the conduit is anchored at both pipe-ends; and (b) the conduit is only anchored at the upstream pipe-end.

5.3. Pipelines anchored against longitudinal movement

The bold dashed line of Fig. 5.28 indicates the solution for a massless anchor block, while the solid line depicts the output for the maximum mass threshold modelled, which can be considered equivalent to the results for an infinite mass or a fixed anchor block. Between this range the progress of model output can be observed according to the mass variation. The dashed line of Fig. 5.28-a is equivalent to the solid line of Fig. 5.27; and the dashed line of Fig. 5.28-b is equivalent to the dashed line of Fig. 5.27.

Sensitivity to dry friction at the valve: Dry friction at the valve section is analysed by first fixing the valve mass to $m_v = 6 \text{ kg}$, which is the real valve mass of the studied piping system, and then varying the Coulomb's friction coefficient μ from 0 to 3.33. No pipe supports or anchor blocks are considered throughout the pipe, which is free to move in the longitudinal direction. The model output from this analysis is depicted in Fig. 5.29, showing the range of possible solutions of the four-equation model for the 6 kg moving valve varying the dry friction.

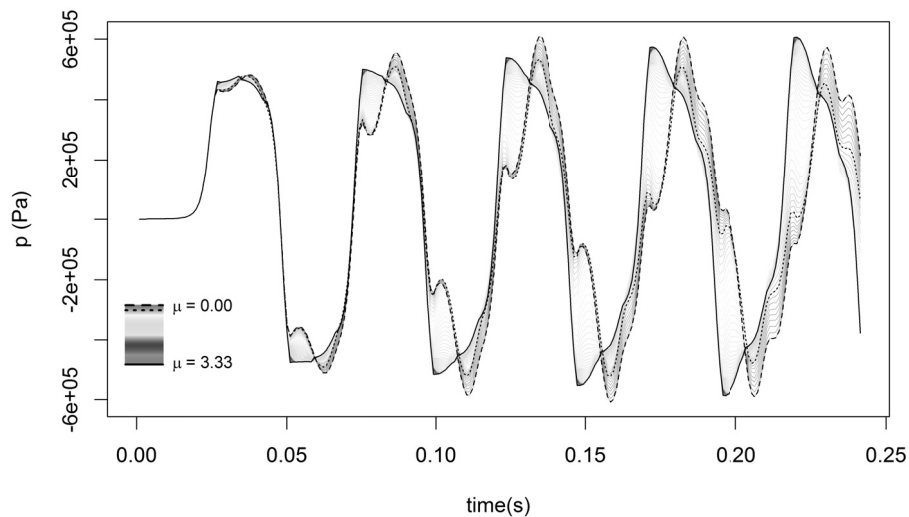


Figure 5.29 – Transient pressures at the downstream pipe-end for the series of simulations varying the dry friction coefficient for a 6 kg mass valve.

The bold dashed line of Fig. 5.29 indicates the solution for a frictionless valve, while the solid line depicts the output for the maximum valve friction threshold modelled, which is equivalent to the results for an almost fixed valve. Between this range the progress of model output can be observed according to the dry friction variation. The bold dotted line corresponds to the value $\mu_k = 0.29$, which is actually the corresponding value for copper sliding over cast iron (Davis, 1997).

Dry friction at anchor blocks: Dry friction at the anchor block section is analysed by first fixing the mass to $m_b = 1 \text{ kg}$, which is the corresponding mass of the pipe segment associated

Chapter 5. Fluid-structure interaction in straight pipelines

to the pipe support, and then varying the Coulomb's friction coefficient μ from 0 to 10. Two different anchoring conditions are assessed: (a) fixing the valve and (b) letting the valve free to move, massless and frictionless. The model output from this analysis is depicted in Fig. 5.30, showing the range of possible solutions of the four-equation model for the varying dry friction.

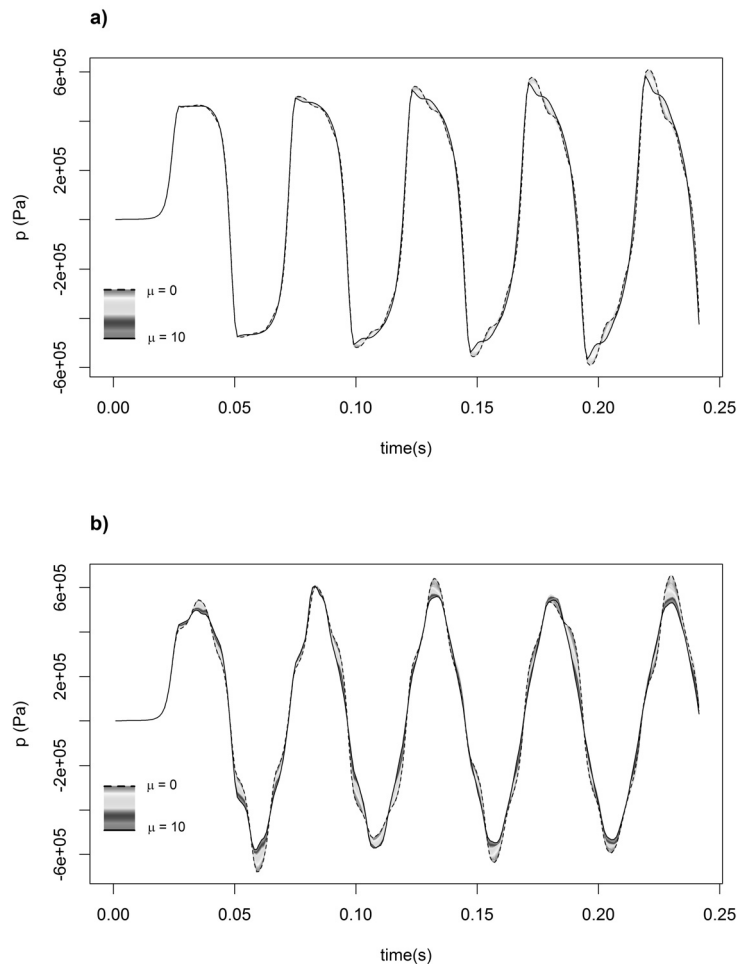


Figure 5.30 – Transient pressures at the downstream pipe-end for the series of simulations varying the dry friction coefficient at the midstream section of the pipe: (a) the conduit is anchored at both pipe-ends; (b) the conduit is anchored only at the upstream end.

The bold dashed lines of Fig. 5.30 indicate the solution for a frictionless anchor block, while the solid lines depict the output for the maximum dry friction threshold modelled, which is equivalent to the results for an almost fixed anchor block. Between this range the progress of model output can be observed according to the dry friction variation. Notice the similarities between the thresholds of Fig. 5.28 and Fig. 5.30.

In general, the system shows a greater sensitivity to the phenomena assessed (*i.e.* inertia

5.3. Pipelines anchored against longitudinal movement

and dry friction) at the downstream valve section rather than at the inner anchor block. The parameter governing the inertia of the valve or anchor blocks is the mass (*i.e.* m_v and m_b), while the parameters governing dry friction are the static Coulomb's friction coefficient μ_s and the kinematic Coulomb's friction coefficient μ_k . In the present sensitivity analysis no distinction between both dry friction coefficients has been done as the goal is the assessment of the overall sensitivity to dry friction. The sensitivity of the numerical model seems to be similar for both inertia and dry friction either at anchor blocks or at the valve.

It is important to highlight that the output resulting from this sensitivity analysis correspond to numerical output that does not have to be especially realistic. For instance, cavitation is not object of study and is not simulated in this assessment, hence the pressure histories presented in Fig. 5.27, 5.28, 5.29 or 5.30 may present values below vapour pressure.

Simulation of the straight copper pipe facility

The straight copper pipe facility described in Subsection 5.3.2 is simulated using the developed four-equation model for the tested configurations. The input parameters of the model are presented in Table 5.5.

Table 5.5 – Input parameters

Parameters for pipe system:						
L (m)	D (m)	e (m)	m_v (kg)	m_b (kg)	t_v (s)	
15.49	0.02	0.001	6	1	0.003	
Parameters for fluid and pipe-wall materials:						
ρ_f (kgm^{-3})	ρ_s (kgm^{-3})	E (GPa)	K (GPa)	ν	μ_s	μ_k
1000	7900	105	2.2	0.33	1.05	0.29
Wave celerities and domain discretization:						
a_1 (ms^{-2})	a_3 (ms^{-2})	dz (m)	dt (s)			
1239	3717	0.286	$2.22 \cdot 10^{-4}$			

Setup-1: In this test the conduit is anchored against longitudinal movement at both downstream and upstream ends. Fig. 5.31 depicts the comparison of numerical results with experimental data. In the first pressure cycles (*v.s.* Fig. 5.31-b), the numerical model seems to be quite accurate regarding to wave shape and timing. However, experimental observations show a higher damping than the numerical results (Fig. 5.31-a). In this setup, the valve is assumed not to move. Although the numerical model is capable of representing dry friction and inertia of the supports, their structural behaviour is not actually described (bending, torsion, *etc.*), so the valve could actually move. As depicted in the previous subsection, the waterhammer wave is very sensitive to the valve movement, hence a minor movement on the valve can be

the reason of the discrepancies observed in the wave damping between measurements and numerical output.

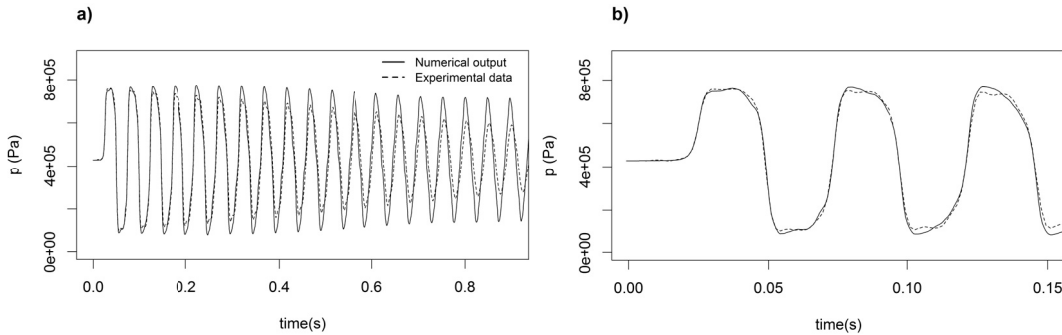


Figure 5.31 – Numerical pressure output *vs.* pressure measurements for a waterhammer test carried out in a conduit anchored against longitudinal movement at both pipe-ends.

Setup-2: For this set-up the conduit is only anchored against longitudinal movement at the upstream end. Numerical results *vs.* experimental data are shown in Fig. 5.32. Very good matching between measurements and numerical output can be observed regarding wave shape, timing and damping. The implemented four-equation model is capable of describing with accuracy the anchoring conditions of Setup-2 for realistic values of valve mass and Coulomb’s dry friction coefficients (μ_s and μ_k). The stick-slip phenomenon is well described as a transition in the wave damping, due to a change from slip to stick state, can be clearly observed in both pressure traces at around $t = 0.3$ s (*vs.* Fig. 5.32-a). Also the FSI induced by the valve movement is well represented as the wave shape and timing are accurate in the first pressure cycles (*vs.* Fig. 5.32-b).

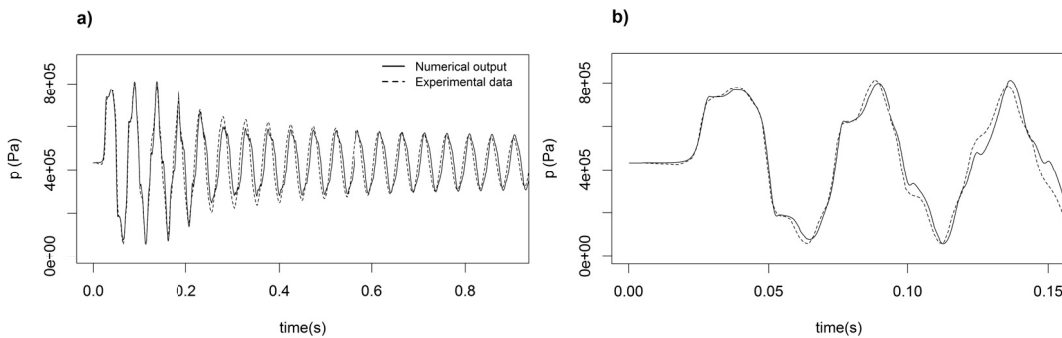


Figure 5.32 – Numerical pressure output *vs.* pressure measurements for a waterhammer test carried out in a conduit anchored against longitudinal movement only at the upstream pipe-end.

Setup-3: Finally, the system is tested for the conduit anchored against longitudinal movement at the midstream and upstream sections of the pipe. Numerical results *vs.* experimental

5.3. Pipelines anchored against longitudinal movement

data are depicted in Fig. 5.33. Anchoring conditions in this setup are also well described by the numerical model. A similar damping transition due to the stick-slip phenomenon can be also observed at around $t = 0.3$ s. Clearly, the major damping mechanism during the first pressure cycles in both setup-2 and 3 is the dry friction induced by the downstream valve movement.

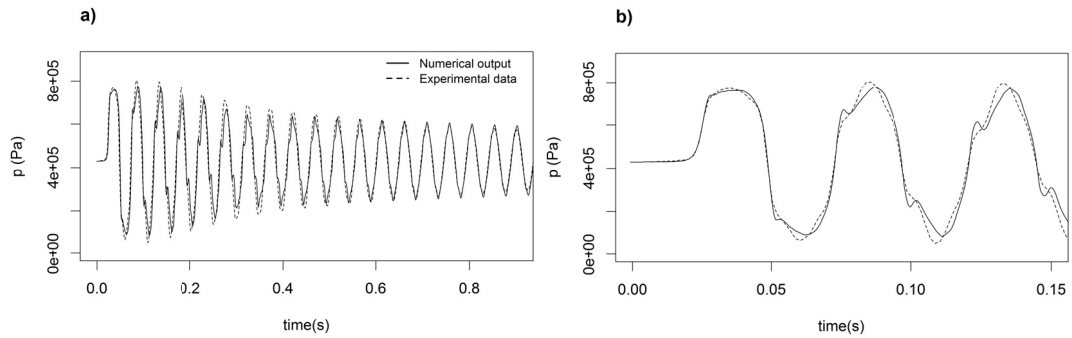


Figure 5.33 – Numerical pressure output *vs.* pressure measurements for a waterhammer test carried out in a conduit anchored against longitudinal movement at the midstream section.

Tests releasing the pipe: Finally, a set of runs was carried out with the goal to simulate the experimental tests where the pipe was released in a stepwise manner: first being fully anchored against longitudinal movement at all supports, then releasing sequentially the pipe supports one by one, from the downstream to the upstream (*cf.* Fig. 5.18). Ten (10) pipe supports homogeneously distributed throughout the conduit, including the downstream section were considered. A total of ten (10) tests were carried out. Fig. 5.34 depicts the experimental data *vs.* the numerical output corresponding to the mentioned sequence of tests.

Fig. 5.34 shows in general:

- similar pressure wave shapes starting from the initial (fully-anchored) set-up, namely in terms of wave amplitudes and frequencies;
- similar pressure signal reaction to the sequential release of the anchor blocks, characterized by an amplification of the initial parts of the pressure wave crests and troughs;
- different amplitudes of second-order perturbations on the initial parts of the pressure wave crest and troughs, which are in the numerical output approximately double from those in the experimental output.

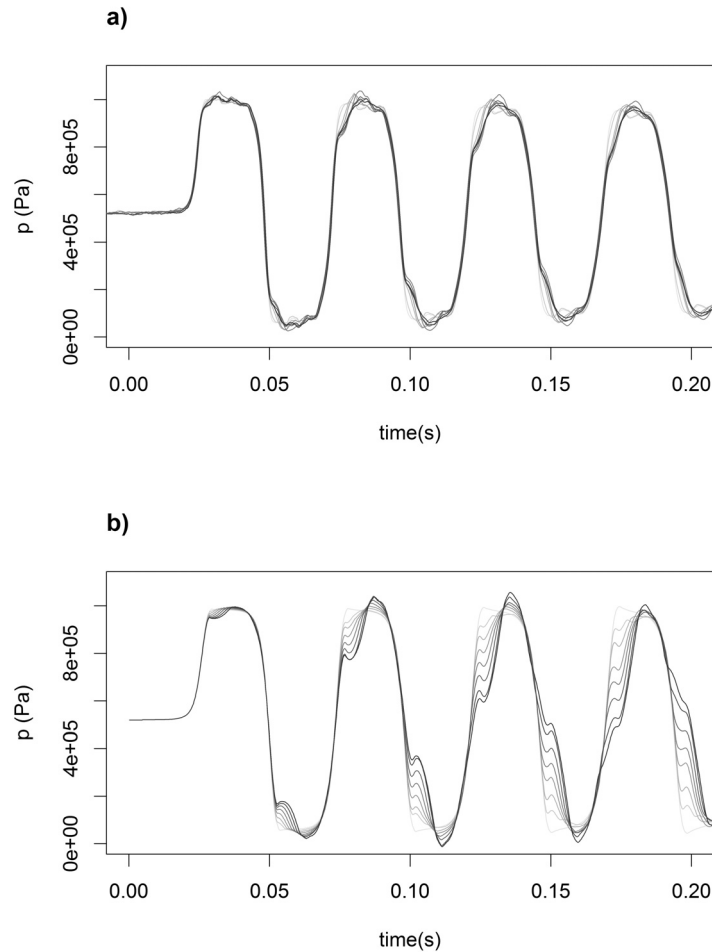


Figure 5.34 – Transient pressures at the downstream pipe-end. Measurements (a) *vs.* numerical pressure output (b) for a set of waterhammer tests consisting on releasing, one support at a time and from downstream to upstream, a fully anchored pipe against longitudinal movement.

5.3.6 Research outcome

A four-equation model was implemented with the goal to describe and investigate the effect of anchor blocks on straight pipelines during hydraulic transients. Inertia of the blocks and the dry friction occurring in the interface between the pipe and the supports were taken into account by means of junction coupling at the anchor blocks sections. In these sections the characteristic lines traveling in the pipe-wall are cut off, while the ones travelling in the fluid are allowed to go through.

The model was tested by establishing an analogy between pipe-block systems and spring-mass systems and then performing a modal analysis allowing some basic degrees-of-freedom. This assessment was first carried out for a fluid-empty conduit and then for a fluid-filled conduit.

For the fluid-empty conduit analysis the model describes successfully the expected vibration modes according to the basic theory of coupled harmonic oscillators. For the fluid-filled conduit, unexpected results were achieved, such as a pumping effect of a 1-DOF bi-anchored pipe where an anchor block located at the midstream is excited by a certain initial velocity.

Once the model was verified, a sensitivity analysis was carried for the basic parameters concerning inertia and dry friction at the valve section and at the anchor block located at the midstream section. This analysis showed that both inertia and dry friction similarly affect the waterhammer wave, more significantly at the downstream pipe section than at the midstream pipe section.

Finally, the numerical model was used to reproduce experimental waterhammer tests carried out for some specific set-ups: setup-1 where the conduit is anchored at both pipe ends; setup-2 where the conduit is only anchored at the upstream end; and setup-3 where the conduit is anchored at the midstream and upstream sections of the pipe. The results show that the numerical model tends to underestimate the wave damping for setup-1, likely due to the non-perfect anchoring of the downstream valve. For setup-2 and 3, the model is very accurate in terms of wave shape, timing and damping. Moreover, it is capable of describing a transition in the wave damping produced by the slip-stick condition, which in the model is conducted by Coulomb's dry friction static and kinematic coefficients.

Additionally, a series of waterhammer tests was carried out consisting of releasing an initially fully anchored pipe, support by support, from the downstream to the upstream end. The numerical model seems to satisfactorily describe the progression of the behaviour of the pipe when it is being released.

The overall outcome of this research gives a valuable insight on the importance of considering the fluid-structure interaction of anchor blocks caused by their resistance to movement, which is their inertia and dry friction. The developed numerical model offers a practical tool allowing the consideration of these effects in daily engineering practice.

5.4 Overview and concluding summary

The chapter approaches the description of hydraulic transients in straight pipelines first focusing on the friction coupling mechanisms and then on the junction coupling by means of the inclusion of internal conditions with the purpose to represent the effect of pipe supports behaviour. The starting point is the basic four-equation model where add-ons are added to account for unsteady skin friction, dry friction, and the anchoring nodes. The models have been successfully validated by means of experimental tests carried out in the SCP pipe rig (*cf.* Subsection 3.2.1).

The first part of the chapter, which focuses on friction coupling mechanisms, concludes that the inclusion of unsteady skin friction in a four-equation model does not differ much from

Chapter 5. Fluid-structure interaction in straight pipelines

the overall skin friction dissipation computed by the traditional quasi-steady assumption. With regard to the dry friction dissipation the computation is distributed throughout the pipe, sidestepping the analysis of dry friction in sections that merit a special treatment, which is the case of the downstream end section. When the valve is free to move its heavier mass and momentum produce a higher dry dissipation that cannot be computed by means of friction coupling but by junction coupling. Consequently, at this stage the four-equation model tends to underestimate dry friction and, therefore, the overall waterhammer wave damping.

The second part of the chapter aims at solving this problem by means of considering the dry friction in the junction coupling mechanism. A complete sensitivity analysis is carried out depicting the influence of the inertia and dry friction of the downstream valve and the anchoring blocks along the pipe. The model was successfully validated for several anchoring set-ups, showing accurate output in terms of wave shape, timing and damping. The overall work shows the importance of taking into account the pipe supports behaviour and the dry friction dissipation. A powerful tool, with a strong applicability potential in daily engineering practices, has been developed considering these effects, showing a high accuracy on the description of hydraulic transients in straight pipelines.

6 General conclusions and future research

6.1 Research overview

Hydraulic transients in liquid filled conduits have been studied focusing the analysis on the fluid-structure interaction occurring in straight and coil pipes and on the main wave dissipating phenomena. In Chapter 2 an extensive state-of-the-art review is presented highlighting the detachment existing between the upgrades developed for the 1D classic waterhammer model and those for the 1D FSI models. An experimental analysis focused on fluid structure interaction and other wave damping phenomena, such as unsteady skin friction, dry friction and pipe-wall viscoelasticity, is presented in Chapter 3. Chapter 4 addresses the specific FSI occurring in pipe coils due to the structure geometry, while the aim of Chapter 5 is the improvement of the FSI modelling of straight pipes, first tackling friction coupling and then junction coupling. The present research is oriented, therefore, to the development of a 1D FSI model for which dissipating phenomena, namely unsteady skin friction and Coulomb's dry friction, are included. Additionally, a robust and accurate novel approach for the modelling of anchor and thrust blocks in straight pipelines is presented.

6.2 Main scientific outcome

Degrees-of-freedom as standpoint for FSI analysis: A new perspective is provided with respect to the theoretical background of FSI 1D modelling by means of a novel classification based on pipe degrees-of-freedom. Governing equations, both for the traditional two-equation model and the more complex four-equation model, are derived by combining the fundamental equations of each DOF and following the basic assumptions stated in literature (*cf.* A). The main scientific contribution of this part of the work is an original standpoint that the author suggests for tackling FSI problems

FSI evidence in multiple pipe rigs: In a second stage, extensive series of experimental data acquired from several pipe rigs, with different pipe materials and geometries, are presented.

Chapter 6. General conclusions and future research

The analysis allows the identification and evaluation of waterhammer wave damping phenomena, namely fluid-structure interaction, pipe-wall viscoelasticity or unsteady skin friction. The understanding of these physical phenomena is crucial for the development, implementation and validation, of waterhammer software. Chapter 3 provides, therefore, valuable and reliable experimental data for waterhammer researchers validating developed solvers.

Pipe coil mechanical breathing effect description: Pipe coils are very convenient in hydraulic laboratories, as they allow long pipes in reduced spaces, however the coil behaviour under transient conditions is not fully understood yet. In Chapter 3 a coil ‘breathing’ effect is pointed out as the cause of a systematic reduction of the waterhammer wave amplitude. To the knowledge of the author, this effect has never been described in literature. The FSI study presented in Chapter 4 finds out the adequate modelling assumptions for a successful simulation of the FSI occurring in pipe coils, bringing insight in the understanding of the behaviour of these pipe systems. The analysis is based on the coil copper facility, where the mechanical breathing effect is more evident from experimental observations. In the coil polyethylene facility, though, the phenomenon is hindered by the pipe-wall viscoelasticity, which is clearly the dominant damping effect.

FSI friction coupling in straight pipelines: Fluid-structure interaction mechanisms, unsteady skin friction and dry friction are used for the model development. First, the work focuses on the friction coupling, where unsteady skin friction and dry friction are implemented and computed distributed throughout the pipe length. The outcome of this study highlights the importance of considering unsteady skin friction when the pipe is fully anchored and the role of dry friction when this is allowed to move.

FSI junction coupling in straight pipelines: In a second approach, internal conditions are added in the model allowing the description of the pipe anchoring and thrust blocks taking into account their resistance to movement due to the inertia and the dry friction. The model is successfully validated and **stick-slip criterion** is pointed out to be crucial for achieving accurate model output. The research contribution of this part of the work is a reliable, efficient and accurate model that allows the description of hydraulic transients in straight pipelines for different anchoring conditions.

6.3 Engineering applications and future research

Several points can be highlighted with regard to the applicability of the presented research work. Nowadays, pipe designs are not only focused on maximum loads but the overall transient wave propagation has to be taken into account. For this purpose, the main wave dissipating phenomena have to be identified and well-described. The present research, with the inclusion of unsteady skin friction and dry friction into 1D FSI models, represents a step forward

in numerical modelling. With respect to pipe coils, they have many industrial engineering applications, being typically used in most heat exchange systems, like cooling systems in power plants, industrial and commercial refrigerators, solar water heaters or radiators for automotive industry. Moreover, coils are very convenient systems for waterhammer research applications as they allow a very long pipe in a quite reduced space. In Chapter 4, a detailed study of the pipe coils behaviour, first static and then dynamic, is carried out pointing out some specific FSI features of the coil systems. As highlighted in the state-of-the-art review (*cf.* Section 2.6), not much research has been done for the description of anchors and pipe supports behaviour during hydraulic transients in pipe systems. Nonetheless, these elements are crucial for the right design of pipelines, guaranteeing their stability and reliability for fast transient events such as pump trip-off or emergency valve manoeuvres. In Section 5.3, a complete FSI model for straight pipelines anchored against longitudinal movement is presented offering a cutting-edge tool for practical engineering purposes. The four-equation model allows simulating different scenarios for pipelines (*e.g.* pipe completely constrained to axial movement or allowed to move for different pipe support stiffness or dry friction with its surrounding), then obtain the maximum and minimum envelopes for all scenarios and, accordingly, design the surge protection measures for the worse scenario. Henceforth recommendations for designing pipelines systems considering FSI can be elaborated by means of the proposed numerical model.

Hysteric damping is a dominant wave dissipation mechanism in plastic pipes. However, pipe-wall viscoelastic behaviour is not so far included in the FSI solvers. The author believes such implementation would bring an interesting insight in hydraulic transients research. A 1D waterhammer model combining fluid-structure interaction, pipe-wall viscoelasticity, unsteady skin friction and dry friction could be validated with the experimental data presented in Chapter 3 and, accordingly, further experiments could be carried out for straight plastic pipelines. The work would offer a complete tool for holistic analyses of the main dissipation mechanisms of waterhammer waves in plastic pipes and new benchmark problems could be proposed based on the upgraded model.

In a further stage, and based on the model proposed in Chapter 5 the rheological behaviour of the supports could be as well analysed. This scientific contribution would bring useful industrial applications in diverse fields, such as vibration damping and noise reduction, earthquake engineering or biomechanics where hysteretic damping takes an important role.

A Derivation of governing equations

A.1 Governing equations

The equations of the system (Eqs. A.1 to A.16) presented hereby correspond to the momentum and continuity conservation equations of a pipe-system with eight degrees-of-freedom, like in the control volume depicted in Fig. 2.3. Eqs. A.1 to A.6 and their associate characteristic equations can be found in Walker & Phillips (1977); Eqs. A.7 to A.16 in Wiggert *et al.* (1987).

1-DOF (fluid):

$$\frac{\partial V}{\partial t} + \frac{1}{\rho_f} \frac{\partial p}{\partial z} = 0 \quad (\text{A.1})$$

$$\frac{1}{K} \frac{\partial p}{\partial t} + \frac{\partial V}{\partial z} = -\frac{2}{r} W \quad (\text{A.2})$$

2-DOF (breathing):

$$\left(\rho_p r e + \rho_f \frac{r^2}{2} \right) \frac{\partial W}{\partial t} = r p - e \sigma_\theta \quad (\text{A.3})$$

$$\frac{\partial \sigma_\theta}{\partial t} - E \nu \frac{\partial U_z}{\partial z} = E \frac{W}{r_m} \quad (\text{A.4})$$

Appendix A. Derivation of governing equations

3-DOF (surging):

$$\frac{\partial U_z}{\partial t} - \frac{1}{\rho_p} \frac{\partial \sigma_z}{\partial z} = 0 \quad (\text{A.5})$$

$$\frac{\sigma_z}{\partial t} - E \frac{\partial U_z}{\partial z} = E\nu \frac{W}{r_m} \quad (\text{A.6})$$

4-DOF (swaying):

$$-\left(\rho_p + \frac{A_f}{A_p} \rho_f\right) \frac{\partial U_x}{\partial t} + \frac{\partial \sigma_x}{\partial z} = 0 \quad (\text{A.7})$$

$$\frac{\partial \sigma_x}{\partial t} - G \frac{\partial U_x}{\partial z} = -GR_y \quad (\text{A.8})$$

5-DOF (heaving):

$$-\left(\rho_p + \frac{A_f}{A_p} \rho_f\right) \frac{\partial U_y}{\partial t} + \frac{\partial \sigma_y}{\partial z} = 0 \quad (\text{A.9})$$

$$\frac{\partial \sigma_y}{\partial t} - G \frac{\partial U_y}{\partial z} = -GR_x \quad (\text{A.10})$$

6-DOF (yawing):

$$-(\rho_p I_p + \rho_f I_f) \frac{\partial R_y}{\partial t} + \frac{\partial M_y}{\partial z} = -\sigma_x A_p \quad (\text{A.11})$$

$$\frac{\partial M_y}{\partial t} - EI_p \frac{\partial R_y}{\partial z} = 0 \quad (\text{A.12})$$

7-DOF (pitching):

$$-(\rho_p I_p + \rho_f I_f) \frac{\partial R_x}{\partial t} + \frac{\partial M_x}{\partial z} = \sigma_y A_p \quad (\text{A.13})$$

$$\frac{\partial M_x}{\partial t} - EI_p \frac{\partial R_x}{\partial z} = 0 \quad (\text{A.14})$$

8-DOF (rolling):

$$-\rho_p J \frac{\partial R_z}{\partial t} + \frac{\partial M_z}{\partial z} = 0 \quad (\text{A.15})$$

$$\frac{\partial M_z}{\partial t} - GJ \frac{\partial R_z}{\partial z} = 0 \quad (\text{A.16})$$

The flow-types defined in Tijsseling & Vardy (2004) and explained in Subsection 2.2.1 concerning no-flow, static/steady, quasi-steady and rigid column flows are mere asymptotic extreme cases of the more general transient flow. Therefore, applying the proper simplifying assumptions governing equations can be derived from the system Eqs. A.1 to A.16 for each flow-type, both for the fluid and the structure.

All the degrees-of-freedom are distinguished in the previous system of equations, hence the analysis of waves celerities can be reduced to the essential wave propagating speeds in each degree-of-freedom. The following formulae (Eqs. A.17 to A.22) define the wave celerities for each wave type considered:

$$a_1 = \sqrt{\frac{K}{\rho_f}} \quad (\text{A.17})$$

$$a_2 = \sqrt{\frac{G}{\rho_p}} \quad (\text{A.18})$$

$$a_3 = \sqrt{\frac{E}{\rho_p}} \quad (\text{A.19})$$

$$a_{4,5} = \sqrt{\frac{GA_p}{\rho_p A_p + \rho_f A_f}} \quad (\text{A.20})$$

$$a_{6,7} = \sqrt{\frac{EI_p}{\rho_p I_p + \rho_f I_f}} \quad (\text{A.21})$$

$$a_8 = \sqrt{\frac{G}{\rho_p}} \quad (\text{A.22})$$

Where,

Appendix A. Derivation of governing equations

- a_1 represents the velocity of the fluid wave in an infinite medium without boundaries, which is the speed of the sound in the fluid and, therefore, corresponds to the 1-DOF;
- a_2 the velocity of the pipe breathing wave propagating in the z coordinate by means of axisymmetric shear stress and is associated with the 2-DOF;
- a_3 the velocity of the pipe surging wave, which is the speed of the sound in the pipe-wall and it propagates in the 3-DOF;
- $a_{4,5}$ the velocity of the pipe swaying and heaving waves, hence associated respectively with the 4-DOF and 5-DOF;
- $a_{6,7}$ the velocity of the pipe yawing wave and pitching waves, hence associated respectively with the 6-DOF and 7-DOF;
- a_8 the velocity of the pipe rolling wave, hence associated with the 8-DOF.

Notice that, due to the pipe axisymmetry, shear and bending wave celerities are equal in both planes.

The advantage of considering the system of equations Eqs. A.1 to A.16 is that there is no need of considering the abstract concept of elastic wave celerity from classic waterhammer theory. The definition and historical development of the waterhammer wave speed is given in Subsection 2.2.7. An in-depth critical analysis of the different interpretations of wave speed in both time and frequency-domains is given in Tijsseling & Vardy (2015).

A.2 Derivation of the governing equations for the classic waterhammer theory

In the classic waterhammer theory, only 1-DOF is described and the distensibility of the pipe in the radial coordinate is taken into account neglecting the radial inertia of the pipe-wall and the fluid and assuming a quasi-steady linear-elastic circumferential deformation of the pipe-wall.

From the one side, if inertial terms ($\partial W/\partial t$) are neglected in the momentum equation of the 2-DOF, Eq. A.3 becomes the well-known hoop stress formula:

$$\sigma_\theta = \frac{rp}{e} \tag{A.23}$$

Applying time partial derivative to both sides of Eq. A.23 and expanding differential terms

$$\frac{\partial \sigma_\theta}{\partial t} = \frac{p}{e} \frac{\partial r}{\partial t} + \frac{r}{e} \frac{\partial p}{\partial t} \tag{A.24}$$

A.2. Derivation of the governing equations for the classic waterhammer theory

the left-hand-side of Eq. A.24 can be written in terms of circumferential strain

$$E \frac{\partial \epsilon_\theta}{\partial t} = \frac{p}{e} \frac{\partial r}{\partial t} + \frac{r}{e} \frac{\partial p}{\partial t} \quad (\text{A.25})$$

and knowing that $\epsilon_\theta = \partial r / r$

$$E \frac{\partial \epsilon_\theta}{\partial t} = \frac{pr}{e} \frac{\partial \epsilon_\theta}{\partial t} + \frac{r}{e} \frac{\partial p}{\partial t} \quad (\text{A.26})$$

Rearranging Eq. A.26 and considering $\frac{pr}{e} \ll E$

$$\frac{\partial \epsilon_\theta}{\partial t} = \frac{r}{eE} \frac{\partial p}{\partial t} \quad (\text{A.27})$$

From the other side, the classic waterhammer theory does not consider any axial movement of the pipe. Hence, in Eq. A.4 $\partial U_z / \partial z = 0$ and becomes

$$\frac{\partial \sigma_\theta}{\partial t} = E \frac{W}{r_m} \quad (\text{A.28})$$

which in terms of circumferential strain is

$$\frac{\partial \epsilon_\theta}{\partial t} = \frac{W}{r_m} \quad (\text{A.29})$$

Combining Eq. A.27 with Eq. A.29 an expression for the radial velocity of the pipe-wall, in function of the inner pressure, is obtained:

$$W = \frac{r^2}{eE} \frac{\partial p}{\partial t} \quad (\text{A.30})$$

Substituting Eq. A.30 into the right-hand-side of the continuity equation of the 1-DOE,

$$\frac{1}{K} \frac{\partial p}{\partial t} + \frac{\partial V}{\partial z} = -\frac{2r}{eE} \frac{\partial p}{\partial t} \quad (\text{A.31})$$

rearranging Eq. A.31

$$\frac{\partial V}{\partial z} + \left(\frac{1}{K} + \frac{D}{eE} \right) \frac{\partial p}{\partial t} = 0 \quad (\text{A.32})$$

Finally, defining the elastic wave celerity as

$$a_h = \sqrt{\frac{K}{\rho_f \left(1 + \frac{DK}{eE} \right)}} \quad (\text{A.33})$$

Appendix A. Derivation of governing equations

the continuity equation Eq. A.34 for classic waterhammer theory is reached:

$$\frac{\partial V}{\partial z} + \frac{1}{\rho_f a_h^2} \frac{\partial p}{\partial t} = 0 \quad (\text{A.34})$$

The fundamental system of equations of the classic waterhammer theory, neglecting damping mechanisms, is therefore composed by Eqs. A.1 and A.34. Forming the following system of equations A.35:

$$\text{two-equation model} \left\{ \begin{array}{l} \frac{\partial V}{\partial t} + \frac{1}{\rho_f} \frac{\partial p}{\partial z} = 0 \\ \frac{\partial V}{\partial z} + \frac{1}{\rho_f a_h^2} \frac{\partial p}{\partial t} = 0 \end{array} \right. \quad (\text{A.35})$$

If the acoustic wave celerity in the fluid is considered ($a_1 = \sqrt{\frac{K}{\rho_f}}$), Eq. A.1 and Eq. A.34 are equivalent. Hence, the only difference between 1-DOF wave propagation and classic waterhammer theory is determined by how the elastic wave celerity is defined. In the first, rigid pipe is assumed, while in the second the distensibility of the pipe is taken into account.

A.3 Derivation of the governing equations for the four-equation model

The four-equation model describes the 1-DOF (fluid) and 3DOF (surging) of the pipe system and takes into account the 2-DOF (breathing) in a similar manner as the classic waterhammer theory.

A.3.1 Continuity in 1-DOF

Subtracting to the 2-DOF continuity equation Poisson ratio times the 3-DOF continuity equation (*i.e.* Eq. A.4 – ν Eq.A.6) the following expression is obtained:

$$\frac{\partial \sigma_\theta}{\partial t} - \nu \frac{\partial \sigma_z}{\partial t} = (1 - \nu^2) E \frac{W}{r} \quad (\text{A.36})$$

Notice that, dividing both sides of Eq. A.36 by E , the left-hand-side is actually the local time rate of change of the circumferential strain. Hoop stress can be written in terms of pressure

A.3. Derivation of the governing equations for the four-equation model

according to Eq. A.23, which is also valid in the present derivation.

$$\frac{1}{e} \frac{\partial pr}{\partial t} - \nu \frac{\partial \sigma_z}{\partial t} = (1 - \nu^2) E \frac{W}{r} \quad (\text{A.37})$$

expanding the differential term

$$\frac{p}{e} \frac{\partial r}{\partial t} + \frac{r}{e} \frac{\partial p}{\partial t} - \nu \frac{\partial \sigma_z}{\partial t} = (1 - \nu^2) E \frac{W}{r} \quad (\text{A.38})$$

considering $\frac{p}{e} \frac{\partial r}{\partial t}$ is negligible and rearranging Eq. A.38

$$W = \frac{\frac{r^2}{e} \frac{\partial p}{\partial t} - r \nu \frac{\partial \sigma_z}{\partial t}}{(1 - \nu^2) E} \quad (\text{A.39})$$

Substituting Eq. A.39 into Eq. A.2

$$\frac{1}{K} \frac{\partial p}{\partial t} + \frac{\partial V}{\partial z} = - \frac{D}{e(1 - \nu^2) E} \frac{\partial p}{\partial t} + \frac{2\nu}{(1 - \nu^2) E} \frac{\partial \sigma_z}{\partial t} \quad (\text{A.40})$$

neglecting second-order Poisson ratio terms and rearranging

$$\frac{\partial V}{\partial z} + \left(\frac{1}{K} + \frac{D}{eE} \right) \frac{\partial p}{\partial t} = \frac{2\nu}{E} \frac{\partial \sigma_z}{\partial t} \quad (\text{A.41})$$

Finally, applying the definition of elastic wave celerity from Eq. A.33, the continuity equation (Eq. A.42) for the 1-DOF of a four-equation model is obtained:

$$\frac{\partial V}{\partial z} + \frac{1}{\rho_f a_h^2} \frac{\partial p}{\partial t} = \frac{2\nu}{E} \frac{\partial \sigma_z}{\partial t} \quad (\text{A.42})$$

A.3.2 Continuity in 3-DOF

Substituting Eq. A.39 into Eq. A.6

$$\frac{\partial \sigma_z}{\partial t} - E \frac{\partial U_z}{\partial z} = \frac{\nu r}{e} \frac{\partial p}{\partial t} - \nu^2 \frac{\partial \sigma_z}{\partial t} \quad (\text{A.43})$$

neglecting second order Poisson ratio terms and rearranging the continuity equation (Eq. A.43)

$$\frac{\partial U_z}{\partial z} - \frac{1}{E} \frac{\partial \sigma_z}{\partial t} = - \frac{\nu r}{eE} \frac{\partial p}{\partial t} \quad (\text{A.44})$$

Appendix A. Derivation of governing equations

Finally, defining the acoustic wave speed in the pipe-wall as

$$a_3 = \sqrt{\frac{E}{\rho_p}} \quad (\text{A.45})$$

and substituting Eq. A.45 into Eq. A.44 the continuity equation of the pipe-wall (Eq. A.46) for the four-equation model is obtained:

$$\frac{\partial U_z}{\partial z} - \frac{1}{\rho_p a_3^2} \frac{\sigma_z}{\partial t} = -\frac{\nu r}{eE} \frac{\partial p}{\partial t} \quad (\text{A.46})$$

The four fundamental equations of a four-equation model are composed, therefore, of Eq. A.1, A.42, A.5 and A.46. Forming the following system of equations A.47:

$$\left. \begin{array}{l} \text{four-equation model} \end{array} \right\} \left\{ \begin{array}{l} \frac{\partial V}{\partial t} + \frac{1}{\rho_f} \frac{\partial p}{\partial z} = 0 \\ \frac{\partial V}{\partial z} + \frac{1}{\rho_f a_h^2} \frac{\partial p}{\partial t} = \frac{2\nu}{E} \frac{\partial \sigma_z}{\partial t} \end{array} \right\} \begin{array}{l} \text{1-DOF} \\ \text{3-DOF} \end{array}$$

$$\left. \begin{array}{l} \frac{\partial U_z}{\partial t} - \frac{1}{\rho_p} \frac{\partial \sigma_z}{\partial z} = 0 \\ \frac{\partial U_z}{\partial z} - \frac{1}{\rho_p a_3^2} \frac{\sigma_z}{\partial t} = -\frac{\nu r}{eE} \frac{\partial p}{\partial t} \end{array} \right\}$$

(A.47)

B MOC transformation for four-equation models

B.1 Introduction

The present appendix aims at explaining the MOC transformation, which consists of transforming the hyperbolic partial differential equations of the four-equation model (Eq. A.47) to a set of ordinary differential equations. The development is based on Forsythe *et al.* (1960) and Tijsseling (1993). First the system of equations is introduced in a general matricial form and then a transformation matrix is derived. During the development, the elements of the original matrices are kept as coefficients aiming at reaching general compatibility equations that will allow the straightforward conversion of any four-equation like system from PDE's to ODE's. At the end of the appendix this algebraic model is applied to the Poisson-uncoupled and Poisson-coupled four-equation models.

B.2 System of equations

The fundamental set of equations for the four-equation model (Eqs. A.47) is presented in this subsection in matricial form. For practical purposes the factors multiplying the differential terms are kept as general coefficients which value is substituted at the very end of the development.

$$A \frac{\partial y}{\partial t} + B \frac{\partial y}{\partial z} = r \quad (\text{B.1})$$

$$y = \left(v \quad p \quad U_z \quad \sigma_z \right)^T \quad (\text{B.2})$$

$$r = \begin{pmatrix} r_1 & r_2 & r_3 & r_4 \end{pmatrix}^T \quad (\text{B.3})$$

$$A = \begin{pmatrix} \alpha_{11} & 0 & 0 & 0 \\ 0 & \alpha_{22} & 0 & \alpha_{24} \\ 0 & 0 & \alpha_{33} & 0 \\ 0 & \alpha_{42} & 0 & \alpha_{44} \end{pmatrix} \quad (\text{B.4})$$

$$B = \begin{pmatrix} 0 & \beta_{12} & 0 & 0 \\ \beta_{21} & 0 & 0 & 0 \\ 0 & 0 & 0 & \beta_{34} \\ 0 & 0 & \beta_{43} & 0 \end{pmatrix} \quad (\text{B.5})$$

B.3 Transformation matrix

Hyperbolic systems can be transformed by means of multiplication by a regular matrix

$$TA \frac{\partial y}{\partial t} + TB \frac{\partial y}{\partial x} = Tr \quad (\text{B.6})$$

For square matrices with distinct real eigenvalues there is a matrix S such that

$$S^{-1} A^{-1} B S = \Lambda \quad (\text{B.7})$$

where Λ is

$$\Lambda = \begin{pmatrix} \lambda_1 & 0 & 0 & 0 \\ 0 & \lambda_2 & 0 & 0 \\ 0 & 0 & \lambda_3 & 0 \\ 0 & 0 & 0 & \lambda_4 \end{pmatrix} \quad (\text{B.8})$$

The T matrix is chosen as

$$T = S^{-1} A^{-1} \quad (\text{B.9})$$

and substituting Eq. B.9 into Eq. B.7 leads to the condition

$$TB = \Lambda TA \quad (\text{B.10})$$

Hence, substituting Eqs. B.4, B.5 and B.8 into Eq. B.10:

$$\begin{aligned}
 & \begin{pmatrix} t_{11} & t_{12} & t_{13} & t_{14} \\ t_{21} & t_{22} & t_{23} & t_{24} \\ t_{31} & t_{32} & t_{33} & t_{34} \\ t_{41} & t_{42} & t_{43} & t_{44} \end{pmatrix} \begin{pmatrix} 0 & \beta_{12} & 0 & 0 \\ \beta_{21} & 0 & 0 & 0 \\ 0 & 0 & 0 & \beta_{34} \\ 0 & 0 & \beta_{43} & 0 \end{pmatrix} = \\
 & \begin{pmatrix} \lambda_1 & 0 & 0 & 0 \\ 0 & \lambda_2 & 0 & 0 \\ 0 & 0 & \lambda_3 & 0 \\ 0 & 0 & 0 & \lambda_4 \end{pmatrix} \begin{pmatrix} t_{11} & t_{12} & t_{13} & t_{14} \\ t_{21} & t_{22} & t_{23} & t_{24} \\ t_{31} & t_{32} & t_{33} & t_{34} \\ t_{41} & t_{42} & t_{43} & t_{44} \end{pmatrix} \begin{pmatrix} \alpha_{11} & 0 & 0 & 0 \\ 0 & \alpha_{22} & 0 & \alpha_{24} \\ 0 & 0 & \alpha_{33} & 0 \\ 0 & \alpha_{42} & 0 & \alpha_{44} \end{pmatrix} \tag{B.11}
 \end{aligned}$$

which is

$$\begin{aligned}
 & \begin{pmatrix} t_{12}\beta_{21} & t_{11}\beta_{12} & t_{14}\beta_{43} & t_{13}\beta_{34} \\ t_{22}\beta_{21} & t_{21}\beta_{12} & t_{24}\beta_{43} & t_{23}\beta_{34} \\ t_{32}\beta_{21} & t_{31}\beta_{12} & t_{34}\beta_{43} & t_{33}\beta_{34} \\ t_{42}\beta_{21} & t_{41}\beta_{12} & t_{44}\beta_{43} & t_{43}\beta_{34} \end{pmatrix} = \\
 & \begin{pmatrix} \lambda_1 t_{11} \alpha_{11} & \lambda_1 (t_{12} \alpha_{22} + t_{14} \alpha_{42}) & \lambda_1 t_{13} \alpha_{33} & \lambda_1 (t_{12} \alpha_{24} + t_{14} \alpha_{44}) \\ \lambda_2 t_{21} \alpha_{11} & \lambda_2 (t_{22} \alpha_{22} + t_{24} \alpha_{42}) & \lambda_2 t_{23} \alpha_{33} & \lambda_2 (t_{22} \alpha_{24} + t_{24} \alpha_{44}) \\ \lambda_3 t_{31} \alpha_{11} & \lambda_3 (t_{32} \alpha_{22} + t_{34} \alpha_{42}) & \lambda_3 t_{33} \alpha_{33} & \lambda_3 (t_{32} \alpha_{24} + t_{34} \alpha_{44}) \\ \lambda_4 t_{41} \alpha_{11} & \lambda_4 (t_{42} \alpha_{22} + t_{44} \alpha_{42}) & \lambda_4 t_{43} \alpha_{33} & \lambda_4 (t_{42} \alpha_{24} + t_{44} \alpha_{44}) \end{pmatrix} \tag{B.12}
 \end{aligned}$$

Eq. B.12 is a system composed by sixteen equations with sixteen unknowns t_{ij} . Let's consider row i :

$$\begin{aligned}
 t_{i2}\beta_{21} &= \lambda_i t_{i1} \alpha_{11} \\
 t_{i1}\beta_{12} &= \lambda_i (t_{i2} \alpha_{22} + t_{i4} \alpha_{42}) \\
 t_{i4}\beta_{43} &= \lambda_i t_{i3} \alpha_{33} \\
 t_{i3}\beta_{34} &= \lambda_i (t_{i2} \alpha_{24} + t_{i4} \alpha_{44}) \tag{B.13}
 \end{aligned}$$

Appendix B. MOC transformation for four-equation models

or what is the same

$$\begin{pmatrix} -\lambda_i \alpha_{11} & \beta_{21} & 0 & 0 \\ \beta_{12} & -\lambda_i \alpha_{22} & 0 & -\lambda_i \alpha_{42} \\ 0 & 0 & -\lambda_i \alpha_{33} & \beta_{43} \\ 0 & -\lambda_i \alpha_{24} & \beta_{34} & -\lambda_i \alpha_{44} \end{pmatrix} \begin{pmatrix} t_{i1} \\ t_{i2} \\ t_{i3} \\ t_{i4} \end{pmatrix} = \begin{pmatrix} 0 \\ 0 \\ 0 \\ 0 \end{pmatrix} \quad (\text{B.14})$$

The system B.14 can be written in matrix notation

$$(B - \lambda_i A)^T t_i = 0 \quad (\text{B.15})$$

If the matrix $(B - \lambda_i A)^T$ is regular, Eq. B.15 has only the trivial solution $t_i = 0$, which leads to a singular matrix T . To obtain a regular matrix T , $(B - \lambda_i A)^T$ has to be singular. Hence

$$|B - \lambda_i A| = 0 \quad (\text{B.16})$$

and the equations of the system B.14 are dependent so one of them can be omitted. The second equation of the system B.14 is omitted if $i = 1$ or $i = 2$, and the fort equation is omitted if $i = 3$ or $i = 4$.

For $i = 1$ and $i = 2$ the eigenvector t_i is calculated as follows:

$$\begin{aligned} -\lambda_i t_{i1} \alpha_{11} + t_{i2} \beta_{21} &= 0 \\ -\lambda_i t_{i3} \alpha_{33} + t_{i4} \beta_{43} &= 0 \\ -\lambda_i t_{i2} \alpha_{24} + t_{i3} \beta_{34} - \lambda_i t_{i4} \alpha_{44} &= 0 \end{aligned} \quad (\text{B.17})$$

or

$$\begin{aligned} t_{i1} &= \frac{t_{i2} \beta_{21}}{\lambda_i \alpha_{11}} \\ t_{i3} &= \frac{t_{i4} \beta_{43}}{\lambda_i \alpha_{33}} \\ t_{i4} &= \frac{\lambda_i t_{i2} \alpha_{24}}{\frac{\beta_{43} \beta_{34}}{\lambda_i \alpha_{33}} - \lambda_i \alpha_{44}} \end{aligned} \quad (\text{B.18})$$

and taking $t_{i2} = \lambda_i$

$$\begin{aligned}
 t_{i1} &= \frac{\beta_{21}}{\alpha_{11}} \\
 t_{i2} &= \lambda_i \\
 t_{i3} &= \frac{\lambda_i \beta_{43} \alpha_{24}}{\frac{\beta_{43} \beta_{34}}{\lambda_i} - \lambda_i \alpha_{33} \alpha_{44}} \\
 t_{i4} &= \frac{\lambda_i^2 \alpha_{24}}{\frac{\beta_{43} \beta_{34}}{\lambda_i \alpha_{33}} - \lambda_i \alpha_{44}}
 \end{aligned} \tag{B.19}$$

For $i = 3$ and $i = 4$ the eigenvector t_i is calculated as follows:

$$\begin{aligned}
 -\lambda_i t_{i1} \alpha_{11} + t_{i2} \beta_{21} &= 0 \\
 t_{i1} \beta_{12} - \lambda_i t_{i2} \alpha_{22} - \lambda_i t_{i4} \alpha_{42} &= 0 \\
 -\lambda_i t_{i3} \alpha_{33} + t_{i4} \beta_{43} &= 0
 \end{aligned} \tag{B.20}$$

or

$$\begin{aligned}
 t_{i1} &= \frac{\lambda_i t_{i4} \alpha_{42} \beta_{21}}{\beta_{12} \beta_{21} - \lambda_i^2 \alpha_{22} \alpha_{11}} \\
 t_{i2} &= \frac{\lambda_i t_{i4} \alpha_{42}}{\frac{\beta_{12} \beta_{21}}{\lambda_i \alpha_{11}} - \lambda_i \alpha_{22}} \\
 t_{i3} &= \frac{t_{i4} \beta_{43}}{\lambda_i \alpha_{33}}
 \end{aligned} \tag{B.21}$$

and taking $t_{i4} = \lambda_i$

$$\begin{aligned}
 t_{i1} &= \frac{\lambda_i^2 \alpha_{42} \beta_{21}}{\beta_{12} \beta_{21} - \lambda_i^2 \alpha_{22} \alpha_{11}} \\
 t_{i2} &= \frac{\lambda_i^2 \alpha_{42}}{\frac{\beta_{12} \beta_{21}}{\lambda_i \alpha_{11}} - \lambda_i \alpha_{22}} \\
 t_{i3} &= \frac{\beta_{43}}{\alpha_{33}} \\
 t_{i4} &= \lambda_i
 \end{aligned} \tag{B.22}$$

Appendix B. MOC transformation for four-equation models

And finally joining the eigenvectors in matricial form, which is Eqs. B.19 for $i = 1, 2$; and Eqs. B.22 for $i = 3, 4$ yields:

$$T = \begin{pmatrix} \frac{\beta_{21}}{\alpha_{11}} & \lambda_1 & \frac{\lambda_1 \beta_{43} \alpha_{24}}{\frac{\beta_{43} \beta_{34}}{\lambda_1} - \lambda_1 \alpha_{33} \alpha_{44}} & \frac{\lambda_1^2 \alpha_{24}}{\frac{\beta_{43} \beta_{34}}{\lambda_1} - \lambda_1 \alpha_{44}} \\ \frac{\beta_{21}}{\alpha_{11}} & \lambda_2 & \frac{\lambda_2 \beta_{43} \alpha_{24}}{\frac{\beta_{43} \beta_{34}}{\lambda_2} - \lambda_2 \alpha_{33} \alpha_{44}} & \frac{\lambda_2^2 \alpha_{24}}{\frac{\beta_{43} \beta_{34}}{\lambda_2} - \lambda_2 \alpha_{44}} \\ \frac{\lambda_3^2 \alpha_{42} \beta_{21}}{\beta_{12} \beta_{21} - \lambda_3^2 \alpha_{22} \alpha_{11}} & \frac{\lambda_3^2 \alpha_{42}}{\frac{\beta_{12} \beta_{21}}{\lambda_3 \alpha_{11}} - \lambda_3 \alpha_{22}} & \frac{\beta_{43}}{\alpha_{33}} & \lambda_3 \\ \frac{\lambda_4^2 \alpha_{42} \beta_{21}}{\beta_{12} \beta_{21} - \lambda_4^2 \alpha_{22} \alpha_{11}} & \frac{\lambda_4^2 \alpha_{42}}{\frac{\beta_{12} \beta_{21}}{\lambda_4 \alpha_{11}} - \lambda_4 \alpha_{22}} & \frac{\beta_{43}}{\alpha_{33}} & \lambda_4 \end{pmatrix} \quad (\text{B.23})$$

B.4 Compatibility equations

Introducing the vector

$$v = TAy \quad (\text{B.24})$$

Eq. B.1 becomes

$$\frac{\partial v}{\partial t} + \Lambda \frac{\partial v}{\partial x} = Tr \quad (\text{B.25})$$

which can be written as a set of four uncoupled equations:

$$\frac{\partial v_i}{\partial t} + \lambda_i \frac{\partial v_i}{\partial x} = (Tr)_i ; \quad i = 1, 2, 3, 4 \quad (\text{B.26})$$

Each of the Eqs. B.26 transforms into an ordinary differential equation

$$\frac{dv_i}{dt} = (Tr)_i ; \quad i = 1, 2, 3, 4 \quad (\text{B.27})$$

when it is considered along a line in the x - t plane having the characteristic direction

$$\frac{dz}{dt} = \lambda_i ; \quad i = 1, 2, 3, 4 \quad (\text{B.28})$$

The Eqs. B.27 are known as the compatibility equations along the characteristic lines with slopes λ_i^{-1} in the x - t plane.

Finally, substituting Eqs. B.23 and B.4 into Eq. B.24 and Eqs. B.23, B.3 and B.24 into Eq. B.27.

B.5. Application to the standard four-equation model

$$\begin{pmatrix}
 \beta_{21} & \lambda_1 \alpha_{22} + \frac{\lambda_1^2 \alpha_{24} \alpha_{42}}{\beta_{43} \beta_{34} - \lambda_1 \alpha_{44}} & \frac{\lambda_1 \beta_{43} \alpha_{24} \alpha_{33}}{\beta_{43} \beta_{34} - \lambda_1 \alpha_{33} \alpha_{44}} & \lambda_1 \alpha_{24} + \frac{\lambda_1^2 \alpha_{24} \alpha_{44}}{\beta_{43} \beta_{34} - \lambda_1 \alpha_{44}} \\
 \beta_{21} & \lambda_2 \alpha_{22} + \frac{\lambda_2^2 \alpha_{24} \alpha_{42}}{\beta_{43} \beta_{34} - \lambda_2 \alpha_{44}} & \frac{\lambda_2 \beta_{43} \alpha_{24} \alpha_{33}}{\beta_{43} \beta_{34} - \lambda_2 \alpha_{33} \alpha_{44}} & \lambda_2 \alpha_{24} + \frac{\lambda_2^2 \alpha_{24} \alpha_{44}}{\beta_{43} \beta_{34} - \lambda_2 \alpha_{44}} \\
 \frac{\lambda_3^2 \alpha_{42} \beta_{21} \alpha_{11}}{\beta_{12} \beta_{21} - \lambda_3^2 \alpha_{22} \alpha_{11}} & \frac{\lambda_3^2 \alpha_{42} \alpha_{22}}{\beta_{12} \beta_{21} - \lambda_3 \alpha_{22}} + \lambda_3 \alpha_{42} & \beta_{43} & \frac{\lambda_3^2 \alpha_{42} \alpha_{24}}{\beta_{12} \beta_{21} - \lambda_3 \alpha_{22}} + \lambda_3 \alpha_{44} \\
 \frac{\lambda_4^2 \alpha_{42} \beta_{21} \alpha_{11}}{\beta_{12} \beta_{21} - \lambda_4^2 \alpha_{22} \alpha_{11}} & \frac{\lambda_4^2 \alpha_{42} \alpha_{22}}{\beta_{12} \beta_{21} - \lambda_4 \alpha_{22}} + \lambda_4 \alpha_{42} & \beta_{43} & \frac{\lambda_4^2 \alpha_{42} \alpha_{24}}{\beta_{12} \beta_{21} - \lambda_4 \alpha_{22}} + \lambda_4 \alpha_{44}
 \end{pmatrix} \frac{d}{dt} \begin{pmatrix} V \\ p \\ U_z \\ \sigma_z \end{pmatrix} =$$

$$\begin{pmatrix}
 r_1 \frac{\beta_{21}}{\alpha_{11}} + r_2 \lambda_1 + r_3 \frac{\lambda_1 \beta_{43} \alpha_{24}}{\beta_{43} \beta_{34} - \lambda_1 \alpha_{33} \alpha_{44}} + r_4 \frac{\lambda_1^2 \alpha_{24}}{\beta_{43} \beta_{34} - \lambda_1 \alpha_{44}} \\
 r_1 \frac{\beta_{21}}{\alpha_{11}} + r_2 \lambda_2 + r_3 \frac{\lambda_2 \beta_{43} \alpha_{24}}{\beta_{43} \beta_{34} - \lambda_2 \alpha_{33} \alpha_{44}} + r_4 \frac{\lambda_2^2 \alpha_{24}}{\beta_{43} \beta_{34} - \lambda_2 \alpha_{44}} \\
 r_1 \frac{\lambda_3^2 \alpha_{42} \beta_{21}}{\beta_{12} \beta_{21} - \lambda_3^2 \alpha_{22} \alpha_{11}} + r_2 \frac{\lambda_3^2 \alpha_{42}}{\beta_{12} \beta_{21} - \lambda_3 \alpha_{22}} + r_3 \frac{\beta_{43}}{\alpha_{33}} + r_4 \lambda_3 \\
 r_1 \frac{\lambda_4^2 \alpha_{42} \beta_{21}}{\beta_{12} \beta_{21} - \lambda_4^2 \alpha_{22} \alpha_{11}} + r_2 \frac{\lambda_4^2 \alpha_{42}}{\beta_{12} \beta_{21} - \lambda_4 \alpha_{22}} + r_3 \frac{\beta_{43}}{\alpha_{33}} + r_4 \lambda_4
 \end{pmatrix} \quad (B.29)$$

B.5 Application to the standard four-equation model

B.5.1 Poisson-uncoupled four-equation model

System coefficients

For the basic Poisson-uncoupled four-equation model solving the system of equations Eq. A.35, and including steady friction dissipation, the coefficients are:

Table B.1 – Coefficients for factor matrices A and B and right-hand-side vector r

Matrix A	Matrix B	Vector r
$\alpha_{11} = 1$	$\beta_{12} = \frac{1}{\rho_f}$	$r_1 = -\frac{f}{4r} V_r V_r $
$\alpha_{22} = \frac{1}{\rho_f a_n^2}$	$\beta_{21} = 1$	$r_2 = 0$
$\alpha_{24} = 0$	$\beta_{34} = -\frac{1}{\rho_p}$	$r_3 = \frac{\rho_f A_f f}{\rho_p A_p 4r} V_r V_r $
$\alpha_{33} = 1$	$\beta_{43} = 1$	$r_4 = 0$
$\alpha_{42} = 0$	–	–
$\alpha_{44} = -\frac{1}{\rho_p a_3^2}$	–	–

Appendix B. MOC transformation for four-equation models

Eigenvalues

The characteristic equation of the system B.1 is:

$$|B - \lambda A| = 0 \quad (\text{B.30})$$

Substituting the values from Eqs. B.4, B.5 into B.30

$$B - \lambda A = \begin{pmatrix} -\lambda\alpha_{11} & \beta_{12} & 0 & 0 \\ \beta_{21} & -\lambda\alpha_{22} & 0 & -\lambda\alpha_{24} \\ 0 & 0 & -\lambda\alpha_{33} & \beta_{34} \\ 0 & -\lambda\alpha_{42} & \beta_{43} & -\lambda\alpha_{44} \end{pmatrix} \quad (\text{B.31})$$

which determinant is

$$|B - \lambda A| = \lambda^4 \alpha_{11} \alpha_{33} (\alpha_{22} \alpha_{44} - \alpha_{24} \alpha_{42}) - \lambda^2 (\alpha_{11} \alpha_{22} \beta_{34} \beta_{43} + \alpha_{33} \alpha_{44} \beta_{12} \beta_{21}) + \beta_{12} \beta_{21} \beta_{34} \beta_{43} \quad (\text{B.32})$$

and assigning the coefficient values of table B.1 into Eq. B.32

$$|B - \lambda A| = \frac{\lambda^2}{\rho_f a_h^2 \rho_p} \left(\frac{\lambda^2}{a_3^2} - 1 \right) + \frac{1}{\rho_f \rho_p} \left(\frac{\lambda^2}{a_h^2} + 1 \right) \quad (\text{B.33})$$

Hence, for the Poisson-uncoupled four-equation model, the solutions of the characteristic equation are:

$$\lambda_1 = +a_h; \quad \lambda_2 = -a_h; \quad \lambda_3 = +a_3; \quad \lambda_4 = -a_3 \quad (\text{B.34})$$

Compatibility equations

Substituting Eq. B.34 and the values of table B.1 into Eq. B.29, the compatibility equations for the basic Poisson-uncoupled four-equation model are:

B.5. Application to the standard four-equation model

$$\begin{pmatrix} 1 & \frac{1}{\rho_f a_h} & 0 & 0 \\ 1 & -\frac{1}{\rho_f a_h} & 0 & 0 \\ 0 & 0 & 1 & -\frac{1}{\rho_p a_3} \\ 0 & 0 & 1 & \frac{1}{\rho_p a_3} \end{pmatrix} \frac{d}{dt} \begin{pmatrix} V \\ p \\ U_z \\ \sigma_z \end{pmatrix} = \begin{pmatrix} -\frac{f}{4r} V_r |V_r| \\ -\frac{f}{4r} V_r |V_r| \\ \frac{\rho_f A_f}{\rho_s A_p} \frac{f}{4r} V_r |V_r| \\ \frac{\rho_f A_f}{\rho_s A_p} \frac{f}{4r} V_r |V_r| \end{pmatrix} \quad (\text{B.35})$$

Notice that, neglecting the RHS terms of the system B.35, the first two equations correspond the ones of classic waterhammer theory (Eq. A.35), while the last two equations to the uncoupled axial pipe movement equations (Eq. A.5 and A.6)

B.5.2 Poisson-coupled four-equation model

System coefficients

For the basic four-equation model solving the system of equations Eq. A.47, and including steady friction dissipation, the coefficients are:

Table B.2 – Coefficients for factor matrices A and B and right-hand-side vector r

Matrix A	Matrix B	Vector r
$\alpha_{11} = 1$	$\beta_{12} = \frac{1}{\rho_f}$	$r_1 = -\frac{f}{4r} V_r V_r $
$\alpha_{22} = \frac{1}{\rho_f a_h^2}$	$\beta_{21} = 1$	$r_2 = 0$
$\alpha_{24} = -\frac{2\nu}{E}$	$\beta_{34} = -\frac{1}{\rho_p}$	$r_3 = \frac{\rho_f A_f}{\rho_p A_p} \frac{f}{4r} V_r V_r $
$\alpha_{33} = 1$	$\beta_{43} = 1$	$r_4 = 0$
$\alpha_{42} = \frac{\nu r}{eE}$	–	–
$\alpha_{44} = -\frac{1}{\rho_p a_3^2}$	–	–

Eigenvalues

Following the same development as the one presented in Subsection B.5.1 and substituting the values of table B.2 into Eq. B.32

$$|B - \lambda A| = \frac{\lambda^2}{\rho_f a_h^2 \rho_p} \left(\frac{\lambda^2}{a_3^2} - 1 \right) + \frac{1}{\rho_f \rho_p} \left(\frac{\lambda^2}{a_h^2} + 1 \right) + \frac{\lambda^4 2\nu^2 r}{eE^2} \quad (\text{B.36})$$

Neglecting second-order Poisson ratio terms (Forsythe *et al.*, 1960; Tijsseling, 1993) the so-

Appendix B. MOC transformation for four-equation models

olutions of the characteristic equations for Poisson-coupled four-equation model are as well

$$\lambda_1 = +a_h; \lambda_2 = -a_h; \lambda_3 = +a_3; \lambda_4 = -a_3 \quad (\text{B.37})$$

If second-order Poisson ratio terms are not neglected

$$\begin{aligned} \lambda_1 &= \sqrt{\frac{1}{2} \left[\left(a_h^2 + a_3^2 + \frac{2v^2 \rho_f r a_h^2}{\rho_p e} \right)^2 - \sqrt{\left(a_h^2 + a_3^2 + \frac{2v^2 \rho_f r a_h^2}{\rho_p e} \right)^4 - 4a_h^2 a_3^2} \right]} \\ \lambda_2 &= -\sqrt{\frac{1}{2} \left[\left(a_h^2 + a_3^2 + \frac{2v^2 \rho_f r a_h^2}{\rho_p e} \right)^2 - \sqrt{\left(a_h^2 + a_3^2 + \frac{2v^2 \rho_f r a_h^2}{\rho_p e} \right)^4 - 4a_h^2 a_3^2} \right]} \\ \lambda_3 &= \sqrt{\frac{1}{2} \left[\left(a_h^2 + a_3^2 + \frac{2v^2 \rho_f r a_h^2}{\rho_p e} \right)^2 + \sqrt{\left(a_h^2 + a_3^2 + \frac{2v^2 \rho_f r a_h^2}{\rho_p e} \right)^4 - 4a_h^2 a_3^2} \right]} \\ \lambda_4 &= -\sqrt{\frac{1}{2} \left[\left(a_h^2 + a_3^2 + \frac{2v^2 \rho_f r a_h^2}{\rho_p e} \right)^2 + \sqrt{\left(a_h^2 + a_3^2 + \frac{2v^2 \rho_f r a_h^2}{\rho_p e} \right)^4 - 4a_h^2 a_3^2} \right]} \end{aligned} \quad (\text{B.38})$$

Compatibility equations

Substituting the eigenvalues Eq. B.37 and the values of table B.2 into Eq. B.29, the compatibility equations for the basic Poisson-coupled four-equation model are:

$$\begin{pmatrix}
 1 & \frac{1}{\rho_f a_h} + \frac{a_h^2 \frac{2v^2 r}{eE^2}}{\frac{1}{\rho_p a_h} - \frac{a_h^2}{\rho_p a_3^2}} & \frac{a_h \frac{2v}{E}}{\frac{1}{\rho_p a_h} - \frac{a_h^2}{\rho_p a_3^2}} & -\frac{a_h 2v}{E} - \frac{a_h^2 \frac{2v}{E \rho_p a_3^2}}{\frac{1}{\rho_p a_h} - \frac{a_h^2}{\rho_p a_3^2}} \\
 1 & -\frac{1}{\rho_f a_h} - \frac{a_h^2 \frac{2v^2 r}{eE^2}}{\frac{1}{\rho_p a_h} - \frac{a_h^2}{\rho_p a_3^2}} & \frac{a_h \frac{2v}{E}}{\frac{1}{\rho_p a_h} - \frac{a_h^2}{\rho_p a_3^2}} & \frac{a_h 2v}{E} + \frac{a_h^2 \frac{2v}{E \rho_p a_3^2}}{\frac{1}{\rho_p a_h} - \frac{a_h^2}{\rho_p a_3^2}} \\
 \frac{a_3^2 \frac{vr}{eE}}{\frac{1}{\rho_f} - \frac{a_3^2}{\rho_f a_h^2}} & a_3 \frac{vr}{eE} + \frac{a_3^2 \frac{vr}{eE \rho_f a_h^2}}{\frac{1}{\rho_f a_3} - \frac{a_3^2}{\rho_f a_h^2}} & 1 & -\frac{1}{\rho_p a_3} - \frac{a_3^2 \frac{2v^2 r}{eE^2}}{\frac{1}{\rho_f a_3} - \frac{a_3^2}{\rho_f a_h^2}} \\
 \frac{a_3^2 \frac{vr}{eE}}{\frac{1}{\rho_f} - \frac{a_3^2}{\rho_f a_h^2}} & -a_3 \frac{vr}{eE} - \frac{a_3^2 \frac{vr}{eE \rho_f a_h^2}}{\frac{1}{\rho_f a_3} - \frac{a_3^2}{\rho_f a_h^2}} & 1 & \frac{1}{\rho_p a_3} + \frac{a_3^2 \frac{2v^2 r}{eE^2}}{\frac{1}{\rho_f a_3} - \frac{a_3^2}{\rho_f a_h^2}}
 \end{pmatrix} \frac{d}{dt} \begin{pmatrix} V \\ p \\ U_z \\ \sigma_z \end{pmatrix} =$$

$$\begin{pmatrix}
 \frac{\rho_f}{\rho_p} \frac{A_f}{A_p} \frac{f}{4r} V_r |V_r| \left(\frac{a_f \frac{2v}{E}}{\frac{1}{\rho_p a_h} - \frac{a_h^2}{\rho_p a_3^2}} \right) - \frac{f}{4r} V_r |V_r| \\
 \frac{\rho_f}{\rho_p} \frac{A_f}{A_p} \frac{f}{4r} V_r |V_r| \left(\frac{a_f \frac{2v}{E}}{\frac{1}{\rho_p a_h} - \frac{a_h^2}{\rho_p a_3^2}} \right) - \frac{f}{4r} V_r |V_r| \\
 \frac{\rho_f}{\rho_p} \frac{A_f}{A_p} \frac{f}{4r} V_r |V_r| - \frac{f}{4r} V_r |V_r| \left(\frac{a_3^2 \frac{vr}{eE}}{\frac{1}{\rho_f} - \frac{a_3^2}{\rho_f a_h^2}} \right) \\
 \frac{\rho_f}{\rho_p} \frac{A_f}{A_p} \frac{f}{4r} V_r |V_r| - \frac{f}{4r} V_r |V_r| \left(\frac{a_3^2 \frac{vr}{eE}}{\frac{1}{\rho_f} - \frac{a_3^2}{\rho_f a_h^2}} \right)
 \end{pmatrix} \quad (B.39)$$

B.6 Summary table

For the sake of implementation the previous systems (Eqs. B.35 and B.39) are simplified to the system Eq. B.40 by means of the coefficients presented in table B.3.

$$\begin{pmatrix}
 \xi_{fV} & \xi_{fp} & \xi_{fU} & -\xi_{f\sigma} \\
 \xi_{fV} & -\xi_{fp} & \xi_{fU} & \xi_{f\sigma} \\
 \xi_{sV} & \xi_{sp} & \xi_{sU} & -\xi_{s\sigma} \\
 \xi_{sV} & -\xi_{sp} & \xi_{sU} & \xi_{s\sigma}
 \end{pmatrix} \begin{pmatrix} V \\ p \\ U \\ \sigma \end{pmatrix} = \begin{pmatrix} SF_f \\ SF_f \\ SF_s \\ SF_s \end{pmatrix} \quad (B.40)$$

Appendix B. MOC transformation for four-equation models

Table B.3 – Compatibility equations coefficients for FSI four-equation model Poisson-uncoupled and Poisson-coupled.

Poisson-uncoupled	
$\xi_{f_V} = 1$ $\xi_{f_p} = \frac{1}{\rho_f a_h}$ $\xi_{f_U} = 0$ $\xi_{f_\sigma} = 0$ $SF_f = -\frac{f}{4r} V_r V_r $ $SF_s = \frac{\rho_f}{\rho_p} \frac{A_f}{A_p} \frac{f}{4r} V_r V_r $	$\xi_{s_V} = 0$ $\xi_{s_p} = 0$ $\xi_{s_U} = 1$ $\xi_{s_\sigma} = \frac{1}{\rho_p a_3}$
Poisson-coupled	
$\xi_{f_V} = 1$ $\xi_{f_p} = \frac{1}{\rho_f a_h} + \frac{a_h^2 \frac{2\nu^2 r}{eE^2}}{\rho_p a_h - \frac{a_h^2}{\rho_p a_3^2}}$ $\xi_{f_U} = \frac{a_h \frac{2\nu}{E}}{\frac{1}{\rho_p a_h} - \frac{a_h^2}{\rho_p a_3^2}}$ $\xi_{f_\sigma} = \frac{a_h 2\nu}{E} - \frac{a_h^2 \frac{2\nu}{E \rho_p a_3^2}}{\frac{1}{\rho_p a_h} + \frac{a_h^2}{\rho_p a_3^2}}$ $SF_f = \frac{\rho_f}{\rho_p} \frac{A_f}{A_p} \frac{f}{4r} V_r V_r \left(\frac{a_h \frac{2\nu}{E}}{\frac{1}{\rho_p a_h} - \frac{a_h^2}{\rho_p a_3^2}} \right) - \frac{f}{4r} V_r V_r $ $SF_s = \frac{\rho_f}{\rho_p} \frac{A_f}{A_p} \frac{f}{4r} V_r V_r - \frac{f}{4r} V_r V_r \left(\frac{a_h^2 \frac{2\nu}{E}}{\frac{1}{\rho_p a_h} + \frac{a_h^2}{\rho_p a_3^2}} \right)$	$\xi_{s_V} = \frac{a_3^2 \frac{\nu r}{eE}}{\frac{1}{\rho_f} - \frac{a_3^2}{\rho_f a_h^2}}$ $\xi_{s_p} = a_3 \frac{\nu r}{eE} + \frac{a_3^2 \frac{\nu r}{eE \rho_f a_h^2}}{\frac{1}{\rho_f a_3} - \frac{a_3^2}{\rho_f a_h^2}}$ $\xi_{s_U} = 1$ $\xi_{s_\sigma} = \frac{1}{\rho_p a_3} + \frac{a_3^2 \frac{2\nu^2 r}{eE^2}}{\frac{1}{\rho_f a_3} - \frac{a_3^2}{\rho_f a_h^2}}$

C Verification of the four-equation model

A verification of the basic implementation of the four-equation model was carried out by means of the simulation of the well known Delft Hydraulics FSI benchmark problems from Tijsseling & Lavooij (1990) and Lavooij & Tijsseling (1989). From their set of FSI problems, Problem A is the most suitable for the verification of the developed four-equation model. It consists of a reservoir-pipe-valve system with length $L = 20 \text{ m}$, inner radius $r = 398.5 \text{ mm}$, pipe-wall thickness $e = 8 \text{ mm}$, Young's modulus $E = 210 \text{ GPa}$, solid density $\rho_p = 7900 \text{ kg/m}^3$, Poisson ratio $\nu = 0.30$, bulk modulus $K = 2.1 \text{ GPa}$, fluid density $\rho_f = 1000 \text{ kg/m}^3$ and initial flow velocity $V_0 = 1 \text{ m/s}$. The valve is closed in one time-step, and both boundary conditions fixed and free moving valve are analysed.

Corresponding wave speeds are $a_h = 1024.7 \text{ m/s}$ and $a_3 = 5280.5 \text{ m/s}$, giving a ratio of $a_h/a_3 = 0.194$. Like in Tijsseling (2003), two different simulations have been carried out: the first simulation approximating the ratio between celerities to $1/5 = 0.2$, and a second simulation considering a more accurate ratio of $13/67 = 0.194$. Figures C.1 show the output of both simulations, for a fixed and for a moving downstream boundary, as well as the Joukowsky solution ($\Delta p = \rho_f a_h \Delta V$).

Appendix C. Verification of the four-equation model

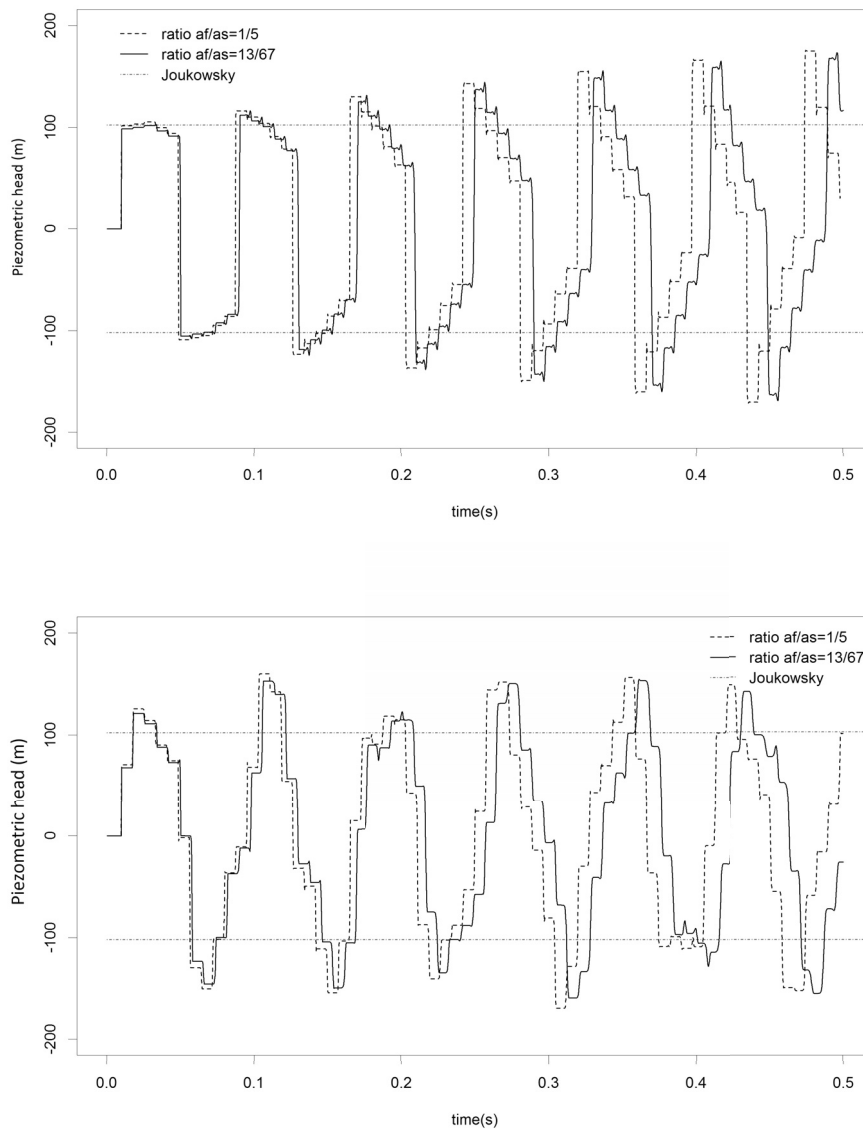


Figure C.1 – Delft Hydraulics benchmark Problem A with (a) fixed boundaries and (b) with a free moving valve.

In the first case, the ratio $\frac{a_h^*}{a_3^*} = \frac{1}{5}$ allows no interpolations at the boundaries for the characteristic lines corresponding to the fluid pressure wave propagation. However, the coarser the adjustment of the wave speed is, the greater the phase shift error becomes. For a ratio $\frac{a_h^*}{a_3^*} = \frac{13}{67}$, the wave speed remains almost with the same value, though, the interpolations at the boundaries are more intensive and, consequently, numerical diffusion and dispersion increase.

When simulating a frictionless system, results reveal two different phenomena: the Poisson

coupling beat, described in Tijsseling (1997), for a system with $\nu = 0.3$ and fixed boundaries (Fig. C.2a); and also a different kind of beat produced in junction coupling, when a massless valve is allowed to move in a Poisson-uncoupled simulation (Fig. C.2b).

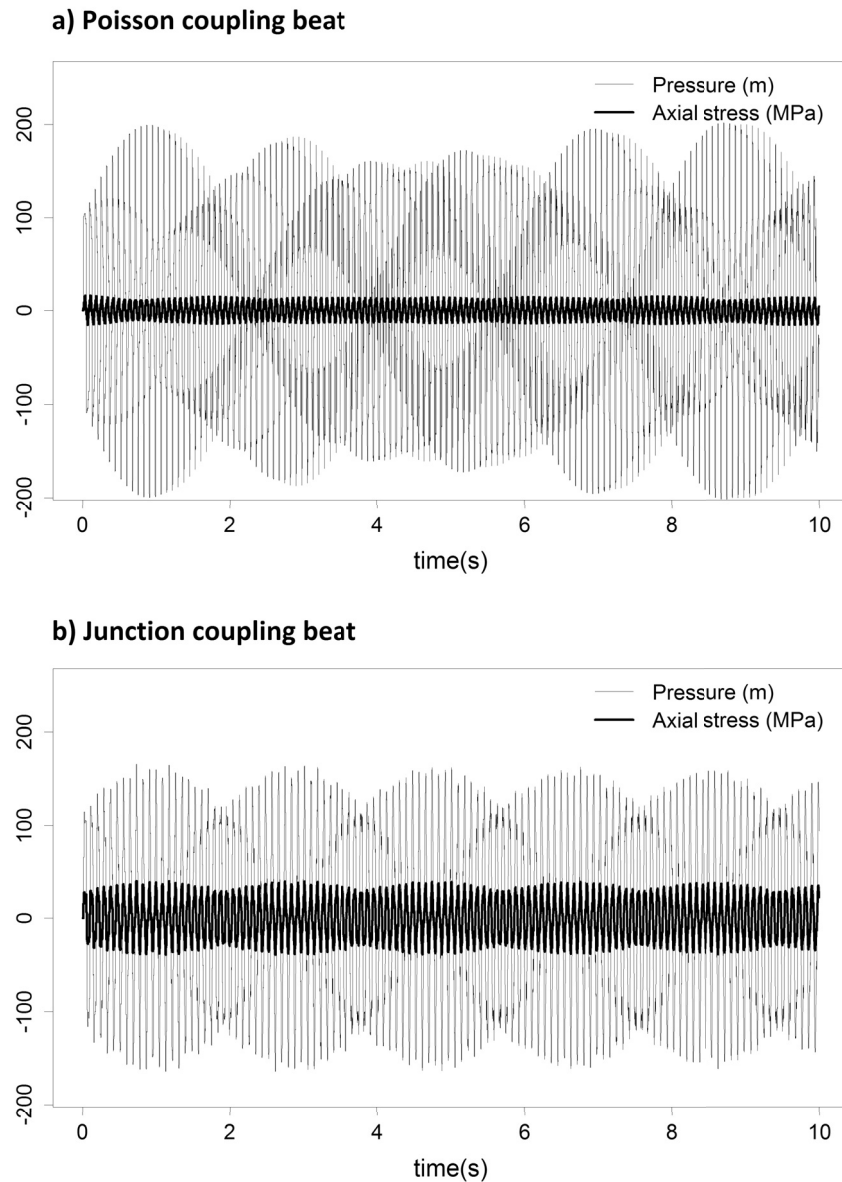


Figure C.2 – Delft Hydraulics benchmark Problem A: (a) pressure output for $\nu = 0.3$ and fixed valve (Poisson coupling beat); (b) pressure output for Poisson-uncoupled and a free moving valve.

Both beats presented in Fig. C.2 have a quite different structural behaviour and different effect on the fluid wave. Comparing the two graphs, the pressure variation amplitude in a fixed valve with Poisson coupling is higher with regard to pressure values but lower with regard

Appendix C. Verification of the four-equation model

to axial stress values. Furthermore, deft observers may notice a 90° phase shift between the axial stress wave and the fluid pressure wave, while in the case of free moving valve there is no apparent shift. The reason lies in the boundary condition imposed in the free moving valve, which balances the forces of the pressure over the valve with the axial stress of the pipe-wall, thus establishing a direct relation between both variables.

D Dry friction implementation in a four-equation model

D.1 Modification of the momentum conservation equation of the pipe-wall

In order to include dry friction dissipation in the physical system the fundamental conservation equations must be adapted. Dry friction affects the momentum conservation equation of the pipe axial movement as depicted in Fig. D.1. In the present appendix the momentum conservation equation of the pipe axial movement is derived.

Similarly to waterhammer fundamental conservation equations derivation (Chaudhry, 2014), beams equation for axial stress waves can be developed from the Reynolds Transport Theorem:

$$\frac{dB_{sys}}{dt} = \frac{d}{dt} \int_{cv} \beta \rho_p dV + [\beta \rho_p A_p (U - W)]_2 - [\beta \rho_p A_p (U - W)]_1 \quad (D.1)$$

Where the subscripts after the square brackets indicate the control volume boundary sections, W their respective velocities, B is the extensive property of the system, which in this case is the pipe-wall momentum ($M = m_s U$), and β is the intensive property:

$$\beta = \lim_{\Delta m \rightarrow 0} U \frac{\Delta m}{\Delta m} = U \quad (D.2)$$

From the second law of Newton we know that:

$$\frac{dM}{dt} = \sum F \quad (D.3)$$

and substituting Eq. D.2 and D.3 into Eq. D.1

$$\frac{d}{dt} \int_{cv} U \rho_p dV + [\rho_p A_p (U - W) U]_2 - [\rho_p A_p (U - W) U]_1 = \sum F \quad (D.4)$$

Appendix D. Dry friction implementation in a four-equation model

Applying Leibnitz's rule of integration and defining $\frac{dz_1}{dt} = W_1$ and $\frac{dz_2}{dt} = W_2$

$$\int_{z_1}^{z_2} \frac{\partial}{\partial t} (\rho_p A_p U) dz + (\rho_p A_p U)_2 W_2 - (\rho_p A_p U)_1 W_1 + [\rho_p A_p (U - W) U]_2 - [\rho_p A_p (U - W) U]_1 = \sum F \quad (D.5)$$

Applying the mean-value theorem to Eq. D.5

$$\frac{\partial}{\partial t} (\rho_p A_p U) \Delta z + (\rho_p A_p U^2)_2 - (\rho_p A_p U^2)_1 = \sum F \quad (D.6)$$

dividing Eq. D.6 by Δz and letting Δz approach 0

$$\frac{\partial}{\partial t} (\rho_p A_p U) + \frac{\partial}{\partial z} (\rho_p A_p U^2) = \lim_{\Delta z \rightarrow 0} \frac{\sum F}{\Delta z} \quad (D.7)$$

and expanding the differential terms in the following manner

$$U \left[\frac{\partial}{\partial t} (\rho_p A_p) + \frac{\partial}{\partial z} (\rho_p A_p U) \right] + \rho_p A_p \frac{\partial U}{\partial t} + \rho_p A_p U \frac{\partial U}{\partial z} = \lim_{\Delta z \rightarrow 0} \frac{\sum F}{\Delta z} \quad (D.8)$$

The term in square brackets of Eq. D.8 is actually the mass conservation equation (Chaudhry, 2014), hence its value is 0 and taking the total derivative of the remaining terms Eq. D.8 becomes

$$\rho_p A_p \frac{dU}{dt} = \lim_{\Delta z \rightarrow 0} \frac{\sum F}{\Delta z} \quad (D.9)$$

Notice that Eq. D.9 is nothing but the second law of Newton applied in an infinitesimal system.

At this point the balance of forces acting on the system may be incorporated in Eq. D.9. Fig. D.1 depicts this balance of forces acting in the axial direction of the pipe.

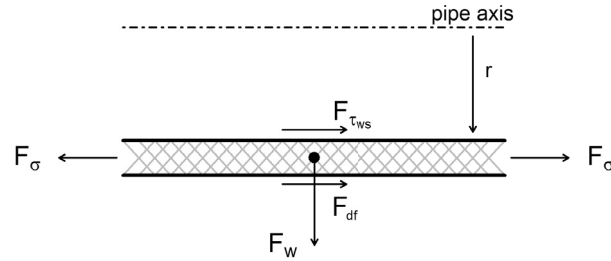


Figure D.1 – Schematic of forces acting in the pipe-wall in the axial direction.

D.1. Modification of the momentum conservation equation of the pipe-wall

The forces acting on the control volume in the axial direction of the pipe are:

$$\begin{aligned}
 F_{\sigma_1} &= \sigma_1 A_p \\
 F_{\sigma_2} &= \sigma_2 A_p \\
 F_w &= (x_2 - x_1) \rho_p A_p g \sin \Theta \\
 F_{\tau_{ws}} &= \tau_{ws} \pi D (z_2 - z_1) \\
 F_{df} &= (z_2 - z_1) (\rho_p A_p + \rho_f A_f) g \cos \Theta \mu \text{sign}(U)
 \end{aligned} \tag{D.10}$$

where F_{df} is the Coulomb's dry friction force, $F_{\tau_{ws}}$ is the skin friction force and Θ is the angle of the pipe respect the horizontal plane.

Let's consider a horizontal pipe. The balance of forces is then

$$\sum F = -\sigma_1 A_p + \sigma_2 A_p + \tau_{ws} \pi D (z_2 - z_1) + (z_2 - z_1) (\rho_p A_p + \rho_f A_f) g \mu \text{sign}(U) \tag{D.11}$$

dividing by Δz and letting Δz approach 0

$$\lim_{\Delta z \rightarrow 0} \frac{\sum F}{\Delta z} = A_p \frac{\partial \sigma}{\partial z} + \tau_{ws} \pi D + (\rho_p A_p + \rho_f A_f) g \mu \text{sign}(U) \tag{D.12}$$

Assuming quasi-steady skin friction the shear stress between the fluid and the pipe-wall can be computed by means of Darcy-Weisbach equation

$$\tau_{ws} = \frac{1}{8} f \rho_f V_r |V_r| \tag{D.13}$$

Substituting Eq. D.13 into Eq. D.12

$$\lim_{\Delta z \rightarrow 0} \frac{\sum F}{\Delta z} = A_p \frac{\partial \sigma}{\partial z} + \frac{f \rho_f A_f}{4r} V_r |V_r| + (\rho_p A_p + \rho_f A_f) g \mu \text{sign}(U) \tag{D.14}$$

and substituting Eq D.14 into Eq. D.9 and dividing by $\rho_p A_p$

$$\frac{dU}{dt} - \frac{1}{\rho_p} \frac{\partial \sigma}{\partial z} = \frac{\rho_f A_f}{\rho_p A_p} \frac{f}{4r} V_r |V_r| + \left(1 + \frac{\rho_f A_f}{\rho_p A_p} \right) g \mu \text{sign}(U) \tag{D.15}$$

Finally expanding the total derivative in Eq. D.15 and neglecting its convective acceleration term, which is much smaller in most engineering applications, the momentum conservation equation Eq. D.16 for the pipe-wall axial movement is obtained:

$$\frac{\partial U}{\partial t} - \frac{1}{\rho_p} \frac{\partial \sigma}{\partial z} = \frac{\rho_f A_f}{\rho_p A_p} \frac{f}{4r} V_r |V_r| + \left(1 + \frac{\rho_f A_f}{\rho_p A_p} \right) g \mu \text{sign}(U) \tag{D.16}$$

D.2 MOC transformation

D.2.1 System coefficients

Following the same MOC transformation development as the one presented in Appendix B, for the four-equation model solving the system of equations Eq. A.47, and including dry friction dissipation in the pipe momentum equation (Eq. D.16), the coefficients are:

Table D.1 – Coefficients for factor matrices A and B and right-hand-side vector r

Matrix A	Matrix B	Vector r
$\alpha_{11} = 1$	$\beta_{12} = \frac{1}{\rho_f}$	$r_1 = -\frac{f}{4r} V_r V_r $
$\alpha_{22} = \frac{1}{\rho_f a_h^2}$	$\beta_{21} = 1$	$r_2 = 0$
$\alpha_{24} = -\frac{2\nu}{E}$	$\beta_{34} = -\frac{1}{\rho_p}$	$r_3 = \frac{\rho_f}{\rho_p} \frac{A_f}{A_p} \frac{f}{4r} V_r V_r + \left(1 + \frac{\rho_f A_f}{\rho_p A_p}\right) g \mu \text{sign}(U)$
$\alpha_{33} = 1$	$\beta_{43} = 1$	$r_4 = 0$
$\alpha_{42} = \frac{\nu r}{eE}$	–	–
$\alpha_{44} = -\frac{1}{\rho_p a_3^2}$	–	–

D.2.2 Eigenvalues

In the Appendix B the solution of the characteristic equation $|B - \lambda A| = 0$ is derived reaching the following four distinct real roots:

$$\lambda_1 = +a_h; \lambda_2 = -a_h; \lambda_3 = +a_3; \lambda_4 = -a_3 \quad (\text{D.17})$$

D.2.3 Compatibility equations

Substituting the eigenvalues Eq. D.17 and the coefficient values from table D.1 into Eq. B.29, the compatibility equations for the modified four-equation model are:

$$\begin{pmatrix}
 1 & \frac{1}{\rho_f a_h} + \frac{a_h^2 \frac{2v^2 r}{eE^2}}{\frac{1}{\rho_p a_h} - \frac{a_h^2}{\rho_p a_3^2}} & \frac{a_h \frac{2v}{E}}{\frac{1}{\rho_p a_h} - \frac{a_h^2}{\rho_p a_3^2}} & -\frac{a_h 2v}{E} - \frac{a_h^2 \frac{2v}{E \rho_p a_3^2}}{\frac{1}{\rho_p a_h} - \frac{a_h^2}{\rho_p a_3^2}} \\
 1 & -\frac{1}{\rho_f a_h} - \frac{a_h^2 \frac{2v^2 r}{eE^2}}{\frac{1}{\rho_p a_h} - \frac{a_h^2}{\rho_p a_3^2}} & \frac{a_h \frac{2v}{E}}{\frac{1}{\rho_p a_h} - \frac{a_h^2}{\rho_p a_3^2}} & \frac{a_h 2v}{E} + \frac{a_h^2 \frac{2v}{E \rho_p a_3^2}}{\frac{1}{\rho_p a_h} - \frac{a_h^2}{\rho_p a_3^2}} \\
 \frac{a_3^2 \frac{vr}{eE}}{\frac{1}{\rho_f} - \frac{a_3^2}{\rho_f a_h^2}} & a_3 \frac{vr}{eE} + \frac{a_3^2 \frac{vr}{eE \rho_f a_h^2}}{\frac{1}{\rho_f a_3} - \frac{a_3}{\rho_f a_h^2}} & 1 & -\frac{1}{\rho_p a_3} - \frac{a_3^2 \frac{2v^2 r}{eE^2}}{\rho_f a_3 \frac{1}{\rho_f a_h^2}} \\
 \frac{a_3^2 \frac{vr}{eE}}{\frac{1}{\rho_f} - \frac{a_3^2}{\rho_f a_h^2}} & -a_3 \frac{vr}{eE} - \frac{a_3^2 \frac{vr}{eE \rho_f a_h^2}}{\frac{1}{\rho_f a_3} - \frac{a_3}{\rho_f a_h^2}} & 1 & \frac{1}{\rho_p a_3} + \frac{a_3^2 \frac{2v^2 r}{eE^2}}{\rho_f a_3 \frac{1}{\rho_f a_h^2}}
 \end{pmatrix} \frac{d}{dt} \begin{pmatrix} V \\ p \\ U_z \\ \sigma_z \end{pmatrix} =$$

$$\begin{pmatrix}
 \left(\frac{\rho_f A_f}{\rho_p A_p} \frac{f}{4r} V_r |V_r| + \left(1 + \frac{\rho_f A_f}{\rho_p A_p} \right) g \mu \text{sign}(U) \right) \left(\frac{a_h \frac{2v}{E}}{\frac{1}{\rho_p a_h} - \frac{a_h^2}{\rho_p a_3^2}} \right) - \frac{f}{4r} V_r |V_r| \\
 \left(\frac{\rho_f A_f}{\rho_p A_p} \frac{f}{4r} V_r |V_r| + \left(1 + \frac{\rho_f A_f}{\rho_p A_p} \right) g \mu \text{sign}(U) \right) \left(\frac{a_h \frac{2v}{E}}{\frac{1}{\rho_p a_h} - \frac{a_h^2}{\rho_p a_3^2}} \right) - \frac{f}{4r} V_r |V_r| \\
 \frac{\rho_f A_f}{\rho_p A_p} \frac{f}{4r} V_r |V_r| + \left(1 + \frac{\rho_f A_f}{\rho_p A_p} \right) g \mu \text{sign}(U) - \frac{f}{4r} V_r |V_r| \left(\frac{a_3^2 \frac{vr}{eE}}{\frac{1}{\rho_f} - \frac{a_3^2}{\rho_f a_h^2}} \right) \\
 \frac{\rho_f A_f}{\rho_p A_p} \frac{f}{4r} V_r |V_r| + \left(1 + \frac{\rho_f A_f}{\rho_p A_p} \right) g \mu \text{sign}(U) - \frac{f}{4r} V_r |V_r| \left(\frac{a_3^2 \frac{vr}{eE}}{\frac{1}{\rho_f} - \frac{a_3^2}{\rho_f a_h^2}} \right)
 \end{pmatrix} \quad (\text{D.18})$$

which for the sake of implementation, using the summary table B.3, the system D.18 is presented in the following form:

$$\begin{pmatrix}
 \xi_{fV} & \xi_{fp} & \xi_{fU} & -\xi_{f\sigma} \\
 \xi_{fV} & -\xi_{fp} & \xi_{fU} & \xi_{f\sigma} \\
 -\xi_{sV} & -\xi_{sp} & \xi_{sU} & -\xi_{s\sigma} \\
 -\xi_{sV} & \xi_{sp} & \xi_{sU} & \xi_{s\sigma}
 \end{pmatrix} \frac{d}{dt} \begin{pmatrix} V \\ p \\ U \\ \sigma \end{pmatrix} = \begin{pmatrix} SF_f + DF_f \\ SF_f + DF_f \\ SF_s + DF_s \\ SF_s + DF_s \end{pmatrix} \quad (\text{D.19})$$

Therefore, the LHS terms of the Poisson-coupled four-equation system remain with equal coefficients as the ones presented in the summary table B.3 and the RHS terms, in function of

Appendix D. Dry friction implementation in a four-equation model

the dissipative phenomena are presented in the Table D.2.

Table D.2 – Compatibility equations coefficients for FSI, skin friction and dry friction terms.

Skin friction	
Frictionless	
$SF_f = 0$	$SF_s = 0$
Steady friction	
$SF_f = \frac{\rho_f}{\rho_p} \frac{A_f}{A_p} \frac{f}{4r} V_r V_r \left(\frac{a_h \frac{2\nu}{E}}{\frac{1}{\rho_p a_h} - \frac{a_h^2}{\rho_p a_3^2}} \right) - \frac{f}{4r} V_r V_r $	$SF_s = \frac{\rho_f}{\rho_p} \frac{A_f}{A_p} \frac{f}{4r} V_r V_r - \frac{f}{4r} V_r V_r \left(\frac{a_3^2 \frac{\nu r}{eE}}{\frac{1}{\rho_f} - \frac{a_3^2}{\rho_f a_h^2}} \right)$
Brunone unsteady friction	
$f = f_s + f_u$	
$f_u = K_b \frac{D}{Vr_i^j Vr_i^j } \frac{Vr_i^j - Vr_i^{j-1}}{dt} - a_h \frac{Vr_i^j - Vr_{i-1}^j}{dx}$	
$SF_f = \frac{\rho_f}{\rho_p} \frac{A_f}{A_p} \frac{f}{4r} V_r V_r \left(\frac{a_h \frac{2\nu}{E}}{\frac{1}{\rho_p a_h} - \frac{a_h^2}{\rho_p a_3^2}} \right) - \frac{f}{4r} V_r V_r $	$SF_s = \frac{\rho_f}{\rho_p} \frac{A_f}{A_p} \frac{f}{4r} V_r V_r - \frac{f}{4r} V_r V_r \left(\frac{a_3^2 \frac{\nu r}{eE}}{\frac{1}{\rho_f} - \frac{a_3^2}{\rho_f a_h^2}} \right)$
Trikha unsteady friction	
$mk = (1, 8.1, 40)$	
$nk = (26.4, 200, 8000)$	
$Yk_{i w}^j = mk_w (Vr_i^j - Vr_i^{j-1}) + e^{-nk_w dt} Yk_i^{j-1}$	
$SF_f = \left(\frac{dt 16\mu}{D^2} \sum Yk_{i w}^j + \frac{f}{4r} Vr_i^j Vr_i^j dt \right) \left(\frac{\rho_f}{\rho_p} \frac{A_f}{A_p} \frac{a_h \frac{2\nu}{E}}{\frac{1}{\rho_p a_h} - \frac{a_h^2}{\rho_p a_3^2}} - 1 \right)$	
$SF_s = \left(\frac{dt 16\mu}{D^2} \sum Yk_{i w}^j + \frac{f}{4r} Vr_i^j Vr_i^j dt \right) \left(\frac{\rho_f}{\rho_p} \frac{A_f}{A_p} - \frac{a_3^2 \frac{\nu r}{eE}}{\frac{1}{\rho_f} - \frac{a_3^2}{\rho_f a_h^2}} \right)$	
Dry friction	
Frictionless	
$DF_f = 0$	$DF_s = 0$
Coulomb's friction	
$DF_f = \left(1 + \frac{\rho_f A_f}{\rho_p A_p} \right) g \mu \text{sign}(U) \left(\frac{a_h \frac{2\nu}{E}}{\frac{1}{\rho_p a_h} - \frac{a_h^2}{\rho_p a_3^2}} \right)$	$DF_s = \left(1 + \frac{\rho_f A_f}{\rho_p A_p} \right) g \mu \text{sign}(U)$

E Extended Joukowski equation

E.1 Introduction

Young, Rankine and Joukowski formulations (Young, 1808; Rankine, 1870; Joukowski, 1904) offer a very useful tool for designing purposes, as they allow an easy computation of the maximum loading during a transient event, either in solids (maximum axial stress) or fluids (maximum inner pressure). Eqs. E.1 and E.2 show these expressions:

$$\Delta\sigma = \rho_p a_p \Delta U \quad (\text{E.1})$$

$$\Delta p = -\rho_f a_h \Delta V \quad (\text{E.2})$$

Young (Eq. E.1) and Joukowski (Eq. E.2) formulae were derived assuming continuous and homogeneous media. However, in a fluid-filled conduit the maximum pressure is frequently influenced by the interaction between the fluid and the pipe structure. Jones & Wood (1972) and Wilkinson (1979) derived Joukowski like expressions modified in order to account for pipe axial movement effect. In their development, though, spring-mass systems were considered for the downstream valve movement. In the present appendix, a derivation of alternative formulae to Joukowski is presented. The development takes into account the 1-DOF and the 2-DOF of the pipe system, and the starting point is the fundamental equations of a four-equation FSI model.

E.2 Governing equations

The starting point is the four fundamental conservation equations (Eqs. A.47). Skalak (1955) introduced a solution of a 1-D four-equation non-dispersive model. Joukowski formula can be derived by means of the method of characteristics from the fluid momentum and continuity equations and by neglecting the RHS terms. Similarly, Young formula can be as well derived by means of the method of characteristics from the pipe momentum and continuity equations and by neglecting the RHS terms.

As explained in the Appendices B and D the compatibility equations, Eqs. B.39, are only valid along the characteristic lines with slopes: $1/a_h$ and $-1/a_h$ for the fluid characteristics, and $1/a_3$ and $-1/a_3$ for the pipe-wall characteristics. The present study focuses on the fluid pressure rise at the downstream boundary. At this location only the positive characteristic equations yield information from previous time history. Rewriting the positive characteristic equations according to the coefficients of table B.3, it yields

$$\xi_{f_p} \frac{dp}{dt} + \xi_{f_v} \frac{dV}{dt} + \xi_{f_\sigma} \frac{d\sigma}{dt} + \xi_{f_U} \frac{dU}{dt} = 0 \quad (\text{E.3})$$

$$\xi_{s_p} \frac{dp}{dt} + \xi_{s_v} \frac{dV}{dt} + \xi_{s_\sigma} \frac{d\sigma}{dt} + \xi_{s_U} \frac{dU}{dt} = 0 \quad (\text{E.4})$$

Eqs. E.3 and E.4 can be solved by integration according to the characteristic grid of Fig. E.1 and following the positive characteristic lines, for the fluid and for the structure

$$\xi_{f_p} \int_{B_0}^{P_1} \frac{dp}{dt} + \xi_{f_v} \int_{B_0}^{P_1} \frac{dV}{dt} + \xi_{f_\sigma} \int_{B_0}^{P_1} \frac{d\sigma}{dt} + \xi_{f_U} \int_{B_0}^{P_1} \frac{dU}{dt} = 0 \quad (\text{E.5})$$

and

$$\xi_{s_p} \int_{A_0}^{P_1} \frac{dp}{dt} + \xi_{s_v} \int_{A_0}^{P_1} \frac{dV}{dt} + \xi_{s_\sigma} \int_{A_0}^{P_1} \frac{d\sigma}{dt} + \xi_{s_U} \int_{A_0}^{P_1} \frac{dU}{dt} = 0 \quad (\text{E.6})$$

E.3. Pressure rise in a conduit only anchored at the upstream end

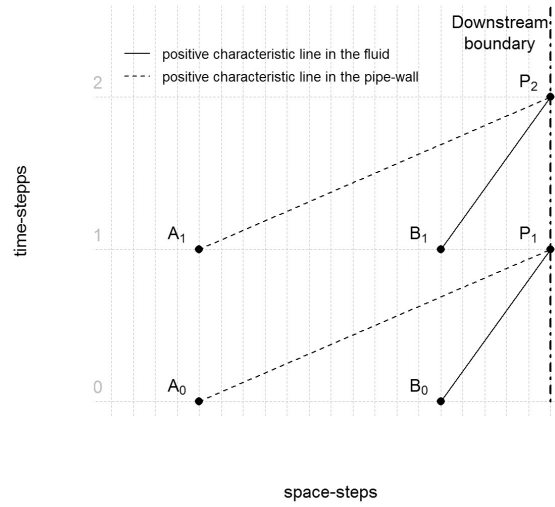


Figure E.1 – Characteristic grid for a four-equation model at the downstream boundary.

Assuming spatially uniform variables during the initial steady state (level 0 in Fig. E.1) Eqs. E.5 and E.6 can be expressed as

$$\xi_{fp} \Delta p + \xi_{fv} \Delta V + \xi_{f\sigma} \Delta \sigma + \xi_{fU} \Delta U = 0 \quad (\text{E.7})$$

and

$$\xi_{sp} \Delta p + \xi_{sv} \Delta V + \xi_{s\sigma} \Delta \sigma + \xi_{sU} \Delta U = 0 \quad (\text{E.8})$$

being Δ the increment of a dependent variable between a certain time-step and the corresponding previous one. Notice that for a known ΔV and $v = 0$, Eq. E.7 becomes Eq. E.2 and, similarly, for a known ΔU and $v = 0$, Eq. E.8 becomes Eq. E.1.

E.3 Pressure rise in a conduit only anchored at the upstream end

E.3.1 Pressure rise in a conduit only anchored at the upstream end

First pressure rise

The boundary conditions at the downstream pipe end for a non-anchored valve taking into account the valve inertia by means of second law of Newton are

$$\Delta V_1 = \Delta U_1 - V_0 \quad (\text{E.9})$$

Appendix E. Extended Joukowski equation

and

$$\Delta\sigma_1 = \frac{A_f}{A_p} \Delta p_1 - \frac{m_v}{A_p} \frac{\Delta U_1}{t_v} \quad (\text{E.10})$$

where Δp_1 and ΔU_1 can be determined by substituting Eqs. E.9 and E.10 into Eqs. E.7 and E.8 obtaining Eqs. E.11 and E.12:

$$\Delta p_1 = \Psi_{p_1} \rho_f a_h V_0 \quad \text{or} \quad H_1 = \Psi_{p_1} \frac{a_h V_0}{g} \quad (\text{E.11})$$

and

$$\Delta U_1 = \Psi_{U_1} V_0 \quad (\text{E.12})$$

where Ψ_{p_1} and Ψ_{U_1} are defined in table E.1. Notice that when $\lim_{m_v \rightarrow \infty}$ and $\lim_{v \rightarrow 0} \Psi_{p_1} \rightarrow 1$ and Eq. E.11 tends to Eq. E.2.

Second pressure rise

Eq. E.11 is analogue to Joukowski formula (Eq. E.2) when the interaction with the piping structure is taken into account for a conduit only anchored in the upstream pipe end. However the pressure rise obtained by Eq. E.11 is not the maximum. Usually, the axial stress wave propagates faster than the pressure wave, hence, during the first pressure peak the stress wave pushes back and forth the downstream pipe-end producing a breathing/pumping effect. To compute the maximum pressure during the first pressure peak a second pressure rise, due to the pumping effect of the second vibrating mode, must be taken into account when the stress wave becomes negative next to the downstream pipe end.

The boundary conditions at the downstream pipe end at the stage of the second pressure rise are

$$\Delta V_2 = \Delta U_2 \quad (\text{E.13})$$

and

$$\Delta\sigma_2 = -2\sigma_1 \quad (\text{E.14})$$

and substituting Eqs. E.13 and E.14 into Eqs. E.7 and E.8 Eqs. E.15 and E.16 are obtained:

$$\Delta p_2 = \Psi_{p_2} \sigma_1 \quad (\text{E.15})$$

and

$$\Delta U_2 = \Psi_{U_2} \sigma_1 \quad (\text{E.16})$$

E.4. Application and validation of the equations

where Ψ_{p_2} and Ψ_{U_2} are defined in table E.1. Notice that Eq. E.16 tends to Young axial stress rise (Eq. E.1) for $\lim_{v \rightarrow 0}$.

Finally, adding the second pressure rise (*i.e.* result of Eq. E.15) to the result of the first pressure rise from Eq. E.11, the maximum overpressure during the first pressure peak is obtained (Eq. E.17):

$$p_{max} = \Psi_{JK} \rho_f a_h V_0 \quad \text{or} \quad H_{max} = \Psi_{JK} \frac{a_h V_0}{g} \quad (\text{E.17})$$

where Ψ_{JK} is defined in table E.1. For $\lim_{m_v \rightarrow \infty}$ and $\lim_{v \rightarrow 0}$ notice that $\Psi_{p_1} \rightarrow 1$ and $\Psi_{p_2} \rightarrow 0$ hence Eq. E.17 becomes Joukowski expression (Eq. E.2).

E.4 Application and validation of the equations

Assuming a mass valve of $m_v = 10$ kg and a manoeuvre time of $t_v = 0.003$ s respective pressure surges were computed applying Eqs. E.2, E.11 and E.15 for the tests carried out in the straight copper pipe facility with the set-up of a non-anchored valve. This calibrated mass valve accounts as well for the downstream hose and connection elements. As depicted in Fig. E.2 the proposed equations show an improved accuracy compared to Joukowski equation.

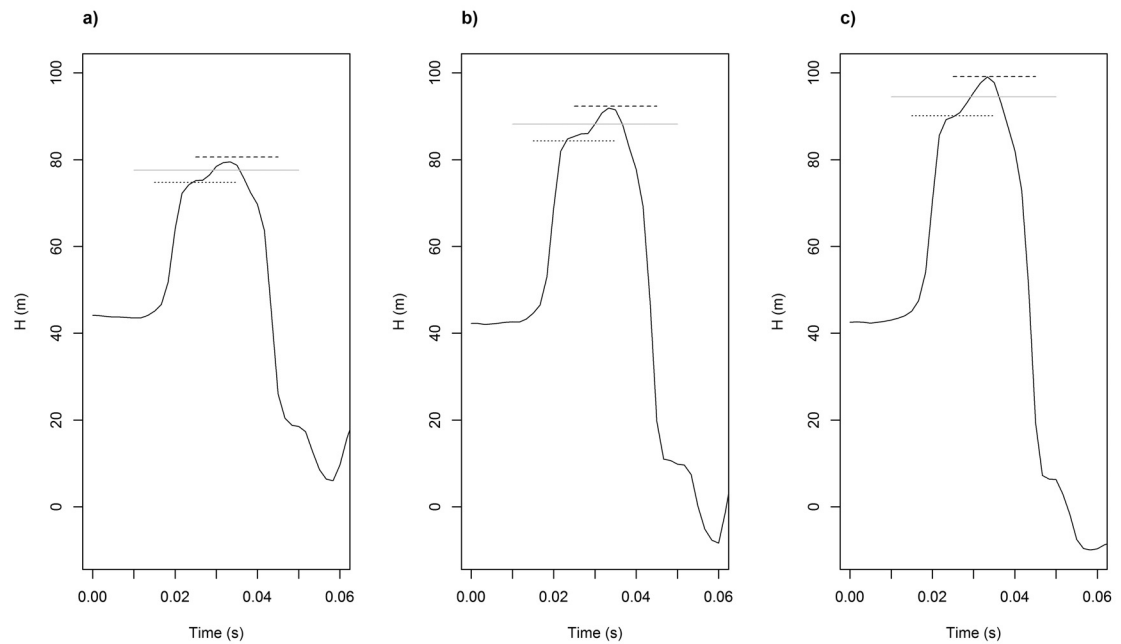


Figure E.2 – Comparison of pressure rise output from Eq. E.2 (grey dotted line), Eq. E.11 (black dotted line) and Eq. E.17 (black dashed line). a) corresponds to the test SCP04, b) to SCP05 and c) to SCP06 (*cf.* Chapter 3).

Appendix E. Extended Joukowski equation

Table E.1 – Coefficients for extended Joukowski equation

First pressure rise coefficients	$\Psi_{p1} = \frac{1}{a_f \rho_f} \frac{\frac{\xi_{fV}}{\xi_{fV} - \xi_{f\sigma} \frac{m_v}{A_p t_v} + \xi_{fU}} - \frac{\xi_{sV}}{\xi_{sV} - \xi_{s\sigma} \frac{m_v}{A_p t_v} + \xi_{sU}}}{\frac{\xi_{fp} + \xi_{f\sigma} \frac{A_f}{A_p}}{\xi_{fV} - \xi_{f\sigma} \frac{m_v}{A_p t_v} + \xi_{fU}} - \frac{\xi_{sp} + \xi_{s\sigma} \frac{A_f}{A_p}}{\xi_{sV} - \xi_{s\sigma} \frac{m_v}{A_p t_v} + \xi_{sU}}}$ $\Psi_{U1} = \frac{\frac{\xi_{fV}}{\xi_{fp} + \xi_{f\sigma} \frac{A_f}{A_p}} - \frac{\xi_{sV}}{\xi_{sp} + \xi_{s\sigma} \frac{A_f}{A_p}}}{\frac{\xi_{fV} - \xi_{f\sigma} \frac{m_v}{A_p t_v} + \xi_{fU}}{\xi_{fp} + \xi_{f\sigma} \frac{A_f}{A_p}} - \frac{\xi_{sV} - \xi_{s\sigma} \frac{m_v}{A_p t_v} + \xi_{sU}}{\xi_{sp} + \xi_{s\sigma} \frac{A_f}{A_p}}}$
Second pressure rise coefficients	$\Psi_{p2} = 2 \frac{\frac{\xi_{f\sigma}}{\xi_{fV} + \xi_{fU}} - \frac{\xi_{s\sigma}}{\xi_{sV} + \xi_{sU}}}{\frac{\xi_{fp}}{\xi_{fV} + \xi_{fU}} - \frac{\xi_{sp}}{\xi_{sV} + \xi_{sU}}}$ $\Psi_{U2} = 2 \frac{\frac{\xi_{f\sigma}}{\xi_{fp}} - \frac{\xi_{s\sigma}}{\xi_{sp}}}{\frac{\xi_{fV} + \xi_{fU}}{\xi_{fp}} - \frac{\xi_{sV} + \xi_{sU}}{\xi_{sp}}}$
Joukowski correction factor	$\Psi_{Jk} = \frac{a_f \rho_f \Psi_{p1} + \left(a_f \rho_f \frac{A_f}{A_p} \Psi_{p1} - \frac{m_v}{A_p t_v} \Psi_{U1} \right) \Psi_{p2}}{a_f \rho_f}$

F Experimental work in the Straight Copper Pipe facility

F.1 Introduction

An extensive experimental programme was carried out at the Straight Copper Pipe facility (SCP) aiming at identifying and distinguishing several features of fluid-structure interaction in straight pipes. The focus was mainly on the influence of pipe supports, skin friction and dry friction dissipation during hydraulic transients. The experimental data presented hereby complements, therefore, the reported in Chapters 3, 4 and 5.

Four different pipe set-ups were tested: the downstream pipe end is anchored (SCP1); the pipe is released and there are no anchors all throughout the pipe (SCP2); the pipe is anchored only in the midstream section (SCP3); the pipe is anchored in the midstream and downstream sections (SCP4). The set-ups were subjected to five different waterhammer waves according to different initial steady states. Tests with sampling frequency at 1200 Hz are presented to show in accuracy the first wave cycles and at 600 Hz to show the overall wave damping.

F.2 Summary test tables

Table F.1 – Summary table for SCP1 tests.

Test ID	frequency (Hz)	test duration (s)	anchoring points	V_0 (m/s)
SCP1 ₁₁	1200	0.15	downstream	0.26
SCP1 ₁₂	600	4.00	downstream	0.26
SCP1 ₂₁	1200	0.15	downstream	0.36
SCP1 ₂₂	600	4.00	downstream	0.36
SCP1 ₃₁	1200	0.15	downstream	0.41
SCP1 ₃₂	600	4.00	downstream	0.41
SCP1 ₄₁	1200	0.15	downstream	0.53
SCP1 ₄₂	600	4.00	downstream	0.53
SCP1 ₅₁	1200	0.15	downstream	0.77
SCP1 ₅₂	600	4.00	downstream	0.77

Appendix F. Experimental work in the Straight Copper Pipe facility

Table F2 – Summary table for SCP2 tests.

Test ID	frequency (Hz)	test duration (s)	anchoring points	V₀ (m/s)
SCP2 ₁₁	1200	0.15	no anchors	0.26
SCP2 ₁₂	600	4.00	no anchors	0.26
SCP2 ₂₁	1200	0.15	no anchors	0.36
SCP2 ₂₂	600	4.00	no anchors	0.36
SCP2 ₃₁	1200	0.15	no anchors	0.41
SCP2 ₃₂	600	4.00	no anchors	0.41
SCP2 ₄₁	1200	0.15	no anchors	0.53
SCP2 ₄₂	600	4.00	no anchors	0.53
SCP2 ₅₁	1200	0.15	no anchors	0.77
SCP2 ₅₂	600	4.00	no anchors	0.77

Table F3 – Summary table for SCP3 tests.

Test ID	frequency (Hz)	test duration (s)	anchoring points	V₀ (m/s)
SCP3 ₁₁	1200	0.15	midstream	0.26
SCP3 ₁₂	600	4.00	midstream	0.26
SCP3 ₂₁	1200	0.15	midstream	0.36
SCP3 ₂₂	600	4.00	midstream	0.36
SCP3 ₃₁	1200	0.15	midstream	0.41
SCP3 ₃₂	600	4.00	midstream	0.41
SCP3 ₄₁	1200	0.15	midstream	0.53
SCP3 ₄₂	600	4.00	midstream	0.53
SCP3 ₅₁	1200	0.15	midstream	0.77
SCP3 ₅₂	600	4.00	midstream	0.77

Table F4 – Summary table for SCP4 tests.

Test ID	frequency (Hz)	test duration (s)	anchoring points	V₀ (m/s)
SCP4 ₁₁	1200	0.15	mid and downstream	0.26
SCP4 ₁₂	600	4.00	mid and downstream	0.26
SCP4 ₂₁	1200	0.15	mid and downstream	0.36
SCP4 ₂₂	600	4.00	mid and downstream	0.36
SCP4 ₃₁	1200	0.15	mid and downstream	0.41
SCP4 ₃₂	600	4.00	mid and downstream	0.41
SCP4 ₄₁	1200	0.15	mid and downstream	0.53
SCP4 ₄₂	600	4.00	mid and downstream	0.53
SCP4 ₅₁	1200	0.15	mid and downstream	0.77
SCP4 ₅₂	600	4.00	mid and downstream	0.77

F.3 Experimental tests

F.3.1 Tests with anchored downstream end (SCP1)

SCP1₁:

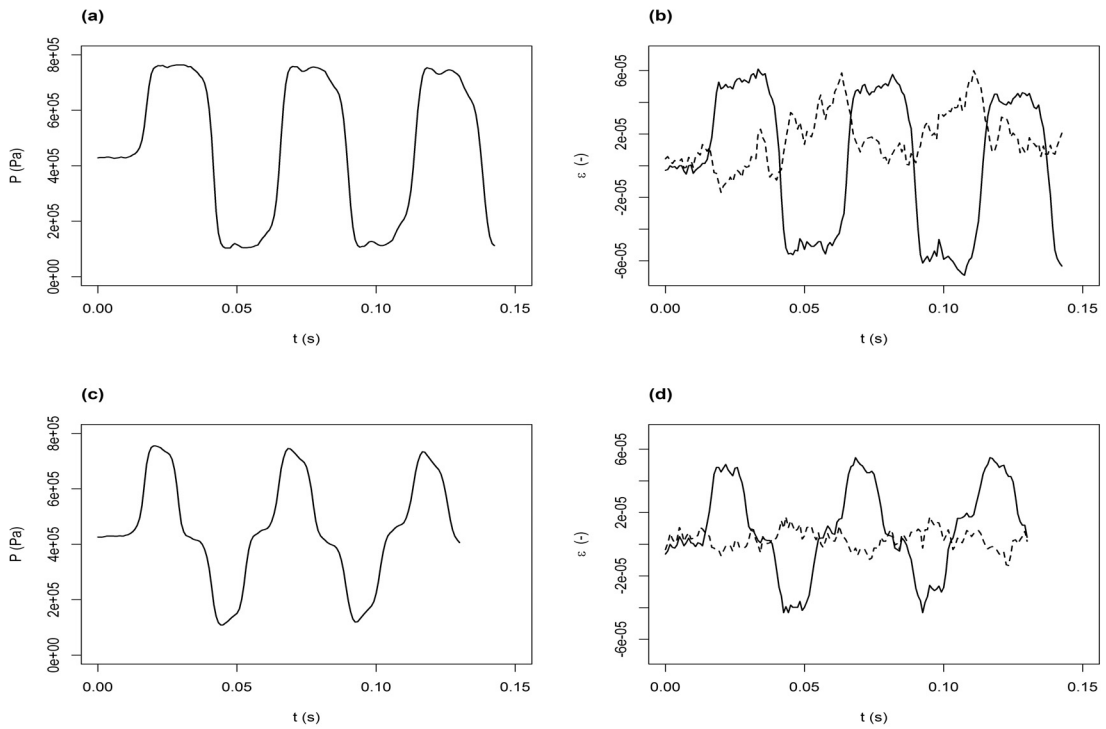


Figure F.1 – (a) Pressure signal at the downstream pipe end; (b) measured strains at the downstream pipe section in the circumferential (solid line) and in the axial (dashed line) directions; (c) pressure signal at the midstream pipe section; (d) measured strains at the midstream pipe section in the circumferential (solid line) and in the axial (dashed line) directions.

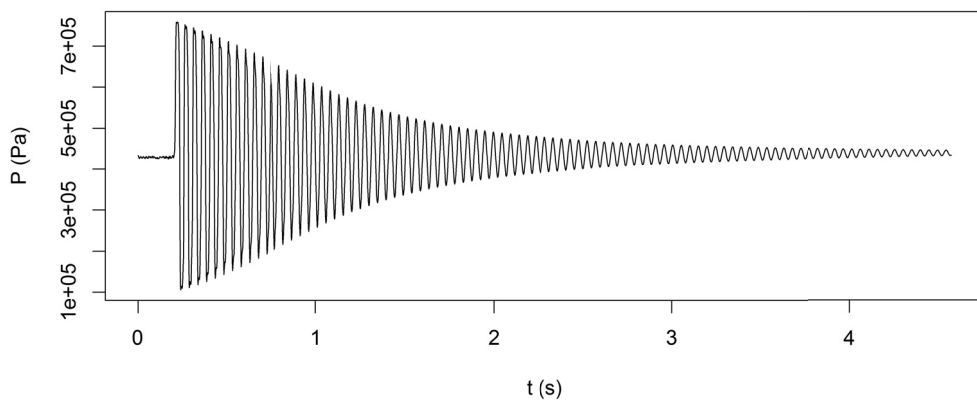


Figure F.2 – Pressure signal at the downstream pipe end.

Appendix F. Experimental work in the Straight Copper Pipe facility

SCP1₂:

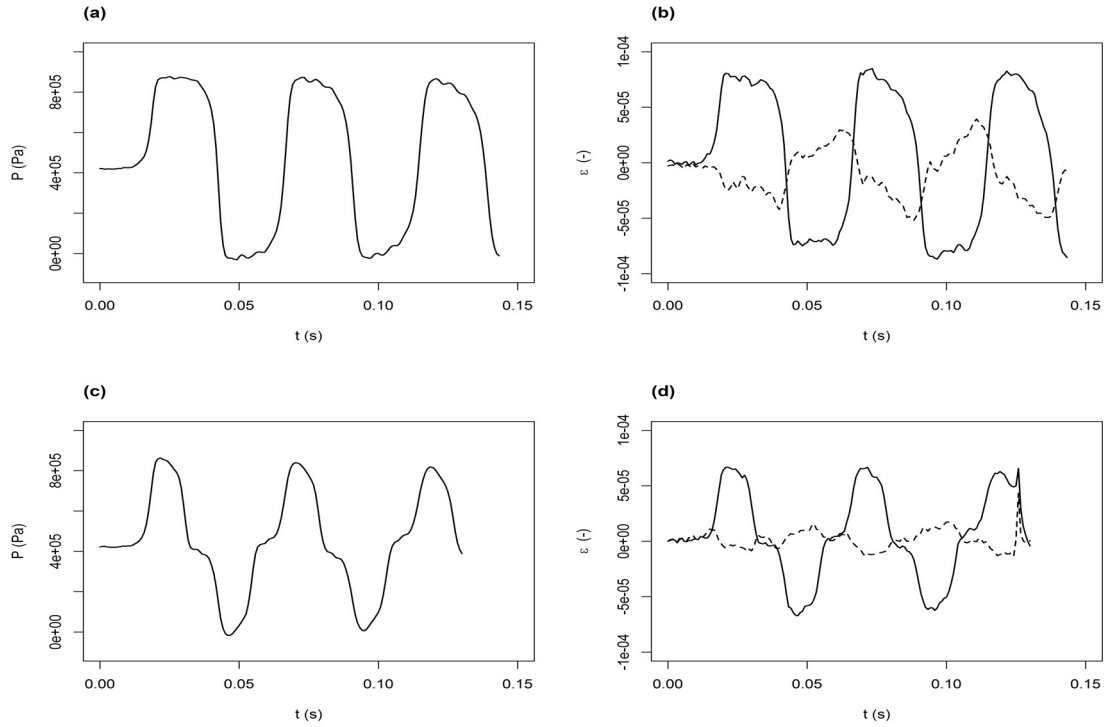


Figure E3 – (a) Pressure signal at the downstream pipe end; (b) measured strains at the downstream pipe section in the circumferential (solid line) and in the axial (dashed line) directions; (c) pressure signal at the midstream pipe section; (d) measured strains at the midstream pipe section in the circumferential (solid line) and in the axial (dashed line) directions.

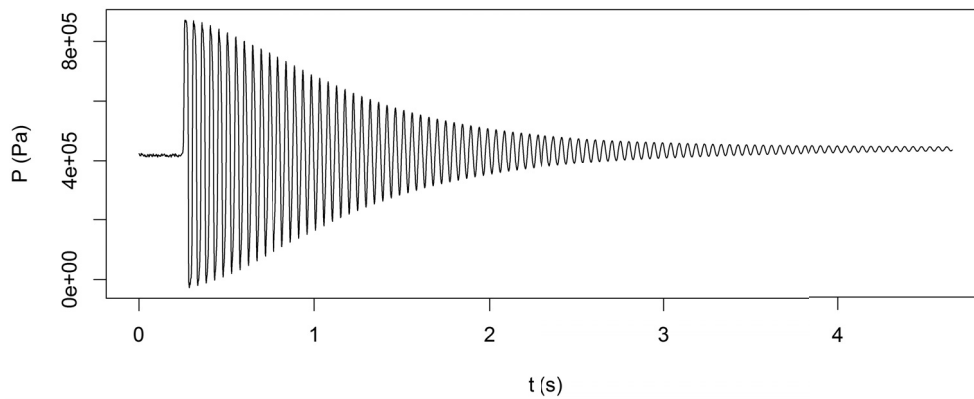


Figure E4 – Pressure signal at the downstream pipe end.

SCP1₃:

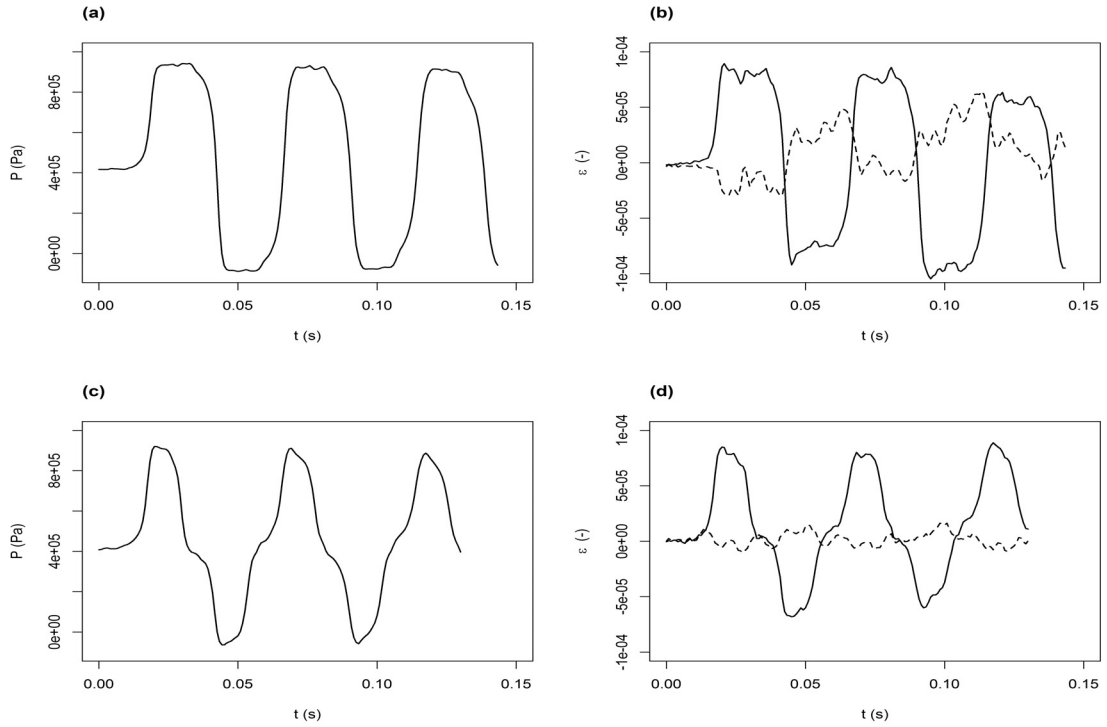


Figure E.5 – (a) Pressure signal at the downstream pipe end; (b) measured strains at the downstream pipe section in the circumferential (solid line) and in the axial (dashed line) directions; (c) pressure signal at the midstream pipe section; (d) measured strains at the midstream pipe section in the circumferential (solid line) and in the axial (dashed line) directions.

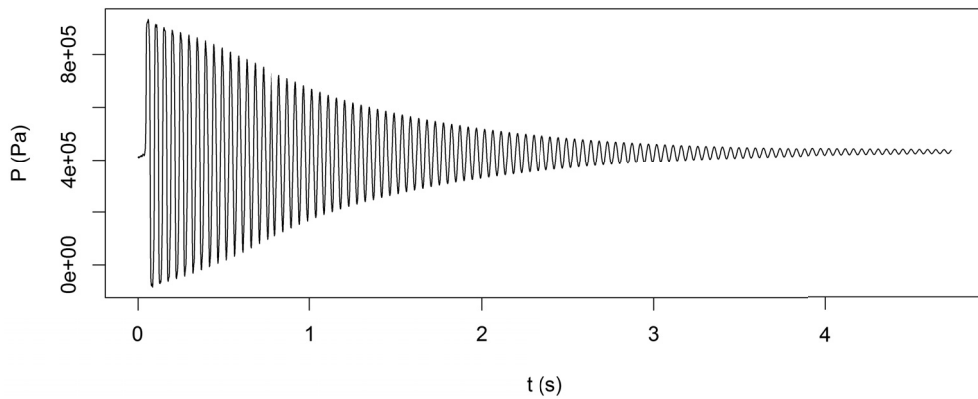


Figure E.6 – Pressure signal at the downstream pipe end.

Appendix F. Experimental work in the Straight Copper Pipe facility

SCP1₄:

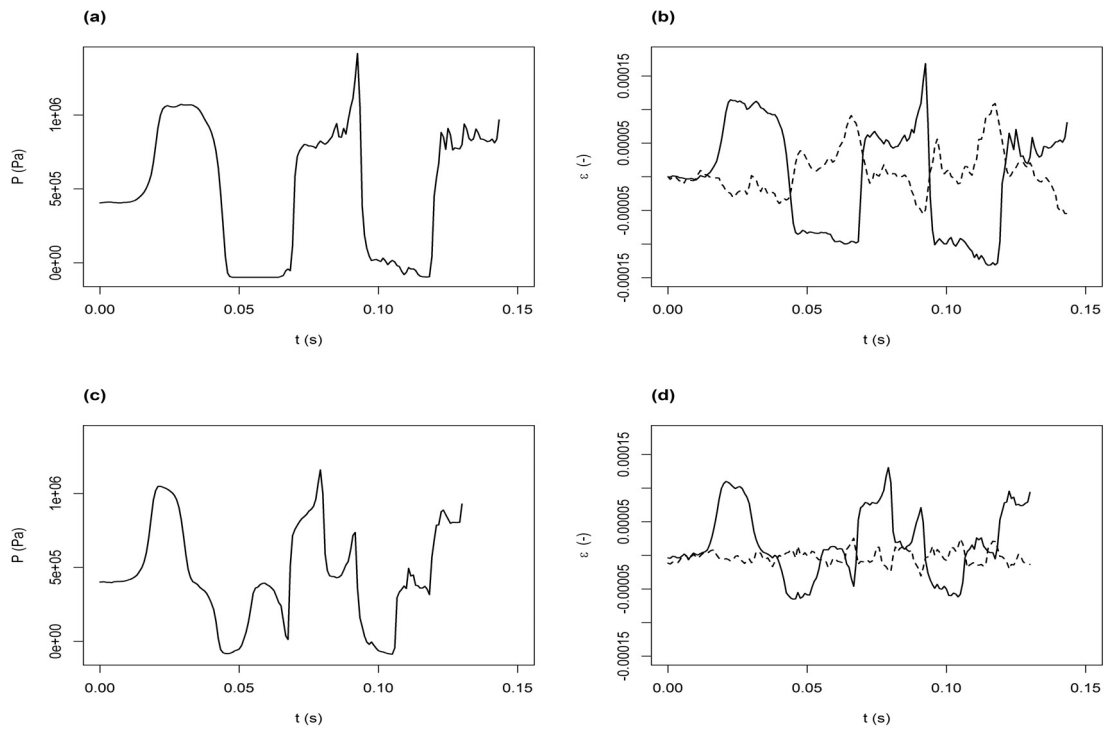


Figure E.7 – (a) Pressure signal at the downstream pipe end; (b) measured strains at the downstream pipe section in the circumferential (solid line) and in the axial (dashed line) directions; (c) pressure signal at the midstream pipe section; (d) measured strains at the midstream pipe section in the circumferential (solid line) and in the axial (dashed line) directions.

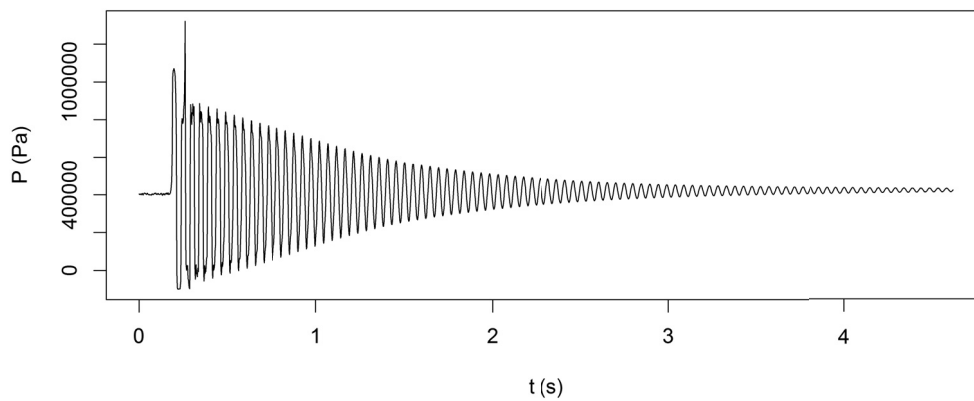


Figure E.8 – Pressure signal at the downstream pipe end.

SCP1₅:

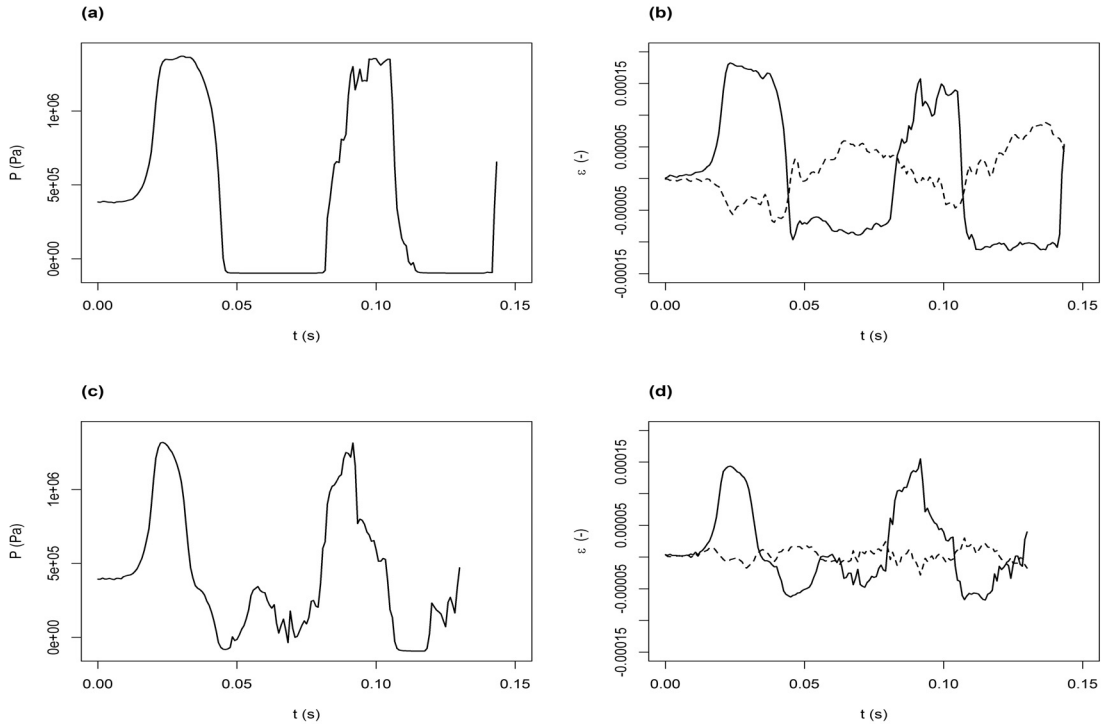


Figure F.9 – (a) Pressure signal at the downstream pipe end; (b) measured strains at the downstream pipe section in the circumferential (solid line) and in the axial (dashed line) directions; (c) pressure signal at the midstream pipe section; (d) measured strains at the midstream pipe section in the circumferential (solid line) and in the axial (dashed line) directions.

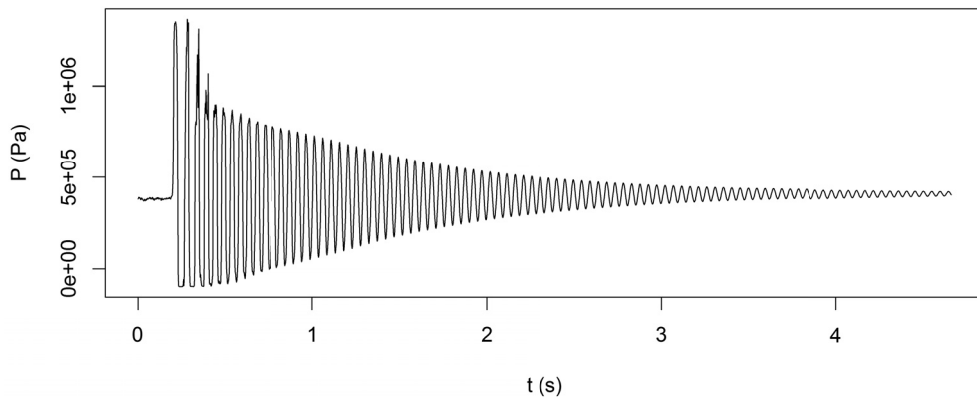


Figure F.10 – Pressure signal at the downstream pipe end.

F.3.2 Tests with no anchors throughout the pipe (SCP2)

SCP2₁:

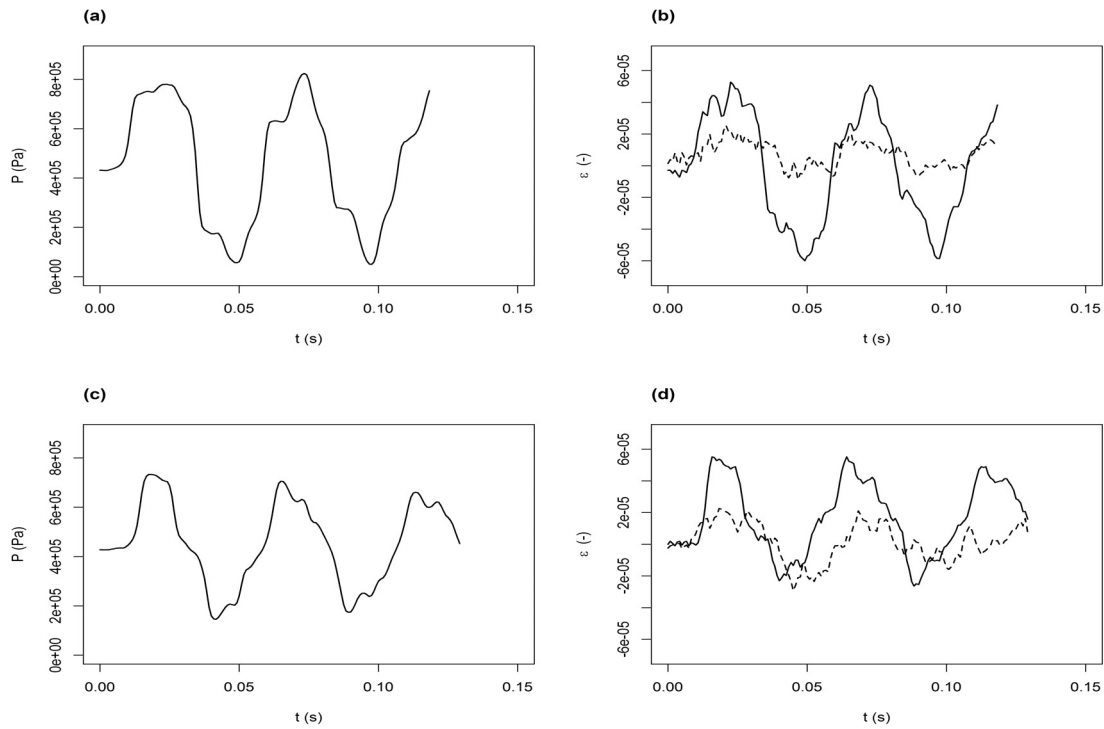


Figure E.11 – (a) Pressure signal at the downstream pipe end; (b) measured strains at the downstream pipe section in the circumferential (solid line) and in the axial (dashed line) directions; (c) pressure signal at the midstream pipe section; (d) measured strains at the midstream pipe section in the circumferential (solid line) and in the axial (dashed line) directions.

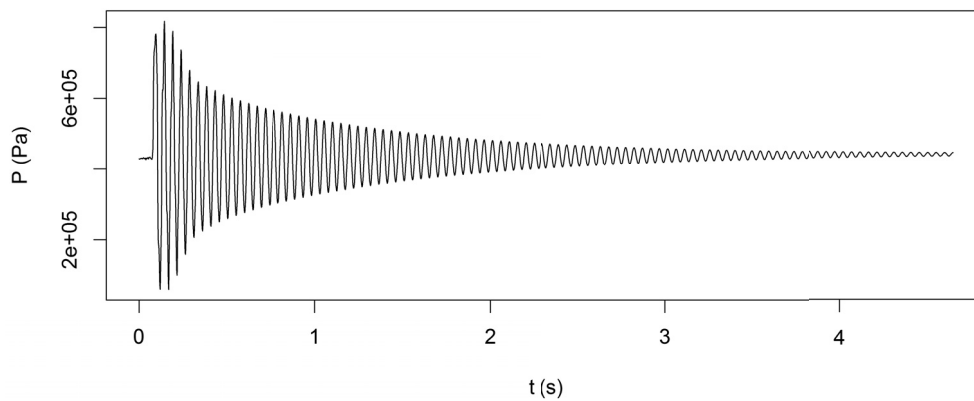


Figure E.12 – Pressure signal at the downstream pipe end.

SCP2₂:

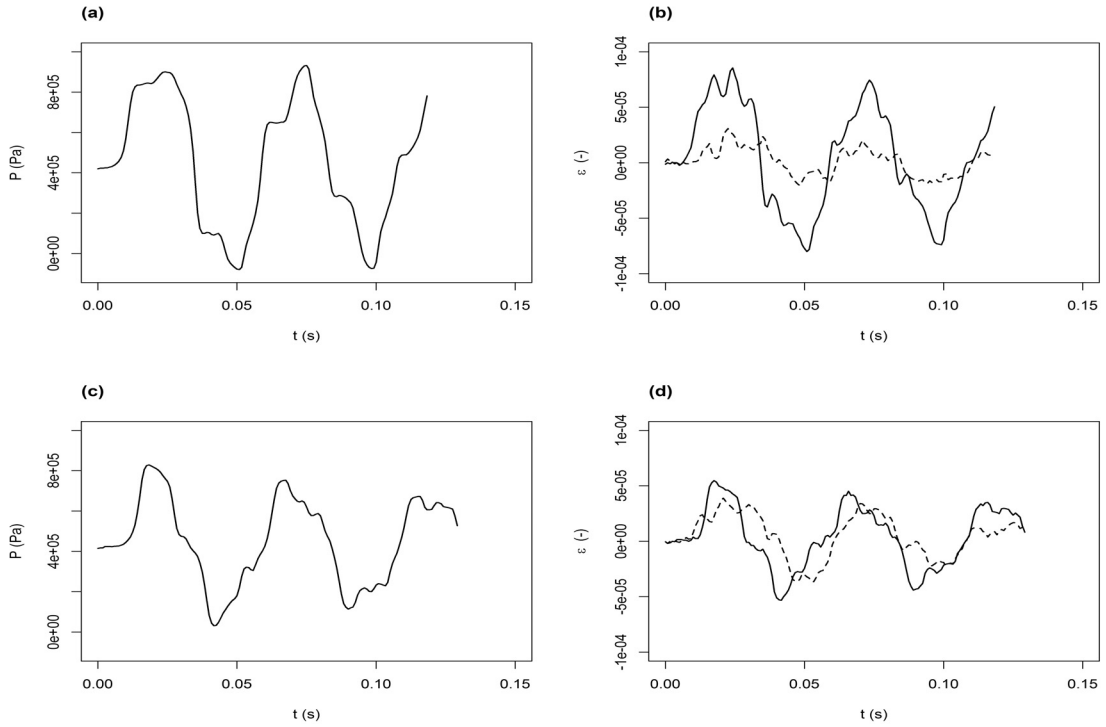


Figure F.13 – (a) Pressure signal at the downstream pipe end; (b) measured strains at the downstream pipe section in the circumferential (solid line) and in the axial (dashed line) directions; (c) pressure signal at the midstream pipe section; (d) measured strains at the midstream pipe section in the circumferential (solid line) and in the axial (dashed line) directions.

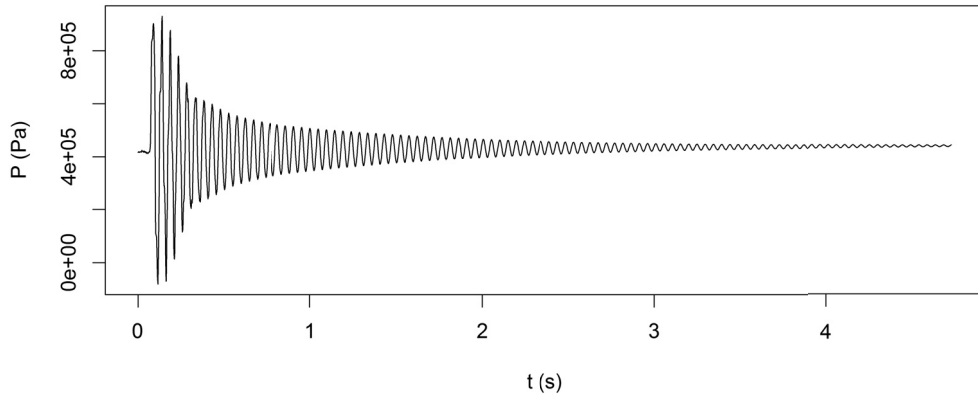


Figure F.14 – Pressure signal at the downstream pipe end.

Appendix F. Experimental work in the Straight Copper Pipe facility

SCP2₃:

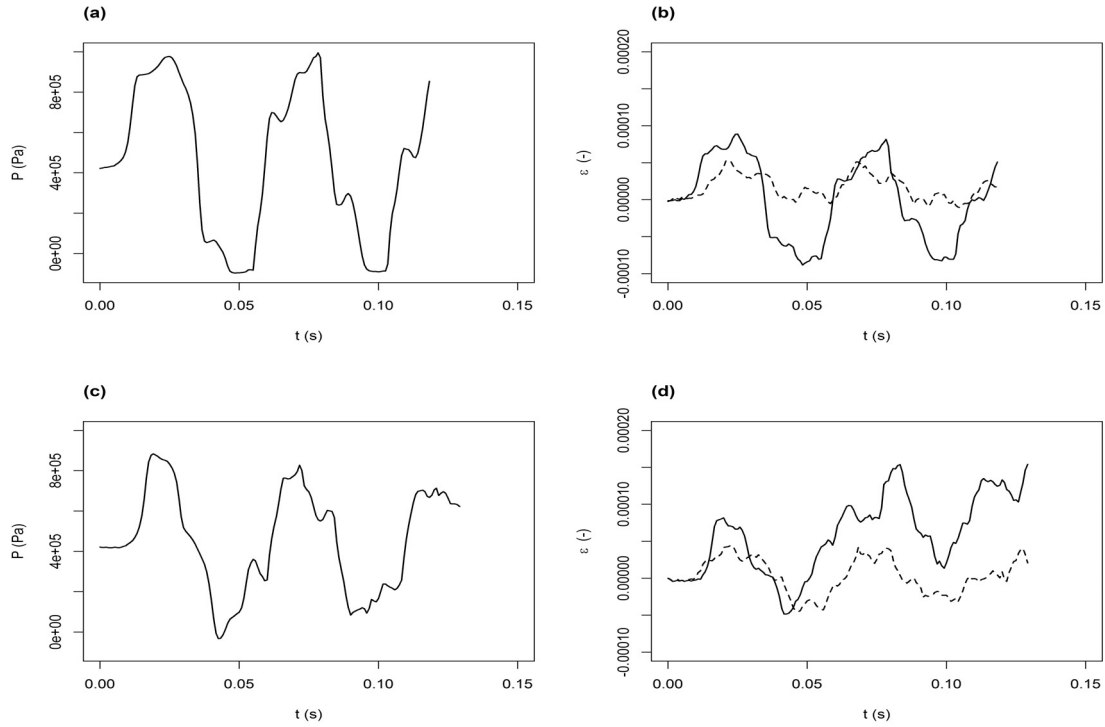


Figure F.15 – (a) Pressure signal at the downstream pipe end; (b) measured strains at the downstream pipe section in the circumferential (solid line) and in the axial (dashed line) directions; (c) pressure signal at the midstream pipe section; (d) measured strains at the midstream pipe section in the circumferential (solid line) and in the axial (dashed line) directions.

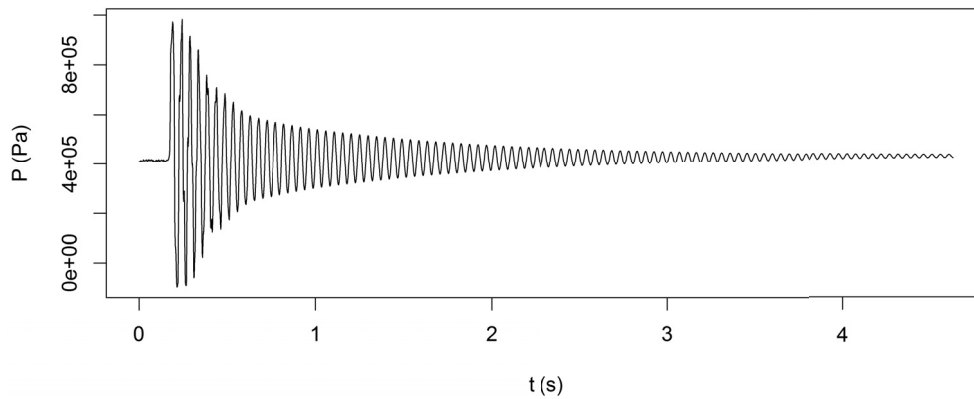


Figure F.16 – Pressure signal at the downstream pipe end.

SCP2₄:

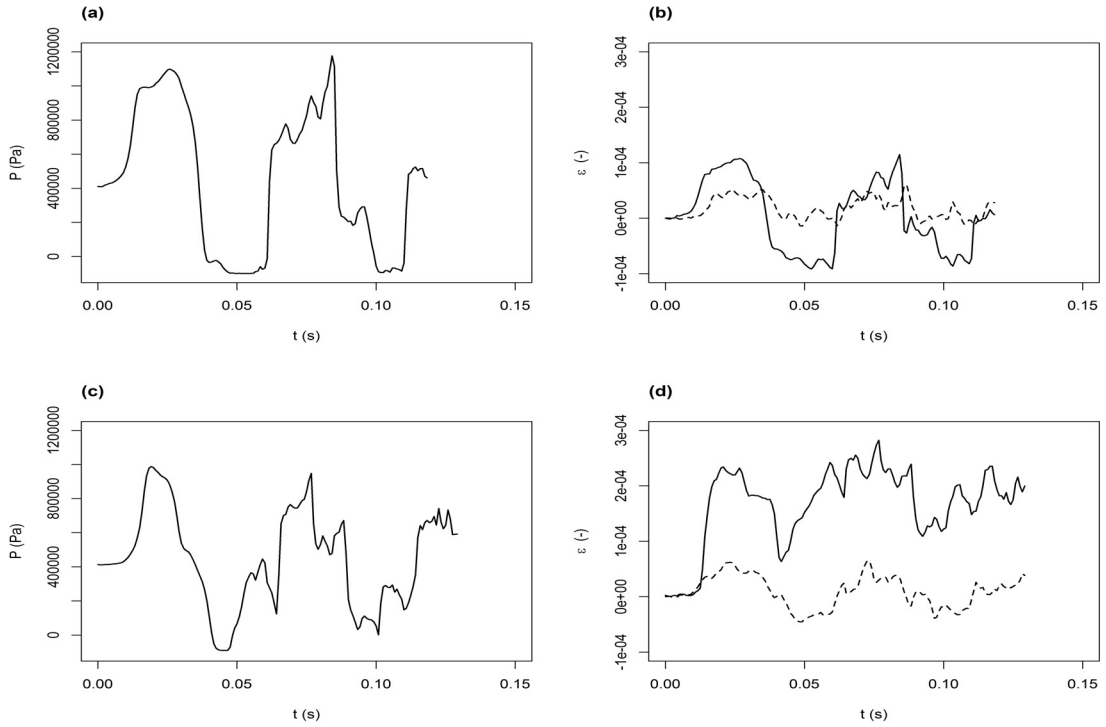


Figure E.17 – (a) Pressure signal at the downstream pipe end; (b) measured strains at the downstream pipe section in the circumferential (solid line) and in the axial (dashed line) directions; (c) pressure signal at the midstream pipe section; (d) measured strains at the midstream pipe section in the circumferential (solid line) and in the axial (dashed line) directions.

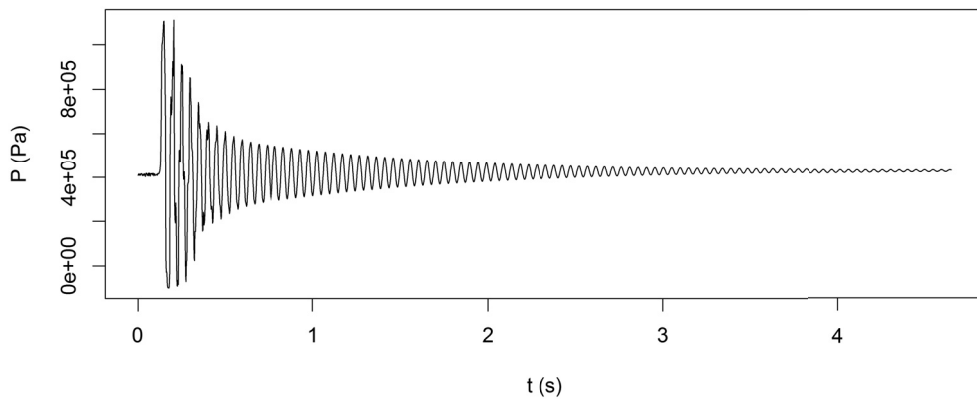


Figure E.18 – Pressure signal at the downstream pipe end.

Appendix F. Experimental work in the Straight Copper Pipe facility

SCP2₅:

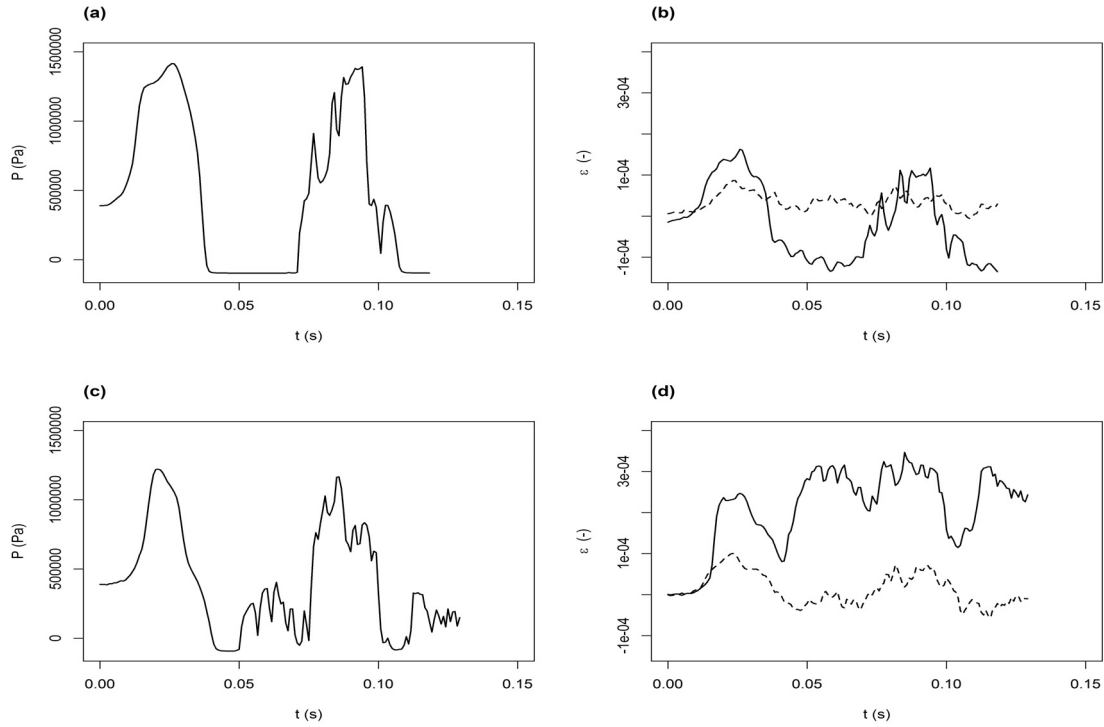


Figure F.19 – (a) Pressure signal at the downstream pipe end; (b) measured strains at the downstream pipe section in the circumferential (solid line) and in the axial (dashed line) directions; (c) pressure signal at the midstream pipe section; (d) measured strains at the midstream pipe section in the circumferential (solid line) and in the axial (dashed line) directions.

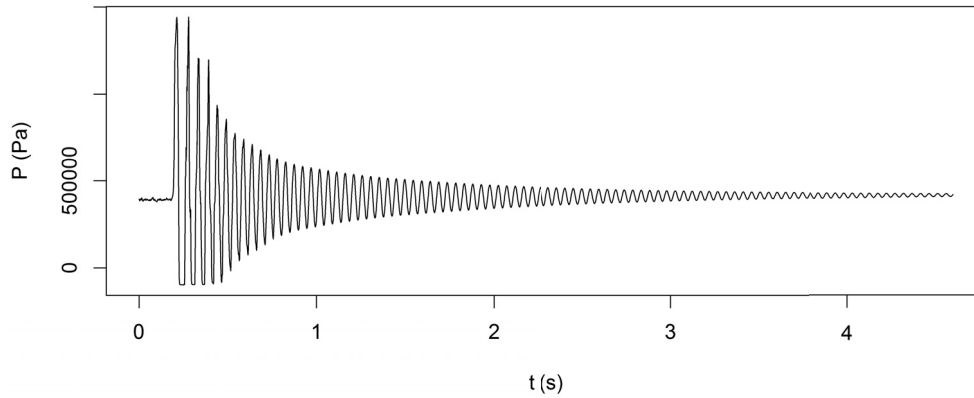


Figure F.20 – Pressure signal at the downstream pipe end.

F.3.3 Tests with pipe midstream section anchored (SCP3)

SCP3₁:

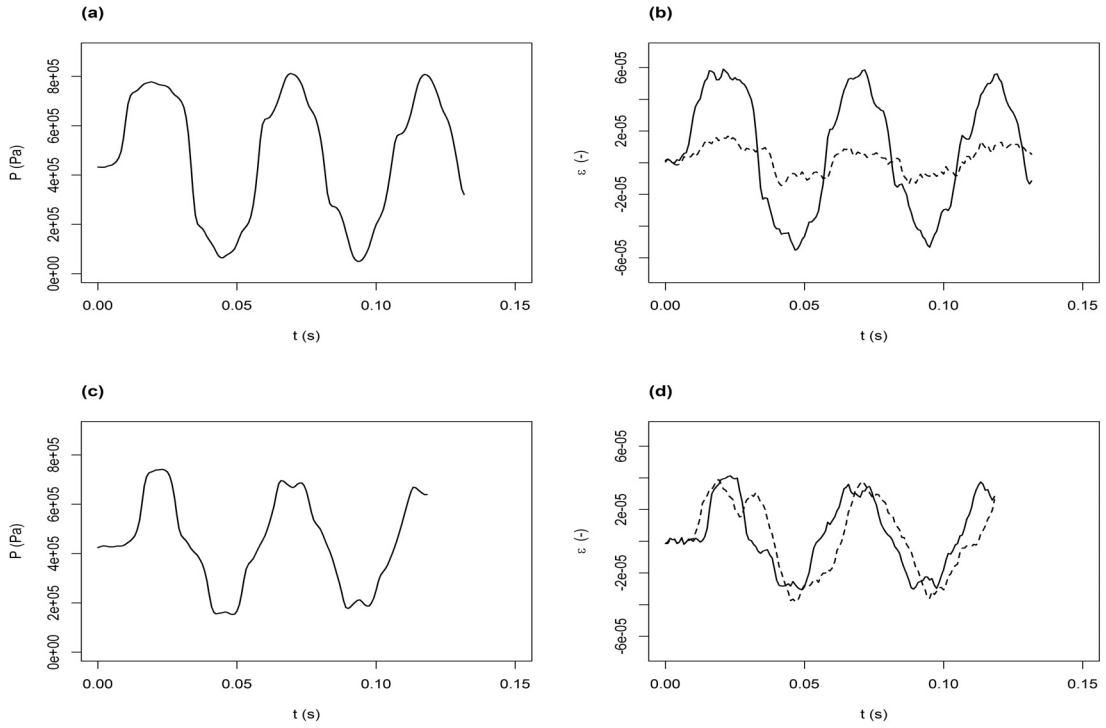


Figure E21 – (a) Pressure signal at the downstream pipe end; (b) measured strains at the downstream pipe section in the circumferential (solid line) and in the axial (dashed line) directions.

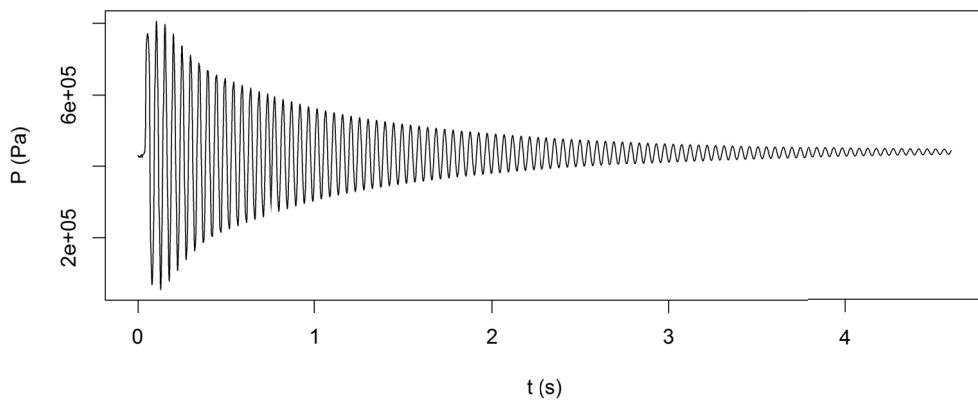


Figure E22 – Pressure signal at the downstream pipe end.

Appendix F. Experimental work in the Straight Copper Pipe facility

SCP3₂:

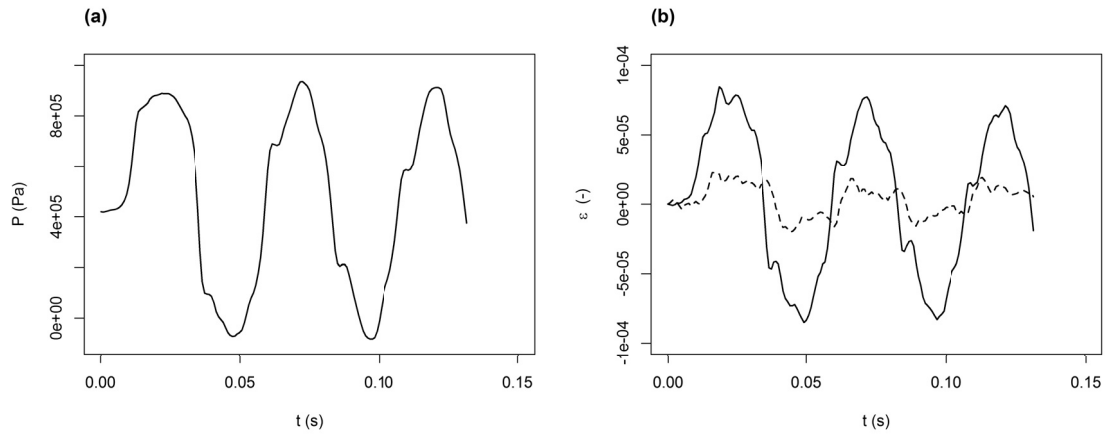


Figure E.23 – (a) Pressure signal at the downstream pipe end; (b) measured strains at the downstream pipe section in the circumferential (solid line) and in the axial (dashed line) directions; (c) pressure signal at the midstream pipe section; (d) measured strains at the midstream pipe section in the circumferential (solid line) and in the axial (dashed line) directions.

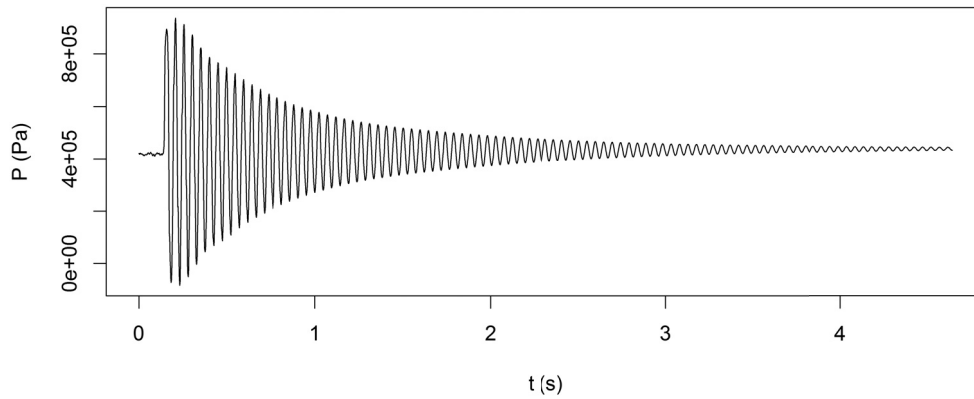


Figure E.24 – Pressure signal at the downstream pipe end.

SCP3₃:

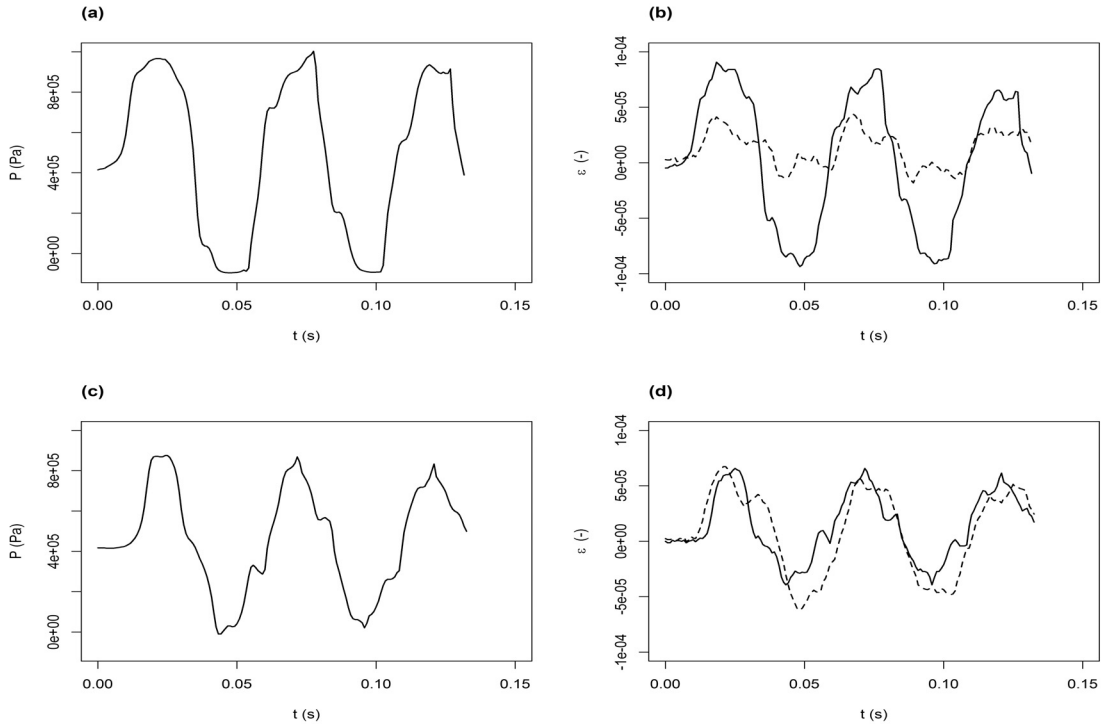


Figure E.25 – (a) Pressure signal at the downstream pipe end; (b) measured strains at the downstream pipe section in the circumferential (solid line) and in the axial (dashed line) directions; (c) pressure signal at the midstream pipe section; (d) measured strains at the midstream pipe section in the circumferential (solid line) and in the axial (dashed line) directions.

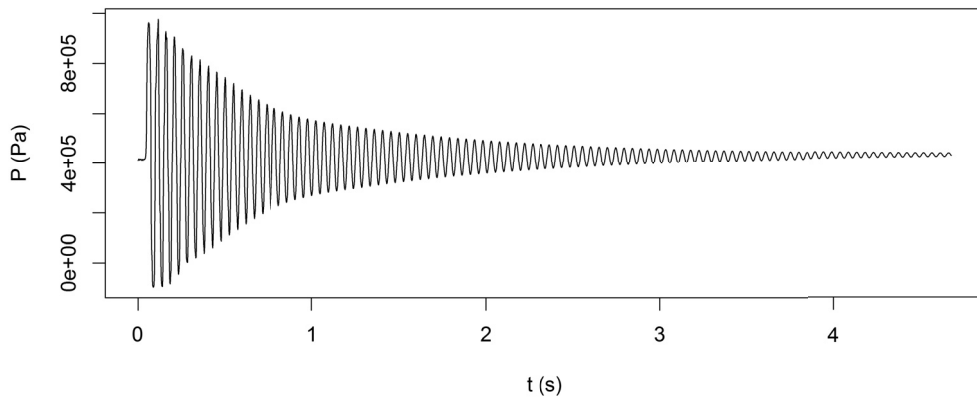


Figure E.26 – Pressure signal at the downstream pipe end.

SCP3₄:

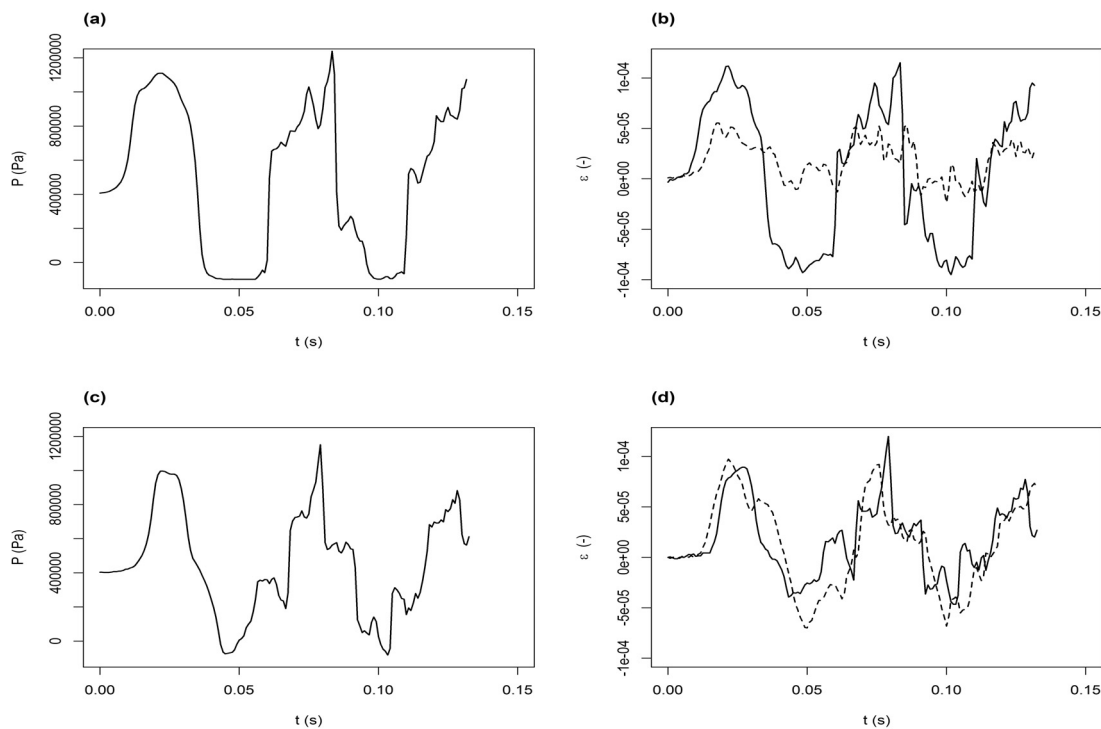


Figure E.27 – (a) Pressure signal at the downstream pipe end; (b) measured strains at the downstream pipe section in the circumferential (solid line) and in the axial (dashed line) directions; (c) pressure signal at the midstream pipe section; (d) measured strains at the midstream pipe section in the circumferential (solid line) and in the axial (dashed line) directions.

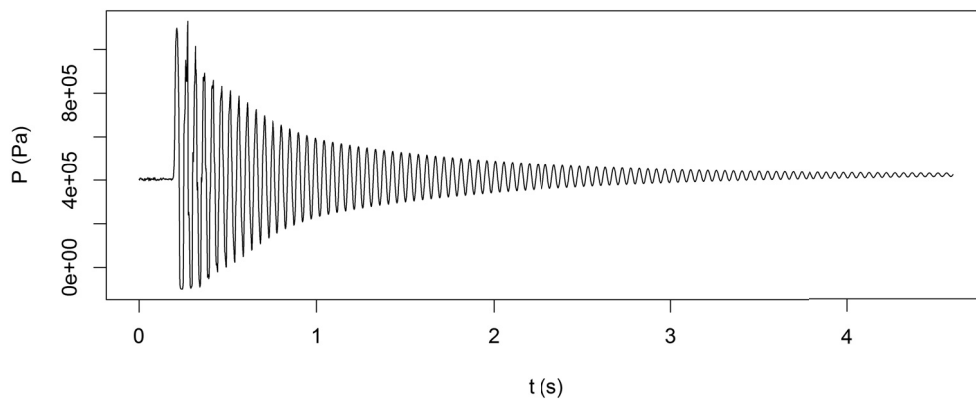


Figure E.28 – Pressure signal at the downstream pipe end.

SCP3₅:

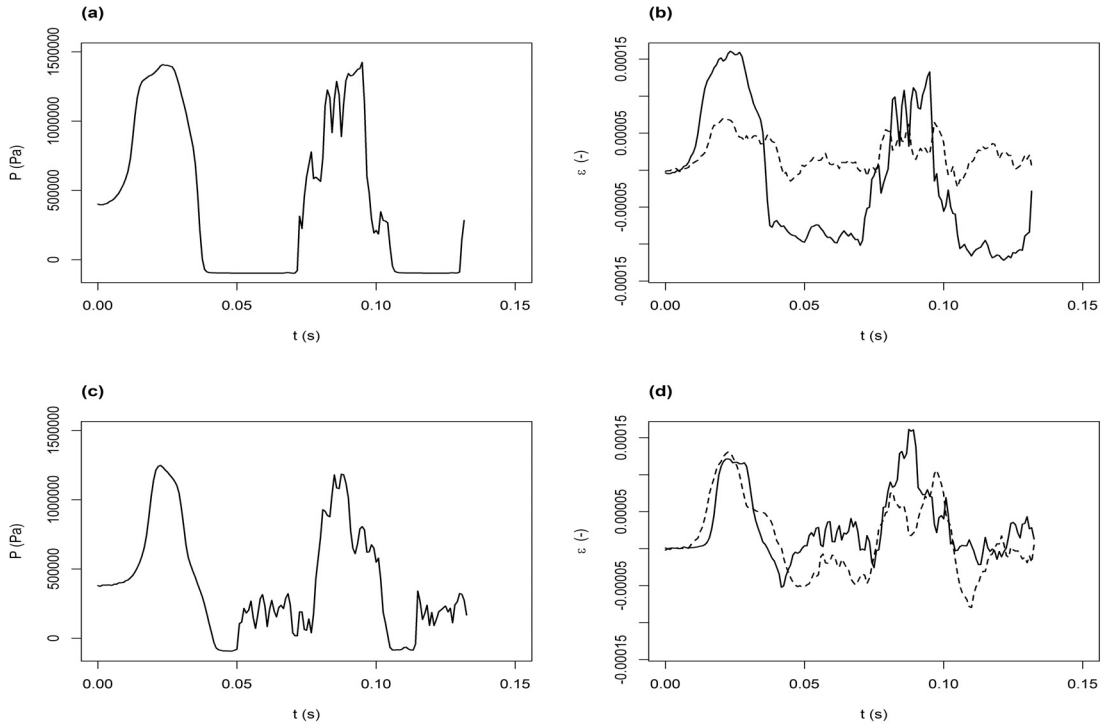


Figure E.29 – (a) Pressure signal at the downstream pipe end; (b) measured strains at the downstream pipe section in the circumferential (solid line) and in the axial (dashed line) directions; (c) pressure signal at the midstream pipe section; (d) measured strains at the midstream pipe section in the circumferential (solid line) and in the axial (dashed line) directions.

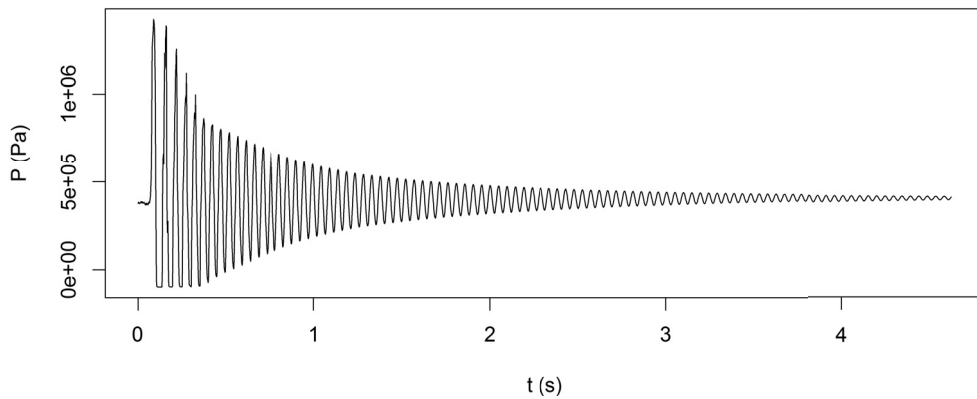


Figure E.30 – Pressure signal at the downstream pipe end.

F.3.4 Tests with pipe midstream and downstream sections anchored (SCP4)

SCP4₁:

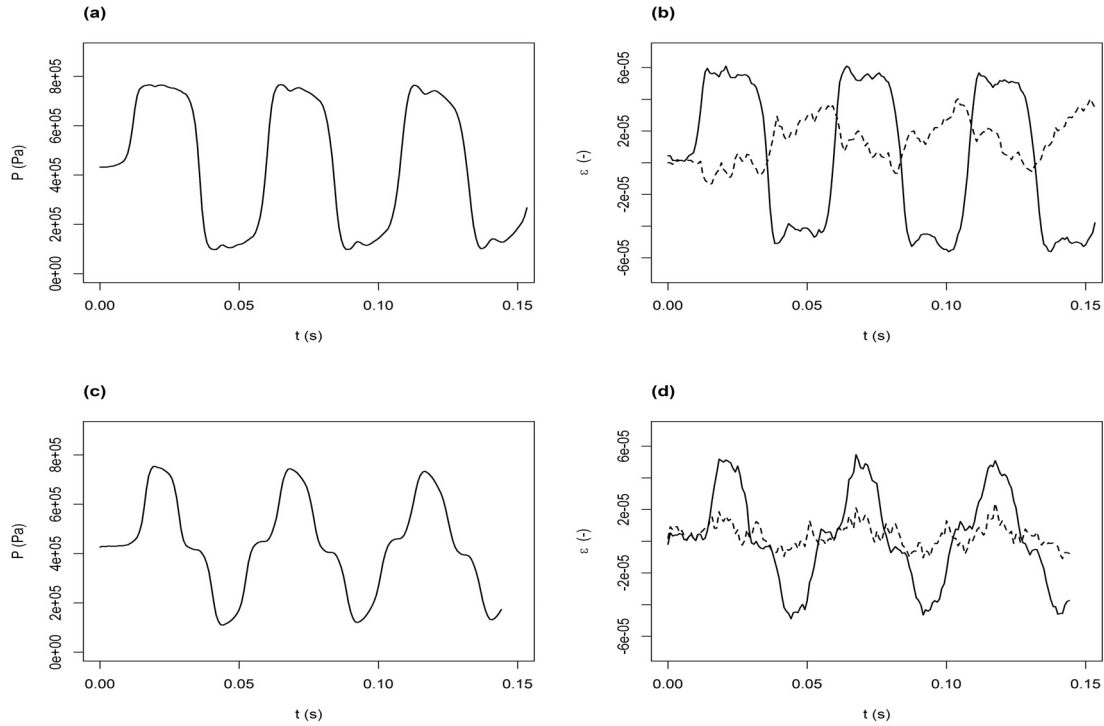


Figure E31 – (a) Pressure signal at the downstream pipe end; (b) measured strains at the downstream pipe section in the circumferential (solid line) and in the axial (dashed line) directions; (c) pressure signal at the midstream pipe section; (d) measured strains at the midstream pipe section in the circumferential (solid line) and in the axial (dashed line) directions.

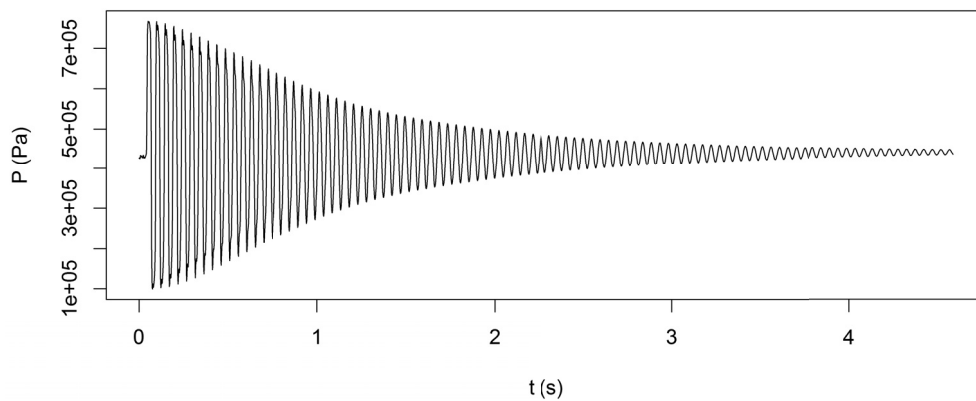


Figure E32 – Pressure signal at the downstream pipe end.

SCP4₂:

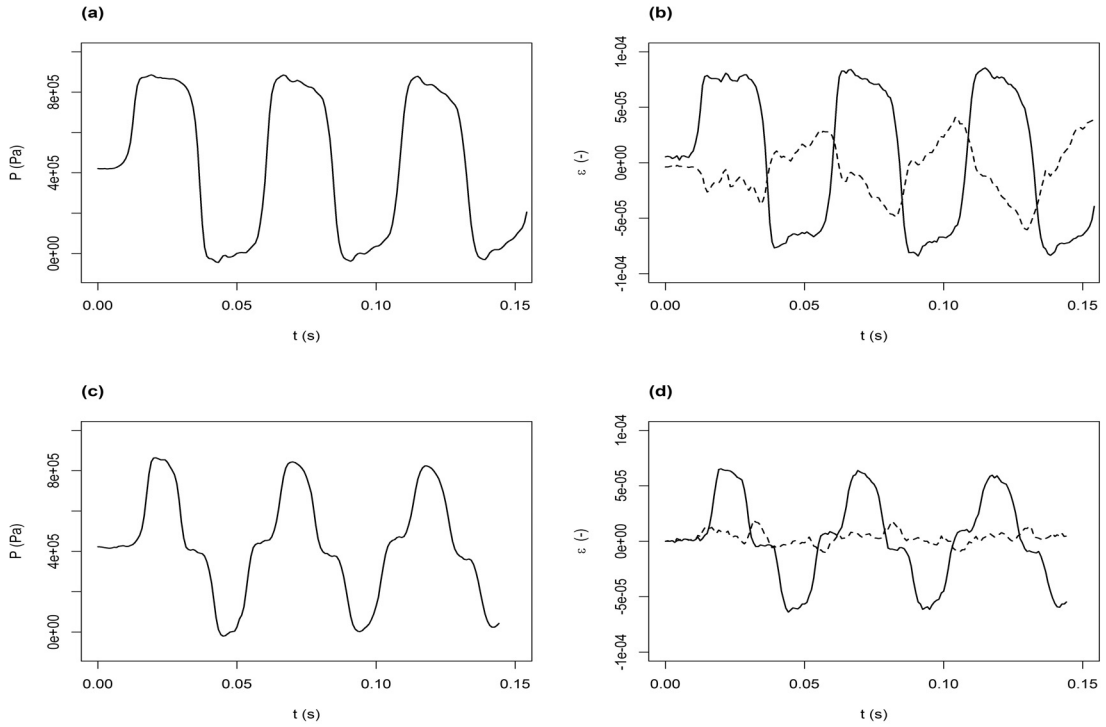


Figure E.33 – (a) Pressure signal at the downstream pipe end; (b) measured strains at the downstream pipe section in the circumferential (solid line) and in the axial (dashed line) directions; (c) pressure signal at the midstream pipe section; (d) measured strains at the midstream pipe section in the circumferential (solid line) and in the axial (dashed line) directions.

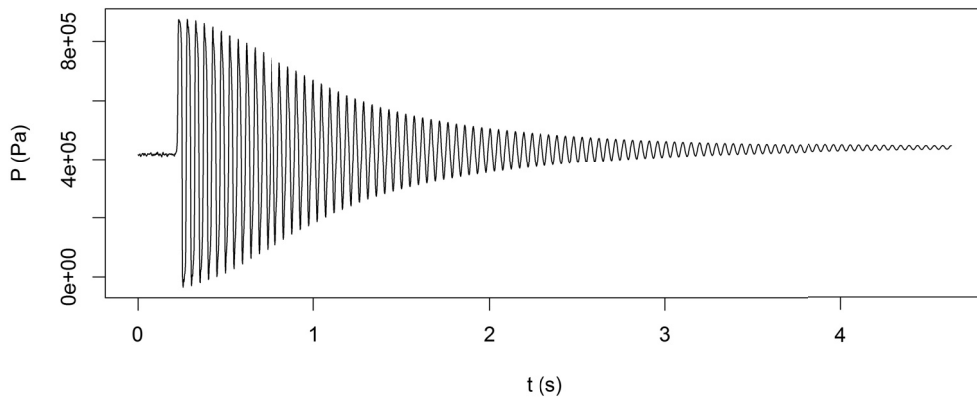


Figure E.34 – Pressure signal at the downstream pipe end.

Appendix F. Experimental work in the Straight Copper Pipe facility

SCP4₃:

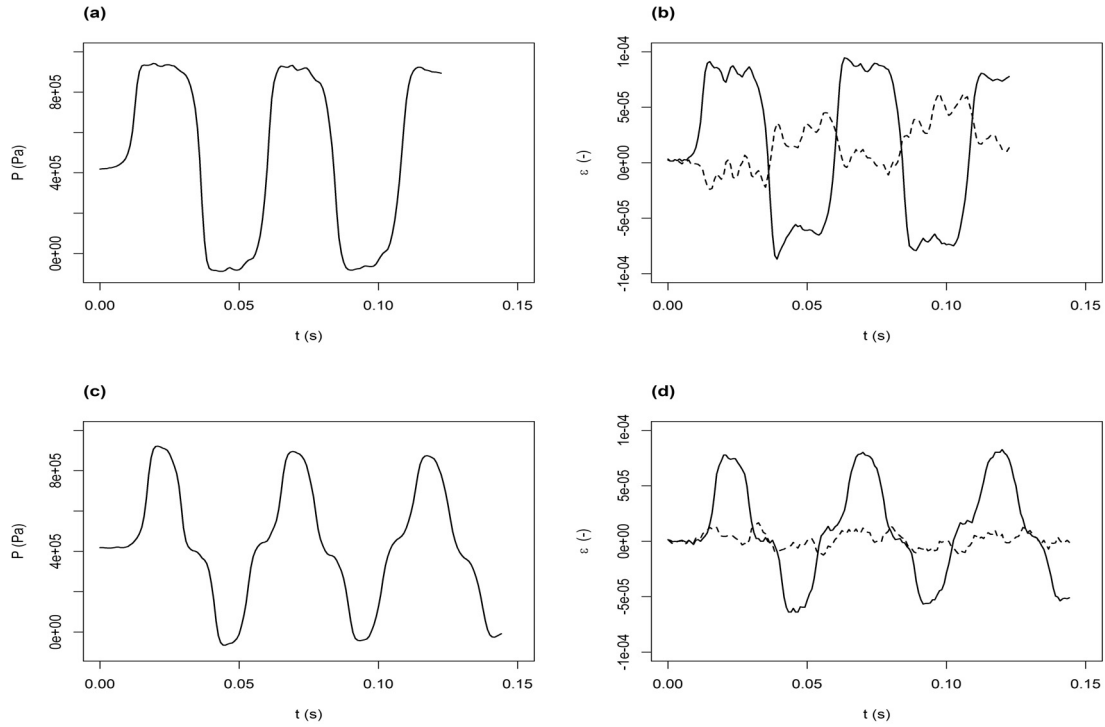


Figure E35 – (a) Pressure signal at the downstream pipe end; (b) measured strains at the downstream pipe section in the circumferential (solid line) and in the axial (dashed line) directions; (c) pressure signal at the midstream pipe section; (d) measured strains at the midstream pipe section in the circumferential (solid line) and in the axial (dashed line) directions.

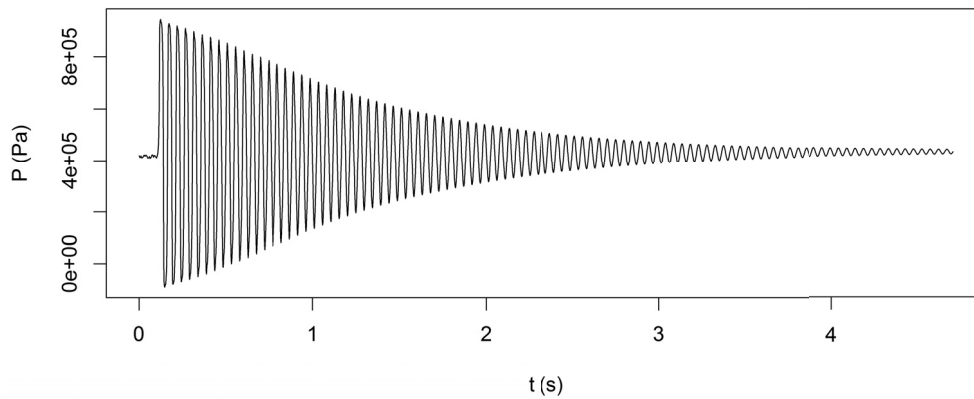


Figure E36 – Pressure signal at the downstream pipe end.

SCP4₄:

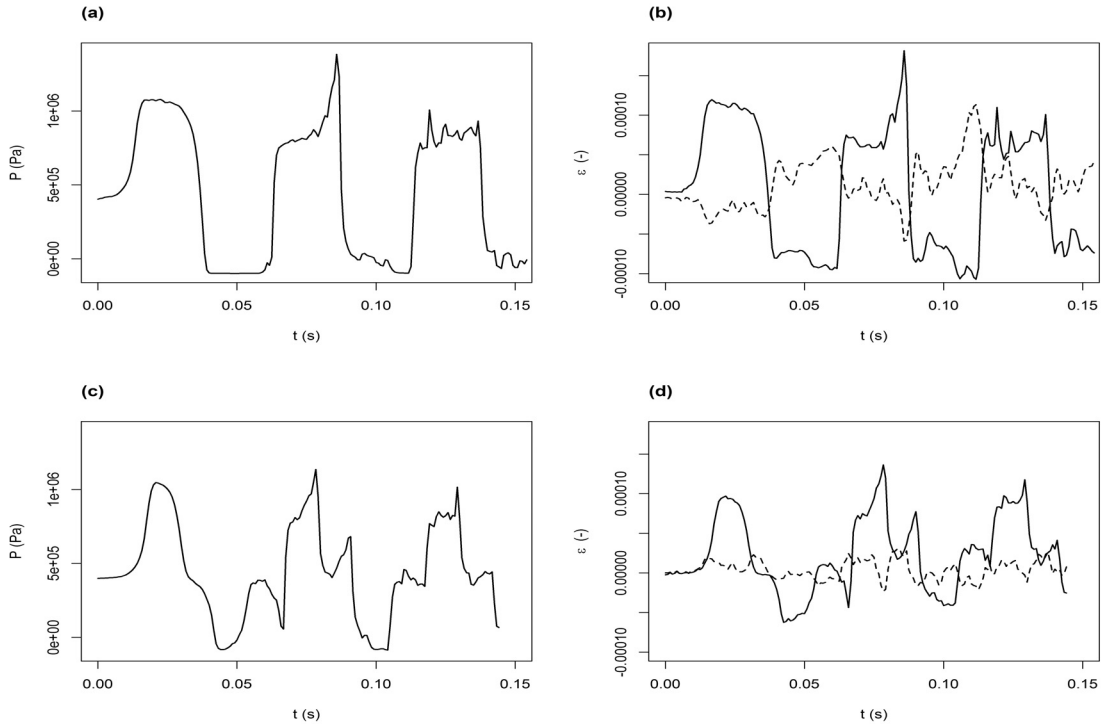


Figure E.37 – (a) Pressure signal at the downstream pipe end; (b) measured strains at the downstream pipe section in the circumferential (solid line) and in the axial (dashed line) directions; (c) pressure signal at the midstream pipe section; (d) measured strains at the midstream pipe section in the circumferential (solid line) and in the axial (dashed line) directions.

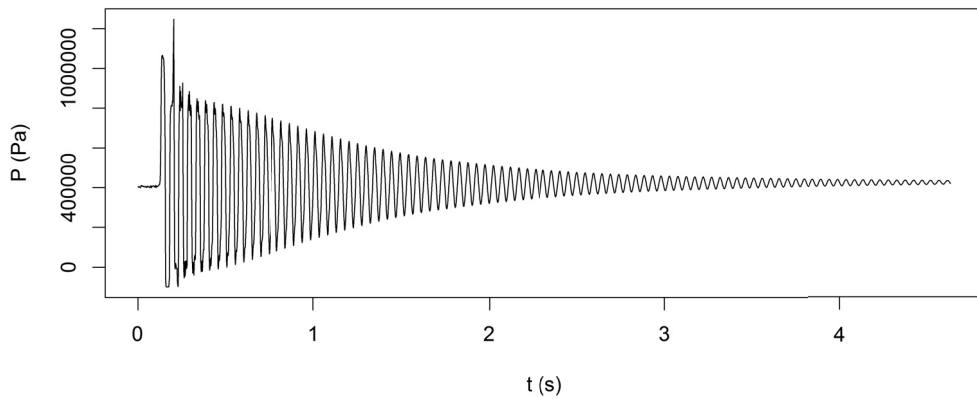


Figure E.38 – Pressure signal at the downstream pipe end.

Appendix F. Experimental work in the Straight Copper Pipe facility

SCP4₅:

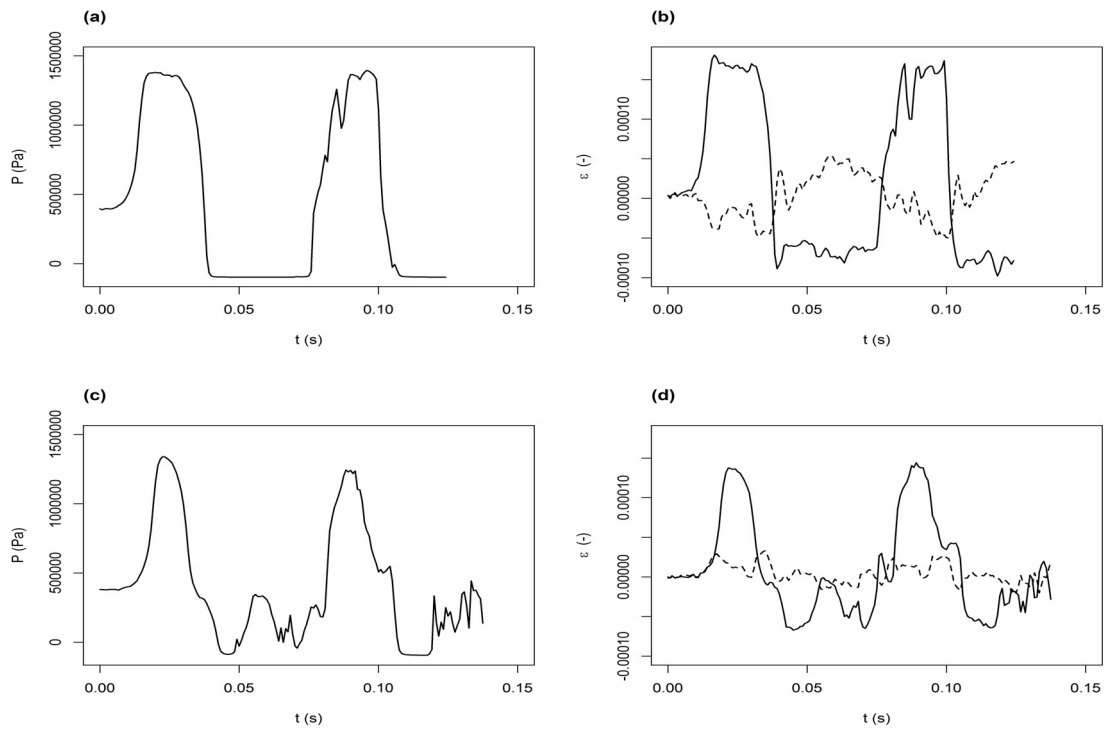


Figure E39 – (a) Pressure signal at the downstream pipe end; (b) measured strains at the downstream pipe section in the circumferential (solid line) and in the axial (dashed line) directions; (c) pressure signal at the midstream pipe section; (d) measured strains at the midstream pipe section in the circumferential (solid line) and in the axial (dashed line) directions.

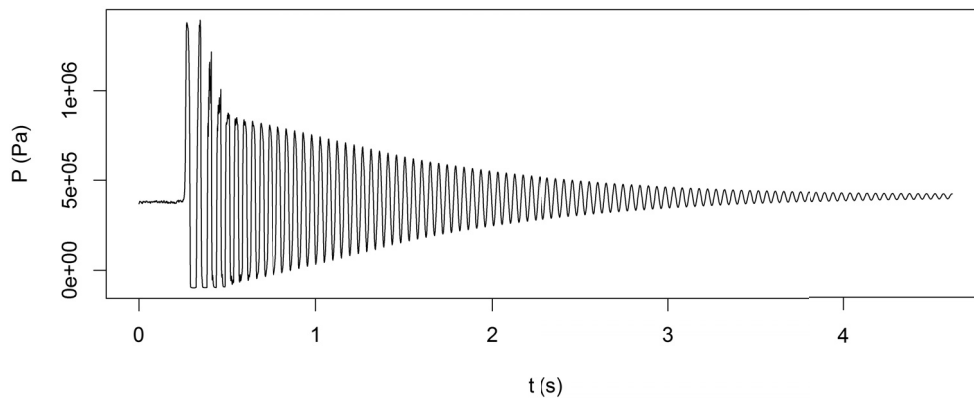


Figure F40 – Pressure signal at the downstream pipe end.

Bibliography

- A-MONEIM, M. & CHANG, Y. (1978). Comparison of icepel code predictions with straight flexible pipe experiments. *Nuclear Engineering and Design* **49**(1), 187–196.
- A-MONEIM, M. & CHANG, Y. (1979). Comparison of icepel predictions with single-elbow flexible piping system experiment. *Journal of Pressure Vessel Technology* **101**(2), 142–148.
- ABBOTT, M. B. (1993). The electronic encapsulation of knowledge in hydraulics, hydrology and water resources. *Advances in water resources* **16**(1), 21–39.
- ADAMKOWSKI, A. (2001). Case study: Lapino powerplant penstock failure. *Journal of hydraulic engineering* **127**(7), 547–555.
- ALLIEVI, L. (1902). Teoria generale del moto perturbato dell'acqua nei tubi in pressione (colpo d'ariete). Translated into English by EE Halmos (1925). *Am. Soc. Civil English* .
- ALLIEVI, L. (1913). Teoria del colpo d'ariete. Translated into English by EE Halmos (1929). *Trans. ASME* .
- ALMEIDA, A. & PINTO, A. (1986). A special case of transient forces on pipeline supports due to water hammer effects. In: *Proceedings of the 5th International Conference on Pressure Surges, Hanover, Germany*, vol. 2224.
- ANDERSON, A. (1976). Menabrea's note on waterhammer: 1858. *Journal of the Hydraulics Division* **102**(1), 29–39.
- ANDERSON, A. (2000). Celebrations and challenges-waterhammer at the start of the 20th and 21st centuries. In: *BHR Group Conference Series Publication*, vol. 39. Bury St. Edmunds; Professional Engineering Publishing; 1998.
- ANDERSON, E. I. A. & JOHNSON, G. (1990). Effect of tube ovaling on pressure wave propagation speed. *Proceedings of the Institution of Mechanical Engineers, Part H: Journal of Engineering in Medicine* **204**(4), 245–251.
- ANDERSON, W. K., NEWMAN, J. C., WHITFIELD, D. L. & NIELSEN, E. J. (2001). Sensitivity analysis for navier-stokes equations on unstructured meshes using complex variables. *AIAA journal* **39**(1), 56–63.

Bibliography

- AXWORTHY, D. H., GHIDAOU, M. S. & MCINNIS, D. A. (2000). Extended thermodynamics derivation of energy dissipation in unsteady pipe flow. *Journal of Hydraulic Engineering* **126**(4), 276–287.
- BAREZ, F., GOLDSMITH, W. & SACKMAN, J. (1979). Longitudinal waves in liquid-filled tubes—I: Theory. *International Journal of Mechanical Sciences* **21**(4), 213–221.
- BATHE, K. & ALMEIDA, C. (1980). A simple and effective pipe elbow element—linear analysis. *Journal of Applied Mechanics* **47**(1), 93–100.
- BATHE, K. & ALMEIDA, C. (1982). A simple and effective pipe elbow element—interaction effects. *Journal of Applied Mechanics* **49**(1), 165–171.
- BELYTSCHKO, T., KARABIN, M. & LIN, J. (1986). Fluid-structure interaction in waterhammer response of flexible piping. *Journal of Pressure Vessel Technology* **108**(3), 249–255.
- BERGANT, A., ROSS SIMPSON, A. & VITKOVSK, J. (2001). Developments in unsteady pipe flow friction modelling. *Journal of Hydraulic Research* **39**(3), 249–257.
- BERGANT, A., SIMPSON, A. R. & TIJSSELING, A. S. (2004). *Water hammer with column separation: a review of research in the twentieth century*. Eindhoven University of Technology, Department of Mathematics and Computer Science.
- BERGANT, A., TIJSSELING, A. S., VITKOVSKÝ, J. P., COVAS, D. I., SIMPSON, A. R. & LAMBERT, M. F. (2008a). Parameters affecting water-hammer wave attenuation, shape and timing. part-1: Mathematical tools. *Journal of Hydraulic Research* **46**(3), 373–381.
- BERGANT, A., TIJSSELING, A. S., VITKOVSKÝ, J. P., COVAS, D. I., SIMPSON, A. R. & LAMBERT, M. F. (2008b). Parameters affecting water-hammer wave attenuation, shape and timing. part-2: Case studies. *Journal of Hydraulic Research* **46**(3), 382–391.
- BETTINALI, F., MOLINARO, P., CICCOTELLI, M. & MICELLOTTA, A. (1991). Transient analysis in piping networks including fluid-structure interaction and cavitation effects. *Transactions SMiRT* **11**, 565–570.
- BIETENBECK, F., PETRUSCHKE, W. & WUENNENBERG, H. (1985). Piping response due to blowdown-significant parameters for a comparison of experimental and analytical results. In: *Transactions of the 8th International Conference on Structural Mechanics in Reactor Technology. Vol. F1 and F2*.
- BLADE, R. J., LEWIS, W. & GOODYKOONTZ, J. H. (1962). *Study of a sinusoidally perturbed flow in a line including a 90 degree elbow with flexible supports*. National Aeronautics and Space Administration (NASA), Lewis Research Center, Cleveland, Ohio.
- BOMBARDIERI, C., TRAUDT, T. & MANFLETTI, C. (2014). Experimental and numerical analysis of water hammer during the filling process of pipelines. In: *Space Propulsion Conference, Cologne, Germany*.

- BONIN, C. (1960). Water-hammer damage to oigawa power station. *Journal of Engineering for Power* **82**(2), 111–116.
- BORZI, A. & PROPST, G. (2003). Numerical investigation of the liebau phenomenon. *Zeitschrift für angewandte Mathematik und Physik ZAMP* **54**(6), 1050–1072.
- BOUABDALLAH, S. & MASSOUH, F. (1997). Fluid-structure interaction in hydraulic networks. *AD- American Society of Mechanical Engineers. Aerospace Division Newsletter* **53-2**, 543–548.
- BOULANGER, A. (1913). *Étude sur la propagation des ondes liquides dans les tuyaux élastiques*, vol. 2. Tallandier.
- BRAUN, E. (1909). Druckschwankungen in Rohrleitungen: mit Berücksichtigung der Elastizität der Flüssigkeit und des Rohrmaterials.
- BRAUN, E. (1910). Die Turbine, Organ der turbinentechnischen Gesellschaft.
- BREKKE, H. (1984). *A stability study on hydro power plant governing including the influence from a quasi nonlinear damping of oscillatory flow and from the turbine characteristics*, vol. 1. Kværner Brug.
- BRITO, M., SANCHES, P., FERREIRA, R. & COVAS, D. (2014). Piv characterization of transient flow in pipe coils. *Procedia Engineering* **89**, 1358–1365.
- BROWN, F. T. & TENTARELLI, S. C. (2001a). Dynamic behavior of complex fluid-filled tubing systems, part 2: System analysis. *Journal of Dynamic Systems, Measurement, and Control* **123**(1), 78–84.
- BROWN, F. T. & TENTARELLI, S. C. (2001b). Dynamic behavior of complex fluid-filled tubing systems—part 1: Tubing analysis. *Journal of Dynamic Systems, Measurement, and Control* **123**(1), 71–77.
- BRUNONE, B., GOLIA, U. & GRECO, M. (1991). Some remarks on the momentum equation for fast transients. In: *Proc., Int. Meeting on Hydraulic Transients and Water Column Separation*. Valencia.
- BRUNONE, B., GOLIA, U. & GRECO, M. (1995). Effects of two-dimensionality on pipe transients modeling. *Journal of Hydraulic Engineering* **121**(12), 906–912.
- BRUNONE, B., KARNEY, B. W., MECARELLI, M. & FERRANTE, M. (2000). Velocity profiles and unsteady pipe friction in transient flow. *Journal of Water Resources Planning and Management* **126**(4), 236–244.
- BUDNY, D., HATFIELD, F. & WIGGERT, D. (1990). An experimental study on the influence of structural damping on internal fluid pressure during a transient flow. *Journal of Pressure Vessel Technology* **112**(3), 284–290.

Bibliography

- BUDNY, D. D., WIGGERT, D. & HATFIELD, F. (1991). The influence of structural damping on internal pressure during a transient pipe flow. *Journal of Fluids Engineering* **113**(3), 424–429.
- BÜRMAN, W. (1975). Water hammer in coaxial pipe systems. *Journal of the Hydraulics Division* **101**(6), 699–715.
- BÜRMAN, W. (1979). Druckstobmessungen an koaxialen rohren. (water hammer measurements on coaxial pipes.). In: *Proc., 3R International*, vol. 18.
- BÜRMAN, W., FESER, G., JANSON, H. & THIELEN, H. (1985). Mathematical simulation of the dynamics of pipelines laid in the open in case of unsteady flows. report on the measurements and numerical simulation of the measurements on the neckar bridge. In: *Universität Karlsruhe, Institut für Hydromechanik, Bericht Nr. 623, Karlsruhe, Germany*.
- BÜRMAN, W., FESER, G., JANSON, H. & THIELEN, H. (1986a). Mathematical simulation of the dynamics of pipelines laid in the open in case of unsteady flows. report on the measurements and numerical simulation of the measurements on the jade transshipment station. In: *Universität Karlsruhe, Institut für Hydromechanik, Bericht Nr. 622, Karlsruhe, Germany*.
- BÜRMAN, W., FESER, G., JANSON, H. & THIELEN, H. (1986b). Mathematical simulation of the dynamics of pipelines laid in the open in case of unsteady flows. report on the second measurements and numerical simulation. In: *Universität Karlsruhe, Institut für Hydromechanik, Bericht Nr. 640, Karlsruhe, Germany*.
- BÜRMAN, W., FESER, G., JANSON, H. & THIELEN, H. (1987). Pressure and acceleration measurements on the pipe bridge of a long-distance water main to study the piping dynamics in case of unsteady flow. In: *Proc., 3R International*, vol. 26.
- BÜRMAN, W. & THIELEN, H. (1988a). Measurement and computation of dynamic reactive forces on pipes containing flow. In: *Proc., 3R International*, vol. 27.
- BÜRMAN, W. & THIELEN, H. (1988b). Measurement and computation of dynamic reactive forces on pipes containing flow. In: *Proc., 3R International*.
- BÜRMAN, W. & THIELEN, H. (1988c). Untersuchung der Bewegung des Befüllstrangs einer Salzkaverne. (Study on the motion of the filling string of a saline cavern.). In: *Proc., 3R International*, vol. 27.
- CAPONE, G., D'AGOSTINO, V., DELLA VALLE, S. & GUIDA, D. (1993). Influence of the variation between static and kinetic friction on stick-slip instability. *Wear* **161**(1), 121–126.
- CARSTENS, M. & ROLLER, J. E. (1959). Boundary-shear stress in unsteady turbulent pipe flow. *Journal of the Hydraulics Division* **85**(2), 67–81.
- CASADEI, F., HALLEUX, J., SALA, A. & CHILLE, F. (2001). Transient fluid–structure interaction algorithms for large industrial applications. *Computer Methods in Applied Mechanics and Engineering* **190**(24), 3081–3110.

- CHAUDHRY, M. H. (2014). *Applied Hydraulic Transients*, ISBN: 978-1-4614-8537-7. New York, NY: Springer New York.
- CHEN, C.-C. (2012). *Noise and vibration in complex hydraulic tubing systems, Continuum Mechanics - Progress in Fundamentals and Engineering Applications, Dr. Yong Gan (Ed.)*, ISBN: 978-953-51-0447-6. INTECH Open Access Publisher.
- CHUNG, Y. & WANG, Z. (2015). Direct numerical investigation of unsteady turbulent pipe flow. In: *Proc., 12th Int. Conf. on Pressure Surges, Dublin*.
- CLARK, R. & REISSNER, E. (1950). Deformations and stresses in bourdon tubes. *Journal of Applied Physics* **21**(12), 1340–1341.
- CLEBSCH, A. (1883). *Théorie de l'élasticité des corps solides*, ISBN-10: 1172177856. Dunod.
- COCCHI, G. (1988). Esperimento sulla resistenza al deflusso con moto vario in un tubo. *Atti della Accademia delle Scienze dell'Istituto di Bologna, Classe di Scienze Fisiche* **276**, 1987–1988.
- COURTNEY, T. H. (1990). *Mechanical behavior of materials*, ISBN-13: 978-1577664253. McGraw-Hill.
- COVAS, D. (2003). *Inverse transient analysis for leak detection and calibration of water pipe systems modelling special dynamic effects*. Ph.D. thesis, Imperial College London (University of London).
- COVAS, D., RAMOS, H., GRAHAM, N. & MAKSIMOVIC, C. (2004a). The interaction between viscoelastic behaviour of the pipe-wall, unsteady friction and transient pressures. In: *International conference on pressure surges*.
- COVAS, D., RAMOS, H., GRAHAM, N. & MAKSIMOVIC, C. (2004b). The interaction between viscoelastic behaviour of the pipe-wall, unsteady friction and transient pressures. In: *International conference on pressure surges, proceedings*.
- COVAS, D., STOIANOV, I., GRAHAM, N., MAKSIMOVIC, C., RAMOS, H. & BUTLER, D. (2002). Hydraulic transients in polyethylene pipes. In: *Proc., 2002 Conf. EWRI. ASCE*.
- COVAS, D., STOIANOV, I., MANO, J. F., RAMOS, H., GRAHAM, N. & MAKSIMOVIC, C. (2005). The dynamic effect of pipe-wall viscoelasticity in hydraulic transients. Part II—model development, calibration and verification. *Journal of Hydraulic Research* **43**(1), 56–70.
- COVAS, D., STOIANOV, I., RAMOS, H., GRAHAM, N. & MAKSIMOVIC, C. (2004c). The dynamic effect of pipe-wall viscoelasticity in hydraulic transients. Part I—experimental analysis and creep characterization. *Journal of Hydraulic Research* **42**(5), 517–532.
- COVAS, D., STOIANOV, I., RAMOS, H., GRAHAM, N., MAKSIMOVIC, Č. & BUTLER, D. (2004d). Water hammer in pressurized polyethylene pipes: conceptual model and experimental analysis. *Urban Water Journal* **1**(2), 177–197.

Bibliography

- DAILY, J., HANKEY JR, W., OLIVE, R. & JORDAAN JR, J. (1955). Resistance coefficients for accelerated and decelerated flows through smooth tubes and orifices. Tech. rep., DTIC Document.
- DAVIDSON, L. & SAMSURY, D. (1969). Liquid-Structure Coupling in Curved Pipes-I. *The Shock and Vibration Bulletin* **40**(4), 197–207.
- DAVIDSON, L. & SAMSURY, D. (1972). Liquid-Structure Coupling in Curved Pipes-II. *The Shock and Vibration Bulletin* **43**(1), 123–135.
- DAVIS, J. R. (1997). *Concise metals engineering data book*, ISBN-13: 978-0871706065. Asm International.
- DE JONG, C. (1994). *Analysis of pulsations and vibrations in fluid-filled pipe systems*, ISBN: 9038600747. TNO Institute of Applied Physics.
- DI LIBERTO, M., DI PIAZZA, I. & CIOFALO, M. (2013). Turbulence structure and budgets in curved pipes. *Computers & Fluids* **88**, 452–472.
- DUAN, H.-F., GHIDAOU, M. S. & TUNG, Y.-K. (2009). An efficient quasi-2d simulation of waterhammer in complex pipe systems. *Journal of Fluids Engineering* **131**(8).
- DWIVEDY, S. (n.d.). Introduction to vibration and stability analysis of mechanical systems .
- ELANSARY, A. & CONTRACTOR, D. (1990). Minimization of stresses and pressure surges. *Journal of Pressure Vessel Technology* **112**(3), 311–316.
- ELANSARY, A. & CONTRACTOR, D. (1994). Valve closure: method for controlling transients. *Journal of Pressure Vessel Technology* **116**(4), 437–442.
- ELANSARY, A. S., CHAUDHRY, M. H. & SILVA, W. (1994). Numerical and experimental investigation of transient pipe flow. *Journal of Hydraulic Research* **32**(5), 689–706.
- ELLIS, J. (1980). A study of pipe-liquid interaction following pump trip and check-valve closure in a pumping station. In: *Proceedings 3rd International Conference on Pressure Surges*, vol. 1.
- ERATH, W., NOWOTNY, B. & MAETZ, J. (1998). Simultaneous coupling of the calculation of pressure waves and pipe oscillations. *3R International* **37**(8), 501.
- ERATH, W., NOWOTNY, B. & MAETZ, J. (1999). Modelling the fluid structure interaction produced by a waterhammer during shutdown of high-pressure pumps. *Nuclear Engineering and Design* **193**(3), 283–296.
- FAN, D. (1989). Fluid-structure interactions in internal flows (Ph.D. thesis). *University of Dundee, Department of Civil Engineering, Dundee, UK* .
- FAN, D. & VARDY, A. (1994). Waterhammer including fluid-structure interactions. In: *Proceedings of the First International Conference on Flow Interaction*.

- FEENY, B., GURAN, A., HINRICHS, N. & POPP, K. (1998). A historical review on dry friction and stick-slip phenomena. *Applied Mechanics Reviews* **51**(5), 321–341.
- FEENY, B. & LIANG, J. (1996). A decrement method for the simultaneous estimation of coulomb and viscous friction. *Journal of Sound and Vibration* **195**(1), 149–154.
- FERRÁS, D., COVAS, D. I. & SCHLEISS, A. J. (2014). Stress–strain analysis of a toric pipe for inner pressure loads. *Journal of Fluids and Structures* **51**, 68–84.
- FERRÁS, D., MANSO, P. A., COVAS, D. I. & SCHLEISS, A. J. (2015a). Comparison of conceptual models for fluid-structure interaction in pipe coils during hydraulic transients. *Journal of Hydraulic Research (under review)*.
- FERRÁS, D., MANSO, P. A., COVAS, D. I. & SCHLEISS, A. J. (2015b). Experimental evidence of damping mechanisms during hydraulic transients in pipe flow. *Journal of Fluids and Structures (submitted)*.
- FORSYTHE, G. E., WASOW, W. R. *et al.* (1960). *Finite-difference methods for partial differential equations*, ISBN 13: 9780471266976. Wiley.
- FOX, G. & MERCKX, K. (1973). Pressure wave transmission in a fluid contained in a plastically deforming pipe. Tech. rep., Hanford Engineering Development Lab., Richland, Wash.(USA).
- FRANKE, P.-G. (1983). Computation of unsteady pipe flow with respect to visco-elastic material properties. *Journal of Hydraulic Research* **21**(5), 345–353.
- FREITAS RACHID, F. & COSTA MATTOS, H. (1995). Pressure transients in damageable elasto-plastic pipes. Tech. rep., American Society of Mechanical Engineers, New York, NY (USA).
- FREITAS RACHID, F. B., DA GAMA, R. M. S. & DA COSTA MATTOS, H. (1994). Modelling of hydraulic transient in damageable elasto-viscoplastic piping systems. *Applied mathematical modelling* **18**(4), 207–215.
- FRIZELL, J. (1898). Pressures resulting from changes of velocity of water in pipes. *Transactions of the American Society of Civil Engineers* **39**(1), 1–7.
- GALE, J. & TISELJ, I. (2005). Applicability of the Godunov's Method for Fundamental Four-Equation FSI Model. In: *Proceedings of International Conference on Nuclear Energy for New Europe 2005*.
- GALE, J. & TISELJ, I. (2006). Eight equation model for arbitrary shaped pipe conveying fluid. In: *Proceedings of the International Conference on Nuclear Energy for New Europe, Portoroz, Slovenia*.
- GALLY, M., GÜNEY, M. & RIEUTORD, E. (1979). An investigation of pressure transients in viscoelastic pipes. *Journal of Fluids Engineering* **101**, 495.

Bibliography

- GHIDAOU, M. S. (2004). On the fundamental equations of water hammer. *Urban Water Journal* **1**(2), 71–83.
- GHIDAOU, M. S., MANSOUR, S. G. & ZHAO, M. (2002). Applicability of quasisteady and axisymmetric turbulence models in water hammer. *Journal of Hydraulic Engineering* **128**(10), 917–924.
- GHIDAOU, M. S., ZHAO, M., MCINNIS, D. A. & AXWORTHY, D. H. (2005). A review of water hammer theory and practice. *Applied Mechanics Reviews* **58**(1), 49–76.
- GHODHBANI, A. & HADJ-TAÏEB, E. (2013). Numerical coupled modeling of water hammer in quasi-rigid thin pipes, isbn: 978-3-642-37142-4. In: *Design and Modeling of Mechanical Systems*. Springer, pp. 253–264.
- GIANNOPAPA, C. G. (2004). *Fluid structure interaction in flexible vessels*. Ph.D. thesis, University of London King's College.
- GOLDBERG, D. E. & BENJAMIN WYLIE, E. (1983). Characteristics method using time-line interpolations. *Journal of Hydraulic Engineering* **109**(5), 670–683.
- GOLDBERG, J. E., KORMAN, T. & BALUCH, M. H. (1974). On the use of various shell theories in the analysis of axisymmetrically loaded circular containers. *Nuclear Engineering and Design* **30**(1), 88–92.
- GOLIA, U. (1990). Sulla valutazione delle forze resistenti nel colpo d'ariete. *Report n 639*.
- GORMAN, D., REESE, J. & ZHANG, Y. (2000). Vibration of a flexible pipe conveying viscous pulsating fluid flow. *Journal of Sound and Vibration* **230**(2), 379–392.
- GREGORY, R. & PAIDOUSSIS, M. (1966). Unstable oscillation of tubular cantilevers conveying fluid. In: *Proceedings of the Royal Society of London A: Mathematical, Physical and Engineering Sciences*, vol. 293. The Royal Society.
- GROMEKA, I. (1883). On the velocity of propagation of wave-like motion of fluids in elastic tubes. *Physical Mathematical Section of the Scientific Society of the Imperial University of Kazan, Russia* **5**, 1–19.
- HACHEM, F. E. & SCHLEISS, A. J. (2011). A review of wave celerity in frictionless and axisymmetrical steel-lined pressure tunnels. *Journal of Fluids and Structures* **27**(2), 311–328.
- HACHEM, F. E. & SCHLEISS, A. J. (2012). Effect of drop in pipe wall stiffness on water-hammer speed and attenuation. *Journal of Hydraulic Research* **50**(2), 218–227.
- HALLIWELL, A. (1963). Velocity of a water-hammer wave in an elastic pipe. *Journal of the Hydraulics Division* **89**(4), 1–21.
- HAMILTON, M. & TAYLOR, G. (1996a). Pressure surge – case studies. In: *Proc. of 7th Int Conf on Pressure Surges and Fluid Transients in Pipelines and Open Channels*, BHR Group, Harrogate, U.K.

- HAMILTON, M. & TAYLOR, G. (1996b). Pressure surge – criteria for acceptability. In: *Proc. of 7th Int Conf on Pressure Surges and Fluid Transients in Pipelines and Open Channels*, BHR Group, Harrogate, U.K.
- HARA, F. (1988). Seismic vibration analysis of fluid-structure interaction in LMFBR piping systems. *Journal of Pressure Vessel Technology* **110**(2), 177–181.
- HATFIELD, F. & WIGGERT, D. (1983). Harmonic analysis of coupled fluid and piping. In: *Proc. of ASCE Engineering Mechanics Speciality Conference, Purdue University, U.S.A.*
- HATFIELD, F. & WIGGERT, D. (1990). Seismic pressure surges in liquid-filled pipelines. *Journal of Pressure Vessel Technology* **112**(3), 279–283.
- HATFIELD, F. & WIGGERT, D. (1991). Water hammer response of flexible piping by component synthesis. *Journal of Pressure Vessel Technology* **113**(1), 115–119.
- HEINSBROEK, A. (1997). Fluid-structure interaction in non-rigid pipeline systems. *Nuclear Engineering and Design* **172**(1), 123–135.
- HEINSBROEK, A. & KRUISBRINK, A. (1993). Fluid-structure interaction in non-rigid pipeline systems-large scale validation experiments. In: *Transactions of the 12. international conference on Structural Mechanics in Reactor Technology (SMiRT). Volume J: Structural dynamics and extreme loads analysis.*
- HEINSBROEK, A. & TIJSSELING, A. (1994). The influence of support rigidity on waterhammer pressures and pipe stresses. In: *Proc of 2nd Int Conf on Water Pipeline Systems, BHR Group.*
- HELMHOLTZ, H. (1882). Report on theoretical acoustics concerning works of the years 1848 and 1849. *Gesammelte wissenschaftliche Abhandlungen* **1**, 233–255.
- HINO, M., SAWAMOTO, M. & TAKASU, S. (1977). Study on the transition to turbulence and frictional coefficient in an oscillatory pipe flow. *Transactions of JSCE* **9**, 282–284.
- HOLMBOE, E. & ROULEAU, W. (1967). The effect of viscous shear on transients in liquid lines. *Journal of Basic Engineering* **89**(1), 174–180.
- HOUSNER, G. (1952). Bending vibrations of a pipe line containing flowing fluid. *Journal of Applied Mechanics-Transactions of the ASME* **19**(2), 205–208.
- HU, C.-K. & PHILLIPS, J. (1981). Pulse propagation in fluid-filled elastic curved tubes. *Journal of Pressure Vessel Technology* **103**(1), 43–49.
- JAEGER, C., KERR, L. & WYLIE, E. (1948). Water hammer effects in power conduits. *Civil Engineering and Public Works Review* **23**(500-503).
- JANELA, J., MOURA, A. & SEQUEIRA, A. (2010). A 3d non-newtonian fluid–structure interaction model for blood flow in arteries. *Journal of Computational and Applied Mathematics* **234**(9), 2783–2791.

Bibliography

- JANSSENS, M., VERHEIJ, J. & THOMPSON, D. (1999). The use of an equivalent forces method for the experimental quantification of structural sound transmission in ships. *Journal of Sound and Vibration* **226**(2), 305–328.
- JELEV, I. (1989). The damping of flow and pressure oscillations in water hammer analysis. *Journal of Hydraulic Research* **27**(1), 91–114.
- JENDRZEJCZYK, J. & CHEN, S. (1985). Experiments on tubes conveying fluid. *Thin-Walled Structures* **3**(2), 109–134.
- JONES, D. R. & ASHBY, M. F. (2005). *Engineering materials 2: an introduction to microstructures, processing and design*, ISBN: 978-0-08-096668-7. Butterworth-Heinemann, Oxford, UK.
- JONES, S. E. & WOOD, D. (1972). The effect of axial boundary motion on pressure surge generation. *Journal of Basic Engineering* **94**(2), 441–446.
- JOUGUET, E., JOUGUET, E., RATEAU, A. & DE SPARRE, M. (1914). Théorie générale des coups de bélier. *Jouguet E, Rateau A, de Sparre M, Étude théorique et expérimentale sur les coups de bélier dans les conduites forcées, Rapport établis à l'occasion du 2e Congrès de la Houille Blanche, Lyon*.
- JOUKOWSKY, N. (1904). On the hydraulic hammer in water supply pipes. *Proceeding of the American Water Works Association* **24**, 341–424.
- JOUNG, I.-B. & SHIN, Y. (1987). A new model on transient wave propagation in fluid-filled tubes. *Journal of Pressure Vessel Technology* **109**(1), 88–93.
- KAGAWA, T., LEE, I., KITAGAWA, A. & TAKENAKA, T. (1983). High speed and accurate computing method of frequency-dependent friction in laminar pipe flow for characteristics method. *Trans. Jpn. Soc. Mech. Eng., Ser. A* **49**(447), 2638–2644.
- KELLNER, A., VOSS, J. & SCHOENFELDER, C. (1983). Fluid-structure-interaction in piping systems: Experiment and theory. In: *Transactions of the 7. international conference on structural mechanics in reactor technology. Vol. B*.
- KERAMAT, A. & TIJSSELING, A. (2012). Waterhammer with column separation, fluid-structure interaction and unsteady friction in a viscoelastic pipe. In: *International Conference on Pressure Surges, Lisbon, Portugal*.
- KOJIMA, E. & SHINADA, M. (1988). Dynamic behavior of a finite length straight pipe subject to water-hammer (2nd report, for a very thin-walled pipe). *Trans. Jpn. Soc. Mech. Eng., Ser. B* **54**, 3346–3353.
- KOMPARE, B., JØRGENSEN, S. E., BRATKO, I. & STEINMAN, F. (1995). *The use of artificial intelligence in ecological modelling: Ph. D. Thesis*. FGG.
- KOO, G. & PARK, Y. (1998). Vibration reduction by using periodic supports in a piping system. *Journal of Sound and Vibration* **210**(1), 53–68.

- KORTEWEG, D. (1878). Ueber die Fortpflanzungsgeschwindigkeit des Schalles in elastischen Röhren. *Annalen der Physik* **241**(12), 525–542.
- KRAUSE, N., GOLDSMITH, W. & SACKMAN, J. (1977). Transients in tubes containing liquids. *International Journal of Mechanical Sciences* **19**(1), 53–68.
- KRUISBRINK, A. (1990). Modelling of safety and relief valves in waterhammer computer codes. In: *Proceedings 3rd International Conference on Developments in Valves and Actuators for Fluid Control, BHRA, Bournemouth, U.K.*
- KRUISBRINK, A. & HEINSBROEK, A. (1992). Fluid-structure interaction in non-rigid pipeline systems - large scale validation tests. In: *Proceedings of the International Conference on Pipeline Systems, BHR Group, Manchester, U.K.*
- KUHN, T. S. (2012). *The structure of scientific revolutions*. University of Chicago press.
- KUIKEN, G. (1988). Amplification of pressure fluctuations due to fluid-structure interaction. *Journal of Fluids and Structures* **2**(5), 425–435.
- KULAK, R. (1982). Some aspects of fluid-structure coupling. Tech. rep., Argonne National Laboratory, Argonne, IL.
- KULAK, R. (1985). Three-dimensional fluid-structure coupling in transient analysis. *Computers & Structures* **21**(3), 529–542.
- KUROKAWA, J., MORIKAWA, M. *et al.* (1986). Accelerated and decelerated flows in a circular pipe: 1st report, velocity profile and friction coefficient. *Japan Society of Mechanical Engineers* .
- KWONG, A. & EDGE, K. (1996). Structure-borne noise prediction in liquid-conveying pipe systems. *Proceedings of the Institution of Mechanical Engineers, Part I: Journal of Systems and Control Engineering* **210**(3), 189–200.
- KWONG, A. & EDGE, K. (1998). A method to reduce noise in hydraulic systems by optimizing pipe clamp locations. *Proceedings of the Institution of Mechanical Engineers, Part I: Journal of Systems and Control Engineering* **212**(4), 267–280.
- LAGRANGE, J. (1788). *Mécanique Analytique (2 vols.)*, ISBN: 9780511701795. Edition Albert Blanchard, Paris.
- LAMB, H. (1898). On the velocity of sound in a tube, as affected by the elasticity of the walls. *Manchester Memoirs* **42**(10), 116.
- LAMBOSSY, P. (1950). Aperçu historique et critique sur le problème de la propagation des ondes dans un liquide compressible enfermé dans un tube élastique. 1. *Helvetica Physiologica et Pharmacologica Acta* **8**(2), 209–227.
- LAPLACE, P. S., BOWDITCH, N. & BOWDITCH, N. I. (1829). Mécanique céleste. *Meccanica* **1**.
- LAVOOIJ, C. (1987). FLUSTRIN: Benchmark problems .

Bibliography

- LAVOOIJ, C. & TIJSSELING, A. S. (1989). Fluid-structure interaction in compliant piping systems. In: *Proc., 6th Int. Conf. on Pressure Surges, Cambridge, U.K.*
- LAVOOIJ, C. & TIJSSELING, A. S. (1991). Fluid-structure interaction in liquid-filled piping systems. *Journal of Fluids and Structures* **5**(5), 573–595.
- LESMEZ, M. W., WIGGERT, D. & HATFIELD, F. (1990). Modal analysis of vibrations in liquid-filled piping systems. *Journal of Fluids Engineering* **112**(3), 311–318.
- LI, Q., YANG, K. & ZHANG, L. (2003). Analytical solution for fluid-structure interaction in liquid-filled pipes subjected to impact-induced water hammer. *Journal of Engineering Mechanics* **129**(12), 1408–1417.
- LOCHER, F., HUNTAMER, J. & O’SULLIVAN, J. (2000). Caution-pressure surges in process and industrial systems may be fatal. In: *BHR Group Conference Series*, vol. 39. Bury St. Edmunds; Professional Engineering Publishing.
- LOH, K. & TIJSSELING, A. S. (2014). Water hammer (with FSI): Exact solution—parallelization and application. In: *ASME 2014 Pressure Vessels and Piping Conference*. American Society of Mechanical Engineers.
- MARTINS, N. M. (2016). Transient flow dynamics in pressurized pipes: CFD modelling and experimental analysis (Ph.D. thesis). Instituto Superior Técnico da Universidade de Lisboa, Portugal.
- MARTINS, N. M., SOARES, A. K., RAMOS, H. M. & COVAS, D. I. (2015a). Entrapped air pocket analysis using CFD. In: *Proc., 12th Int. Conf. on Pressure Surges, Dublin*.
- MARTINS, N. M., SOARES, A. K., RAMOS, H. M. & COVAS, D. I. (2015b). Wall shear stress in unsteady flow analysis using CFD. In: *Proc., 12th Int. Conf. on Pressure Surges, Dublin*.
- MARTINS, N. M., SOARES, A. K., RAMOS, H. M. & COVAS, D. I. (2016). CFD modeling of transient flow in pressurized pipes. *Computers & Fluids* **126**, 129–140.
- MCDONALD, D. A. (1974). *Blood flow in arteries*, isbn-13: 9780713142136 .
- MEIBNER, E. & FRANKE, G. (1977). Influence of pipe material on the dampening of water-hammer. In: *Proceedings of the 17th Congress of the International Association for Hydraulic Research*.
- MENDILUCE, E. (1987). El golpe de ariete en impulsiones. *Librería Editorial Bellisco. Madrid* .
- MESERVE, R. A. (1987). *Safety issues at the defense production reactors: a report to the US Department of Energy*. National Academies.
- MICHAUD, J. (1878). ‘coups de bélier dans les conduites. étude des moyens employés pour en atténuer les effects. *Bull. Soc. Vaudoise Ing. Arch* **4**(3), 4.

- MITOSEK, M. & ROSZKOWSKI, A. (1998). Empirical study of water hammer in plastics pipes. *Plastics rubber and composites processing and applications* **27**(9), 436–439.
- MOENS, A. (1998). The pulsation. *The Netherlands : E.J. Brill* .
- MOSER, M., HECKL, M. & GINTERS, K.-H. (1986). On wave propagation of fluid-filled circular cylindrical tubes. In: *Acustica*, 60.
- MOUSSOU, P., LAFON, P., POTAPOV, S., PAULHIAC, L. & TIJSSELING, A. (2004). Industrial cases of fsi due to internal flows. In: *Proc. of the 9th Int. Conf. on Pressure Surges*, vol. 1.
- MUELLER, W. (1987). Uncoupled and coupled analysis of a large HDR pipe. In: *Transactions of the 9th international conference on structural mechanics in reactor technology. Vol. F*.
- NAKORYAKOV, V., SOBOLEV, V., SHRIEBER, I. & SHTIVEL'MAN, B. Y. (1976). Water hammer and propagation of perturbations in elastic fluid-filled pipes. *Fluid Dynamics* **11**(4), 493–498.
- NEWTON, I. (1686). *Philosophiae Naturalis Principia Mathematica*, ISBN: 84-487-0140-2. Royal Society Press, London.
- NICHOLS, W., O'ROURKE, M. & VLACHOPOULOS, C. (2011). *McDonald's blood flow in arteries: theoretical, experimental and clinical principles*, ISBN: 9780340985014. CRC Press.
- OBRADOVI'Ć, P. (1990). Fluid-structure interactions: an accident which has demonstrated the necessity for FSI analysis. In: *15th IAHR Symposium on Hydraulic Machinery and Cavitation, Belgrade, Yugoslavia*.
- PAIDOUSSIS, M. & LAITHIER, B. (1976). Dynamics of Timoshenko beams conveying fluid. *Journal of Mechanical Engineering Science* **18**(4), 210–220.
- PAIDOUSSIS, M. P. & ISSID, N. (1974). Dynamic stability of pipes conveying fluid. *Journal of Sound and Vibration* **33**(3), 267–294.
- PEZZINGA, G. & SCANDURA, P. (1995). Unsteady flow in installations with polymeric additional pipe. *Journal of Hydraulic Engineering* **121**(11), 802–811.
- RACHID, F., MATTOS, H. & STUCKENBRUCK, S. (1992). Water hammer in inelastic pipes: an approach via internal variable constitutive theory. In: *Proceedings of the International Conference on Unsteady Flow and Fluid Transients*.
- RACHID, F. & STUCKENBRUCK, S. (1989). Transients in liquid and structure in viscoelastic pipes. In: *Proceedings of the 6th International Conference on Pressure Surges, BHRA, Cambridge, U.K.*
- RACHID, F. B. F. & MATTOS, H. S. C. (1999). On the suitability of the low Mach number assumption in the modelling of the damage induced by pressure transients in piping systems. *Journal of Fluids Engineering* **121**(1), 112–117.

Bibliography

- RACHID, F. F. & COSTA MATTOS, H. (1998). Modelling of pipeline integrity taking into account the fluid-structure interaction. *Int. J. Numer. Methods Fluids* **28**, 337–355.
- RACHID, F. F., COSTA MATTOS, H. & STUCKENBRUCK, S. (1991). Fluidstructure interaction in elasto-viscoplastic piping systems. In: *Proc of first ASME & JSME Joint Fluids Engineering Conf.*
- RACHID, F. F. & MATTOS, H. C. (1994). Model for structural failure of elasto-viscoplastic pipelines. *Meccanica* **29**(3), 293–304.
- RAMOS, H., COVAS, D., BORGA, A. & LOUREIRO, D. (2004). Surge damping analysis in pipe systems: modelling and experiments. *Journal of Hydraulic Research* **42**(4), 413–425.
- RANKINE, W. M. (1870). On the thermodynamic theory of waves of finite longitudinal disturbance. *Philosophical Transactions of the Royal Society of London*, 277–288.
- REGETZ, J. (1960). An experimental determination of the dynamic response of a long hydraulic line. *Washington: National Aeronautics and Space Administration (NASA), Technical Note, D-576*.
- REISSNER, E., CLARK, R. & GILROY, R. (1952). Stresses and deformations of torsional shells of an elliptical cross section with applications to the problems of bending of curved tubes and the bourdon gage. *Transaction of ASME, Journal of Applied Mechanics*, 37–48.
- RESAL, H. (1876). Note on the small motions of incompressible fluids in an elastic tube. *Journal de Mathematiques Pures et Appliquees* **3**(2), 342–344.
- RIEDELMEIER, S., BECKER, S. & SCHLÜCKER, E. (2014). Damping of water hammer oscillations—comparison of 3D CFD and 1D calculations using two selected models for pipe friction. *PAMM* **14**(1), 705–706.
- RIEUTFORD, E. & BLANCHARD, A. (1979). Ecoulement non-permanent en conduite viscoelastique—coup de bélier. *J. Hydraul. Res. IAHR* **17**(1), 217–229.
- RIEUTORD, E. (1982). Transient response of fluid viscoelastic lines. *Journal of Fluids Engineering* **104**, 335.
- ROMANDER, C., SCHWER, L. & CAGLIOSTRO, D. (1980). Response of water-filled thin-walled pipes to pressure pulses: experiments and analysis. *Journal of Pressure Vessel Technology* **102**(1), 56–61.
- RUTTEN, M. (1998). Fluid-solid interaction in large arteries (Ph.D. thesis). Eindhoven Univ of Technology, Dept of Mechanical Engineering, Eindhoven, The Netherlands.
- SAFWAT, H. H. & VAN DER POLDER, J. (1973). Friction–frequency dependence for oscillatory flows in circular pipe. *Journal of the Hydraulics Division* **99**(10158 Paper).

- SCHOHL, G. (1993). Improved approximate method for simulating frequency-dependent friction in transient laminar flow. *Transactions-American Society of Mechanical Engineers Journal of Fluids Engineering* **115**, 420–420.
- SCHWARZ, W. (1978). *Druckstoßberechnung unter Berücksichtigung der Radial-und Längsverschiebungen der Rohrwandung*. Eigenverl. des Inst. für Wasserbau, Univ. Stuttgart.
- SEIDE, P. (1975). *Small elastic deformations of thin shells*. Noordhoff International Pub.
- SHARP, B. & THENG, K. (1987). Water hammer attenuation in uPVC pipe. In: *Proc., Conf. on Hydraulics in Civil Engineering*.
- SHUY, E. & APELT, C. (1987). Experimental studies of unsteady shear stress in turbulent flow in smooth round pipes. In: *Conf. on Hydraulics in Civil Engineering*.
- SILVA-ARAYA, W. F. & CHAUDHRY, M. H. (1997). Computation of energy dissipation in transient flow. *Journal of Hydraulic Engineering* **123**(2), 108–115.
- SIMÃO, M., FERREIRA, J., MORA-RODRIGUEZ, J. & RAMOS, H. (2016a). Identification of DVT diseases using numerical simulations. *Medical & Biological Engineering & Computing* , 1–19.
- SIMÃO, M., MORA, J. & RAMOS, H. M. (2015a). Fluid–structure interaction with different coupled models to analyse an accident occurring in a water supply system. *Journal of Water Supply: Research and Technology-Aqua* **64**(3), 302–315.
- SIMÃO, M., MORA-RODRIGUEZ, J. & RAMOS, H. M. (2015b). Interaction between hydraulic transient events and structure vibration. In: *Proc., 12th Int. Conf. on Pressure Surges, Dublin*.
- SIMÃO, M., MORA-RODRIGUEZ, J. & RAMOS, H. M. (2015c). Mechanical interaction in pressurized pipe systems: Experiments and numerical models. *Water* **7**(11), 6321–6350.
- SIMÃO, M., MORA-RODRIGUEZ, J. & RAMOS, H. M. (2016b). Dynamic response behind an accident occurred in a main wss. *European Journal of Environmental and Civil Engineering* , 1–21.
- SINHA, A. (2010). *Vibration of mechanical systems, ISBN-13: 978-1107694170*. Cambridge University Press.
- SKALAK, R. (1955). An extension of the theory of water hammer. Tech. rep. Columbia Univ New York Dept of Civil Engineering and Engineering Mechanics.
- SOARES, A. K., COVAS, D. I. & RAMOS, H. M. (2012). Damping analysis of hydraulic transients in pump-rising main systems. *Journal of Hydraulic Engineering* **139**(2), 233–243.
- SOARES, A. K., COVAS, D. I., RAMOS, H. M. & REIS, L. F. R. (2009). Unsteady flow with cavitation in viscoelastic pipes. *International Journal of Fluid Machinery and Systems* **2**(4), 269–277.

Bibliography

- SOARES, A. K., COVAS, D. I. & REIS, L. F. (2008). Analysis of PVC pipe-wall viscoelasticity during water hammer. *Journal of Hydraulic Engineering* **134**(9), 1389–1394.
- STECKI, J. & DAVIS, D. (1986). Fluid transmission lines—distributed parameter models part 1: A review of the state of the art. *Proceedings of the Institution of Mechanical Engineers, Part A: Journal of Power and Energy* **200**(4), 215–228.
- STEELANT, J. (2015). Multi-phase fluid-hammer in aerospace applications. In: *Proc., 12th Int. Conf. on Pressure Surges, Dublin*.
- STREETER, V. L. & WYLIE, E. B. (1978). *Hydraulic Transients*, ISBN-13: 9780070621749. University Microfilms.
- STUCKENBRUCK, S. & WIGGERT, D. (1986). Unsteady flow through flexible tubing with coupled axial wall motion. In: *5th International Conference on Pressure Surges Hannover Germany, Proceedings*.
- SUO, L. & WYLIE, E. (1990). Complex wavespeed and hydraulic transients in viscoelastic pipes. *Journal of Fluids Engineering* **112**(4), 496–500.
- SZYMANSKI, P. (1930). Sur l'écoulement non permanent du fluide vis queux dans le tuyau applied mech. In: *Congress 3rd., Paris, I*.
- SZYMKIEWICZ, R. & MITOSEK, M. (2005). Analysis of unsteady pipe flow using the modified finite element method. *Communications in Numerical Methods in Engineering* **21**(4), 183–199.
- SZYMKIEWICZ, R. & MITOSEK, M. (2007). Numerical aspects of improvement of the unsteady pipe flow equations. *International journal for numerical methods in fluids* **55**(11), 1039–1058.
- TENTARELLI, S. (1990). *Propagation of Noise and Vibration in Complex Hydraulic Tubing Systems*. Ph.D. thesis, Lehigh University, Department of Mechanical Engineering, Bethlehem, U.S.A.
- TENTARELLI, S. C. & BROWN, F. T. (2001). Dynamic behavior of complex fluid-filled tubing systems—part 2: System analysis. *Journal of Dynamic Systems, Measurement, and Control* **123**(1), 78–84.
- THIELEN, H. & BURMANN, W. (1980). Calculation and protection of pipe lines laid in the open against undue internal pressure and reactive forces resulting from water hammer. *3 R international* **19**, 622–628.
- THORLEY, A. (1969). Pressure transients in hydraulic pipelines. *Journal of Basic Engineering* **91**(3), 453–460.
- THORLEY, A. (1976). *A survey of investigations into pressure surge phenomena*. Research Memorandum ML83. City University, Department of Mechanical Engineering, London, UK.

- TIJSSELING, A. (1996). Fluid-structure interaction in liquid-filled pipe systems: a review. *Journal of Fluids and Structures* **10**(2), 109–146.
- TIJSSELING, A. (1997). Poisson-coupling beat in extended waterhammer theory. *ASME-publications-ad* **53**, 529–532.
- TIJSSELING, A. (2003). Exact solution of linear hyperbolic four-equation system in axial liquid-pipe vibration. *Journal of Fluids and Structures* **18**(2), 179–196.
- TIJSSELING, A. (2007). Water hammer with fluid–structure interaction in thick-walled pipes. *Computers & Structures* **85**(11), 844–851.
- TIJSSELING, A., FAN, D. & VARDY, A. (1994). Transient fluid-structure interaction and cavitation in a single-elbow pipe system. In: *Proceedings of the First International Conference on Flow Interaction*.
- TIJSSELING, A. & HEINSBROEK, A. (1999). The influence of bend motion on waterhammer pressures and pipe stresses. In: *ASME & JSME Joint Fluids Engineering Conf, Symp S–290*. ASME-FED 248.
- TIJSSELING, A. & LAVOOIJ, C. (1990). Waterhammer with fluid-structure interaction. *Applied Scientific Research* **47**(3), 273–285.
- TIJSSELING, A. & VARDY, A. (1996a). Axial modelling and testing of a pipe rack. In: *BHR group conference series publication*, vol. 19. Mechanical Engineering Publications Limited.
- TIJSSELING, A. & VARDY, A. (1996b). On the suppression of coupled liquid/pipe vibrations. In: *Hydraulic Machinery and Cavitation*. Springer, pp. 945–954.
- TIJSSELING, A., VARDY, A. & FAN, D. (1996). Fluid-structure interaction and cavitation in a single-elbow pipe system. *Journal of Fluids and Structures* **10**(4), 395–420.
- TIJSSELING, A. S. (1993). *Fluid-structure interaction in case of waterhammer with cavitation*. Ph.D. thesis, TU Delft, Delft University of Technology.
- TIJSSELING, A. S. & ANDERSON, A. (2004). A precursor in waterhammer analysis-rediscovers johannes von kries. In: *Proceedings of the 9th International Conference on Pressure Surges*. Citeseer.
- TIJSSELING, A. S., LAMBERT, M. F., SIMPSON, A. R., STEPHENS, M. L., VÍTKOVSKÝ, J. P. & BERGANT, A. (2008). Skalak's extended theory of water hammer. *Journal of Sound and Vibration* **310**(3), 718–728.
- TIJSSELING, A. S. & VARDY, A. E. (2004). Time scales and FSI in unsteady liquid-filled pipe flow. In: *The 9th International Conference on Pressure Surges, SJ Murray ed., Chester, UK, BHR Group, Cranfield, UK*. Citeseer.

Bibliography

- TIJSSELING, A. S. & VARDY, A. E. (2015). What is wave speed? In: *Proc., 12th Int. Conf. on Pressure Surges, Dublin*.
- TISELJ, I. (2015). State-of-the-art modelling of multi-phase transients. In: *Proc., 12th Int. Conf. on Pressure Surges, Dublin*.
- TRENKLE, C. J. (1979). Failure of riveted and forge-welded penstock. *Journal of the Energy Division* **105**(1), 93–102.
- TRIKHA, A. K. (1975). An efficient method for simulating frequency-dependent friction in transient liquid flow. *ASME Transactions Journal of Fluids Engineering* **97**, 97–105.
- URBANOWICZ, K. & TIJSSELING, A. (2015). Work and life of Piotr Szymański. In: *Proc., 12th Int. Conf. on Pressure Surges, Dublin*.
- VALENTIN, R. A., PHILLIPS, J. W. & WALKER, J. S. (1979). Reflection and transmission of fluid transients at an elbow. Tech. rep., Argonne National Lab., IL (USA).
- VARDY, A. & ALSARRAJ, A. (1989). Method of characteristics analysis of one-dimensional members. *Journal of Sound and Vibration* **129**(3), 477–487.
- VARDY, A. & ALSARRAJ, A. (1991). Coupled axial and flexural vibration of 1-D members. *Journal of Sound and Vibration* **148**(1), 25–39.
- VARDY, A. & BROWN, J. (1996). On turbulent, unsteady, smooth-pipe friction. In: *BHR Group Conference Series*, vol. 19. Mechanical Engineering Publications Limited.
- VARDY, A. & BROWN, J. (2003). Transient turbulent friction in smooth pipe flows. *Journal of Sound and Vibration* **259**(5), 1011–1036.
- VARDY, A. & BROWN, J. (2004). Transient turbulent friction in fully rough pipe flows. *Journal of Sound and Vibration* **270**(1), 233–257.
- VARDY, A. & FAN, D. (1986). Water hammer in a closed tube. In: *Proc. 5th Int. Conf. on Pressure Surges*.
- VARDY, A. & FAN, D. (1987). Constitutive factors in transient internal flows. In: *Proc. of the Int. Conf. on Numerical Methods in Engineering: Theory and Applications (NUMETA 87)*, Swansea, United Kingdom, vol. 2.
- VARDY, A. & FAN, D. (1989). Flexural waves in a closed tube. In: *Proc of 6th Int Conf on Pressure Surges, BHRA*.
- VARDY, A., FAN, D. & TIJSSELING, A. (1996). Fluid-structure interaction in a T-piece pipe. *Journal of Fluids and Structures* **10**(7), 763–786.
- VARDY, A. E. & BROWN, J. M. (1995). Transient, turbulent, smooth pipe friction. *Journal of Hydraulic Research* **33**(4), 435–456.

- VARDY, A. E. & HWANG, K.-L. (1991). A characteristics model of transient friction in pipes. *Journal of Hydraulic Research* **29**(5), 669–684.
- VARDY, A. E. & HWANG, K.-L. (1993). A weighting function model of transient turbulent pipe friction. *Journal of Hydraulic Research* **31**(4), 533–548.
- VARDY, A. E. & TIJSSELING, A. S. (2015). Method of characteristics: (why) is it so good? In: *Proc., 12th Int. Conf. on Pressure Surges, Dublin*.
- VECCIO, R. S., SINHA, S. K., BRUCK, P. M., ESSELMAN, T. C. & ZYSK, G. (2015). The 2007 new york city steam explosion: post-accident analysis. In: *Proc., 12th Int. Conf. on Pressure Surges, Dublin*.
- VITKOVSKY, J. P., LAMBERT, M. F., SIMPSON, A. R. & BERGANT, A. (2000). Advances in unsteady friction modelling in transient pipe flow. In: *International Conference on Pressure Surges (8th: 2000: The Hague, The Netherlands)*.
- VON KRIES, J. (1883). Ueber die beziehungen zwischen druck und geschwindigkeit, welche bei der wellenbewegung in elastischen schlaefluchen bestehen. *On the relations between pressure and velocity, which exist in the wavelike motion in elastic tubes. Festschrift der* **56**, 67–88.
- WALKER, J. & PHILLIPS, J. (1977). Pulse propagation in fluid-filled tubes. *Journal of Applied Mechanics* **44**(1), 31–35.
- WANG, C., PIZZICA, P., GVILDYS, J. & SPENCER, B. (1989). Analysis of fluid-structure interaction and structural response of chernobyl-4 reactor. Tech. rep., Argonne National Lab., IL (USA).
- WARD, I. M. & SWEENEY, J. (2012). *Mechanical properties of solid polymers, ISBN: 978-1-4443-1950-7*. John Wiley & Sons.
- WARE, A. & WILLIAMSON, R. (1982). Blazer: a relap5/modi post processor to generate force-time history input data for structural computer codes. *Am. Soc. Mech. Eng., Pressure Vessels Piping Div., (Tech. Rep.) PVP; (United States)* **64**(CONF-820601-).
- WATHEN, A., GALDI, G., RANNACHER, R., ROBERTSON, A. & TUREK, S. (2009). Hemodynamical flows: Modeling, analysis and simulation, isbn: 978-3-7643-7805-9.
- WEAVER JR, W., TIMOSHENKO, S. P. & YOUNG, D. H. (1990). *Vibration problems in engineering, ISBN 978-0-471-63228-3*. John Wiley & Sons.
- WEBBER, W. (1866). Theory of waves propagating in water or other incompressible liquids contained in elastic pipes **18**, 353–357.
- WEIJDE, P. (1985). Prediction of pressure surges and dynamic forces in pipeline systems, influence of system vibrations on pressures and dynamic forces (fluid–structure interaction). In: *Transactions of the Symposium on Pipelines, Utrecht, The Netherlands*.

Bibliography

- WIGGERT, D. (1983). Fluid-structure interaction in piping systems. In: *Proceedings Druckstoßberechnung von Rohrleitungssystemen, Haus der Technik*. Essen, Germany.
- WIGGERT, D. (1986). Coupled transient flow and structural motion in liquid-filled piping systems: a survey. In: *Proceedings of the ASME Pressure Vessels and Piping Conference*. Chicago, USA.
- WIGGERT, D., HATFIELD, F. & STUCKENBRUCK, S. (1985a). Analysis of liquid and structural transients in piping by the method of characteristics. In: *Fluid Transients in Fluid-Structure Interaction-1985*.
- WIGGERT, D., HATFIELD, F. & STUCKENBRUCK, S. (1987). Analysis of liquid and structural transients in piping by the method of characteristics. *Journal of Fluids Engineering* **109**(2), 161–165.
- WIGGERT, D., OTWELL, R. & HATFIELD, F. (1985b). The effect of elbow restraint on pressure transients. *Journal of Fluids Engineering* **107**(3), 402–406.
- WIGGERT, D. C. & TIJSELING, A. S. (2001). Fluid transients and fluid-structure interaction in flexible liquid-filled piping. *Applied Mechanics Reviews* **54**(5), 455–481.
- WILKINSON, D. (1977). *The Dynamic Response of Pipework Systems to Water Hammer*.
- WILKINSON, D. (1979). Acoustic and mechanical vibrations in liquid-filled pipework systems. In: *Vibration in Nuclear Plant. Proceedings of international conference held at Keswick, UK in May 1978*.
- WILLIAMS, D. (1977). Waterhammer in non-rigid pipes: precursor waves and mechanical damping. *Journal of Mechanical Engineering Science* **19**(6), 237–242.
- WOOD, D. J. (1968). A study of the response of coupled liquid flow-structural systems subjected to periodic disturbances. *Journal of Basic Engineering* **90**(4), 532–540.
- WOOD, D. J. (1969). Influence of line motion on waterhammer pressures. *Journal of the Hydraulics Division* **95**(3), 941–960.
- WOOD, D. J. & CHAO, S. (1971). Effect of pipeline junctions on water hammer surges. *Transportation Engineering Journal* **97**(3), 441–457.
- WOOD, F. M. (1970). *History of water-hammer*. 65. Department of Civil Engineering, Queen's University.
- WU, J.-S. & SHIH, P.-Y. (2001). The dynamic analysis of a multispans fluid-conveying pipe subjected to external load. *Journal of Sound and Vibration* **239**(2), 201–215.
- WYLIE, E. B., STREETER, V. L. & SUO, L. (1993). *Fluid transients in systems*, ISBN-13: 978-0139344237. Prentice Hall Englewood Cliffs, NJ.

- YANG, K., LI, Q. & ZHANG, L. (2004). Longitudinal vibration analysis of multi-span liquid-filled pipelines with rigid constraints. *Journal of Sound and Vibration* **273**(1), 125–147.
- YOUNG, F. & HUNTER, S. (1979). Hydraulic transients in liquid-filled pipelines during earthquakes. *Lifeline Earthquake Engineering—Buried Pipelines, Seismic Risk and Instrumentation*.
- YOUNG, T. (1808). Hydraulic investigations, subservient to an intended croonian lecture on the motion of the blood. *Philosophical Transactions of the Royal Society of London* **98**, 164–186.
- YU, J. & KOJIMA, E. (1998). Wave propagation in fluids contained in finite-length anisotropic viscoelastic pipes. *The Journal of the Acoustical Society of America* **104**(6), 3227–3235.
- ZANGANEH, R., AHMADI, A. & KERAMAT, A. (2015). Fluid–structure interaction with viscoelastic supports during waterhammer in a pipeline. *Journal of Fluids and Structures* **54**, 215–234.
- ZARZYCKI, Z. (1997). Hydraulic resistance of unsteady turbulent liquid flow in pipes. In: *BHR Group Conference Series*.
- ZARZYCKI, Z. (2000). On weighting function for wall shear stress during unsteady turbulent pipe flow. In: *BHR Group Conference Series*, vol. 39. Bury St. Edmunds; Professional Engineering Publishing; 1998.
- ZHANG, X., HUANG, S. & WANG, Y. (1994). The FEM of fluid structure interaction in piping pressure transients. In: *Proceedings of the First International Conference on Flow Interaction*.
- ZHOU, L., LIU, D. & KARNEY, B. (2013). Investigation of hydraulic transients of two entrapped air pockets in a water pipeline. *Journal of Hydraulic Engineering* **139**(9), 949–959.
- ZHOU, L., LIU, D.-Y. & OU, C.-Q. (2011). Simulation of flow transients in a water filling pipe containing entrapped air pocket with VOF model. *Engineering Applications of Computational Fluid Mechanics* **5**(1), 127–140.
- ZIELKE, W. (1968). Frequency-dependent friction in transient pipe flow. *Journal of Basic Engineering* **90**, 109.
- ZINGONI, A. (1997). *Shell structures in civil and mechanical engineering: theory and closed-form analytical solutions*. Inst of Civil Engineers Pub.



Curriculum vitae

DAVID FERRAS

(david.ferras@gmail.com)

KEY COMPETENCES AND SKILLS

Civil engineer with 10 years of experience in consultancy, water management and research.
Fields of expertise: Numerical modelling, water management, hydropower, pipeline engineering, urban water and drainage networks, hydraulic transients, computational hydraulics.

EDUCATION

Instituto Superior Técnico (IST) and
Ecole Polytechnique Fédérale de Lausanne (EPFL) *September 2016*
PhD research: Fluid-structure interaction, unsteady friction and pipe rheological behaviour in pressurized transient flows

University of Nice - Sophia Antipolis (FR)
Brandenburg University of Technology Cottbus (DE)
Budapest University of Technology and Economics (HU)
Technical University of Catalonia (ES) and
Newcastle University (UK) *September 2012*
MSc Hydro-Informatics and Water Management (EuroAqua), specialization in software engineering and modelling

Technical University of Catalonia (UPC) *June 2006*
Civil engineering diploma, specialization in Hydrology and Hydraulics

PROFESSIONAL EXPERIENCE

Ecole Polytechnique Fédérale de Lausanne (EPFL) September 2012 - September 2016
Research and teaching assistant *Lausanne, Switzerland*

- Student project work supervisions.
- Collaboration in lectures on “Réseaux hydrauliques et énergétiques” with Dr Giovanni de Cesare.

Vrije Universiteit Brussel (VUB) February 2012 - September 2012
Internship/MSc Thesis *Brussels, Belgium*

- Collaboration in AfroMaison project (Africa at mesoscale -FP7 project-).
- Evaluation of different concepts of spatially distributed hydrological models in the Upper Blue Nile River basin using remote sensing data (SWAT, R).

Ecole Polytechnique Fédérale de Lausanne (EPFL) June 2011 - September 2011
Internship *Lausanne, Switzerland*

- Collaboration in ADAPT project (African Dams Project).
- Database (phpMyAdmin).
- Calibration and sensitivity analysis of hydrological model (SWAT, MatLab).

EMATSA (“Agua de Barcelona” Group) February 2006 - September 2010
Project engineer and operations *Tarragona, Spain*

- Urban drainage simulation (MOUSE, MIKE-URBAN, INFOWORKS).
- Master plans and projects of drainage networks.
- Technical assistance of sewerage works.

SOREA (“Aguas de Barcelona” Group)
Project engineer

September 2005 February 2006
Barcelona, Spain

- Urban drainage simulation (MOUSE).
- Master plans and projects of drainage networks.

EPTISA
Part-time

September 2004 September 2005
Barcelona, Spain

- Roadway projects, hydrology and drainage studies (HEC-RAS).
- Environmental impact analyses.

LANGUAGES

Catalan: native; Spanish: native; English: fluent.

PROGRAMMING LANGUAGES

MATLAB, R, C++

HONORS AND AWARDS

John F. Kennedy Student Paper Competition. 1st prize in the 36th IAHR World Congress, 2015.

FCT doctoral grant for the PhD joint doctoral initiative between IST (Lisbon) and EPFL (Lausanne) from Oct.2012 to Oct.2016.

Erasmus Mundus scholarship for the Master course Euroaquae during the academic years 2010-2012.

PUBLICATIONS AND CONFERENCES

- D. Ferras, P. Manso, D. Covas, A.J. Schleiss. Fluid-structure interaction in straight pipelines anchored against longitudinal movement. *Submitted at the Journal of Sound and Vibration (April 2016)*.
- D. Ferras, P. Manso, D. Covas, A.J. Schleiss. Fluid-structure interaction in straight pipelines: friction coupling mechanisms. *Accepted for publication at the Journal of Computers and Structures (June 2016)*.
- D. Ferras, P. Manso, D. Covas, A.J. Schleiss. Experimental evidence of damping mechanisms during hydraulic transients in pipe flow. *Accepted for publication at the Journal of Fluids and Structures (June 2016)*.
- D. Ferras, P. Manso, D. Covas, A.J. Schleiss. Hydraulic transients in straight and coil pipe rigs. *Proc. of 12th International Conference on Pressure Surges, Dublin 2015*.
- D. Ferras. Fluid-structure interaction in pipe coils during hydraulic transients: numerical and experimental analysis. *Proc. of 36th IAHR World Congress, The Hague 2015*.
- D. Ferras, D. Covas, A.J. Schleiss. Stress-strain analysis of a coiled copper pipe for inner pressure loads. *Proc. of 3rd IAHR Europe Congress: Water-Engineering and Research, number EPFL-CONF-198531, page 279. Faculty of Engineering of University of Porto, 2014*.

Appendix F. *Curriculum vitae*

- D. Ferras, P. Manso, D. Covas, A.J. Schleiss. Comparison of conceptual models for fluid-structure interaction in pipe coils during hydraulic transients. *Submitted at the Journal of Hydraulic Research (July 2014)*.
- D. Ferras, D. Covas, A.J. Schleiss. Stress-strain analysis of a toric pipe for inner pressure loads. *Journal of Fluids and Structures*, 51:68-84, 2014.
- T. Cohen Liechti, J. Matos, D. Ferras, J.L. Boillat and A.J. Schleiss. Hydrological modelling of the Zambezi River Basin taking into account floodplain behaviour by a modified reservoir approach. *International Journal of River Basin Management*, 12(1):29-41, 2014.
- A. van Griensven, K. Kilonzo, D. Ferras, D. Nyolei, T. Alemaheyu and J. van der Kwast. Are distributed models able to predict the hydrological impacts of land use change? In *IAHS-PUB symposium*, Delft, October 23-25, 2012.
- D. Ferras, A. van Griensven, E. White, M.Z Easton. Evaluation of different concepts of spatially distributed hydrological models in the Upper Blue Nile river basin using remote sensing data. In *IAHS-PUB symposium*, Delft, October 23-25, 2012.

